frontiers | Research Topics

Marine biological materials: Functional mechanisms and environmental impacts from the molecular to the macro-scale

Edited by
Gary H. Dickinson, Rebecca Metzler and Shiguo Li

Published in
Frontiers in Marine Science

ISSN 1664-8714
ISBN 978-2-83251-656-0
DOI 10.3389/978-2-83251-656-0

About Frontiers

Frontiers is more than just an open access publisher of scholarly articles: it is a pioneering approach to the world of academia, radically improving the way scholarly research is managed. The grand vision of Frontiers is a world where all people have an equal opportunity to seek, share and generate knowledge. Frontiers provides immediate and permanent online open access to all its publications, but this alone is not enough to realize our grand goals.

Frontiers journal series

The Frontiers journal series is a multi-tier and interdisciplinary set of open-access, online journals, promising a paradigm shift from the current review, selection and dissemination processes in academic publishing. All Frontiers journals are driven by researchers for researchers; therefore, they constitute a service to the scholarly community. At the same time, the *Frontiers journal series* operates on a revolutionary invention, the tiered publishing system, initially addressing specific communities of scholars, and gradually climbing up to broader public understanding, thus serving the interests of the lay society, too.

Dedication to quality

Each Frontiers article is a landmark of the highest quality, thanks to genuinely collaborative interactions between authors and review editors, who include some of the world's best academicians. Research must be certified by peers before entering a stream of knowledge that may eventually reach the public - and shape society; therefore, Frontiers only applies the most rigorous and unbiased reviews. Frontiers revolutionizes research publishing by freely delivering the most outstanding research, evaluated with no bias from both the academic and social point of view. By applying the most advanced information technologies, Frontiers is catapulting scholarly publishing into a new generation.

What are Frontiers Research Topics?

Frontiers Research Topics are very popular trademarks of the *Frontiers journals series*: they are collections of at least ten articles, all centered on a particular subject. With their unique mix of varied contributions from Original Research to Review Articles, Frontiers Research Topics unify the most influential researchers, the latest key findings and historical advances in a hot research area.

Find out more on how to host your own Frontiers Research Topic or contribute to one as an author by contacting the Frontiers editorial office: frontiersin.org/about/contact

Marine biological materials: Functional mechanisms and environmental impacts from the molecular to the macro-scale

Topic editors

Gary H. Dickinson — The College of New Jersey, United States

Rebecca Metzler — Colgate University, United States

Shiguo Li — Research Center for Eco-environmental Sciences, Chinese Academy of Sciences (CAS), China

Citation

Dickinson, G. H., Metzler, R., Li, S., eds. (2023). *Marine biological materials: Functional mechanisms and environmental impacts from the molecular to the macro-scale*. Lausanne: Frontiers Media SA.

doi: 10.3389/978-2-83251-656-0

Table of contents

frontiers | Frontiers in Marine Science

TYPE Editorial
PUBLISHED 30 January 2023
DOI 10.3389/fmars.2023.1145835

OPEN ACCESS

EDITED AND REVIEWED BY
Ciro Rico,
Institute of Marine Sciences of Andalusia (CSIC), Spain

*CORRESPONDENCE
Gary H. Dickinson
dickinga@tcnj.edu
Shiguo Li
sgli@rcees.ac.cn
Rebecca A. Metzler
rmetzler@colgate.edu

SPECIALTY SECTION
This article was submitted to Marine Molecular Biology and Ecology, a section of the journal Frontiers in Marine Science

RECEIVED 16 January 2023
ACCEPTED 23 January 2023
PUBLISHED 30 January 2023

CITATION
Dickinson GH, Li S and Metzler RA (2023) Editorial: Marine biological materials: Functional mechanisms and environmental impacts from the molecular to the macro-scale. *Front. Mar. Sci.* 10:1145835. doi: 10.3389/fmars.2023.1145835

Editorial: Marine biological materials: Functional mechanisms and environmental impacts from the molecular to the macro-scale

Gary H. Dickinson[1]*, Shiguo Li[2,3]* and Rebecca A. Metzler[3]*

[1]Department of Biology, The College of New Jersey, Ewing NJ, United States, [2]Research Center for Eco-Environmental Sciences, Chinese Academy of Sciences, Beijing, China, [3]College of Resources and Environment, University of Chinese Academy of Sciences, Beijing, China, [4]Department of Physics and Astronomy, Colgate University, Hamilton NY, United States

KEYWORDS

biomineralization, adhesion, ocean acidification (OA), climate change, biofouling, exoskeleton, material properties, environmental variation

Editorial on the Research Topic
Marine biological materials: Functional mechanisms and environmental impacts from the molecular to the macro-scale

Introduction

Marine organisms rely on a broad range of structurally and mechanically diverse materials for success in the world's oceans. Among many others, examples include structural materials involved in protection, locomotion, and nourishment (e.g., shells, skeletons, exoskeletons, claws and other feeding structures) and functional materials (e.g., adhesives, holdfasts, defensive secretions, signaling structures). In all cases, these materials are hierarchical with their success depending on multiple levels of biological complexity, from the molecular, to the nano- and micro-scales, to the whole organism scale. These materials have served, and continue to serve, as inspiration for biomimetic materials and approaches (e.g., nacre-inspired composites, exosuits, green fluorescent protein, hydrogels). Understanding the complexities of such materials may also allow us to address current and future major economic and ecological challenges (e.g., biofouling by marine adhesive organisms, shellfish aquaculture yields). A critical aspect of the study of marine biological materials is assessment of how environment affects functional properties and the mechanistic basis for such changes if they occur. Increases in global sea temperatures, reductions in pH (ocean acidification) and associated alterations in carbonate chemistry, variations in salinity and dissolved oxygen content, and anthropogenic noise and pollution, have all been documented to affect structural and functional materials, with the magnitude of the response often taxon-specific. In this Research Topic, we bring together a collection of articles that explore the relationship between environment and marine biological materials through a lens of either the *fundamental mechanisms of function of a material* or the *effects of environment on the material* (Figure 1). All studies incorporated an integrative approach, employing a range of experimental techniques to assess questions of interest at multiple levels of biological complexity.

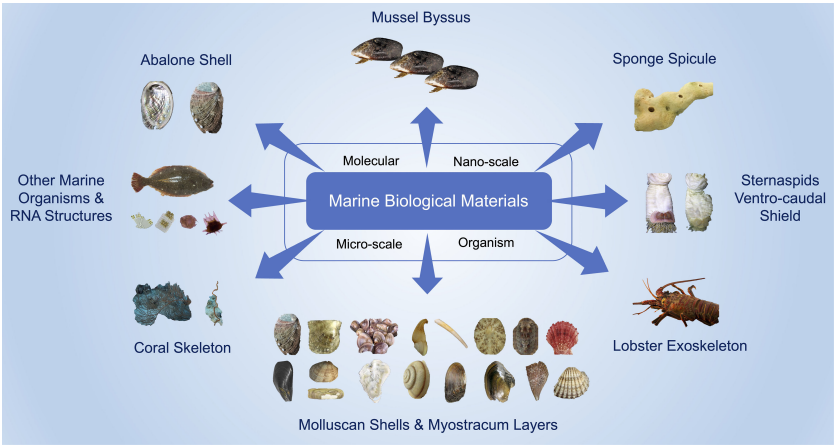

FIGURE 1
Marine organisms and biological materials investigated in this Research Topic.

Fundamental mechanisms of function of marine biological materials

Half of the articles within this Research Topic further our understanding of the basic mechanisms involved in biological materials synthesis and development, with each article focused on a different taxonomic group. Two studies assessed mineralized shell structure and composition within the context of evolutionary history. Dong et al. investigated the myostracum layer in 11 different living mollusks and compared them with that of a fossilized ammonoid. The authors found a high degree of conservation in structure (columnar prisms) and composition (aragonite) among the examined species. Ge et al. studied the ventro-caudal shields of two closely related tube-forming polychaetes. The authors found that the distinctive morphology and composition of the shields likely stems from difference in growth environment, resulting in differential gene regulation. The results emphasize the importance of genetic information in the analysis of biomineralization. In two additional studies, researchers employed novel proteomic techniques to characterize the function and properties of specific proteins involved in the biological material formation process. Work by Drake and Mass assessed the protein component of the sclerotized chitin skeleton of two species of black corals. Hundreds of proteins were identified with a clear compositional distinction from that of stony corals, namely a lack of acidic amino acids. Pozzolini et al. identified 21 diverse proteins, including cathepsins with silicateins and several lysosome enzyme-like proteins, within *Petrosia ficiformis* sponge silica spicules, and propose a lysosomal origin of silicification in these animals. Lastly, the work of Zhang et al. focused on materials at the molecular scale, assessing the role of Drosha, a ribonuclease enzyme. The authors found microRNA (miRNAs) and small interfering RNA (siRNAs) to play an important role in development and metamorphosis of Japanese flounder.

Effects of environment on marine biological materials

The other half of the articles within this Research Topic assessed the effects of environment, broadly speaking, on the formation and properties of marine biological materials. Three of the articles assessed biological materials in mollusks. Huang and Zhang provide a broad review of molluscan shell biomineralization, with a focus on the shell organic matrix, including shell matrix proteins (SMPs), and their effect on minerology. The authors place this work within the context of changes in seawater chemistry over geologic time (e.g., shifts between calcitic and aragonitic seas), encouraging the field to consider the role of environment on biomineralization. Ji et al. characterized shell structure and protein composition and activity following exposure to extreme heat, finding that proteins remained bioactive in mineralization even after exposure to 200°C. The third article on mollusks, by Zhao et al., documented the effects of anthropogenic noise on mussel byssal attachment. The authors showed diminished mechanical properties and down-regulation of genes involved in byssus formation when mussels were exposed to simulated anthropogenic noise. Lowder et al., assessed the effects of reduced pH (ocean acidification) on the mineralized exoskeleton of a crustacean, the California spiny lobster. Exoskeleton mineral content and mechanical properties were reduced at low pH, but in a complex and body-region-dependent manner in which reduced mineral content did not correlate directly with reductions in mechanical properties. A final study, Xu et al., assessed phototrophic microbial communities within the Baltic Sea using 16S rRNA. The authors were able to correlate phototrophic abundance and composition with a broad range of environmental conditions including temperature, pH, salinity, and dissolved oxygen content.

Conclusions and future directions

The collection of articles presented within this Research Topic demonstrate the diversity of biological materials within the marine realm, with materials from seven distinct taxonomic groups represented (Figure 1). Within the field, studies that assess *fundamental mechanisms* of biological material synthesis and development inform work of researchers assessing the *effects of environment* and vice versa. We propose three recommendations

for work on marine biological materials, which, taken individually or in combination, may advance the field. *First*, projects should couple functionality of materials at the whole organism level with the mechanistic basis for that functionality at the meso-, micron-, and molecular scales. For example, researchers might quantify the degree of protection a shell provides against predator attack with characterization of the structure, mechanical properties, and composition of the shell. Importantly, this work should be published together in a single, comprehensive study to enable direct links between levels of complexity. *Second*, researchers should embrace biological variability. Variability among individuals is inherent to biological systems and in fact is the basis for evolution by natural selection. As demonstrated in this Research Topic, researchers studying biological materials include marine biologists, geoscientist, physicists, molecular biologists, engineers, statisticians, among others. Each field brings their own views, and researchers unfamiliar with biological variability may view anomalous results as unwanted outliers, removing them from the dataset. Assuming experiments were run with care, however, these outliers can often provide valuable insight on the range of properties that are possible and may suggest the potential for adaptation within a population. *Lastly*, and particularly for studies on the effects of environment, researchers should publish negative results. There is often a publication bias towards results that show significant or dramatic effects of environment on materials properties, as these results are viewed as more exciting or important within the field. Negative findings, however, are integral to our understand of how these materials respond to environmental change and may inform decisions on where conservation or aquaculture efforts should be focused.

Author contributions

GD wrote the first draft of the manuscript. All authors contributed to manuscript revisions, and read and approved the submitted version.

Funding

GD and RM are supported by the US National Science Foundation, Divisions of Material Research (DMR-1905466 to GD and DMR-1905619 to RAM). SL is supported by the Youth Innovation Promotion Association, Chinese Academy of Sciences (Grant number 2018054).

Conflict of interest

The authors declare that the research was conducted in the absence of any commercial or financial relationships that could be construed as a potential conflict of interest.

Publisher's note

frontiers in Marine Science

ORIGINAL RESEARCH
published: 23 December 2021
doi: 10.3389/fmars.2021.821019

Mussel Byssal Attachment Weakened by Anthropogenic Noise

*Xinguo Zhao[1,2], Shuge Sun[3], Wei Shi[3], Xuemei Sun[1,2], Yan Zhang[1,2], Lin Zhu[1,2], Qi Sui[1,2], Bin Xia[1,2], Keming Qu[1], Bijuan Chen[1,2] and Guangxu Liu[3]**

[1] Yellow Sea Fisheries Research Institute, Chinese Academy of Fishery Sciences, Qingdao, China, [2] Laboratory for Marine Ecology and Environment Science, Qingdao National Laboratory for Marine Science and Technology, Qingdao, China, [3] College of Animal Sciences, Zhejiang University, Hangzhou, China

The increasing underwater noise generated by anthropogenic activities has been widely recognized as a significant and pervasive pollution in the marine environment. Marine mussels are a family of sessile bivalves that attach to solid surfaces via the byssal threads. They are widely distributed along worldwide coastal areas and are of great ecological and socio-economic importance. Studies found that anthropogenic noise negatively affected many biological processes and/or functions of marine organisms. However, to date, the potential impacts of anthropogenic noise on mussel byssal attachment remain unknown. Here, the thick shell mussels *Mytilus coruscus* were exposed to an ambient underwater condition (~50 dB re 1 μPa) or the playbacks of pile-driving noise (~70 or ~100 dB re 1 μPa) for 10 days. Results showed that the noise significantly reduced the secretion of byssal threads (e.g., diameter and volume) and weakened their mechanical performances (e.g., strength, extensibility, breaking stress, toughness and failure location), leading to a 16.95–44.50% decrease in mussel byssal attachment strength. The noise also significantly down-regulated the genes expressions of seven structural proteins (e.g., mfp-1, mfp-2, mfp-3, mfp-6, preCOL-P, preCOL-NG, and preCOL-D) of byssal threads, probably mediating the weakened byssal attachment. Given the essential functions of strong byssal attachment, the findings demonstrate that the increasing underwater anthropogenic noise are posing a great threat to mussel population, mussel-bed community and mussel aquaculture industry. We thus suggest that future work is required to deepen our understanding of the impacts of anthropogenic noise on marine invertebrates, especially these with limited locomotion ability, like bivalves.

Keywords: anthropogenic noise, mussel, byssal thread, attachment, mechanical performance, gene expression

OPEN ACCESS

Edited by:
Shiguo Li,
Research Center for Eco-Environmental Sciences, Chinese Academy of Sciences (CAS), China

Reviewed by:
Huaxin Gu,
Shanghai Ocean University, China
Haoyu Guo,
Zhejiang Ocean University, China
Youji Wang,
Shanghai Ocean University, China

****Correspondence:***
Guangxu Liu
guangxu_liu@zju.edu.cn
orcid.org/0000-0002-1039-7801

Specialty section:
This article was submitted to Marine Molecular Biology and Ecology, a section of the journal Frontiers in Marine Science

Received: *23 November 2021*
Accepted: *06 December 2021*
Published: *23 December 2021*

Citation:
Zhao X, Sun S, Shi W, Sun X, Zhang Y, Zhu L, Sui Q, Xia B, Qu K, Chen B and Liu G (2021) Mussel Byssal Attachment Weakened by Anthropogenic Noise. Front. Mar. Sci. 8:821019. doi: 10.3389/fmars.2021.821019

INTRODUCTION

The underwater noise generated by anthropogenic activities such as shipping, oil and gas exploration, and the installation of renewable energy devices, has now been widely recognized as a significant and pervasive pollution in the marine environment (Duarte et al., 2021). Anthropogenic noise undoubtedly alters the acoustic signature of marine ecosystems and poses a great threat to marine organisms (Jerem and Mathews, 2021). What's worse, given the growing levels of human activities, the underwater anthropogenic noise levels likely continue to increase in the foreseeable

future (Duarte et al., 2021). Over the past decades, the potential impacts of anthropogenic noise on marine organisms have raised global attention (Peng et al., 2015; Popper et al., 2020). Studies demonstrate that a wide variety of biological processes and physiological functions of marine organisms can be negatively affected by anthropogenic noise, such as acoustic communication (Di Iorio and Clark, 2010; Alves et al., 2021), auditory sensitivity (Kastelein et al., 2018; Vieira et al., 2021), foraging behavior (Purser and Radford, 2011; Wale et al., 2013), antipredator behavior (Simpson et al., 2015; Kok et al., 2021), reproduction (de Jong et al., 2018; Smott et al., 2018) and embryonic development (de Soto et al., 2013; Nedelec et al., 2015). However, to date, most studies were conducted on marine mammals and fishes (Erbe et al., 2018; Popper and Hawkins, 2019), and the effects of anthropogenic noise on marine invertebrates, especially bivalves, received much less attention (Di Franco et al., 2020; Wale et al., 2021).

Marine bivalves, one class of benthic invertebrate, are able to detect substrate-borne and water-borne sound through contact with both substrate and surrounding water (Roberts et al., 2015; Vazzana et al., 2016; Charifi et al., 2017). Among marine invertebrates, bivalves are likely to be particularly vulnerable to anthropogenic noise, since their benthic habit and limited locomotion ability make them unable to escape from a noise area (Day et al., 2017; Vazzana et al., 2020). More importantly, marine bivalves are of great ecological and socio-economic importance, such as: (1) using as a source of human food, (2) increasing biodiversity of local marine ecosystem through creating habitats for other organisms, (3) improving seawater quality by filtering the water and removing particulates within, (4) attenuating global warming and ocean acidification through carbon fixation, and (5) mitigating ocean eutrophication through filtering large quantities of organic matter from the water column and the production of biodeposits (Vaughn and Hoellein, 2018; Suplicy, 2020; van der Schatte Olivier et al., 2020). Limited available studies show that anthropogenic noise disrupts the larval development of the New Zealand scallop *Pecten novaezelandiae* (de Soto et al., 2013), causes physiological harm and/or alters behavior in adult marine bivalves, including the razor clam *Sinonovacula constricta* (Peng et al., 2016), the Mediterranean mussel *Mytilus galloprovincialis* (Vazzana et al., 2020), the blood clam *Tegillarca granosa* (Shi et al., 2019), the blue mussel *M. edulis* (Wale et al., 2019), and the scallop *P. fumatus* (Day et al., 2017). However, there are species-specific and ontogenetic variations of noise-induced changes (Wale et al., 2021). Despite the current advance, the full extent to which anthropogenic noise affects marine bivalves is still poorly understood. Regarding their critical ecological roles and socio-economic importance, it is urgent to deepen our understanding of the effects of anthropogenic noise on marine bivalves.

Marine mussels are a family of sessile bivalve species that are widely distributed along worldwide coastal areas (Zhao et al., 2020). They attach to a wide array of substrata with their strong holdfast structure, the byssal threads (Waite, 1983). The byssal thread includes three parts: (1) the proximal region, which has a corrugated surface and is highly extensible; (2) the distal region, that is smoother, stiffer and approximately twice the length of the proximal region; and (3) the adhesive plaque, which adheres to the substrate (Bell and Gosline, 1996). Marine mussels can also attach to one another via byssal threads, and thereby form mussel aggregates or mussel beds, thus improving stability and protection against predation and environmental perturbations, increasing fertilization success, and providing habitats for other organisms (Borthagaray and Carranza, 2007; Liu et al., 2011; Christensen et al., 2015; Kong et al., 2019). A strong byssal attachment is thus essential for mussel survival, self-defense, reproduction and their ecological functions (Bandara et al., 2013; Sui et al., 2017; Shang et al., 2019). Hence, any potential impacts of anthropogenic noise on byssal attachment could have fundamental ecological implications for marine mussels and ecosystems. Given this, an understanding of noise effects in this regard is crucial. However, to date, the potential impacts of anthropogenic noise on mussel byssal attachment remain unknown.

Due to its ecological and economical importance, and wide distribution along the coastal areas of China, Korea and Japan (Li et al., 2015; Sui et al., 2015), the thick shell mussel *M. coruscus* was chosen and used as a testing organism in this study. A laboratory-based experiment was performed to investigate the effects of anthropogenic noise (specifically playback of pile-driving noise, an impulsive sound source) on byssal thread number, morphology and mechanical performance, and thereby the overall byssal attachment strength of mussel individual. Importantly, the expression levels of seven key genes encoding structural proteins of byssal threads, including four mussel foot proteins (mfp-1, mfp-2, mfp-3, and mfp-6) and three precursor collagen proteins (preCOL-P, preCOL-NG, and preCOL-D), were also determined to reveal the underlying molecular responses of marine mussels to anthropogenic noise.

MATERIALS AND METHODS

Animal Collection and Acclimation

Adult thick shell mussels *M. coruscus* with similar size (shell length of 102.1 ± 5.5 mm) were collected from Shengsi Islands, Zhejiang, China (30°73′ N and 122°45′ E) and directly transported to the Qingjiang Station of Zhejiang Mariculture Research Institute. The mussels were transported in air, mimicking the natural condition during low tide. Following carefully cleaning of epibionts without damaging their shells, the mussels were acclimated in filtered and UV-irradiated natural seawater (temperature of 22.5 ± 0.4°C, pH of 8.09 ± 0.06, and salinity of 23.8 ± 0.4 PSU) with continuous aeration for 2 weeks. The mussels were fed twice daily (e.g., at 08:00∼08:30 and 19:00∼19:30) with the microalgae *Platymonas subcordiformis* to satiation. Excess food and feces were removed daily with seawater change (e.g., at 18:00∼19:00), in which two thirds of the seawater was removed by siphoning, followed by refilling with filtered and UV-irradiated seawater.

Experimental Design and Anthropogenic Noise Exposure

Following acclimation, mussels were randomly assigned to a control and two anthropogenic noise input groups. The ambient

condition without any additional anthropogenic sound input serviced as the control, while the underwater sound pressure levels of the two anthropogenic noise input groups were set at ∼70 and ∼100 dB re 1 μPa to mimic the underwater conditions with different degrees of anthropogenic sound, according to previous studies (Hildebrand, 2009; Slabbekoorn et al., 2010; Peng et al., 2016). The pile-driving sound recorded previously (Solan et al., 2016) was used as the source of anthropogenic noise input in this study. For the two anthropogenic noise input groups, mussels were exposed to playbacks of the pile-driving noise at respective underwater sound pressure levels. The experiment was performed with circular buckets (diameter of 60 cm, depth of 70 cm) filled with filtered and UV-irradiated natural seawater with a depth of 50 cm. For all groups, the circular bucket had a circular glass chamber (diameter of 20 cm, depth of 10 cm) centered on its floor, and each contained two individual mussels (**Figure 1**). The reason why each chamber contained only two mussels was to avoid the formation of mussel aggregate and its potential effects on sound propagation and the underwater sound pressure level.

A submersible loudspeaker (UW-30, Electro-Voice, Indiana, United States; frequency response 0.1–10 kHz; impedance 8 ohms; power-handling capacity 30 watts) was positioned in the center of the circular tank at a depth of 20 cm below the water surface and oriented toward the floor to generate the desired acoustic conditions (**Figure 1**). The submersible loudspeaker was driven using a power amplifier player (AV-296, SAST, Guangdong, China; power-handling capacity 150 watts). The action acoustic conditions were determined using the acoustics recording unit, which included a bioacoustics recorder (Song Meter SM2+, Wildlife Acoustics, MA, United States; 96 kHz sampling rate), and a calibrated omni-directional hydrophone (HIT-96-MIN, High Tech; Long Beach, Mississippi, United States; flat frequency response 0.02–30 kHz, sensitivity −164 dB re 1 V/μPa). To test whether there were any variations of the underwater sound pressure levels at different positions, the hydrophone was placed near the bottom of the circular bucket at 5 cm, 15 cm, and 25 cm away from the center (**Figure 1**). Acquired acoustic data were analyzed with the Soundscape Analysis Software SACS V1.0 (Register number: 2014SR216788), and underwater sound pressure levels were obtained following the described method (Peng et al., 2016). During the entire experimental period, mussels were fed twice daily, and seawater was continuously aerated and renewed daily as described above. The seawater parameters, including temperature, pH and salinity, were kept as described above. Since the control and two anthropogenic noise input groups were conducted simultaneously in a laboratory, the experimental circular buckets were equipped with anti-vibration shielding to avoid the potential effects of the high sound pressure level noise on the acoustic conditions of other groups. The experiment plan was replicated five times with different individuals for each time and under identical experimental conditions. The experiment lasted for 10 days, and no animal mortality was observed.

Following exposure, one of the two mussels in the circular glass chamber was randomly selected, dissected and immediately frozen in liquid nitrogen for further gene expression analysis.

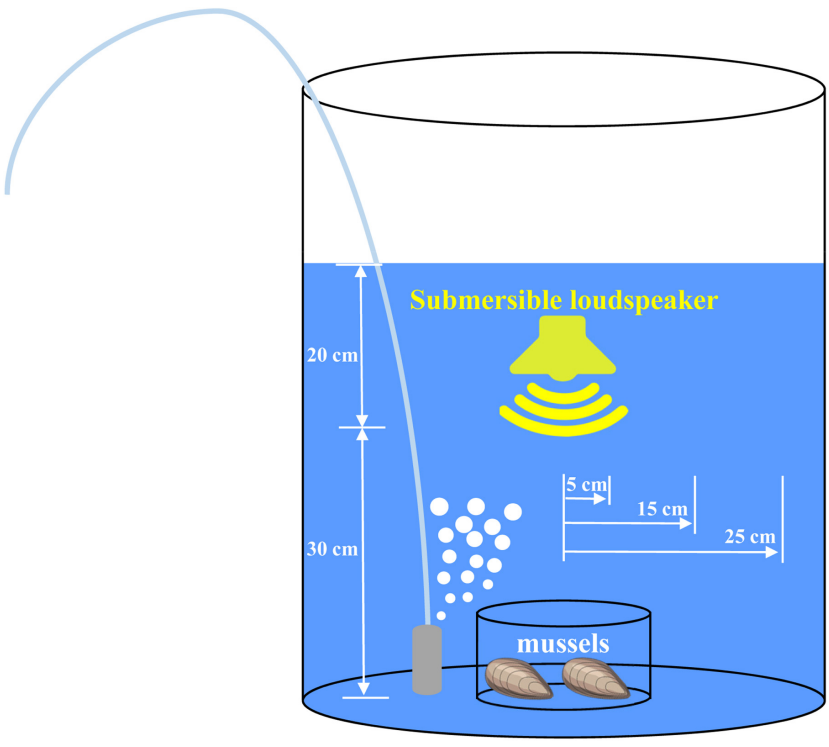

FIGURE 1 | Schematic diagram of the experimental setup and the positions where underwater acoustic conditions were determined.

After carefully removing the existing byssal threads without damaging foot organ, the other mussel was allowed to regrow for 24 h to secret new byssal threads. During the 24 h incubation, the experimental conditions were identical with those of the 10-day experimental period.

Byssal Thread Collection and Quantitative Analysis

After regrowing for 24 h, the full-length byssal threads of mussels were carefully collected according to the method described previously (Zhao et al., 2017). Briefly, newly secreted byssal threads were cautiously removed from the substrate one by one. Mussels were dissected by severing the adductor muscles. The full-length byssal threads were then carefully excised at their attachment points to foot. After collection, the number of newly secreted byssal threads per mussel was manually counted. The length (mm) of each byssal thread was determined using a digital Vernier caliper with a precision of 0.01 mm. Digital image of each byssal thread was obtained using a CCD camera mounted on a microscope (BX53, Olympus, Japan). Diameters of three independent locations of the byssal thread were measured through image analysis using the free-access software ImageJ Version 1.51j8[1], and the mean value of them was used as the diameter (d; μm) of the byssal thread. Byssal thread was assumed to be cylindrical (Bell and Gosline, 1996), and the cross-sectional area (mm^2) of each byssal thread was calculated from the obtained diameter using the equation: cross-sectional area = $\pi \times (d/2)^2$. The volume (mm^3) of each byssal thread was calculated by multiplying the cross-sectional area by the length.

Mechanical Property Analysis of Byssal Thread

After quantitative analysis, mechanical properties of byssal thread were determined using a universal testing machine (AGS-J, Shimadzu, Japan) following the methods described previously (Zhao et al., 2017). The adhesive plaque was glued to a metal stub secured in the lower platform of the testing machine, while the proximal end of byssal thread was sandwiched between cardboard and further clamped at the upper grip of the testing machine. Tensile test of byssal thread was conducted in air at room temperature at a loading rate of 10 mm/min until failure occurred, mimicking the natural air exposure condition during low tide.

The breaking force (N), also named thread strength, was determined as the force required to break a single byssal thread. The breaking strain (%), also called thread extensibility was measured as the extension at failure, divided by the unstressed thread length. The breaking stress (N/mm^2) was calculated as the value of breaking force divided by cross-sectional area. The toughness (J/cm^3) was measured as the energy absorbed per unit volume until thread failure occurred. The location of failure (e.g., proximal, distal or adhesive plaque) was noted, and failure occurrence at each location was expressed as the percentage of the number of threads tested. When failure occurred at the grip, the corresponding data were discarded from analysis to avoid underestimating the actual mechanical properties (Bell and Gosline, 1996; Moeser and Carrington, 2006).

According to previous studies (Bell and Gosline, 1996; Zhao et al., 2017; Shi et al., 2020), the overall mussel attachment strength was estimated as the potential maximal attachment strength (N) with the formula: attachment = average thread strength × thread number. Prior to the estimation, the average thread strength was calculated as the mean value of all thread strengths for a given mussel individual.

RNA Isolation, Real-Time PCR and Gene Expression Analysis

Following dissection, the foot tissue was immediately frozen in liquid nitrogen and stored at −80°C upon use. Total RNA was extracted using TRIzol Reagent (Invitrogen, 15596018) following the manufacturer's protocol. DNA contamination in the RNA sample was removed by treating with DNase I (Invitrogen, 18047019). The RNA quality was checked by 1.0% formaldehyde-denatured agarose gel electrophoresis. The RNA concentration was quantified using a NanoDrop 1000 spectrophotometer (Thermo Fisher Scientific). The cDNA was synthesized with the high-quality total RNA using the M-MLV First Strand Kit (Invitrogen, C28025-032) according to the manufacturer's protocol. Real-time PCR was conducted using a CFX96 Real-Time System (Bio-Rad, United States) with a total reaction volume of 10 μL containing 5 μL of SsoFast EvaGreen Supermix (Bio-Rad, 1725201AP), 0.5 μL of each primer (10 μM), 2 μL of cDNA template and 2 μL of double-distilled water. The cycle conditions were 95°C for 5 min, 40 cycles of 94°C for 20 s, 61°C for 20 s, and 72°C for 20 s. The specificity of each amplification reaction was verified by analyzing the melting curve. The relative gene expression level was calculated using the $2^{-\Delta\Delta Ct}$ method (Livak and Schmittgen, 2001) with the *18S rRNA* gene as the internal reference. The expression of *18S rRNA* has been verified to be stable under ambient and different noise exposure conditions. The gene-specific primers using in this study were listed in **Table 1**.

Statistical Analysis

One-way ANOVAs were performed to show the effects of position (i.e., distance to the center of the concentric circle vertically below the sound source) on the underwater sound

TABLE 1 | Gene-specific primers used in real-time PCR.

Gene	Forward primer (5′–3′)	Reverse primer (5′–3′)
18S rRNA	CCTTGGTGCTCTTGATTGA	GAACTACGACGGTATCTGAT
mfp-1	TGGCTACAATTCAAGAACTG	AGAGAAGGATGAGAACGAAT
mfp-2	CGGTCACAGAAGCATCAT	CATCCTCATCGTCGTCATAT
mfp-3	TTTGCTGGCTTTAGTCCTT	ACCGCTATTCCATCCCTTA
mfp-6	CGGTGATTATGATTACAGAGG	GAAGACAGCATCCAGCAT
preCOL-P	GATCTTCACATGCATCAGC	CACTGCCACCTCCTAAAC
preCOL-NG	ACAAGGACCACAAGGAGAA	ACACCACCAACACCAGTT
preCOL-D	ACCAAGAGGAGATAGAGGAG	GGCTGTTCTGAGGTCTTC

[1]https://imagej.nih.gov/ij/

pressure level, and the effects of anthropogenic noise on byssal thread production, morphology, mechanical parameters and gene expression levels. *Post-hoc* Tukey's multiple tests were conducted to compare differences among groups. Prior to analysis, homogeneity of variance and normality of data were verified with the Levene's test and Shapiro-Wilk's tests, respectively. Chi-square test was performed to compare failure occurrences at each location. Data are presented as the mean ± SD, and a p-value less than 0.05 was considered to indicate statistically significance.

RESULTS

The Underwater Sound Pressure Level

One-way ANOVAs showed that the distance to the center of the concentric circle vertically below the sound source had no significant effect on the underwater sound pressure levels near the bottom of the circular bucket, indicating no significant difference between the underwater sound pressure levels at 5, 15, and 25 cm away from the center (**Table 2**). As shown in **Table 2**, the underwater sound pressure level of the control group was ∼55 dB re 1 μPa that was much lower than those of the two anthropogenic noise input groups. Additionally, the actual underwater sound pressure levels of the two anthropogenic noise input groups were generally consistent with the nominal values that set at ∼70 and ∼100 dB re 1 μPa. Given this situation, experimental results were therefore analyzed and reported with nominal underwater sound pressure levels.

Byssal Thread Production and Morphology

The average number of newly secreted byssal threads per mussel was slightly reduced from 46.6 (100%) to 43.4 (93.13%) and 41 (87.98%) after the 10-day exposure to the 70 and 100 dB re 1 μPa anthropogenic noise, but no significant effect was observed [$F_{(2,12)}$ = 3.47, p = 0.06] (**Figure 2A**). The length of newly secreted byssal thread was also not significantly affected after the 10-day exposure [$F_{(2,12)}$ = 2.9, p = 0.09] (**Figure 2B**). However, a significant effect of anthropogenic noise on the diameter of the byssal thread was detected [$F_{(2,12)}$ = 6.71, p = 0.01]. The diameter of mussels exposed to 70 and 100 dB re 1 μPa noise decreased to approximately 97.18 and 93.50% of that of the control, respectively (**Figure 2C**). Compared with the control, the average volume of the byssal thread was significantly declined to about 87.09 and 80.40% of that of the control upon 70 and 100 dB re 1 μPa noise exposure, respectively [$F_{(2,12)}$ = 11.22, p = 0.002] (**Figure 2D**).

TABLE 2 | The underwater sound pressure levels (dB re 1 μPa) near the bottom of the circular bucket at 5, 15, and 25 cm away from the center of the concentric circle vertically below the sound source (n = 10 per distance, mean ± SD).

Group	Underwater sound pressure levels at distances to the center		
	5 cm	15 cm	25 cm
Control	55.02 ± 2.60[a]	55.19 ± 2.73[a]	55.03 ± 1.95[a]
70 dB re 1 μPa noise input	74.16 ± 1.77[a]	74.15 ± 2.44[a]	73.95 ± 1.70[a]
100 dB re 1 μPa noise input	101.82 ± 2.61[a]	101.09 ± 1.96[a]	100.62 ± 2.15[a]

Means not sharing the same superscript are significantly different (Tukey's HSD, $p < 0.05$).

Mechanical Properties of Byssal Threads

The breaking force of byssal thread was significantly reduced for mussels exposed to the 70 and 100 dB re 1 μPa anthropogenic noise [$F_{(2,\ 12)}$ = 66.67, $p = 3.17 \times 10^{-7}$], which were approximately 89.27 and 63.41% of that of the control (**Figure 3A**). The breaking stress of byssal thread was significantly decreased after the 10-day exposure [$F_{(2,12)}$ = 21.62, $p = 1.05 \times 10^{-4}$]. Compared to control, the breaking stress was declined by about 5.57 and 27.84% for mussels exposed to 70 and 100 dB re 1 μPa anthropogenic noise, respectively (**Figure 3B**). The breaking strain of byssal thread was also significantly reduced by anthropogenic noise exposure [$F_{(2,12)}$ = 39.58, $p = 5.20 \times 10^{-6}$]. The breaking strain of mussels exposed to 70 and 100 dB re 1 μPa anthropogenic noise were significantly decreased to approximately 80.27 and 65.93% of that of the control, respectively (**Figure 3C**). Similarly, the toughness of byssal thread was significantly affected by anthropogenic noise exposure as well [$F_{(2,12)}$ = 75.70, $p = 1.57 \times 10^{-7}$]. The toughness of the 70 and 100 dB re 1 μPa anthropogenic noise exposure groups were remarkably declined to approximately 76.06 and 48.07% of that of the control, respectively (**Figure 3D**).

Location of Byssal Thread Failure

As shown in the **Figure 4**, the thread failure occurred at either the proximal region or the adhesive plaque. The occurrence of thread failure located in the adhesive plaque was significantly increased by anthropogenic noise exposure (χ^2 = 35.92, df = 2, $p < 0.0001$). For the control group, only 24% thread failure occurred in the adhesive plaque, while it was increased to approximately 34 and 64% for the 70 and 100 dB re 1 μPa anthropogenic noise exposure groups, respectively.

The Overall Mussel Attachment Strength

The overall mussel attachment strength was significantly weakened by anthropogenic noise exposure [$F_{(2,12)}$ = 64.31, $p = 3.86 \times 10^{-7}$] (**Figure 5**). Compared to the control, the potential maximal attachment strength of mussels treated with 70 and 100 dB re 1 μPa anthropogenic noise was significantly decreased by 16.95 and 44.50%, respectively.

Gene Expressions of Byssal Proteins

One-way ANOVAs showed that the expression levels of *mfp-1*, *mfp-2*, *mfp-3,* and *mfp-6* were significantly affected by anthropogenic noise exposure (**Figures 6A–D**). Compared to the control, the expression levels of *mfp-1* were significantly decreased by 34.81 and 46.28% for mussels exposed to 70 and 100 dB re 1 μPa anthropogenic noise, respectively (**Figure 6A**). Although the fold-change varied, the expression patterns of *mfp-2*, *mfp-3,* and *mfp-6* were similar to that of

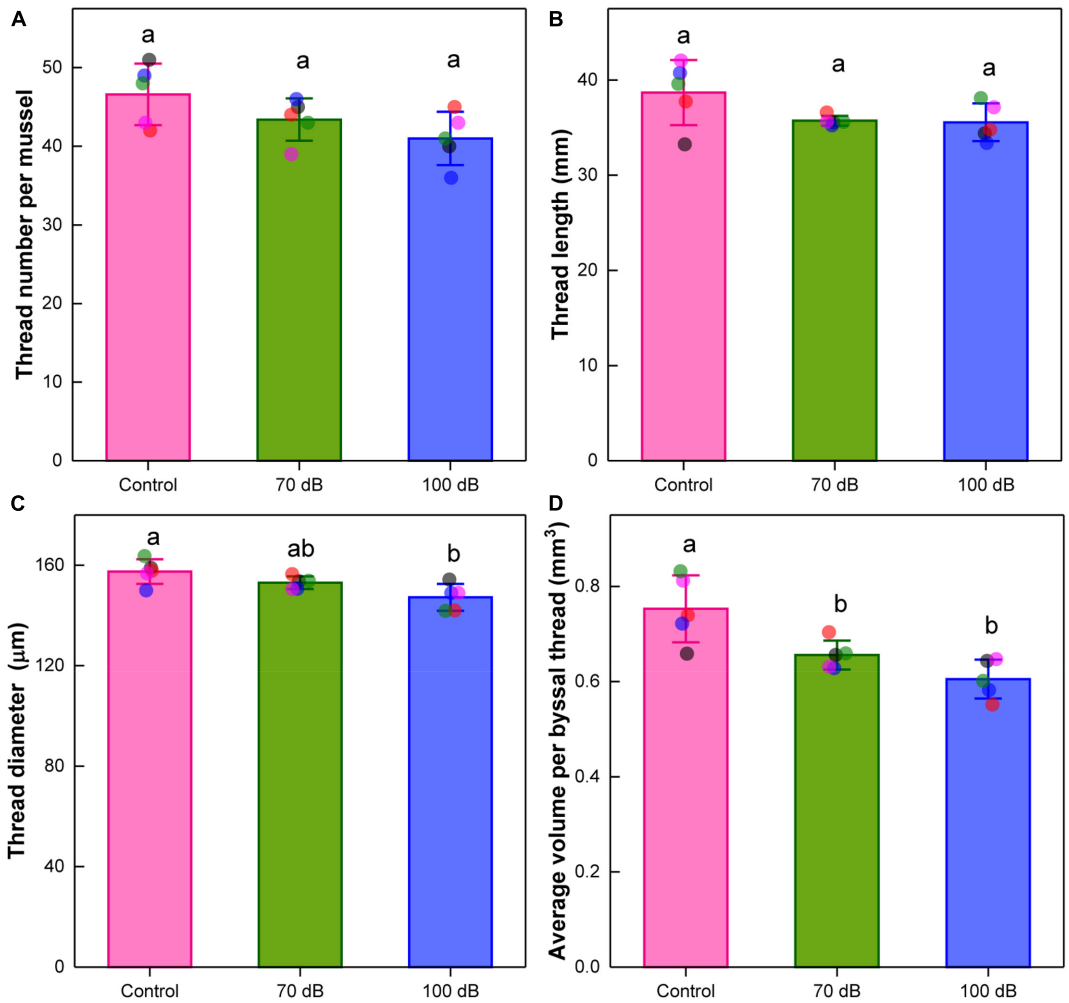

FIGURE 2 | Effects of anthropogenic noise exposure on the **(A)** number, **(B)** thread length, **(C)** thread diameter, and **(D)** volume of byssal threads newly produced by the thick shell mussel *Mytilus coruscus* (n = 5 per group, mean ± SD). Means not sharing the same superscript are significantly different (Tukey's HSD, $p < 0.05$).

mfp-1, showing the down-regulation upon anthropogenic noise exposure (**Figures 6B–D**). Significant effects of anthropogenic noise on the expression levels of *preCOL-P*, *preCOL-NG,* and *preCOL-D* were observed as well (**Figures 6E–G**). The expression levels of *preCOL-P* of mussels exposed to 70 and 100 dB re 1 μPa anthropogenic noise were significantly reduced to 48.81 and 28.95% of that of control, respectively (**Figure 6E**). Similarly, for mussels treated by 70 and 100 dB re 1 μPa anthropogenic noise, the expression levels of *preCOL-NG* were, respectively, decreased to 93.69 and 48.47%, and the expression levels of *preCOL-D* were, respectively, down-regulated to 68.16 and 50.07%, compared to those of control (**Figures 6F,G**).

DISCUSSION

Our results suggest that exposure to playbacks of the pile-driving noise had significant negative effects on byssal thread production and mechanical performances of the thick shell mussel *M. coruscus*, leading to reductions in the diameter, average volume, strength (i.e., breaking force), extensibility (i.e., breaking strain), breaking stress and toughness of individual byssal thread. Additionally, byssal threads of control mussels were commonly broken at the proximal region, while those of noise-treated mussels were largely fractured at the adhesive plaque, indicating the weakest part of byssal thread shifted from the proximal region to the adhesive plaque upon exposure to playbacks of the pile-driving noise. These noise-induced changes led to a 16.95–44.50% decrease in the overall byssal attachment strength, greatly limiting mussels' ability to attach firmly on substratum. On the one hand, the weakened byssal attachment would undoubtedly increase dislodgement risk of mussel individuals in natural habitats and commercial suspension cultures (O'Donnell et al., 2013), and subsequently make them more vulnerable to predators and environmental turbulence (e.g., waves) at the individual level. On the other hand, the weakened byssal attachment might also hinder the formation and maintenance of mussel beds, and in turn impair the recruitment, anti-predation capability

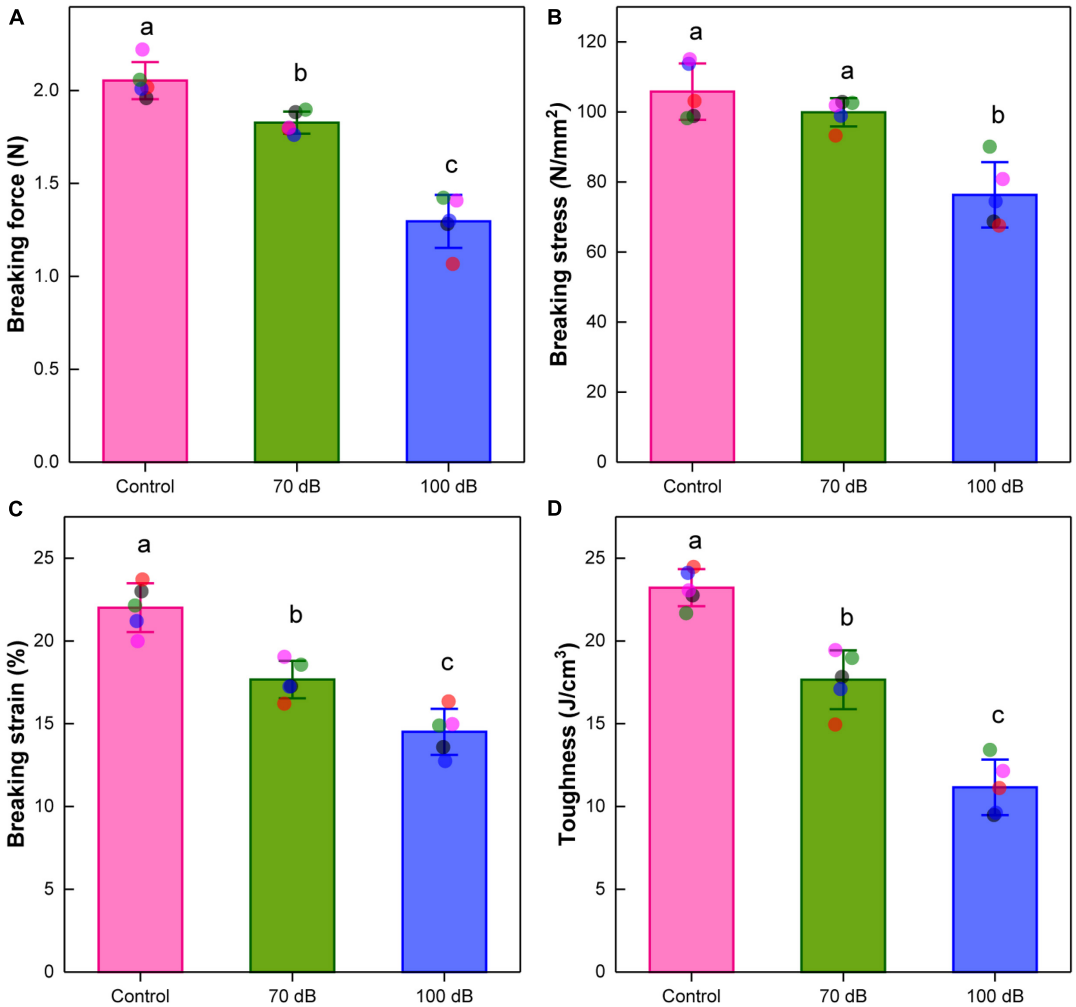

FIGURE 3 | Effects of anthropogenic noise exposure on the **(A)** breaking force, **(B)** breaking stress, **(C)** breaking strain, and **(D)** toughness of byssal threads newly produced by the thick shell mussel *Mytilus coruscus* (n = 5 per group, mean ± SD). Means not sharing the same superscript are significantly different (Tukey's HSD, $p < 0.05$).

and ecological functions of mussel population. We therefore conclude that anthropogenic noise (e.g., the pile-driving noise) has negative impacts on both mussel individuals and population through hampering byssal attachment, which in turn pose a great threat to mussel bed communities and the mussel aquaculture industry.

The noise-induced decline in byssal thread production (i.e., the decrease in the diameter and volume of byssal thread, and the down-regulation of genes encoding structural proteins of byssal thread) might be due to limited energy availability. It has been shown that the energetic cost of byssal thread production is substantial, requiring 8–10% of a mussel's total energy expenditure (Hawkins and Bayne, 1985; Lurman et al., 2013; Roberts et al., 2021). However, studies have suggested that anthropogenic noise adversely affected the feeding behavior and metabolism activity of marine bivalves, including mussels, which seems to result in energy deficiency (Peng et al., 2016; Spiga et al., 2016; Shi et al., 2019; Wale et al., 2019; Vazzana et al., 2020). For example, exposure to ship noise playbacks led to a 12% reduction in oxygen consumption and an 84% decrease in filtration rate of the blue mussel *M. edulis* (Wale et al., 2019). Under this circumstance, energy availability could be limited and mussels must allocate a relatively few energy to biological processes that are less critical for individual survival (Lachance et al., 2011; Shang et al., 2021). We suggest that upon exposure to the pile-driving noise, mussels tended to limit the energy allocation to byssal attachment, thus leading to the down-regulation of genes expression levels of byssal proteins and the decrease in byssal thread diameter and volume of the thick shell mussel *M. corucus* in this study. It is worth noting that there was no significant alteration in byssal thread number and length. However, these were not opposite to the results described above. As known, to attach firmly on the substrate, mussel individuals must produce enough byssal threads angled away from the shell to the ideal places where they want to anchor (Bell and Gosline, 1996). However, the down-regulation of genes expression levels

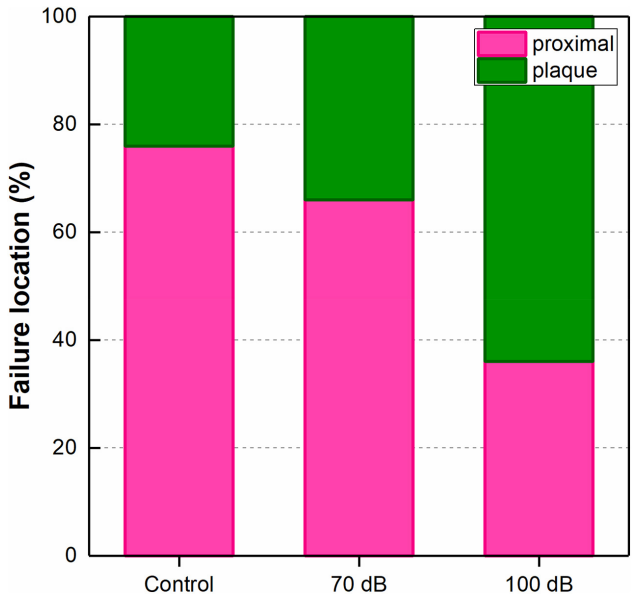

FIGURE 4 | Effects of anthropogenic noise exposure on failure occurrence (%) at each location of byssal thread newly produced by the thick shell mussel *Mytilus coruscus* (n = 5 per group, χ^2 = 35.92, df = 2, p < 0.0001).

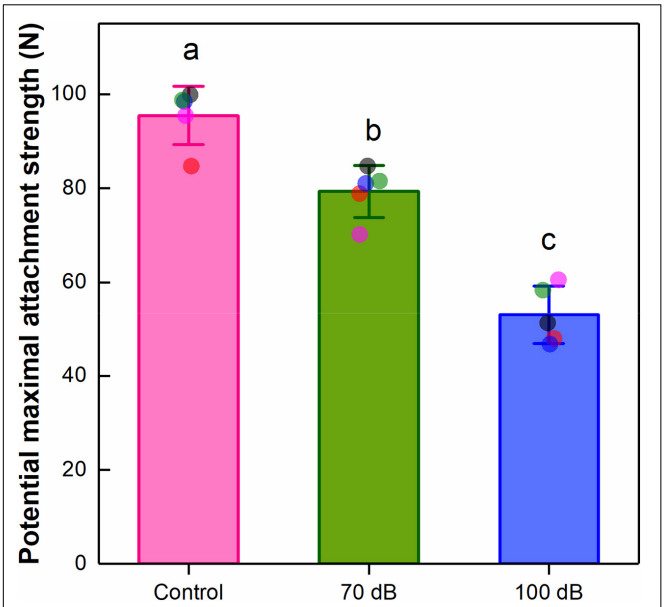

FIGURE 5 | Effects of anthropogenic noise exposure on the potential maximal attachment strength of the thick shell mussel *Mytilus coruscus* (n = 5 per group, mean ± SD). Means not sharing the same superscript are significantly different (Tukey's HSD, p < 0.05).

of byssal proteins and the decrease in thread volume suggest that less byssal proteins were synthesized, indicating there was insufficient materials for mussel individuals to produce byssal threads like before. Under this circumstance, decreasing thread diameter but keeping thread number and length should be an adaptive strategy to meet the lowest requirements for mussel attachment.

The noise-induced reduction in mechanical performances of byssal thread can be attributed to a series of reasons. Morphological, the decrease in mechanical properties could be firstly owing to the morphological alterations of byssal thread. For example, the reduction in strength (i.e., breaking force), extensibility (i.e., breaking strain) and toughness might result from the thinner individual byssal thread. However, given the negative correlation between breaking stress and thread diameter, breaking stress was still decreased with the thread diameter reducing. This suggests that except morphological alterations, there must be other reasons contributing to the reduction in mechanical performances of byssal threads. Our results show that the mRNA levels of genes encoding structural proteins of byssal threads, including four mussel foot proteins (mfp-1, mfp-2, mfp-3, and mfp-6) and three precursor collagen proteins (preCOL-P, preCOL-NG, and preCOL-D), were significantly down-regulated upon exposure to the pile-driving noise. As known, the down-regulation of genes expression levels may not guarantee the reduction in translation of byssal proteins, but taken together with the decrease in thread volume, we suggest that levels of the four mussel foot proteins (mfp-1, mfp-2, mfp-3, and mfp-6) and the three precursor collagen proteins (preCOL-P, preCOL-NG, and preCOL-D) were, to some extent, down-regulated. It has been proven that the protective cuticle of byssal thread is comprised solely of mfp-1, while the inner collagenous core is mainly made of preCOL-P, preCOL-NG, and preCOL-D (~81% of the dry weight) (Silverman and Roberto, 2010). The other identified mussel foot proteins, including mfp-2, mfp-3, and mfp-6, are confined exclusively to the adhesive plaque (Lee et al., 2011). The preCOL-P is essential for the remarkable extensibility at the proximal region, and the preCOL-D provides the excellent stiffness property at the distal region of the byssal thread (Bandara et al., 2013). The preCOL-NG, distributed uniformly throughout the proximal and distal region, is considered to mediate the interaction between preCOL-P and preCOL-D, and thereby combines the remarkable extensibility and high strength properties of byssal thread (Bandara et al., 2013). These evidences show that the four mussel foot proteins (mfp-1, mfp-2, mfp-3, and mfp-6) and the three precursor collagen proteins (preCOL-P, preCOL-NG, and preCOL-D) are critical for the mechanical performances of byssal threads. Regarding this, the down-regulation of structural proteins of byssal threads should be one reason underlying the weakened mechanical properties and the shift of the weakest part of byssal thread.

It has been revealed that the mechanoreceptors within mussel foot participate in byssal threads secretion and adhesion (LaCourse and Northrop, 1978; Amini et al., 2017). Briefly, once mussel foot probes an ideal substrate, the mechanoreceptors and their downstream signal transduction pathways would be activated. The mussel then starts to fabricate byssal threads and subsequently attaches on the substrate. Importantly, the mechanoreceptors are also highly sensitive to mechanical waterborne vibration or acoustic particle motion and thus essential for mussel sound detection (Roberts et al., 2015;

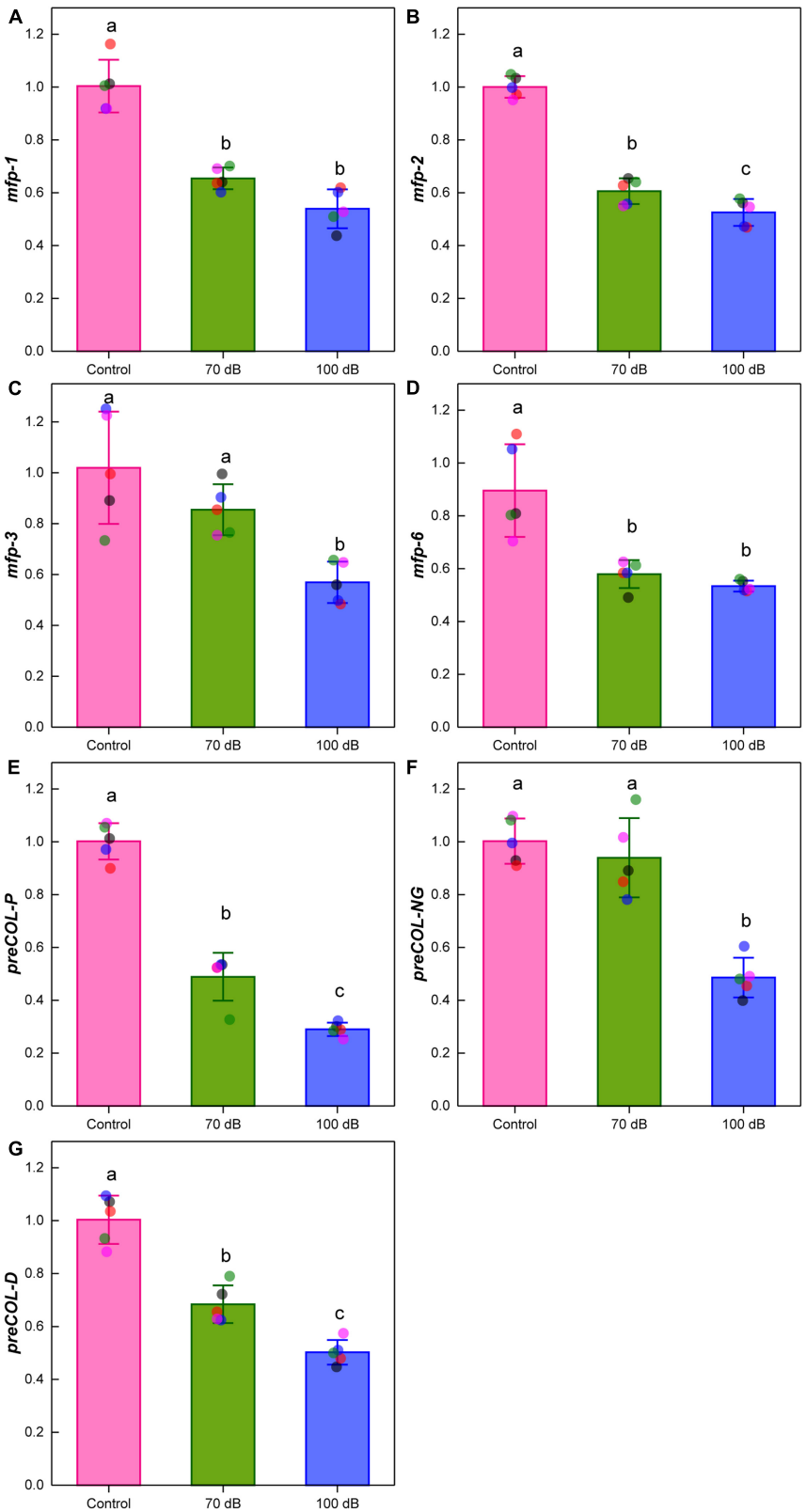

FIGURE 6 | Effects of anthropogenic noise exposure on the expression levels of genes encoding structural proteins of byssal threads, including **(A)** mfp-1, **(B)** mfp-2, **(C)** mfp-3, **(D)** mfp-6, **(E)** preCOL-P, **(F)** preCOL-NG and **(G)** preCOL-D in the thick shell mussel *Mytilus coruscus* (n = 5 per group, mean ± SD). Means not sharing the same superscript are significantly different (Tukey's HSD, $p < 0.05$).

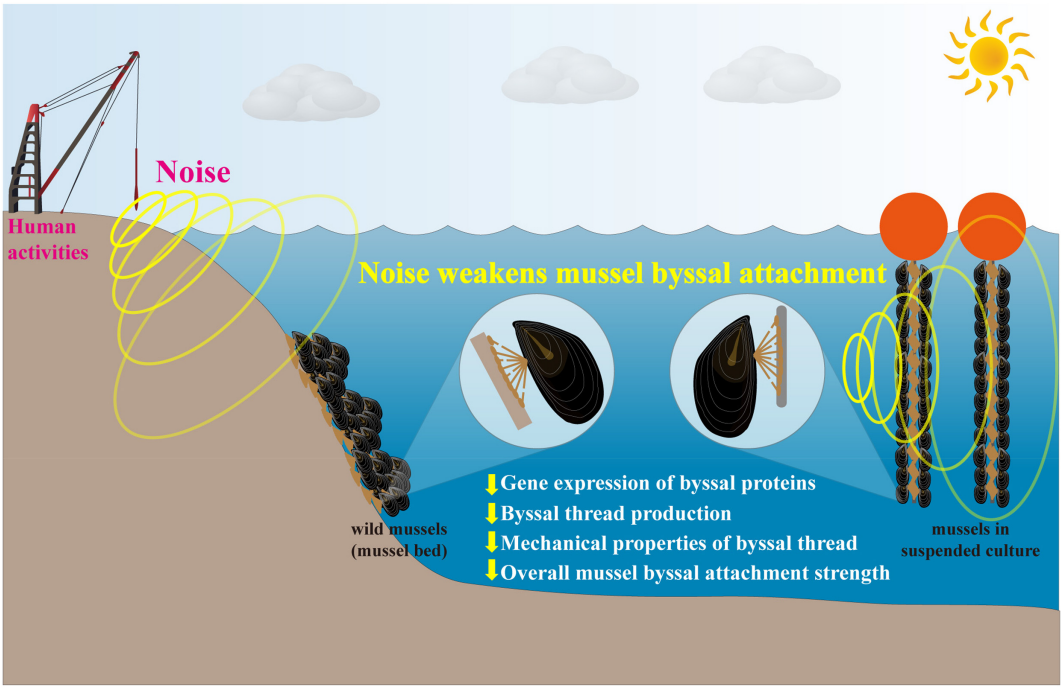

FIGURE 7 | Schematic diagram showing the main findings and implications of this study. Exposure to playbacks of the pile-driving noise significantly weakened gene expression of byssal proteins, secretion of byssal threads and their mechanical performances, which eventually led to a 16.95–44.50% decrease in the overall mussel byssal attachment strength. In conclusion, anthropogenic noise (e.g., the pile-driving noise) has negative impacts on both mussel individuals and population through hampering byssal attachment, in turn posing a great threat to mussel-bed community and mussel aquaculture industry.

Vazzana et al., 2016). These suggest that mechanoreceptors mediate both mussel byssal attachment and sound detection. Thus, it is reasonable to infer that there might be any cross-talk between the two signal transduction pathways. In this way, the biological function of the mechanoreceptors in byssal attachment may be interfered by the coexisting noise. In turn, the process of byssal threads secretion and adhesion was disrupted, finally leading to the observed reduction in byssal thread production and mechanical performances in this study. In a word, the dysfunction, if any, of the mechanoreceptors might be one reason mediating the noise-induced alteration in mussel byssal attachment. Of course, empirical evidences are required to validate this assumption.

CONCLUSION

In conclusion, this study found that 10-day continuous exposure to playbacks of the pile-driving noise significantly weakened gene expression of byssal proteins, secretion of byssal threads and their mechanical performances, which eventually led to a 16.95–44.50% decrease in the overall mussel byssal attachment strength (**Figure 7**). Given the essential functions of strong byssal attachment, these findings suggest that the increasing underwater anthropogenic noise is posing a great threat to mussel population, mussel-bed community and mussel aquaculture industry. We thus suggest that future work is needed to enhance our understanding of the impacts of anthropogenic noise on marine invertebrates, especially these with limited locomotion ability, like bivalves.

DATA AVAILABILITY STATEMENT

The original contributions presented in the study are included in the article/supplementary material, further inquiries can be directed to the corresponding author/s.

AUTHOR CONTRIBUTIONS

XZ and GL conceived and designed this study. XZ and SS performed the whole experiments and collected the data. XZ wrote the manuscript, while other authors reviewed and revised the manuscript. GL provided oversight of the project. All authors gave final approval for publication and contributed to data analysis and interpretation.

FUNDING

This work was funded by the Shandong Provincial Natural Science Foundation (No. ZR2020QC209), the National Natural Science Foundation of China (No. 42106195), the Central Public-interest Scientific Institution Basal Research Fund, CAFS (No. 2020TD12), and the Central Public-interest Scientific Institution Basal Research Fund, YSFRI, CAFS (No. 20603022021005).

REFERENCES

Alves, D., Vieira, M., Amorim, M. C. P., and Fonseca, P. J. (2021). Boat noise interferes with lusitanian toadfish acoustic communication. *J. Exp. Biol.* 224:jeb234849. doi: 10.1242/jeb.234849

Amini, S., Kolle, S., Petrone, L., Ahanotu, O., Sunny, S., Sutanto, C. N., et al. (2017). Preventing mussel adhesion using lubricant-infused materials. *Science* 357, 668–673. doi: 10.1126/science.aai8977

Bandara, N., Zeng, H., and Wu, J. (2013). Marine mussel adhesion: biochemistry, mechanisms, and biomimetics. *J. Adhes. Sci. Technol.* 27, 2139–2162. doi: 10.1080/01694243.2012.697703

Bell, E. C., and Gosline, J. M. (1996). Mechanical design of mussel byssus: material yield enhances attachment strength. *J. Exp. Biol.* 199, 1005–1017. doi: 10.1242/jeb.199.4.1005

Borthagaray, A. I., and Carranza, A. (2007). Mussels as ecosystem engineers: their contribution to species richness in a rocky littoral community. *Acta Oecol.* 31, 243–250. doi: 10.1016/j.actao.2006.10.008

Charifi, M., Sow, M., Ciret, P., Benomar, S., and Massabuau, J.-C. (2017). The sense of hearing in the *Pacific oyster, Magallana gigas*. *PLoS One* 12:e0185353. doi: 10.1371/journal.pone.0185353

Christensen, H. T., Dolmer, P., Hansen, B. W., Holmer, M., Kristensen, L. D., Poulsen, L. K., et al. (2015). Aggregation and attachment responses of blue mussels, *Mytilus edulis*—impact of substrate composition, time scale and source of mussel seed. *Aquaculture* 435, 245–251. doi: 10.1016/j.aquaculture.2014.09.043

Day, R. D., McCauley, R. D., Fitzgibbon, Q. P., Hartmann, K., and Semmens, J. M. (2017). Exposure to seismic air gun signals causes physiological harm and alters behavior in the scallop *Pecten fumatus*. *Proc. Natl. Acad. Sci. U.S.A.* 114, E8537–E8546. doi: 10.1073/pnas.1700564114

de Jong, K., Amorim, M. C. P., Fonseca, P. J., Fox, C. J., and Heubel, K. U. (2018). Noise can affect acoustic communication and subsequent spawning success in fish. *Environ. Pollut.* 237, 814–823. doi: 10.1016/j.envpol.2017.11.003

de Soto, N. A., Delorme, N., Atkins, J., Howard, S., Williams, J., and Johnson, M. (2013). Anthropogenic noise causes body malformations and delays development in marine larvae. *Sci. Rep.* 3:2831. doi: 10.1038/srep02831

Di Franco, E., Pierson, P., Di Iorio, L., Calò, A., Cottalorda, J. M., Derijard, B., et al. (2020). Effects of marine noise pollution on mediterranean fishes and invertebrates: a review. *Mar. Pollut. Bull.* 159:111450. doi: 10.1016/j.marpolbul.2020.111450

Di Iorio, L., and Clark, C. W. (2010). Exposure to seismic survey alters blue whale acoustic communication. *Biol. Lett.* 6, 51–54. doi: 10.1098/rsbl.2009.0651

Duarte, C. M., Chapuis, L., Collin, S. P., Costa, D. P., Devassy, R. P., Eguiluz, V. M., et al. (2021). The soundscape of the *Anthropocene ocean*. *Science* 371:eaba4658. doi: 10.1126/science.aba4658

Erbe, C., Dunlop, R., and Dolman, S. (2018). "Effects of noise on marine mammals," in *Effects of Anthropogenic Noise on Animals*, eds H. Slabbekoorn, R. J. Dooling, A. N. Popper, and R. R. Fay (New York, NY: Springer), 277–309.

Hawkins, A. J. S., and Bayne, B. L. (1985). Seasonal variation in the relative utilization of carbon and nitrogen by the mussel mytilus edulis: budgets, conversion efficiencies and maintenance requirements. *Mar. Ecol. Prog. Ser.* 25, 181–188. doi: 10.3354/meps025181

Hildebrand, J. A. (2009). Anthropogenic and natural sources of ambient noise in the ocean. *Mar. Ecol. Prog. Ser.* 395, 5–20. doi: 10.3354/meps08353

Jerem, P., and Mathews, F. (2021). Trends and knowledge gaps in field research investigating effects of anthropogenic noise. *Conserv. Biol.* 35, 115–129. doi: 10.1111/cobi.13510

Kastelein, R. A., Helder-Hoek, L., Kommeren, A., Covi, J., and Gransier, R. (2018). Effect of pile-driving sounds on harbor seal (*Phoca vitulina*) hearing. *J. Acoust. Soc. Am.* 143, 3583–3594. doi: 10.1121/1.5040493

Kok, A., Hulten, D., Timmerman, K., Lankhorst, J., Visser, F., and Slabbekoorn, H. (2021). Interacting effects of short-term and long-term noise exposure on antipredator behaviour in sand gobies. *Anim. Behav.* 172, 93–102. doi: 10.1016/j.anbehav.2020.12.001

Kong, H., Clements, J. C., Dupont, S., Wang, T., Huang, X., Shang, Y., et al. (2019). Seawater acidification and temperature modulate anti-predator defenses in two co-existing *Mytilus* species. *Mar. Pollut. Bull.* 145, 118–125. doi: 10.1016/j.marpolbul.2019.05.040

Lachance, A.-A., Hennebicq, R., Myrand, B., Sévigny, J.-M., Kraffe, E., Marty, Y., et al. (2011). Biochemical and genetic characteristics of suspension-cultured mussels (*Mytilus edulis*) in relation to byssal thread production and losses by fall-off. *Aquat. Living Resour.* 24, 283–293. doi: 10.1051/alr/2011115

LaCourse, J. R., and Northrop, R. B. (1978). A preliminary study of mechanoreceptors within the anterior byssus retractor muscle of *Mytilus edulis* L. *Biol. Bull.* 155, 161–168. doi: 10.2307/1540873

Lee, B. P., Messersmith, P. B., Israelachvili, J. N., and Waite, J. H. (2011). Mussel-inspired adhesives and coatings. *Annu. Rev. Mater. Res.* 41, 99–132. doi: 10.1146/annurev-matsci-062910-100429

Li, L., Lu, W., Sui, Y., Wang, Y., Gul, Y., and Dupont, S. (2015). Conflicting effects of predator cue and ocean acidification on the mussel *Mytilus coruscus* byssus production. *J. Shellfish Res.* 34, 393–400. doi: 10.2983/035.034.0222

Liu, G., Stapleton, E., Innes, D., and Thompson, R. (2011). Aggregational behavior of the blue mussels *Mytilus edulis* and *Mytilus trossulus*: a potential pre-zygotic reproductive isolation mechanism. *Mar. Ecol.* 32, 480–487. doi: 10.1111/j.1439-0485.2011.00446.x

Livak, K. J., and Schmittgen, T. D. (2001). Analysis of relative gene expression data using real-time quantitative PCR and the $2^{-\Delta\Delta Ct}$ method. *Methods* 25, 402–408. doi: 10.1006/meth.2001.1262

Lurman, G. J., Hilton, Z., and Ragg, N. L. C. (2013). Energetics of byssus attachment and feeding in the green-lipped mussel *Perna canaliculus*. *Biol. Bull.* 224, 79–88. doi: 10.1086/BBLv224n2p79

Moeser, G. M., and Carrington, E. (2006). Seasonal variation in mussel byssal thread mechanics. *J. Exp. Biol.* 209, 1996–2003. doi: 10.1242/jeb.02234

Nedelec, S. L., Simpson, S. D., Morley, E. L., Nedelec, B., and Radford, A. N. (2015). Impacts of regular and random noise on the behaviour, growth and development of larval Atlantic cod (*Gadus morhua*). *Proc. R. Soc. B* 282:20151943. doi: 10.1098/rspb.2015.1943

O'Donnell, M. J., George, M. N., and Carrington, E. (2013). Mussel byssus attachment weakened by ocean acidification. *Nat. Clim. Change* 3, 587–590. doi: 10.1038/nclimate1846

Peng, C., Zhao, X., and Liu, G. (2015). Noise in the sea and its impacts on marine organisms. *Int. J. Env. Res. Public Health* 12, 12304–12323. doi: 10.3390/ijerph121012304

Peng, C., Zhao, X., Liu, S., Shi, W., Han, Y., Guo, C., et al. (2016). Effects of anthropogenic sound on digging behavior, metabolism, Ca^{2+}/Mg^{2+} ATPase activity, and metabolism-related gene expression of the bivalve *Sinonovacula constricta*. *Sci. Rep.* 6:24266. doi: 10.1038/srep24266

Popper, A. N., and Hawkins, A. D. (2019). An overview of fish bioacoustics and the impacts of anthropogenic sounds on fishes. *J. Fish Biol.* 94, 692–713. doi: 10.1111/jfb.13948

Popper, A. N., Hawkins, A. D., and Thomsen, F. (2020). Taking the Animals' perspective regarding anthropogenic underwater sound. *Trends Ecol. Evol.* 35, 787–794. doi: 10.1016/j.tree.2020.05.002

Purser, J., and Radford, A. N. (2011). Acoustic noise induces attention shifts and reduces foraging performance in three-spined sticklebacks (*Gasterosteus aculeatus*). *PLoS One* 6:e17478. doi: 10.1371/journal.pone.0017478

Roberts, E. A., Newcomb, L. A., McCartha, M. M., Harrington, K. J., LaFramboise, S. A., Carrington, E., et al. (2021). Resource allocation to a structural biomaterial: induced production of byssal threads decreases growth of a marine mussel. *Funct. Ecol.* 35, 1222–1239. doi: 10.1111/1365-2435.13788

Roberts, L., Cheesman, S., Breithaupt, T., and Elliott, M. (2015). Sensitivity of the mussel *Mytilus edulis* to substrate-borne vibration in relation to anthropogenically generated noise. *Mar. Ecol. Prog. Ser.* 538, 185–195. doi: 10.3354/meps11468

Shang, Y., Gu, H., Chang, X., Li, S., Sokolova, I., Fang, J. K. H., et al. (2021). Microplastics and food shortage impair the byssal attachment of thick-shelled mussel *Mytilus coruscus*. *Mar. Environ. Res.* 171:105455. doi: 10.1016/j.marenvres.2021.105455

Shang, Y., Wang, X., Kong, H., Huang, W., Hu, M., and Wang, Y. (2019). Nano-ZnO impairs anti-predation capacity of marine mussels under seawater acidification. *J. Hazard. Mater.* 371, 521–528. doi: 10.1016/j.jhazmat.2019.02.072

Shi, W., Guan, X., Sun, S., Han, Y., Du, X., Tang, Y., et al. (2020). Nanoparticles decrease the byssal attachment strength of the thick shell mussel *Mytilus coruscus*. *Chemosphere* 257:127200. doi: 10.1016/j.chemosphere.2020.127200

Shi, W., Han, Y., Guan, X., Rong, J., Du, X., Zha, S., et al. (2019). Anthropogenic noise aggravates the toxicity of cadmium on some physiological characteristics of the blood clam *Tegillarca granosa*. *Front. Physiol.* 10:377. doi: 10.3389/fphys.2019.00377

Silverman, H. G., and Roberto, F. F. (2010). "Byssus formation in *Mytilus*," in *Biological Adhesive Systems*, eds J. von Byern and I. Grunwald (Vienna: Springer), 273–283.

Simpson, S. D., Purser, J., and Radford, A. N. (2015). Anthropogenic noise compromises antipredator behaviour in European eels. *Glob. Change Biol.* 21, 586–593. doi: 10.1111/gcb.12685

Slabbekoorn, H., Bouton, N., van Opzeeland, I., Coers, A., ten Cate, C., and Popper, A. N. (2010). A noisy spring: the impact of globally rising underwater sound levels on fish. *Trends Ecol. Evol.* 25, 419–427. doi: 10.1016/j.tree.2010.04.005

Smott, S., Monczak, A., Miller, M. E., and Montie, E. W. (2018). Boat noise in an estuarine soundscapea potential risk on the acoustic communication and reproduction of soniferous fish in the may river, South Carolina. *Mar. Pollut. Bull.* 133, 246–260. doi: 10.1016/j.marpolbul.2018.05.016

Solan, M., Hauton, C., Godbold, J. A., Wood, C. L., Leighton, T. G., and White, P. (2016). Anthropogenic sources of underwater sound can modify how sediment-dwelling invertebrates mediate ecosystem properties. *Sci. Rep.* 6:20540. doi: 10.1038/srep20540

Spiga, I., Caldwell, G. S., and Bruintjes, R. (2016). Influence of pile driving on the clearance rate of the blue mussel, *Mytilus edulis* (L.). *Proc. Mtgs. Acoust.* 27:040005. doi: 10.1121/2.0000277

Sui, Y., Hu, M., Huang, X., Wang, Y., and Lu, W. (2015). Anti-predatory responses of the thick shell mussel *Mytilus coruscus* exposed to seawater acidification and hypoxia. *Mar. Environ. Res.* 109, 159–167. doi: 10.1016/j.marenvres.2015.07.008

Sui, Y., Liu, Y., Zhao, X., Dupont, S., Hu, M., Wu, F., et al. (2017). Defense responses to short-term hypoxia and seawater acidification in the thick shell mussel *Mytilus coruscus*. *Front. Physiol.* 8:145. doi: 10.3389/fphys.2017.00145

Suplicy, F. M. (2020). A review of the multiple benefits of mussel farming. *Rev. Aquacult.* 12, 204–223. doi: 10.1111/raq.12313

van der Schatte Olivier, A., Jones, L., Vay, L. L., Christie, M., Wilson, J., and Malham, S. K. (2020). A global review of the ecosystem services provided by bivalve aquaculture. *Rev. Aquacult.* 12, 3–25. doi: 10.1111/raq.12301

Vaughn, C. C., and Hoellein, T. J. (2018). Bivalve impacts in freshwater and marine ecosystems. *Annu. Rev. Ecol., Evol.* 49, 183–208. doi: 10.1146/annurev-ecolsys-110617-062703

Vazzana, M., Celi, M., Maricchiolo, G., Genovese, L., Corrias, V., Quinci, E. M., et al. (2016). Are mussels able to distinguish underwater sounds? Assessment of the reactions of *Mytilus galloprovincialis* after exposure to lab-generated acoustic signals. *Comput. Biochem. Physiol. Mol. Integr. Physiol.* 201, 61–70. doi: 10.1016/j.cbpa.2016.06.029

Vazzana, M., Ceraulo, M., Mauro, M., Papale, E., Dioguardi, M., Mazzola, S., et al. (2020). Effects of acoustic stimulation on biochemical parameters in the digestive gland of mediterranean mussel *Mytilus galloprovincialis* (Lamarck, 1819). *J. Acoust. Soc. Am.* 147, 2414–2422. doi: 10.1121/10.0001034

Vieira, M., Beauchaud, M., Amorim, M. C. P., and Fonseca, P. J. (2021). Boat noise affects meagre (*Argyrosomus regius*) hearing and vocal behaviour. *Mar. Pollut. Bull.* 172:112824. doi: 10.1016/j.marpolbul.2021.112824

Waite, J. H. (1983). Adhesion in byssally attached bivalves. *Biol. Rev.* 58, 209–231. doi: 10.1111/j.1469-185X.1983.tb00387.x

Wale, M. A., Briers, R. A., and Diele, K. (2021). Marine invertebrate anthropogenic noise research – Trends in methods and future directions. *Mar. Pollut. Bull.* 173:112958. doi: 10.1016/j.marpolbul.2021.112958

Wale, M. A., Briers, R. A., Hartl, M. G. J., Bryson, D., and Diele, K. (2019). From DNA to ecological performance: effects of anthropogenic noise on a reef-building mussel. *Sci. Total Environ.* 689, 126–132. doi: 10.1016/j.scitotenv.2019.06.380

Wale, M. A., Simpson, S. D., and Radford, A. N. (2013). Noise negatively affects foraging and antipredator behaviour in shore crabs. *Anim. Behav.* 86, 111–118. doi: 10.1016/j.anbehav.2013.05.001

Zhao, X., Guo, C., Han, Y., Che, Z., Wang, Y., Wang, X., et al. (2017). Ocean acidification decreases mussel byssal attachment strength and induces molecular byssal responses. *Mar. Ecol. Prog. Ser.* 565, 67–77. doi: 10.3354/meps11992

Zhao, X., Han, Y., Chen, B., Xia, B., Qu, K., and Liu, G. (2020). CO_2-driven ocean acidification weakens mussel shell defense capacity and induces global molecular compensatory responses. *Chemosphere* 243:125415. doi: 10.1016/j.chemosphere.2019.125415

Conflict of Interest: The authors declare that the research was conducted in the absence of any commercial or financial relationships that could be construed as a potential conflict of interest.

Publisher's Note: All claims expressed in this article are solely those of the authors and do not necessarily represent those of their affiliated organizations, or those of the publisher, the editors and the reviewers. Any product that may be evaluated in this article, or claim that may be made by its manufacturer, is not guaranteed or endorsed by the publisher.

frontiers in Marine Science

ORIGINAL RESEARCH
published: 06 January 2022
doi: 10.3389/fmars.2021.773210

Spatial Distribution, Diversity, and Activity of Microbial Phototrophs in the Baltic Sea

Peihang Xu[1], Christian Furbo Reeder[1,2] and Carolin Regina Löscher[1,2]*

[1] Nordcee, Department of Biology, University of Southern Denmark, Odense, Denmark, [2] Danish Institute for Advanced Study, University of Southern Denmark, Odense, Denmark

Microbial plankton is essential for ocean biogeochemistry. As part of the prokaryotic phototrophic microbial community, both oxygenic phototrophs (OP) and anoxygenic phototrophs (AP) are widely distributed in the ocean and may play a significant role in carbon flow and oxygen production. However, comparative studies of microbial OP and AP have received very little attention, even though their different roles might be important in various marine environments, especially in oxygen minimum zones (OMZ). We explored the spatial distribution of the microbial community in the Baltic Sea, including an OMZ region, with a particular focus on the distribution and activity of OP and AP. We used 16S rRNA amplicon sequencing in combination with a qPCR-based quantification of photosynthesis marker genes. We found that specific bacterial groups dominated surface and intermediate depths, the OMZ, and deep waters, respectively. Salinity, temperature, oxygen, and depth were significant factors explaining the microbial community composition and distribution. A high diversity of OP and AP was observed, including OP-Chlorophyta, Diatoms, Cyanobacteria and Cryptomonads, and AP-Proteobacteria and Chloroflexota. OP were more abundant at most stations compared to AP. OP showed high photosynthetic activity and more photosynthesis activity in higher temperature and upper waters, while AP photosynthesis cannot be detected in most stations. Both, cyanobacterial and eukaryotic OP preferred to live in higher temperature and upper waters, but Cyanobacteria also preferred to live in oxic water while the whole OP community showed preference to live in higher salinity area. However, AP did not show any significant hydrochemical preference but prefer to live with OP community. The Baltic Sea is exposed to multiple climate change related stressors, such as warming, decreasing salinity, and deoxygenation. This study contributes to understanding and interpretation of how microbial community, especially phototrophic groups, might shift in their distribution and activity in a changing ocean like the Baltic Sea.

Keywords: microbial plankton, oxygenic phototrophs, anoxygenic phototrophs, photosynthesis activity, *puf*M, *psb*A, oxygen minimum zones, environmental factors

OPEN ACCESS

Edited by:
Rebecca Metzler, Colgate University, United States

Reviewed by:
Kasia Piwosz, National Marine Fisheries Research Institute, Poland
Eric Capo, Umeå University, Sweden

****Correspondence:***
Peihang Xu
peihang@biology.sdu.dk

Specialty section:
This article was submitted to Marine Molecular Biology and Ecology, a section of the journal Frontiers in Marine Science

Received: *09 September 2021*
Accepted: *14 December 2021*
Published: *06 January 2022*

Citation:
Xu P, Reeder CF and Löscher CR (2022) Spatial Distribution, Diversity, and Activity of Microbial Phototrophs in the Baltic Sea. Front. Mar. Sci. 8:773210. doi: 10.3389/fmars.2021.773210

INTRODUCTION

Microbial plankton has a global and major impact on ocean biogeochemistry (Falkowski et al., 2008), and its distribution and importance has been studied throughout many ocean areas (Brown et al., 2009; Alves Junior et al., 2015; Fernandes et al., 2020). However, there are still gaps in the fundamental ecological information about the biogeographical and spatial distributions of these organisms and their interaction with their environment. Among microbial plankton, oxygenic phototrophs (OP) are the key group to take up carbon and the main contributor to marine primary production (Raven, 2009). OP consist of two groups, Cyanobacteria and Eukaryotic algae (Liu et al., 2016), which carry out photosynthesis using chlorophyll (Chl) through photosystem I (PSI) and II (PSII) and release O_2 during this process (Luuc et al., 1999). On the other hand, anoxygenic phototrophs (AP), especially aerobic anoxygenic phototrophs (AAP), have been considered to have a unique role in the ocean carbon cycle due to their ability to generate energy by capturing light and faster growth rates than other bacterioplankton (Koblížek et al., 2007; Ferrera et al., 2011; Garcia-Chaves et al., 2016). AAP are photoheterotrophs, while the other group of AP, anaerobic anoxygenic phototrophs (AnAP), are photoautotrophs under the presence of light and anoxic conditions (Yurkov and Beatty, 1998; Koblížek, 2015; Imhoff, 2017). Both AAP and AnAP could use bacteriochlorophyll (BChl) to capture light and produce ATP through either type-I or type-II photosystems without releasing O_2 (Imhoff et al., 2018; Fecskeová et al., 2019). The major group of AP, belonging to Proteobacteria (such as orders Sphingomonadales and Rhodobacterales), have been shown to be abundant and diverse in the ocean, and may play an important but underestimated role in marine productivity and energy flow (Karl, 2002; Yutin et al., 2007; Boeuf et al., 2013). As both OP and AP could use light as an energy source, and play important roles in biogeochemical cycle and energy flow in the ocean, the relative distribution and activity of OP and AP shifting to different environment could influence carbon and oxygen dynamics vital for ocean ecology.

The diversity and abundance of AP, especially AAP, has been studied in many marine environments using different methods, such as qPCR and metagenomics using the AP photosynthesis specific marker gene *puf*M [encoding the Type-2 photosynthetic reaction center subunit M (Imhoff et al., 2018)], *bch*Y (encoding both the Type-1 and Type-2 photosynthesis chlorophyllide oxidoreductase subunit Y) (Yutin et al., 2007, 2009; Salka et al., 2008; Bibiloni-Isaksson et al., 2016; Cuadrat et al., 2016), and BChl-based fluorescence detection (Cottrell et al., 2006; Lami et al., 2007; Zhang and Jiao, 2007). By screening the specific marker genes in the metagenome database from the Global Ocean Sampling Expedition, AAP account for 1–10% of total prokaryotes in the surface ocean (Yutin et al., 2007). Similar quantities were obtained when using fluorescence detection, with the average abundance 1–7% of total prokaryotes in oligotrophic ocean areas including the Mediterranean (1–4% in Hojerová et al., 2011), 2–15% of total prokaryotes in shelf seas (Koblížek, 2015), and 1–12% in a late spring bloom situation in the Baltic Sea (Montecchia et al., 2006). A substantially higher fraction of AAP of around 25% of total bacteria was detected in the oligotrophic South Pacific Ocean (Lami et al., 2007).

Modern approaches to quantify prokaryotic OP in parallel to AP included chlorophyll a (Chla) quantification (Koblížek et al., 2006, 2007; Hojerová et al., 2011), and flow cytometry to determine abundances of Cyanobacteria (*Synechococcus* and *Prochlorococcus*), but also autotrophic eukaryotes (Zhang and Jiao, 2007; Liu et al., 2010). Other approaches used metagenomics to target the OP photosynthesis-specific marker genes *psb*A (a PSII reaction center protein D1) and *psa*A (PSI P700 Chla apoprotein A1) (Alcamán-Arias et al., 2018; Sieradzki et al., 2018). By comparing specific marker gene abundances in a metagenome from the upper seawater (< 40 m) of the coastal area of the San Pedro Channel in the Pacific Ocean (Sieradzki et al., 2018), OP-PSI related genes were 2–3 times more abundant than AAP photosynthesis related genes. In surface waters of the Mediterranean coast, *Synechococcus* was substantially more abundant than AAP (2–14% vs. 0.2–6.3% of total prokaryotes) (Ferrera et al., 2014). In a depth profile of the Kuroshio Current water system of the East China Sea, various OP peaked in surface waters, while AAP reached a maximum abundance between 42 and 76 m water depth (Zhang and Jiao, 2007). Many environmental variables have been proposed to influence the abundance and distribution of OP and AP, respectively. These include temperature, salinity, light attenuation, and nutrient concentrations (Paerl, 2012; Ferrera et al., 2014; Liu et al., 2016). However, comparative studies of the ecology of OP and AP are still quite rare, and the role of AP is yet not well understood. Furthermore, most studies only focus on AAP in oxic environments, but AnAP in anoxic water may play an increasing role in the future while anoxic ocean water might expand to even reach euphotic zone, as oxygen-depleted ocean regions have already increased over the last 50–100 years, and are predicted to further expand and intensify (Van Cappellen et al., 2008; Levin, 2018).

The Baltic Sea is an example of a marine region with expanding oxygen depleted waters. It is characterized as a large semi-enclosed and shallow brackish sea affected by deoxygenation, acidification, and anthropogenic nutrient pollution. Over the last 115 years, the Baltic Sea has experienced a severe expansion of oxygen depleted waters, which today cover an area of 12,000–70,000 km^2 (Rutgersson et al., 2014; Reusch et al., 2018). Coastal waters of the Baltic Sea are especially prone to increased nutrient pollution causing eutrophication, frequent events of anoxia and hypoxia, and shifts from benthic to pelagic primary production (Carstensen et al., 2014; Rutgersson et al., 2014; Breitburg et al., 2018; Reusch et al., 2018). Different conditions with regard to deoxygenation, acidification and nutrient status have been studied in the various sub-basins of the Baltic Sea, and steep gradients of salinity and overlapping gradients of biologically relevant elements introduce dramatic geographical and seasonal changes of the microbial community (Mašín et al., 2006; Conley et al., 2009; Bentzon-Tilia et al., 2015). Salinity has been described as a driving factor for community shifts in the Baltic Sea, e.g., Actinobacteria dominating low-salinity areas, while high-salinity areas are dominated by Proteobacteria and Bacteroidetes (Dupont et al., 2014). Typically,

the Baltic Sea primary producer community is dominated by Diatoms and Dinophytes from March to May and by Cyanobacteria and to a lesser extent by Dinophytes and Chlorophytes from September to October (Stoń et al., 2002; Norbent and Steffen, 2003). In addition, AAP (∼12% of total bacteria) were identified in the Baltic Sea waters (< 50 m), with a maximum in summer and a minimum in winter (Mašín et al., 2006). Due to the combination of climate-related threats, the Baltic Sea has been described as a "time machine" for how future oceans could respond to climate change (Reusch et al., 2018). This makes it an interesting environment to investigate the pattern of microbes and different phototrophs in a future ocean analog, which, especially, in relation to oxygen-depleted areas requires further research.

To address this topic, we studied the spatial pattern of bacterial diversity and abundance in the Baltic Sea, with a specific focus on AP and OP (without eukaryotic algae), using 16S rRNA amplicon sequencing. An oxygen minimum zone (OMZ) was included in our sampling strategy. We also used qPCR targeting specific marker genes of AP and OP (including eukaryotic algae) to detect and compare their diversity and distribution. The most common used marker genes, *puf*M and *bch*Y, were used for targeting AP. The *psb*A gene was used for targeting OP. We further used gene expression profiles of *psb*A and *puf*M genes (Sharon et al., 2007; Kong et al., 2014; Alcamán-Arias et al., 2018; Fecskeová et al., 2019), as well as carbon fixation rates to understand photosynthesis activity in the different basins of the Baltic Sea. Here, we investigate the spatial pattern of expression of *psb*A and *puf*M and compare their roles in different Baltic Sea environments to extend the understanding of how the role of those different groups of phototrophic groups in a changing ocean.

MATERIALS AND METHODS

Environmental Sampling and Processing

Samples were collected during a cruise from Sep. 17th to Sep. 28th, 2019, on the German research vessel RV Alkor (Alkor528). The Baltic Sea water was collected at depths between 3 and 115 m at the following locations: Kiel Fjord (K06), Arkona Basin (AB21, AB31), Bornholm Basin (BB23, BB15, BB08, BB31) and Gotland Basin (GB84, GB90a, GB107, GB108) (**Figure 1**). The samples were collected with a 10L Niskin bottle rosette water sampler, equipped with a conductivity-temperature-depth (CTD) sensor. pH was measured by the PHM210 standard pH meter (Radiometer Analytical, Meterlab). For Chla analysis, 0.5 L of seawater was collected and immediately filtered through 45 mm GF/F Whatman filters with a pore size of 0.7 μm and stored at −20°C for further later usage. Chla was extracted using 100% acetone from homogenized filters, and clear extracts were analyzed using trilogy laboratory fluorometer (Turner Designs). A serial dilution of a Chla standard (Sigma Aldrich, St Louis, United States) was used to calibrate for the fluorometer. For dissolved inorganic carbon (DIC) analysis, 12 ml water was filled bubble free in 12 ml exetainers, fixed immediately with 20 μl saturated mercury chloride solution and stored at room temperature. The analysis was carried out following the method described in Hall and Aller (1992) with a standard solution of 2 mM $NaHCO_3$. For carbon fixation rates, water samples were filled bubble-free into 2.4 L glass bottles. Subsequently, 1 ml $H^{13}CO_3$ solution (1 g per 50 ml, Sigma-Aldrich, Saint Louis Missouri, United States) was added to each bottle through an air-tight septum and bottles were shaken to mix properly. After 24 h of incubation time in natural light conditions on the ship's deck, samples were filtered through pre-combusted (450°C, 4–6 h) 45 mm 0.7 GF/F Whatman filters and then stored at −20°C until further analysis. Filters were acidified and dried before analysis on an Elemental Analyzer Flash EA 1112 series (Thermo Fisher) connected to an isotope ratio mass spectrometer (Finnigan Delta Plus XP, Thermo Fisher Scientific). Triplicate samples were measured for Chla, DIC and carbon fixation rates analysis.

Nucleic Acid Extraction, Library Preparation and Sequencing

For DNA and RNA analysis, 0.5–1 L of seawater was collected and immediately filtered onto a 0.22 μm MCE membrane filter (Merck Millipore Ltd., Ireland) and stored at −80°C for 10 months until further analysis. To extract the DNA and RNA, filters were flash-frozen in liquid nitrogen and crushed. DNA and RNA were extracted using the MasterPure Complete (MPC) DNA and RNA Purification Kit (Lucigen, United States), according to the manufacturer's protocol. Nucleic acids were quality checked on a spectrofluorometer (MySpec, VWR, Radnor, United States). DNase I, Amplification Grade (Invitrogen, Thermo Fisher Scientific, United Kingdom), was used to digest DNA in all RNA samples before further analysis. The purity of RNA was checked via qPCR for *puf*M and *psb*A using RNA as a template. No amplification could be detected. Subsequently, cDNA was generated from the DNase I-treated RNA samples following the instructions of the QuantiTect Reverse Transcription Kit (Qiagen, Hilden, Germany). In total, 16 samples of DNA were sequenced using Illumina Miseq sequencing targeting the V1-2 regions of the 16S rRNA, which was amplified using the primer pair 27F (5′ → 3′ AGAGTTTGATCCTGGCTCAG) and 338R (5′ → 3′ TGCTGCCTCCCGTAGGAGT) (Peiffer et al., 2013). After an initial denaturation at 98°C for 30 s, 30 cycles of 98°C for 9 s, 55°C for 60 s, and 72°C for 90 s were run. PCRs were run using a Phusion Hot start II High-Fidelity DNA Polymerase (500U) according to the manufacturer's instructions with the buffer provided. Library preparations and sequencing was carried out at the Institute for Clinical Molecular Biology (IKMB), University of Kiel (Germany). Sequences were submitted to the National Center for Biotechnology Information GenBank database under the accession number SAMN20309768-SAMN20309783. Bcl2fastq v2.18 (Illumina) was used to perform demultiplexing and adaptor cutting. Subsequently, the raw paired-end reads were put into DADA2 (v1.14.2) (Callahan et al., 2016) in R (R Core Team, 2020) (v 3.6.3) for quality filtering [truncLen = c(240,200), maxEE = c(2,2), truncQ = 2, rm.phix = TRUE], sequence

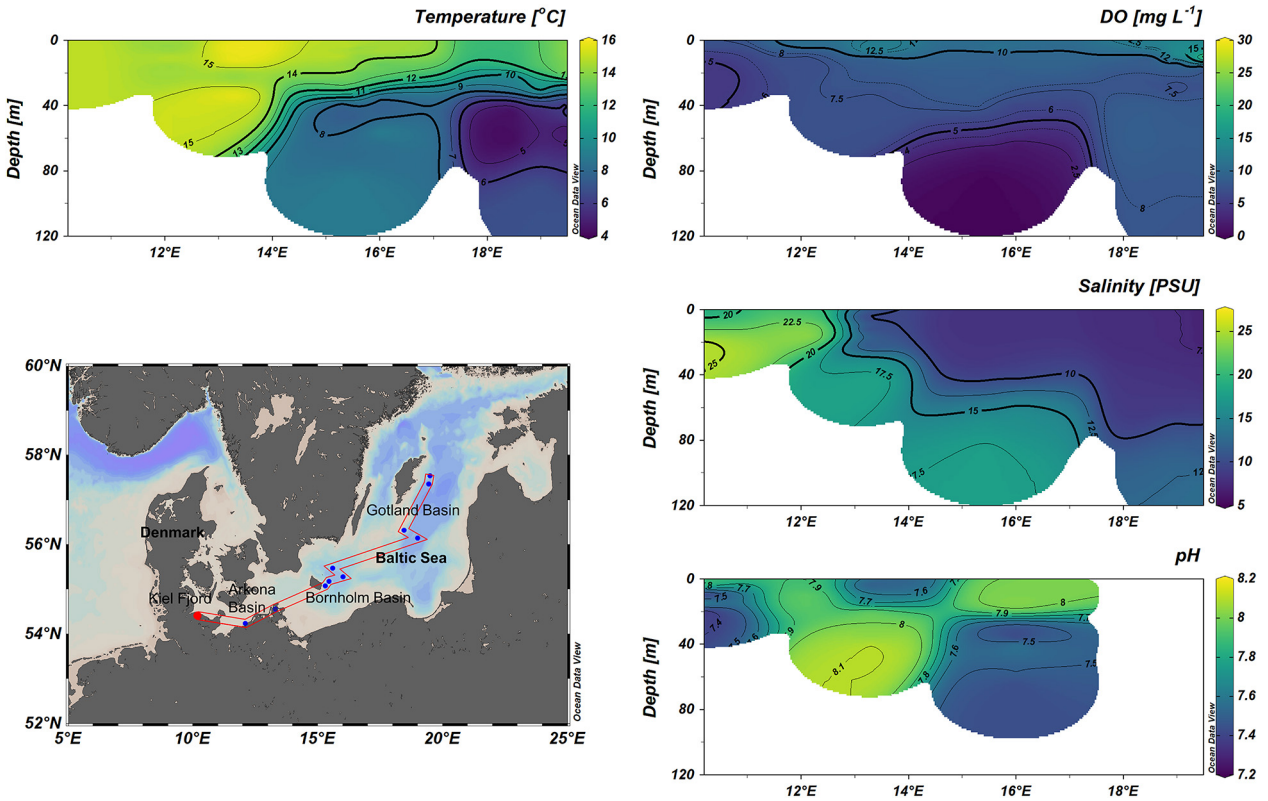

FIGURE 1 | Sampling distributions and vertical profiles of temperature, salinity, pH, and concentrations of dissolved oxygen in the Baltic Sea.

variant calling and taxonomic assignment with SILVA (v138) (Quast et al., 2013).

Statistical and Functional Analysis of 16S rRNA Amplicon Sequencing

An amplicon sequencing variant (ASV) table generated by DADA2 was used for downstream analysis. All reads of 16 samples were rarefied to the lowest final reads among the samples before further analysis. The ampvis2 package (v. 2.6.7) (Andersen et al., 2018) was used to assess the taxonomic richness (Shannon diversity, Observed ASVs) and plot heatmaps. Beta diversity of samples was plotted based on basins and depths using canonical correspondence analysis (CCA) in the ampvis2 package. The oxygen minimum zone (O_2 < 0.5 mg L^{-1}) was highlighted in the CCA plot. Distance-based redundancy analysis (db-RDA) was performed to explain the contribution of each environmental factor in driving the whole microbial community with the vegan package (v 2.5–7) (Oksanen et al., 2013). Furthermore, based on the taxonomic ASV table, phototrophic bacteria were extracted and used to compare the spatial distribution between AP and OP. The anoxygenic phototrophic purple bacteria belonging to Proteobacteria were extracted based on groups summarized by Imhoff (Imhoff et al., 2018). However, as many species cannot be diagnosed down to genus and species levels in an ASV table, all the families involving AP were extracted although it may contain non-phototrophic chemotrophs. Therefore, the AP group extracted from microbial community might be overestimated.

Clone Library Construction for *puf*M, *bch*Y, and *psb*A Genes

The *puf*M, *bch*Y and *psb*A genes were amplified by PCR from environmental DNA samples. The *puf*M gene was targeted using the primer set *puf*M-557F and *puf*M-750R (forward: CGCACCTGGACTGGAC, reverse: CCATGGTCCAGCGCCAGAA), generating a product length of 229 bp (Ahn et al., 2014). The *bch*Y primer set was *bch*Y-F and *bch*Y-R (forward: CCNCARACNATGTGYCCNGCNTTYGG, reverse: GGRTCNRCNGGRAANATYTCNCC), generating a product length of 510 bp (Yutin et al., 2009). The *psb*A gene was amplified with the primer set *psb*A-F and *psb*A-R (forward: GTITTYCARGCIGARCAYAAYATIYTIATGCAYCC, reverse: CCRTTIARRTTRAAIGCCATIGT), resulting in a product length of 344 bp (Kong et al., 2014). The PCR conditions are given in **Supplementary Table 1**. Each PCR reaction mixture contained 0.25 μl Taq-Polymerase (5 U μl^{-1}), 1μl of each primer (20 pmol μl^{-1}), 5μl dNTPs (2 mM), 5 μl Taq-buffer (10x) and 5 μl $MgCl_2$ (25 mM), 1 μl DNA template, 1 μl BSA and distilled water in a final volume of 50 μl. All PCR products were purified using the E.Z.N.A. gel extraction kit (Omega Bio-Tek, Inc., United States), and then Topo TA cloned (Invitrogen, Life Technologies Grand Islands, NY, United States) Sanger Sequencing was carried out at

the Institute for Clinical Molecular Biology (IKMB), University of Kiel (Germany). Trimmed and quality checked nucleotide sequences were aligned with closest references, and maximum likelihood trees were generated using the MEGA-X software (v 10.1.7) with the ClustalW alignment algorithm (Kumar et al., 2018) (Tamura-Nei Model, 500 bootstraps). Clone sequences generated in our study were submitted to the National Center for Biotechnology Information GenBank database and assigned accession numbers (MZ960574 to MZ960756).

Quantitative PCR for *puf*M and *psb*A Genes

Quantitative PCR were used to quantify *puf*M and *psb*A gene copy numbers (DNA) and gene expression abundance (mRNA). The primers used for *puf*M and *psb*A genes were the same set as described in clone library construction. The qPCR conditions for *puf*M amplification were set as following: an initial step at 95°C for 15 min, followed by 40 cycles of 95°C for 30 s, 58°C for 30 s, 72°C for 30 s. The qPCR conditions for *psb*A amplification were set as following: an initial step at 95°C for 15 min, followed by 45 cycles of 95°C for 30 s, 50°C for 50 s, 72°C for 50 s. Each qPCR reaction mixture was 25 μl, containing 1 μl of DNA template and 12.5 μl RealQ plus 2 × Master Mix (Amplicon PCR enzymes and reagents, Denmark), 0.5 μl BSA (20 mg ml^{-1}) and 0.25 μl of each primer (20 pmol μl^{-1}) and 10.5 μl distilled water. Known concentrations of plasmids containing *puf*M or *psb*A were used to make standard curves. Reactions with no template were running as negative control with each plate. All standards and samples were running in duplicate.

Statistical Analyses

A Pearson correlation test was performed to analyze the correlation between photosynthesis gene abundances, photosynthesis transcript abundances, transcriptional activity, phototrophic abundances in the microbial community and environmental parameters. A one-way ANOVA was performed to analyze the significant difference between AP and OP photosynthesis gene groups. Both methods were conducted using GraphPad Prism (v 9.2.0, GraphPad Software, United States).

RESULTS

Biogeochemistry During the Cruise

Our cruise took place in fall, and depth profiles from the Kiel Fjord, the Arkona Basin, the Bornholm Basin and the Gotland Basin varied between basins (**Table 1** and **Figure 1**). In Kiel Fjord and west of the Arkona Basin, the water temperature and salinity were quite similar across all depths (< 20 m), ranging from 14 to 15℃, and from 18.74 to 25.8 PSU, respectively. From the east of Arkona Basin to the Bornholm and Gotland Basins, salinity was much lower (6.97–18.5 PSU) compared to the Kiel Fjord and west of the Arkona Basin, and it was higher in deep waters than other water depths. In Bornholm and Gotland Basins, water temperatures were generally higher in surface waters (12–15.6℃) and decreased in deeper waters (4–8.8℃). In all stations, dissolved oxygen (DO) profiles were similar, with higher DO level in surface waters comparing to other water depths. Oxygen-depleted waters were observed in the Bornholm Basin, especially at stations BB23 and BB15, with O_2 concentrations below 0.4 mg L^{-1} in subsurface waters (around 65 ∼ 80 m). Chla concentrations were high in waters of the Kiel Fjord (< 20 m), ranging from 2.26 ± 1.31 μg L^{-1} and 3.39 ± 1.21 μg L^{-1}. Generally, Chla concentrations were higher in surface waters (5 m) and decreased over depth (< 70 m, < 0.01 μg L^{-1}) in Arkona Basin, Bornholm Basin and Gotland Basin. Except for an extremely low data point at a depth of 41 m at station BB15, the carbon fixation rate was similar at depth between 3 and 20 m across all stations, ranging from 0.027 to 0.068 μmol C L^{-1} d^{-1}.

Prokaryotic Community Structure

A total of 89 bacterial phyla were identified from all our 16 samples, involving 8 stations of three basins and 1–3 depths in each station (**Supplementary Figure 1**). Proteobacteria, Actinobacteriota and Bacteroidota dominated the bacterial community in all samples, accounting for 15.9–55.8%, 5.4–36.6%, and 9.9–27%, respectively. Campilobacterota or Desulfobacterota were prominent phyla only in deep waters of GB (32.8–38.2% and 9.5–14.4%, respectively). In contrast, Cyanobacteria were dominant in surface waters (< 8 m) and decreased dramatically to 0.5% in deep waters. In the level of order, except for deep samples from below 85 m, the SAR11 clade belonging to Proteobacteria was the top order in most samples (**Figure 2**). Flavobacteriales and Microtrichales belonging to Bacteroidota and Actinobacteriota, respectively, were also top orders in many samples (**Figure 2**). In oxygen depleted waters, especially at station BB23 at 85 m water depth, the dominant orders were substantially different compared to other samples, with Thiomicrospirales representing 15.9%, Rhodospirillales representing 10.6% and the SAR406 clade representing 17.1% (**Figure 2**).

In terms of the alpha diversity of bacterial communities present in the different samples, there were 167–406 ASVs identified across the three basins (AB, BB, and GB), and the Shannon indices ranged from 3.65 to 4.93 (**Table 2**). Moreover, the Shannon diversity of samples was low (< 4) in samples from deeper waters (BB23_85 m, GB107_112 m, GB108_115 m). Notably, the highest number of ASVs was observed in oxygen depleted waters (O_2 = 0.08 mg L^{-1}, BB15_65 m).

Canonical correspondence analysis (CCA) was used to analyze the beta diversity that separated the samples into abundance-based microbial community composition (**Figure 3**). Samples were grouped based on water depth, oxygen level, and location. For the profile for water depth and oxygen levels, the samples were grouped into surface water (0–12 m, DO: 7.5–14.4 mg L^{-1}), intermediate water (20–48 m, DO: 5–8.4 mg L^{-1}), OMZ (65–85 m, DO < 0.1 mg L^{-1}) and deep water (112–115 m, DO: 7.7–7.9 mg L^{-1}). The community structure showed substantial differences between OMZ, and deep water, compared to intermediate and surface waters. SAR11 clade and Flavobacteriales were the main groups dominating in surface and intermediate waters (**Figure 2**). Campilobacterota, Desulfobacterota, and Latescibacterota were only abundant in

TABLE 1 | Hydrographical profile in one fjord and three different basins of the Baltic Sea.

Basins	Sampling station	Coordinates: latitude, longitude	Measuring water depth (m)	Temperature (°C)	Sanility (PSU)	Dissolved oxygen (mg L^{-1})	pH	DIC (mM)	Chla (μg L^{-1})	Carbon fixation rate (μmol C L^{-1} d^{-1})
Kiel Fjord	K06	54.415°N, 10.204°E	2–21	15	18.74–25.8	4.6–8.16	7.96–8 (3–5 m) 7.23–7.73 (7–20 m)	1.91–2.08 (3–5 m) 1.93–2.28 (7–20 m)	2.26 ± 1.31 (5 m) 3.39 ± 1.21 (15 m)	0.030 ± 0.005 (3 m) 0.027 ± 0.016 (5 m) 0.031 ± 0.011 (10 m)
Arkona Basin	AB31	54.240°N, 12.100°E	2–16	14–15	20.69–24.57	6.96–12.1	7.92–7.96 (2–15 m)	1.90–2.37 (2–15 m)		
	AB21	54.565°N, 13.300°E	4–42	14–16	9.2–18.5	7.41–13.96	7.46–7.61 (4–12 m) 8–8.13 (22–42 m)	1.55–1.65 (4–12 m) 1.82–2.10 (22–42 m)		0.037 ± 0.006 (4 m) 0.043 ± 0.01 (6 m) 0.047 ± 0.007 (12 m)
Bornholm Basin	BB23	55.175°N, 15.449°E	4–85	7–16	8.14–17.95	0.04–9.39			2.97 ± 0.48 (5 m) 0 ± 0.01 (80 m)	
	BB15	55.276°N, 16.001°E	7–65	7–15	8.23–16.82	0.08–9.91	8.01–8.03 (7–15 m) 7.33–7.66 (36–65 m)	1.66–1.69 (7–15 m) 1.75–2.11 (36–65 m)	2.16 ± 1.57 (5 m) 0.01 ± 0 (70 m)	0.034 ± 0.022 (7 m) 0.051 ± 0.033 (15 m) 0.005 ± 0.0003 (41 m)
	BB08	55.475°N, 15.600°E	5–20	12–13	8.27–8.29	7.8–14.37				0.042 ± 0.003 (5 m) 0.052 ± 0.013 (10 m) 0.059 ± 0.007 (20 m)
	BB31	55.075°N, 15.301°E	10–40	6–16	8.13–8.4	7.83–9.35				
Gotland Basin	GB84	56.150°N, 19.000°E	5–100	5–13	7.63–12.65	6.93–16.1			1.16 ± 0.26 (5 m) 0.01 ± 0 (80 m)	0.050 ± 0.007 (4 m) 0.057 ± 0.023 (8 m) 0.068 ± 0.017 (18 m)
	GB90a	56.320°N, 18.459°E	4–60	4–12	7.7–8.57	7–13.21				
	GB107	57.360°N, 19.439°E	4–112	4–14	7.01–12.92	6.71–12.88				
	GB108	57.540°N, 19.500°E	10–115	6–14	6.97–12.97	7.32–8.23				

K, Kiel Fjord; AB, Arkona Basin; BB, Bornholm Basin; GB, Gotland Basin.

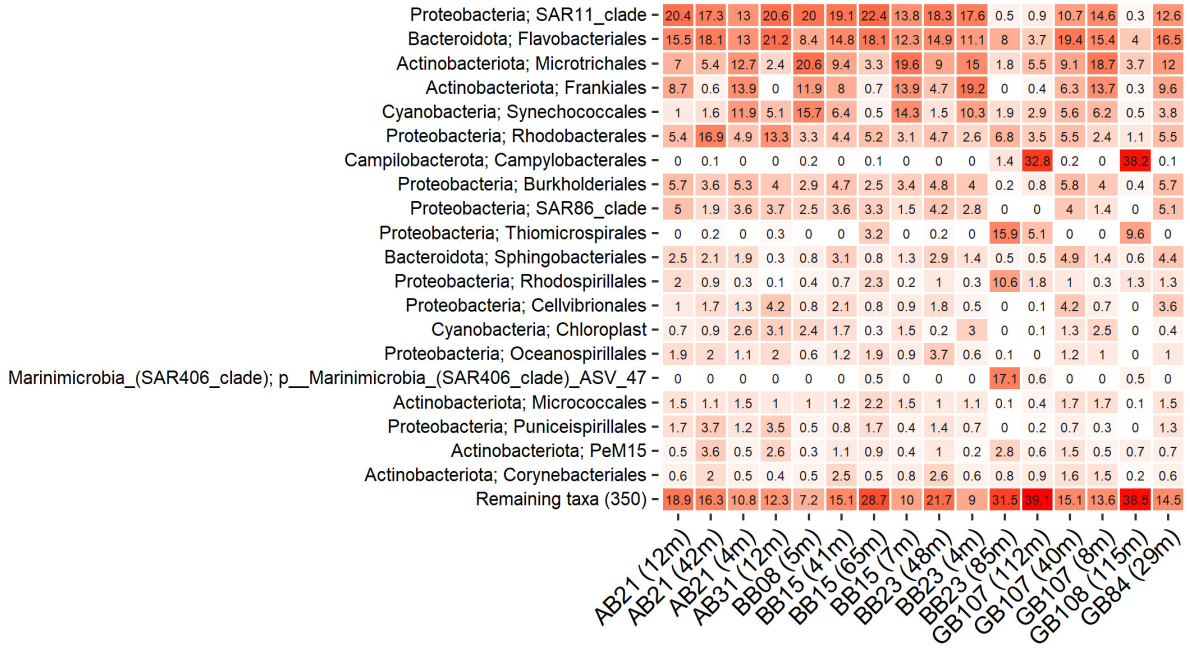

FIGURE 2 | Percentage of relative abundance based on depth-wise stations of microbial order at three basins in the Baltic Sea.

TABLE 2 | Physical factors and bacterial diversity estimates for water collected from three basins in the Baltic Sea.

Sampling station	Measuring water depth (m)	Temperature (°C)	Sanility (PSU)	Dissolve oxygen (mg L^{-1})	Final reads (assigned taxonomy)	ASVs (after rarefying samples)	Shannon (H) (after rarefying samples)
AB31	12	14.539	24.22	6.99	18,886	219	4.544
AB21	4	15.506	9.2	12.96	12,818	243	4.604
AB21	12	15.641	9.48	8.03	29,286	363	4.929
AB21	42	15.357	18.5	7.46	16,513	266	4.601
BB08	5	13.267	8.27	14.37	15,114	199	4.253
BB15	7	14.965	8.23	9.66	31,990	279	4.443
BB15	41	7.129	9.72	5.02	32,057	351	4.924
BB15	65	8.281	16.82	0.08	36,585	406	4.830
BB23	4	15.528	8.14	9.39	11,984	182	4.294
BB23	48	7.448	10.56	6.68	20,267	269	4.636
BB23	85	8.577	17.95	0.04	4,931	167	3.900
GB84	29	11.497	7.74	6.93	16,782	255	4.628
GB107	8	14	7.02	13.8	24,958	260	4.614
GB107	40	5.006	7.93	8.43	17,906	298	4.827
GB107	112	7.108	12.92	7.74	13,790	293	3.933
GB108	115	7.189	12.97	7.92	15,971	276	3.653

deep water, while SAR406 clade and Rhodospirillales only dominated in OMZ water. Thiomicrospirales was in a high abundance both in OMZ and deep water. The community structure differed less between surface and intermediate water samples, of which the abundances of Microtrichales, Frankiales and Synechococcales differed mostly. Using an dbRDA-based biplot, depth and oxygen concentration showed a significant impact on the microbial community structure and distribution (**Figure 4**). Likewise, salinity and temperature were strongly related to changes in the microbial community structure. Overall, 40% of variation in community structure could be constrained by these four variables.

Phototrophic Bacterial Community

We found similar relative abundances of AP and OP (Cyanobacteria) in all 16 amplicon datasets, with AP representing 1.58–18.11% (6.47% on average) and OP representing 0.47–20.18% (8.29% on average, **Figure 5**). OP outnumbered AP in

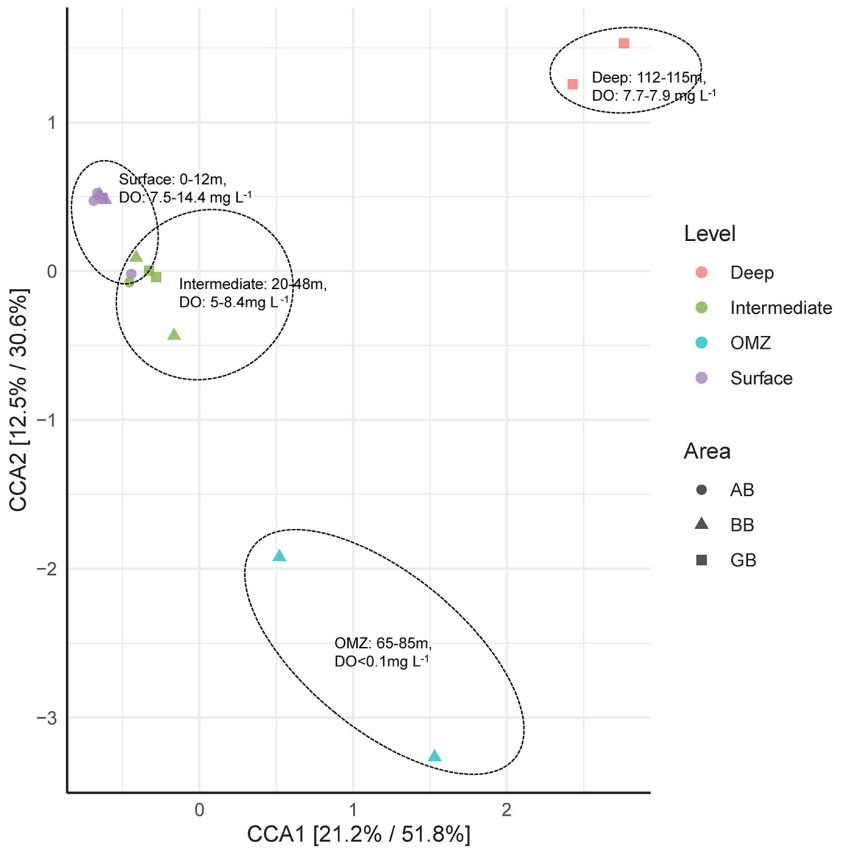

FIGURE 3 | Canonical correspondence analysis (CCA) plot depicting microbial composition from four groups of water areas (surface; intermediate; OMZ; deep) across three basins (AB, BB, and GB) in the Baltic Sea.

surface waters shallower than 8 m, while AP were more abundant in waters below 8 m. Relative abundances of OP decreased from 16.04% ± 3.48% in surface waters to 4.77% ± 3.76% in waters below (< 8 m). Relative AP abundances did not vary only with depth but also along the cruise track with higher abundances in the Arkona Basin (11.21% ± 6.2%), followed by the Bornholm Basin (5.04% ± 1.3%), and the Gotland Basin (4.68% ± 2.37%). These different distributions may be due to their different adaptation to their environmental surroundings. OP abundances were negatively correlated with depth and positively correlated oxygen, and temperature, while AP abundances were positively correlated with salinity (**Table 3**).

The phototrophic bacterial community consisted mainly of three phyla, including OP-Cyanobacteria, AP-Proteobacteria and AP-Chloroflexota (**Figure 6**). In the AP community, Rhodobacterales which belong to Alphaproteobacteria was the main order out of 10, representing 1.14–16.89% of the total bacteria. The rest of Proteobacteria accounted for 0.06–1.70%, this includes Alphaproteobacteria (Rhodospirillales, Rhizobiales, Sphingomonadales, and Caulobacterales), Betaproteobacteria (Burkholderiales), and Gammaproteobacteria (Chromatiales, Cellvibrionales, and Methylococcales). We further found Chloroflexales as the only order in Chloroflexota, with an abundance of less than 0.34%. For the OP community, Synechococcales was the dominant order among six orders, representing 0.47–15.66%. Chloroplasts was also shown with a relative abundance of up to 3.1% in upper layers (< 12 m). The rest of OP accounted only for less than 1.78% of total bacteria except the unclassified Cyanobacteria, including Caenarcaniphilales, Vampirovibrionales, and Cyanobacteriales. It has to be noted that Caenarcaniphilales and Vampirovibrionales are non-photosynthetic Cyanobacteria (Soo et al., 2014, 2015). Generally, it is important to mention that a family-level description of the AP community based on 16S rRNA amplicon sequencing might include non-photosynthetic strains imposing a methodological limitation on this type of analysis (Kasalický et al., 2018). Therefore, we complemented our 16S rRNA-based approach with an analysis of functional genes of photosynthesis to clearly identify representatives of the AP and OP community.

Diversity of Anoxygenic Phototrophs and Oxygenic Phototrophs Obtained From Photosynthetic Marker Genes

OP belonging to nine groups were detected by *psb*A (**Figure 7** and **Supplementary Figure 2**, **62** sequences in total). Besides uncultured organisms and uncultured cyanophages (19.4% each), the majority of *psb*A sequences belonged to Chlorophyta

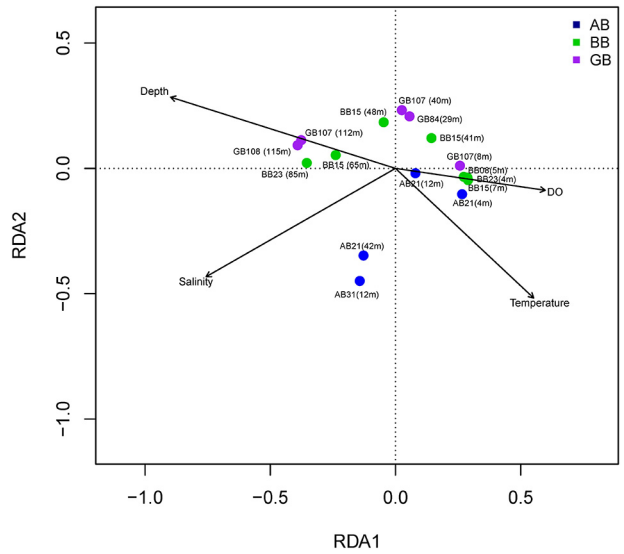

FIGURE 4 | db-RDA biplot of environmental variables and microbial community in different samples. Different samples and environmental variables are plotted on RDA axes 1 and 2. Arrows denote biplot scores for the different constraining environmental variables.

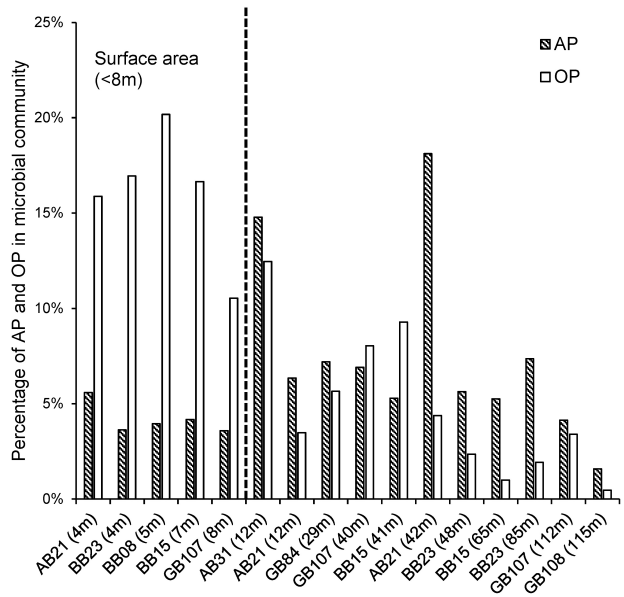

FIGURE 5 | Relative abundance of AP and OP (Cyanobacteria) in microbial community in the Baltic Sea.

(green algae, 32.3%), and Cyanobacteria (17.7%). The rest of *psb*A sequences was affiliated with Diatoms (9.7%) and Cryptomonads (1.6%).

In the AP community, phototrophic Proteobacteria was the only phyla that was detected by both *bch*Y and *puf*M with 38 and 78 sequences in total, respectively (**Figure 7** and **Supplementary Figures 3**, **4**). We recovered a majority of uncultured Proteobacteria in both *bch*Y and *puf*M sequence pools (57.9 and 48.7%). Among the characterizable sequences, a majority of *bch*Y and *puf*M (31.6 and 24.4%) were affiliated with Alphaproteobacteria, with highest similarity to Rhodobacterales (15.8 and 17.9%). The rest of *bch*Y sequences that were affiliated with Alphaproteobacteria belonged to Rhizobiales (15.8%). *puf*M sequences were affiliated with other Alphaproteobacteria, with 2.6, 2.6, and 1.3% belonging to the orders Sphingomonadales, Rhizobiales and Rhodospirillales, respectively. Further, we found *bch*Y and *puf*M sequences affiliated with Betaproteobacteria, all belonging to Burkholderiales (10.5 and 11.5% in each). In addition, 15.4% of *puf*M sequences were affiliated with Gammaproteobacteria, belonging to Chromatiales.

A characterization of AP groups using *puf*M showed variations between surface waters (0–20 m), mixed layer (29–50 m) and deeper waters (50–115 m). The highest diversities of AP-*puf*M were found in the mixed layer, with 57 sequences belonging to 6 groups and the majority belonging to Rhodobacterales expect for uncultured Proteobacteria (**Figure 8** and **Supplementary Figure 5**). Substantially less sequences could be recovered from surface and deep water samples, with only 7 and 19 sequences, respectively (**Supplementary Figures 6**, **7**).

Abundance and Activity of Anoxygenic Phototrophs and Oxygenic Phototrophs

We explored the abundance and activity of AP and OP in the Baltic Sea using *puf*M and *psb*A relative gene abundances and transcript abundances (gene expression). The activity of OP was also explored using *psb*A transcriptional activity, which was estimated by the ratio of *psb*A in transcript abundance vs. gene abundance. The abundance of AP varied from $5.84*10^4 \pm 2.06*10^4$ to $3.72*10^7 \pm 1.83*10^7$ *puf*M gene copies L^{-1}, with an exceptionally high abundance of $6.39*10^9 \pm 3.55*10^9$ *puf*M gene copies L^{-1} in the depth of 10 m in K06, and the abundance of OP varied from $5.13*10^5 \pm 1.18*10^5$ to $4.23 *10^8 \pm 7.45*10^7$ *psb*A gene copies L^{-1} (**Figures 9**, **10**). The spatial distribution patterns of *puf*M and *psb*A relative gene abundances were similar, with highest abundances present in surface waters of station K06 and lowest abundances present in the deep waters of station GB108. Both, *puf*M and *psb*A relative gene abundances were frequently higher in surface waters and in the mixed layer (< 45 m), comparing to samples from deeper waters (**Figures 11A,B**). This was coherent with the Pearson correlation output, which showed the *psb*A gene abundance was positively correlated with the *puf*M gene abundance (**Table 3**). Similar to the vertical distribution of *psb*A gene abundance, *psb*A transcript abundance was higher in surface and mixed layer waters than in deeper waters, ranging from $2.2*10^5 \pm 2.05*10^4$ to $1.07*10^8 \pm 1.21*10^7$ copies L^{-1} (**Figures 10**, **11C**). Consequently, *psb*A transcriptional activity was similar across the basins and depths except for the Kiel Fjord (**Figure 11D**). For the *puf*M transcript abundance, however, only 5 samples out of 23 samples could be detected in the detection range of RT-qPCR. These five samples were from surface and mixed layer water (< 45 m), with highest *puf*M transcript abundance at $3.07*10^4 \pm 5.3*10^3$

TABLE 3 | Pearson correlations of the gene abundance, transcript abundance, and transcriptional activity of *puf*M and *psb*A with environmental variables, carbon fixation rate, and OP or AP abundance in microbial community.

Measurement	*puf*M gene (copies L^{-1}) *n* = 49	*psb*A gene (copies L^{-1}) *n* = 49	*psb*A transcript (copies L^{-1}) *n* = 23	*psb*A transcriptional activity *n* = 23	OP abundance in microbial community (%), *n* = 16	AP abundance in microbial community (%), *n* = 16
Depth	*r* = –0.134	***r* = –0.395**	***r* = –0.600**	*r* = 0.236	***r* = –0.760**	*r* = –0.150
	p = 0.360	***p* = 0.005**	***P* = 0.003**	*p* = 0.278	***p* < 0.001**	*p* = 0.579
Temperature (℃)	*r* = 0.143	***r* = 0.391**	***r* = 0.536**	*r* = –0.010	***r* = 0.573**	*r* = 0.300
	p = 0.328	***p* = 0.005**	***p* = 0.008**	*p* = 0.965	***p* = 0.020**	*p* = 0.265
Salinity (PSU)	*r* = 0.192	***r* = 0.303**	*r* = 0.234	*r* = 0.031	*r* = –0.352	***r* = 0.677**
	p = 0.187	***p* = 0.034**	*p* = 0.283	*p* = 0.887	*p* = 0.182	***p* = 0.004**
Dissolved oxygen (mg L^{-1})	*r* = –0.010	*r* = 0.053	*r* = 0.330	*r* = 0.362	***r* = 0.688**	*r* = –0.204
	p = 0.947	*p* = 0.719	*p* = 0.124	*p* = 0.090	***p* = 0.003**	*p* = 0.449
DIC, *n* = 18 for gene (mM)	*r* = 0.056	*r* = 0.061	–	–	–	–
	p = 0.826	*p* = 0.809	–	–	–	–
pH, *n* = 18	*r* = 0.224	*r* = 0.352	–	–	–	–
	p = 0.371	*p* = 0.152	–	–	–	–
Carbon fixation rate, *n* = 15 (μmol C L^{-1} d^{-1})	*r* = –0.273	*r* = –0.333	–	–	–	–
	p = 0.325	*p* = 0.226	–	–	–	–
Chla, n = 4 (mg L^{-1})	*r* = 0.054	*p* = 0.013	–	–	–	–
	p = 0.946	*r* = 0.987	–	–	–	–
*puf*M gene (copies L^{-1}) *n* = 49	–	***r* = 0.572**	–	–	–	*r* = –0.100
	–	***p* < 0.001**	–	–	–	*p* = 0.713
*psb*A gene (copies L^{-1}) *n* = 49	–	–	–	–	***r* = 0.791**	–
	–	–	–	–	***p* < 0.001**	–
*psb*A transcript (copies L^{-1}) *n* = 23	–	***r* = 0.727**	–	–	–	–
	–	***p* < 0.0001**	–	–	–	–

n means number of samples used for analyzing. Bold values mean the Pearson correlation is significant (p < 0.05).

copies L^{-1} in 45 m of GB108 station. Even this highest *puf*M transcript abundance was still around 1–4 orders of magnitude lower than *psb*A. Therefore, in general, the gene abundance and transcript abundance of *psb*A is higher than of *puf*M, except the extremely high gene abundance of *puf*M at station K06 (**Figure 12**).

Overall, when considering all the environmental variables and carbon fixation rates, *psb*A gene abundance and *psb*A transcript abundances were negatively correlated with depth, and positively correlated with temperature (**Table 3**). *Psb*A gene abundance and AP abundance in the microbial community were positively correlated with salinity. Furthermore, OP-Cyanobacteria abundance in microbial community were all positively correlated with oxygen. In addition, *psb*A gene abundance was positively correlated with OP-Cyanobacteria abundance in the microbial community.

DISCUSSION

The Baltic Sea has been described as a time machine for the future coastal ocean due to its early history of multi-stressor disturbance related to climate change, such as warming waters, expanding of oxygen-depleted areas, acidification, nutrient pollution (Reusch et al., 2018). Previous studies have shown how some of these ambient factors impact the distribution of microbes (Herlemann et al., 2016; Lindh and Pinhassi, 2018). However, effects of these ambient factors on the Baltic Sea on microbial phototrophic groups, including both OP and AP, have not been explored systematically. Understanding the factors that drive the relative distribution and activity of OP and AP is, however, important as these functional groups use light as energy source and contribute to carbon flow and oxygen dynamics.

Hydrochemical Conditions in the Baltic Sea

Stratified patterns of temperature, salinity and pH were clearly observed during our cruise, representing a typical situation in the Baltic Sea (**Table 1** and **Figure 1**). Oxygen depletion is typically caused by benthic processes in the Baltic Sea, and anoxic waters continuously occurred and expanded over the last 100 years, which especially strong in summer due

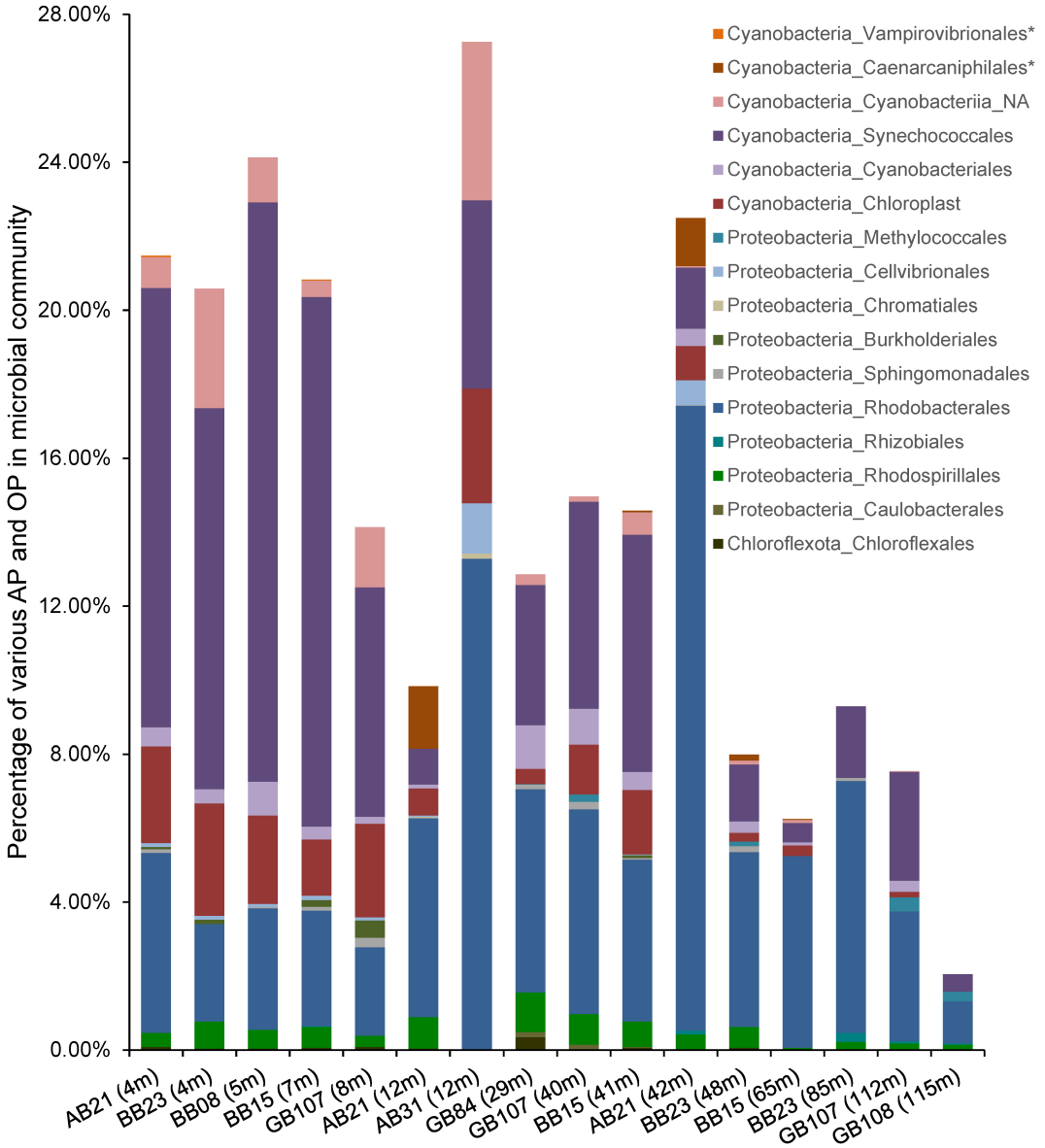

FIGURE 6 | Percentage of various AP and OP (Cyanobacteria) in the microbial community in the Baltic Sea. * Means non-phototrophic Cyanobacteria.

to stratification of water column (Koskinen et al., 2011; Reusch et al., 2018).

Bacterial Communities and Driving Factors

Dominant microbial groups play important roles in the biogeochemical cycles in the ocean, such as the uptake of dissolved organic materials (Kirchman, 2002) or nitrogen fixation (Farnelid et al., 2013). Their roles and interactions could change in different environments due to their diverse metabolisms (Thureborn et al., 2013; Broman et al., 2017). Our data show a high proportion of SAR11 bacteria in both oxic and anoxic waters in the upper and mixed water column (< 65 m), but not in deep waters (> 85 m) (**Figure 2**). The role of SAR11 in oxic waters is mainly related to aerobic organic carbon oxidation. However in anoxic waters, it is linked to the loss of nitrogen (Tsementzi et al., 2016). Due to the requirement of an unusual range of nutrients, the biochemical interactions between SAR11 and other plankton is complex (Giovannoni, 2017). This may lead to the extremely low abundance of SAR11 in deep waters, where the community composition radically changed. SAR406, Thiomicrospirales and Rhodospirillales, dominated in deep anoxic waters (**Figure 2**); those are groups with anaerobic or microaerophilic metabolisms (Pajares et al., 2020). In the deep and oxic Gotland Basin, high relative abundances of the sulfur-oxidizing Campylobacterales and the sulfate-reducing Desulfobacterota (**Supplementary Figure 1**) may suggest the

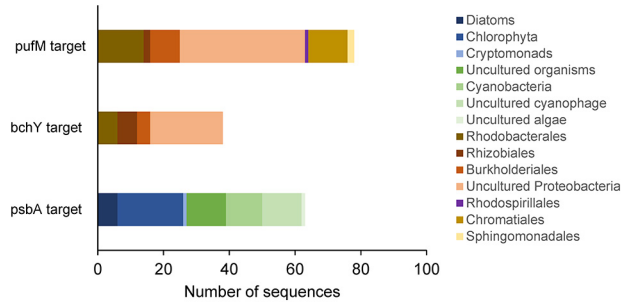

FIGURE 7 | Taxonomic composition of all samples based on three marker genes targeted sequences, *puf*M, *bch*Y, *psb*A.

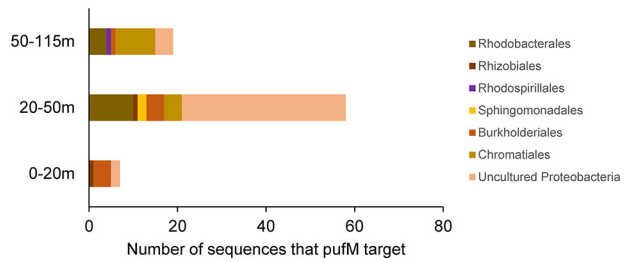

FIGURE 8 | Taxonomic composition of three group of samples that collected from three depth profiles (0–20, 20–50, 50–115 m) based on *puf*M marker genes targeted sequences.

possible occurrence of H_2S in the deeper water column or sediment (Koskinen et al., 2011; Adam and Perner, 2018), which was detected below the depth of 140 m in previous studies (Salka et al., 2008). Flavobacteriales reached a relatively high abundance in all the samples (**Figure 2**), and, as those microbes can hydrolyze organic material from diverse sources, they are key for various carbon transformations (Thureborn et al., 2013).

Despite the variability of water conditions in the different basins, the pattern of microbial community along depth gradients was much clearer than with latitudinal gradients (**Figure 3**). The same phenomenon was also observed in the northern Baltic Sea (Gulf of Finland), in which pelagic samples clustered based on sampling depth instead of sampling site (Koskinen et al., 2011). In addition, temperature, salinity, and dissolved oxygen were significant in shaping the bacterial communities in the Baltic Sea (**Figure 4**). Previous studies have shown that salinity, temperature and seasonal differences (between July and February) were key factors shaping the bacterial community in the Baltic Sea, with a stronger impact of salinity (Herlemann et al., 2011, 2016). Dissolved oxygen was considered a crucial factor influencing microbial community composition in other OMZs, such as the Arabian Sea and the Gulf of Finland of the Baltic Sea (Koskinen et al., 2011; Fernandes et al., 2020). The dominant groups in other OMZs were, however, different, for example, SAR11 was present in high abundance in the OMZ of the Arabian Sea, the tropical Mexican Pacific, and in this study, but not in the Gulf of Finland of the Baltic Sea. SAR 406 and Thiomicrospirales abundant in the OMZ during this study and in the tropical Mexican Pacific were not abundant or even present in the other two OMZs (Koskinen et al., 2011; Fernandes et al., 2020; Pajares et al., 2020).

The highest diversity of microbial ASVs occurred in anoxic waters during our study (**Table 2**). A similar observation was made before in the Mexican Pacific, where a higher microbial diversity was detected in the oxygen minimum zone than in the euphotic zone (Pajares et al., 2020). A possible explanation might be that multiple electron acceptors could be used for microbial respiration, which increases the niche availability at anoxic conditions. In oxic waters, however, oxygen is mainly utilized and not restricted, resulting in a relatively lower niche availability (Stevens and Ulloa, 2008).

Distribution and Diversity of Anoxygenic Phototrophs and Oxygenic Phototrophs

The diversity of AP was mostly consistent between both, 16S rRNA amplicon sequencing and *puf*M or *bch*Y marker gene analyses (**Figure 6** and **Supplementary Figures 3**, **4**). Rhodobacterales, belonging to Alphaproteobacteria, have been shown to be the major group both in abundance and diversity (**Figures 6**, **7**). Five other orders of AP, including Rhizobiales and Burkholderiales, were recovered by both methods. Four more orders of AP including Chloroflexales and Cellvibrionales were observed only by 16S rRNA amplicon sequencing. Some groups could taxonomically not be identified, possibly due to the lack of specific corresponding references in the database. The composition of AP was coherent with the previous study that investigated using *puf*M marker gene in four basins (< 40 m) of the Baltic Sea, which found the major group belonging to Rhodobacterales and the rest of them to Gammaproteobacteria (Salka et al., 2008). On the other hand, although *puf*M has been widely used to represent the abundance of AP, our data show that there was no significant correlation between the AP abundance in the microbial community based on 16S rRNA sequencing and *puf*M gene abundance (**Table 3**, $p = 0.679$). This may be due to the limitation of each technique, such as the primer bias of the real-time PCR (Yutin et al., 2005), a potentially unprecise affiliation caused by exporting short genomic regions and a bias of universal primers (Cariou et al., 2018). Also, an explanation could be a potential presence of multiple gene copies within one cell as found in a number of Cyanobacteria (Golden et al., 1986). The *puf*M gene abundance, ranging mostly from 10^4 to 10^7 copies L^{-1} (**Figure 9**), was a bit lower than in other previous studies conducted on the east coast of Australia and in subtropical karst catchments of southwest of China (Bibiloni-Isaksson et al., 2016; Li et al., 2017), where they were typically found ranging from 10^5 to 10^8 copies L^{-1}.

Compared to AP diversity, the diversity of OP was higher, including eukaryotic algae, and Cyanobacteria (**Figures 6**, **7**). In addition, Cyanophages were found by targeting the *psb*A photosynthesis gene (**Figure 7** and **Supplementary Figure 2**), and Cyanophage photosynthesis genes were suggested to help support its host's photosynthesis activity during its process of infection (Sharon et al., 2007). Although *psb*A gene abundance included not only Cyanobacteria but also eukaryotic algae and

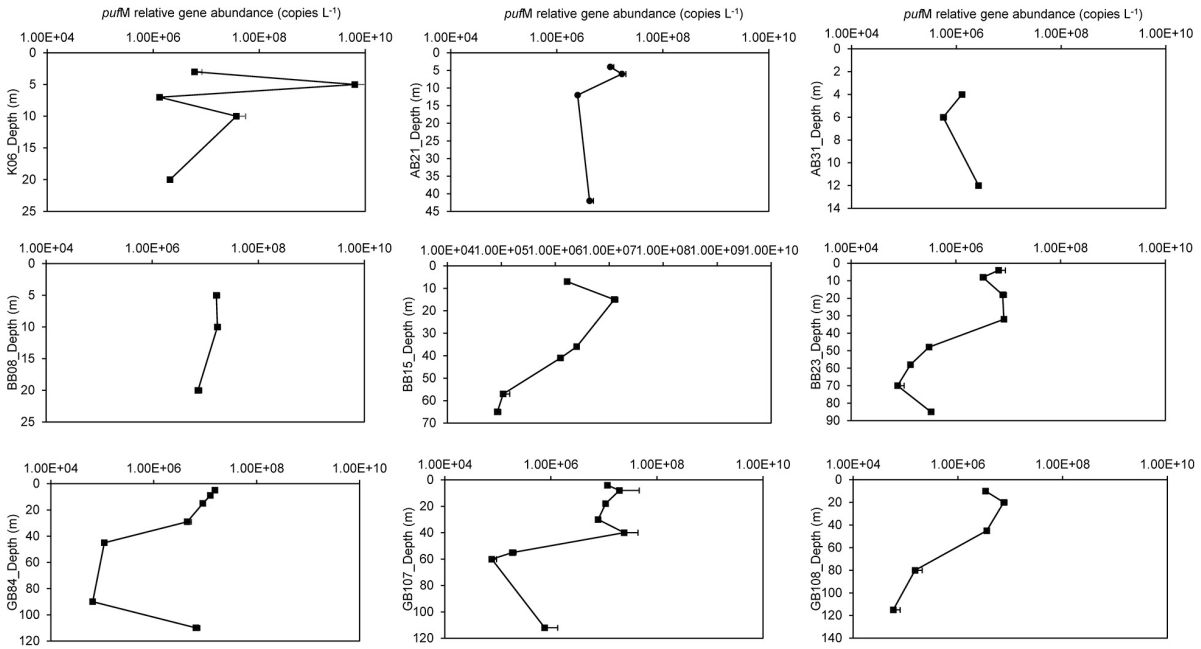

FIGURE 9 | Spatial distribution patterns of gene copy number (DNA) of the AP photosynthetic gene, *puf*M.

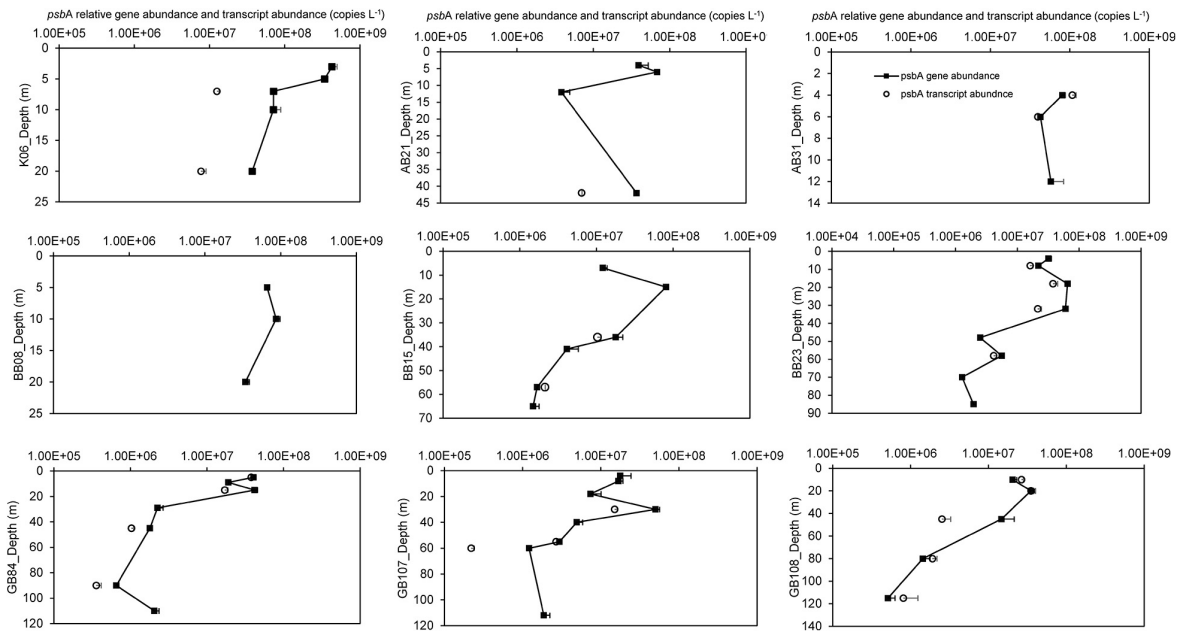

FIGURE 10 | Spatial distribution patterns of gene copy number (DNA) and transcript (mRNA) abundance of the OP photosynthetic gene, *psb*A.

other groups, the abundance of Cyanobacteria in the microbial community (%) and OP-*psb*A were significantly correlated (**Table 3**, $r = 0.791$, $p < 0.001$). This indicated that either the distribution patterns of these OP groups were quite similar, or Cyanobacteria might be a dominant group in the OP pool. Some earlier studies used microscopy to investigate the abundance of either Cyanobacteria or specific eukaryotic algae groups, such as Diatoms and Dinoflagellates, mainly focusing on the surface waters of the Baltic Sea (Norbent and Steffen, 2003; Mašín et al., 2006; Salka et al., 2008; Camarena-Gómez et al., 2021). Those studies showed that Diatoms were the dominant group in phytoplankton spring bloom communities (Camarena-Gómez et al., 2021), and *Synechococcus* occurred in a high relative abundance in the surface water during summer time

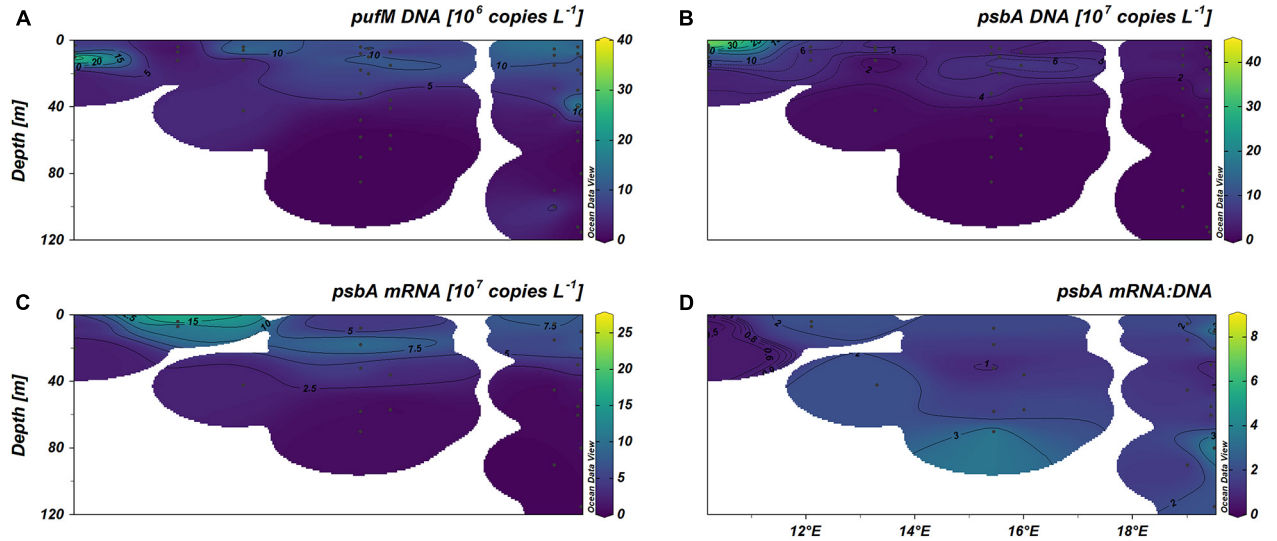

FIGURE 11 | (A,B) Spatial distribution of gene copy number (DNA) of the AP and OP photosynthetic gene (*puf*M and *psb*A, respectively), **(C)** spatial distribution of transcript (mRNA) abundance of the OP photosynthetic gene (*psb*A), **(D)** transcriptional activity of *psb*A expressed as the ratio of mRNA to DNA.

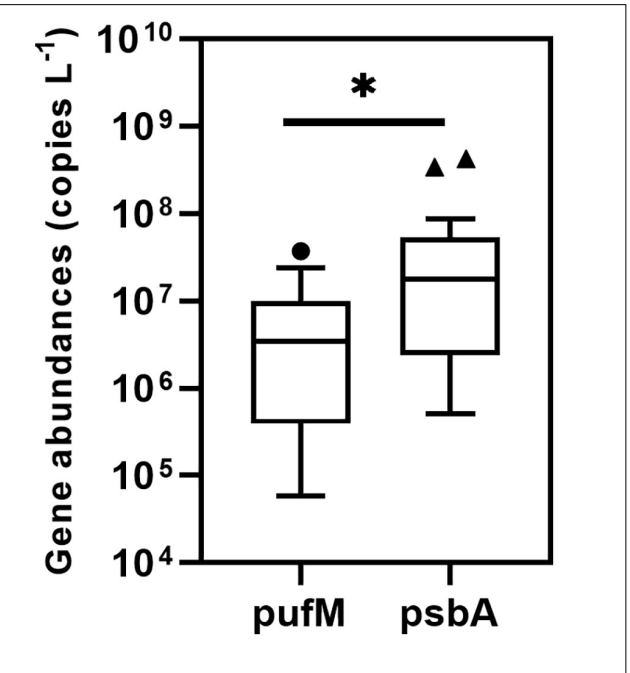

FIGURE 12 | Gene abundance of anoxygenic photosynthesis (AP, *puf*M) and OP photosystem-II (OP-PSII, *psb*A) in 49 samples. Note: the *puf*M gene copy number in KO6_5 m is around $6.39*10^9$copies L^{-1}, which is not shown in the figure. * Means the significant difference between two groups ($p < 0.05$).

in the Baltic Sea (Herlemann et al., 2016). Previous studies have shown that Cyanobacterial blooms occurred almost every summer in the Baltic Sea, and the dominant species were *Nodularia spumigena*, *Aphanizomenon flos-aquae,* and *Anabaena* app., belonging to the order Nostocales (Vahtera et al., 2007; Kahru et al., 2020). The sampling time of our study was in September, and the summer blooms had already passed. But we still detected some of the typical bloom species, such as *Nodularia spumigena*, *Aphanizomenon flos-aquae*, and different Diatoms (**Supplementary Figure 2**). In addition to these species, other oxygenic phototrophs may also bloom as the Baltic Sea harbors a diversity of OP groups (**Supplementary Figure 2**), including Chlorophyta. Our study was the first investigating all OP groups and comparing their abundance and composition to AP using both 16S rRNA amplicon sequencing and photosynthesis marker genes in various depth profiles of the Baltic Sea.

Environmental Factors Impacting the Distribution and Activity of Anoxygenic Phototrophs and Oxygenic Phototrophs

Due to the metabolic dependence on light, both AP and OP are mostly detected in the photic zone, which is typically shallow in the Baltic Sea, reaching water depths of 20–30 m (Wasmund and Siegel, 2008). Several studies have shown that AP were more abundant in the mixed layer than in surface and deep waters, and different groups of OP preferred to be in surface layer, especially *Synechococcus* (Sieracki et al., 2006; Zhang and Jiao, 2007; Hojerová et al., 2011; Bibiloni-Isaksson et al., 2016). In line with this, the abundance of AP was found to have a maximum between 20 and 40 m also in the Mediterranean Sea (Hojerová et al., 2011). Also in the coastal waters of Australia, AP abundances were higher at depths between 20 and 50 m than at depth between 0 and 20 m and declined considerably below 50 m water depth (Bibiloni-Isaksson et al., 2016). In the Sargasso Sea, the maximum of AP abundance occurred from 15 to 60 m, with lower abundance in surface and deep waters, while OP groups—*Synechococcus*, *Prochlorococcus* and other eukaryotes—were most abundant at the surface, at 60 and 30 m (Sieracki et al., 2006).

A similar pattern was observed in the east China Sea, with the OP components (*Synechococcus*, *Prochlorococcus*, and pico-sized eukaryotes) peaking in surface waters and AP peaking between 42 and 76 m (Zhang and Jiao, 2007). Our study also showed that OP-Cyanobacteria abundance was much higher than AP in surface waters shallower than 8 m, while the pattern was inverted below 8 m (**Figure 5**). Nevertheless, when comparing the specific marker gene abundance of OP and AP, OP-*psb*A gene abundance was higher than AP-*puf*M gene abundance in most samples (**Figure 12**), and both were higher in the photic zone than in deep water (**Figures 11A,B**). This was coherent with a previous study using metagenomic sequencing on samples from the mixed layer between 5 and 40 m at coastal stations of the San Pedro Channel in the Pacific Ocean, which showed the normalized abundance of OP (*psa*A) was 2 –3 times higher than AP (*puf*M) (Sieradzki et al., 2018). However, in surface waters of the South-Eastern Mediterranean Sea, the normalized abundance of OP-*psa*A, ranging from 2.4 to 14.2%, was not significantly different with AP-*puf*M, ranging from 3.5 to 10.4%, within the metagenomic database, even though the abundance of OP was much higher than AP as determined by epifluorescence microscopy (Dubinsky et al., 2017). The difference between those studies may be due to the different sampling depths, seasons, and environmental surroundings. Our data showed that depth had a significant impact on OP-Cyanobacteria and OP-*psb*A gene abundance (**Table 3**), and one of the main reasons could be light availability (Michelou et al., 2007). Several studies have shown that there was a significant positive correlation between AP abundance and chlorophyll (Jiao et al., 2007; Hojerová et al., 2011). Although our data did not have enough samples to analyze the precise correlation between Chla and AP abundance, the strong correlation (**Table 3**, $r = 0.572$, $p < 0.001$) between OP-*psb*A and AP-*puf*M gene abundances could indicate that the niche of AP was connected to OP, in more productive regions or shelf waters (Cottrell et al., 2006; Sieracki et al., 2006). OP community is the key group of contributor to primary productivity (Raven, 2009). Our data, however, did not indicate any solid correlation between OP photosynthesis gene abundances and carbon fixation rates in the seawater (**Table 3**), which might be due to the incomparability of gene abundance to activity in terms of rates. Another reason might be an insufficient sample size for carbon fixation rates. Further, as our sampling time was in September, it fell into a period with low primary productivity and might therefore not be fully representative.

Our DNA-based studies showed a detailed picture of the phototrophic community, but information about their activity remains elusive. Therefore, it is important to examine not only existence or abundance of the functional genes, but also gene expression. However, RNA-based studies exploring photosynthetic gene activity are rare. Data on the comparison of OP and AP gene expressions is even less available, and only found in a few metatranscriptomic studies (Vila-Costa et al., 2013; Sieradzki et al., 2018; Linz et al., 2020). The above mentioned study conducted in the San Pedro Channel in the Pacific Ocean showed the AP-*puf*M transcriptional activity (RNA: DNA ratio) was significantly lower than OP-*psa*A (Sieradzki et al., 2018). Our data show a similar pattern, with even the highest AP-*puf*M transcript abundance across all the samples still much lower than OP-*psb*A. The low level of *puf*M gene expression could be due to both the low gene abundance and the sampling time. It has been shown that the gene expressions of the *puf* cluster occurs mostly at night (Voget et al., 2015; Fecskeová et al., 2019) and our samples were all collected during daytime. During the daytime, light exposure could cause repression of photosynthesis gene expression, as shown for several AP species, e.g., *Roseobacter denitrificans* and *Dinoroseobacter shibae* (Nishimura et al., 1996; Tomasch et al., 2011). It is worth mentioning that in a recent diel study using metatranscriptomics, AP photosynthesis gene expression peaked during the night, while OP photosynthesis gene expression peaked during the day (Linz et al., 2020). The depth profiles of OP-*psb*A gene expression could also mainly be due to its gene abundances, as *psb*A transcript abundance was significantly related to *psb*A gene abundance ($r = 0.727$, $p < 0.0001$) (**Table 3**).

Not only light, but also factors, such as salinity, temperature, and nutrient status, have been explored as possible factors regulating the abundance and activity of OP and AP. In the Baltic Sea, water temperature was positively related to the blooming of both Cyanobacteria and filamentous algal species, especially green algae (Takolander et al., 2017; Kahru et al., 2020). For specific cyanobacterial species, e.g., *Synechococcus* sp., temperature was positively correlated to their *psb*A gene abundance under N-repleted conditions (Fernández-González et al., 2020). Our data also indicated that OP group in the Baltic Sea had a strong and positive correlation with temperature in the range between 4 and 16℃ (**Table 3**). Furthermore, we found that OP photosynthetic metabolism is more active at warmer temperatures. On the other hand, seasonal studies showed temperature to also have a positive impact on AP abundance in seawater (Lamy et al., 2011; Ferrera et al., 2014; Auladell et al., 2019). A study about spatial distribution of AP conducted in the northwest Atlantic suggested low temperature may limit AP cell abundances, with a threshold at below 6℃ and above 10℃ (Sieracki et al., 2006). A recent microcosm study showed higher temperatures can enhance the net growth rate of AP by comparing three temperatures, 10, 20, and 30℃ (Sato-Takabe et al., 2019). However, our data do not show a significant connection between temperature and AP-*puf*M abundance (**Table 3**, $r = 0.143$, $p = 0.328$). This inconsistency may be because of the differences of temperature range and grazers impacting the AP community. Ocean acidification has an impact on the abundance of both OP and AP groups (Sala et al., 2016; Li et al., 2017), and its impact related to the nutrient status. The available data points from the present study do not allow for a more precise investigation of the correlation between pH or DIC and AP or OP groups (**Table 3**).

On the other hand, abundance of OP groups, including phototrophic picoplankton and Cyanobacteria, were found to be strongly correlated with salinity in various areas (Šantić et al., 2017; Auladell et al., 2019). Our data also found that OP, but

not OP-Cyanobacteria, showed a significantly positive correlation with salinity (**Table 3**). OP photosynthetic activity, however, does not have a strong correlation with salinity. Nonetheless, OP-Cyanobacteria preferred to live in higher oxygen waters (**Table 3**). However, DO did not have significant positive impacts on both OP (with eukaryotic algae) (p = 0.719) and AP (p = 0.947) communities, and OP photosynthetic activity (p = 0.09) (**Table 3**). Although there might be different demands for oxygen between OP and AP, and OP but not AP produce oxygen while they carry out photosynthesis, DO did not seem to be a key factor for phototrophic abundance and activity. Therefore, both OP and AP may not be negatively impacted by oxygen-depleted waters expanding in the Baltic Sea but might even benefit from an expanding niche. This suggestion has, however, a limitation as we did not cover the full oxygen range in our sampling and could therefore have missed a threshold in the low oxygen to anoxic range.

CONCLUSION

This study provides important insights for understanding the distribution and structure of both the microbial community and phototrophs, especially focusing on the comparison of the distribution and activity of AP and OP in the Baltic Sea which is exposed to multiple climate-related threats. Microbial community assemblages were correlated with environmental factors such as salinity, temperature, oxygen, and depth. Different dominant microbial groups were observed in the OMZ, deep, and surface and intermediate waters.

Both, AP and OP, displayed a high diversity. OP groups, including Eukaryotic algae and Cyanobacteria, were more abundant than AP in most areas. OP photosynthesis was quite active crossing all stations, while most AP photosynthesis cannot be detected that might be due to the daytime of sampling. Both OP (only Cyanobacteria) and OP (with Eukaryotic algae) preferred to live in higher temperature and upper waters, but Cyanobacteria had another preference of oxic water, while the whole OP community preferred to live in higher salinity area. AP did not show any significant physico-chemical preference but prefer to live with OP community. OP showed more photosynthesis activity in higher temperature and upper waters. As the changing Baltic Sea will see higher temperatures, lower salinity, expanding of deoxygenation, and other problems, this study could help to interpret how these phototrophic groups might shift in distribution and activity in a long-term analog.

DATA AVAILABILITY STATEMENT

The datasets presented in this study can be found in online repositories. The names of the repository/repositories and accession number(s) can be found below: NCBI (accession: SAMN20309768-SAMN20309783, MZ960574 to MZ960756).

AUTHOR CONTRIBUTIONS

CL designed the study. CR conducted the sampling, conducted experiments for biogeochemical parameters, and analyzed the data. PX conducted molecular experiments and performed all the statistical analysis with the contribution of CL and CR. PX wrote the manuscript. All authors contributed to manuscript revision, read, and approved the submitted version.

FUNDING

Financial support was provided by the Villum Foundation (grants no: #24911, to CL; grants no. #16518 to D. Canfield).

ACKNOWLEDGMENTS

We appreciate the support from the captain, crew and the chief scientist J. Süling for Alkor 528 during the Cruise. We are grateful for the financial support for the Cruise provided by the European Union's Horizon 2020 Research and Innovation Program (Grant agreement no. 774499 to J. Javidpour, GoJelly project). We acknowledge E. Laursen and R. Orloff Holm for their technical assistance. We further acknowledge the Nordcee labs at SDU and the GEOMAR-Helmholtz Centre for Ocean Research Kiel for giving access to their research facilities. We are grateful to the China Scholarship Council, for granting a scholarship to PX (China Scholarship Council Studentship with the University of Southern Denmark (grant no. 201908440275) and to the Villum Foundation (grant no. 24911). We acknowledge D. Canfield for supporting experiment supplies [Villum Foundation (grants no. 16518)]. We thank the reviewers KP and EC, as well as the editor for their help with improving the manuscript.

SUPPLEMENTARY MATERIAL

The Supplementary Material for this article can be found online at: https://www.frontiersin.org/articles/10.3389/fmars.2021.773210/full#supplementary-material

REFERENCES

Adam, N., and Perner, M. (2018). Microbially mediated hydrogen cycling in deep-sea hydrothermal vents. *Front. Microbiol.* 9:2873. doi: 10.3389/fmicb.2018.02873

Ahn, K., Lee, K. B., Kim, Y. J., and Koo, Y. M. (2014). Quantitative analysis of the three main genera in effective microorganisms using qPCR. *Korean J. Chem. Eng.* 31, 849–854. doi: 10.1007/s11814-013-0274-6

Alcamán-Arias, M. E., Pedrós-Alió, C., Tamames, J., Fernández, C., Pérez-Pantoja, D., Vásquez, M., et al. (2018). Diurnal changes in active carbon and nitrogen pathways along the temperature gradient in porcelana hot spring microbial mat. *Front. Microbiol.* 9:2353. doi: 10.3389/fmicb.2018.02353

Alves Junior, N., Meirelles, P. M., de Oliveira Santos, E., Dutilh, B., Silva, G. G. Z., Paranhos, R., et al. (2015). Microbial community diversity and physical–chemical features of the Southwestern Atlantic ocean. *Arch. Microbiol.* 197, 165–179. doi: 10.1007/s00203-014-1035-6

Andersen, K. S., Kirkegaard, R. H., Karst, S. M., and Albertsen, M. (2018). Ampvis2: an R package to analyse and visualise 16S rRNA amplicon data. *bioRxiv* [Preprint]. doi: 10.1101/299537

Auladell, A., Sánchez, P., Sánchez, O., Gasol, J. M., and Ferrera, I. (2019). Long-term seasonal and interannual variability of marine aerobic anoxygenic photoheterotrophic bacteria. *ISME J.* 13, 1975–1987. doi: 10.1038/s41396-019-0401-4

Bentzon-Tilia, M., Traving, S. J., Mantikci, M., Knudsen-Leerbeck, H., Hansen, J. L. S., Markager, S., et al. (2015). Significant N2 fixation by heterotrophs, photoheterotrophs and heterocystous cyanobacteria in two temperate estuaries. *ISME J.* 9, 273–285. doi: 10.1038/ismej.2014.119

Bibiloni-Isaksson, J., Seymour, J. R., Ingleton, T., van de Kamp, J., Bodrossy, L., and Brown, M. V. (2016). Spatial and temporal variability of aerobic anoxygenic photoheterotrophic bacteria along the east coast of Australia. *Environ. Microbiol.* 18, 4485–4500. doi: 10.1111/1462-2920.13436

Boeuf, D., Cottrell, M. T., Kirchman, D. L., Lebaron, P., and Jeanthon, C. (2013). Summer community structure of aerobic anoxygenic phototrophic bacteria in the western Arctic Ocean. *FEMS Microbiol. Ecol.* 85, 417–432. doi: 10.1111/1574-6941.12130

Breitburg, D., Levin, L. A., Oschlies, A., Grégoire, M., Chavez, F. P., Conley, D. J., et al. (2018). Declining oxygen in the global ocean and coastal waters. *Science* 359:eaam7240. doi: 10.1126/science.aam7240

Broman, E., Sachpazidou, V., Pinhassi, J., and Dopson, M. (2017). Oxygenation of hypoxic coastal Baltic sea sediments impacts on chemistry, microbial community composition, and metabolism. *Front. Microbiol.* 8:2453. doi: 10.3389/fmicb.2017.02453

Brown, M. V., Philip, G. K., Bunge, J. A., Smith, M. C., Bissett, A., Lauro, F. M., et al. (2009). Microbial community structure in the North Pacific ocean. *ISME J.* 3, 1374–1386. doi: 10.1038/ismej.2009.86

Callahan, B. J., McMurdie, P. J., Rosen, M. J., Han, A. W., Johnson, A. J. A., and Holmes, S. P. (2016). DADA2: High-resolution sample inference from Illumina amplicon data. *Nat. Methods* 13, 581–583. doi: 10.1038/nmeth.3869

Camarena-Gómez, M. T., Ruiz-González, C., Piiparinen, J., Lipsewers, T., Sobrino, C., Logares, R., et al. (2021). Bacterioplankton dynamics driven by interannual and spatial variation in diatom and dinoflagellate spring bloom communities in the Baltic Sea. *Limnol. Oceanogr.* 66, 255–271. doi: 10.1002/lno.11601

Cariou, M., Ribière, C., Morlière, S., Gauthier, J. P., Simon, J. C., Peyret, P., et al. (2018). Comparing 16S rDNA amplicon sequencing and hybridization capture for pea aphid microbiota diversity analysis. *BMC Res. Notes* 11:461. doi: 10.1186/s13104-018-3559-3

Carstensen, J., Andersen, J. H., Gustafsson, B. G., and Conley, D. J. (2014). Deoxygenation of the Baltic Sea during the last century. *Proc. Natl. Acad. Sci. U.S.A.* 111, 5628–5633. doi: 10.1073/pnas.1323156111

Conley, D. J., B̈jorck, S., Bonsdorff, E., Carstensen, J., Destouni, G., Gustafsson, B. G., et al. (2009). Hypoxia-related processes in the Baltic Sea. *Environ. Sci. Technol.* 43, 3412–3420. doi: 10.1021/es802762a

Cottrell, M. T., Mannino, A., and Kirchman, D. L. (2006). Aerobic anoxygenic phototrophic bacteria in the mid-Atlantic bight and the north Pacific gyre. *Appl. Environ. Microbiol.* 72, 557–564. doi: 10.1128/AEM.72.1.557-564.2006

Cuadrat, R. R. C., Ferrera, I., Grossart, H. P., and Dávila, A. M. R. (2016). Picoplankton bloom in global south? A high fraction of aerobic anoxygenic phototrophic bacteria in metagenomes from a coastal bay (Arraial do Cabo-Brazil). *OMICS* 20, 76–87. doi: 10.1089/omi.2015.0142

Dubinsky, V., Haber, M., Burgsdorf, I., Saurav, K., Lehahn, Y., Malik, A., et al. (2017). Metagenomic analysis reveals unusually high incidence of proteorhodopsin genes in the ultraoligotrophic Eastern Mediterranean Sea. *Environ. Microbiol.* 19, 1077–1090. doi: 10.1111/1462-2920.13624

Dupont, C. L., Larsson, J., Yooseph, S., Ininbergs, K., Goll, J., Asplund-Samuelsson, J., et al. (2014). Functional tradeoffs underpin salinity-driven divergence in microbial community composition. *PLoS One* 9:e89549. doi: 10.1371/journal.pone.0089549

Falkowski, P. G., Fenchel, T., and Delong, E. F. (2008). The microbial engines that drive earth's biogeochemical cycles. *Science* 320, 1034–1039. doi: 10.1126/science.1153213

Farnelid, H., Bentzon-Tilia, M., Andersson, A. F., Bertilsson, S., Nter Jost, G., Labrenz, M., et al. (2013). Active nitrogen-fixing heterotrophic bacteria at and below the chemocline of the central Baltic Sea. *ISME J.* 7, 1413–1423. doi: 10.1038/ismej.2013.26

Fecskeová, L. K., Piwosz, K., Hanusová, M., Nedoma, J., Znachor, P., and Koblížek, M. (2019). Diel changes and diversity of pufM expression in freshwater communities of anoxygenic phototrophic bacteria. *Sci. Rep.* 9:18766. doi: 10.1038/s41598-019-55210-x

Fernandes, G. L., Shenoy, B. D., and Damare, S. R. (2020). Diversity of bacterial community in the oxygen minimum zones of Arabian Sea and Bay of Bengal as deduced by Illumina sequencing. *Front. Microbiol.* 10:3153. doi: 10.3389/fmicb.2019.03153

Fernández-González, C., Pérez-Lorenzo, M., Pratt, N., Moore, C. M., Bibby, T. S., and Marañón, E. (2020). Effects of temperature and nutrient supply on resource allocation, photosynthetic strategy, and metabolic rates of *Synechococcus* sp. *J. Phycol.* 56, 818–829. doi: 10.1111/jpy.12983

Ferrera, I., Borrego, C. M., Salazar, G., and Gasol, J. M. (2014). Marked seasonality of aerobic anoxygenic phototrophic bacteria in the coastal NW Mediterranean Sea as revealed by cell abundance, pigment concentration and pyrosequencing of pufM gene. *Environ. Microbiol.* 16, 2953–2965. doi: 10.1111/1462-2920.12278

Ferrera, I., Gasol, J. M., Sebastián, M., Hojerová, E., and Kobížek, M. (2011). Comparison of growth rates of aerobic anoxygenic phototrophic bacteria and other bacterioplankton groups in coastal mediterranean waters. *Appl. Environ. Microbiol.* 77, 7451–7458. doi: 10.1128/AEM.00208-11

Garcia-Chaves, M. C., Cottrell, M. T., Kirchman, D. L., Ruiz-González, C., and Del Giorgio, P. A. (2016). Single-cell activity of freshwater aerobic anoxygenic phototrophic bacteria and their contribution to biomass production. *ISME J.* 10, 1579–1588. doi: 10.1038/ismej.2015.242

Giovannoni, S. J. (2017). SAR11 bacteria: the most abundant plankton in the oceans. *Ann. Rev. Mar. Sci.* 9, 231–255. doi: 10.1146/annurev-marine-010814-015934

Golden, S. S., Brusslan, J., and Haselkorn, R. (1986). Expression of a family of psbA genes encoding a photosystem II polypeptide in the cyanobacterium *Anacystis nidulans* R2. *EMBO J.* 5, 2789–2798. doi: 10.1002/j.1460-2075.1986.tb04569.x

Hall, P. O. J., and Aller, R. C. (1992). Rapid, small-volume, flow injection analysis for $\sum$CO2, and NH4+ in marine and freshwaters. *Limnol. Oceanogr.* 37, 1113–1119. doi: 10.4319/lo.1992.37.5.1113

Herlemann, D. P. R., Labrenz, M., Jürgens, K., Bertilsson, S., Waniek, J. J., and Andersson, A. F. (2011). Transitions in bacterial communities along the 2000 km salinity gradient of the Baltic Sea. *ISME J.* 5, 1571–1579. doi: 10.1038/ismej.2011.41

Herlemann, D. P. R., Lundin, D., Andersson, A. F., Labrenz, M., and Jürgens, K. (2016). Phylogenetic signals of salinity and season in bacterial community composition across the salinity gradient of the Baltic Sea. *Front. Microbiol.* 7:1883. doi: 10.3389/fmicb.2016.01883

Hojerová, E., Mašín, M., Brunet, C., Ferrera, I., Gasol, J. M., and Koblížek, M. (2011). Distribution and growth of aerobic anoxygenic phototrophs in the Mediterranean Sea. *Environ. Microbiol.* 13, 2717–2725. doi: 10.1111/j.1462-2920.2011.02540.x

Imhoff, J. F. (2017). *Diversity of Anaerobic Anoxygenic Phototrophic Purple Bacteria*, ed. P. C. Hallenbeck (Cham: Springer). doi: 10.1007/978-3-319-46261-5

Imhoff, J. F., Rahn, T., Künzel, S., and Neulinger, S. C. (2018). Photosynthesis is widely distributed among *Proteobacteria* as demonstrated by the phylogeny of pufLM reaction center proteins. *Front. Microbiol.* 8:2679. doi: 10.3389/fmicb.2017.02679

Jiao, N., Zhang, Y., Zeng, Y., Hong, N., Liu, R., Chen, F., et al. (2007). Distinct distribution pattern of abundance and diversity of aerobic anoxygenic phototrophic bacteria in the global ocean. *Environ. Microbiol.* 9, 3091–3099. doi: 10.1111/j.1462-2920.2007.01419.x

Kahru, M., Elmgren, R., Kaiser, J., Wasmund, N., and Savchuk, O. (2020). Cyanobacterial blooms in the Baltic Sea: correlations with environmental factors. *Harmful Algae* 92:101739. doi: 10.1016/j.hal.2019.101739

Karl, D. M. (2002). Hidden in a sea of microbes. *Nature* 415, 590–591. doi: 10.1038/415590b

Kasalický, V., Zeng, Y., Piwosz, K., Šimek, K., Kratochvilová, H., and Koblížek, M. (2018). Aerobic anoxygenic photosynthesis is commonly present within the genus *Limnohabitans*. *Appl. Environ. Microbiol.* 84, e2116–e2117. doi: 10.1128/AEM.02116-17

Kirchman, D. L. (2002). The ecology of *Cytophaga*-Flavobacteria in aquatic environments. *FEMS Microbiol. Ecol.* 39, 91–100. doi: 10.1016/S0168-6496(01)00206-9

Koblížek, M. (2015). Ecology of aerobic anoxygenic phototrophs in aquatic environments. *FEMS Microbiol. Rev.* 39, 854–870. doi: 10.1093/femsre/fuv032

Koblížek, M., Falkowski, P. G., and Kolber, Z. S. (2006). Diversity and distribution of photosynthetic bacteria in the Black Sea. *Deep. Res. Part II Top. Stud. Oceanogr.* 53, 1934–1944. doi: 10.1016/j.dsr2.2006.03.019

Koblížek, M., Mašín, M., Ras, J., Poulton, A. J., and Prášil, O. (2007). Rapid growth rates of aerobic anoxygenic phototrophs in the ocean. *Environ. Microbiol.* 9, 2401–2406. doi: 10.1111/j.1462-2920.2007.01354.x

Kong, W., Li, W., Romancova, I., Prášil, O., and Morgan-Kiss, R. M. (2014). An integrated study of photochemical function and expression of a key photochemical gene (psbA) in photosynthetic communities of Lake Bonney (McMurdo Dry Valleys, Antarctica). *FEMS Microbiol. Ecol.* 89, 293–302. doi: 10.1111/1574-6941.12296

Koskinen, K., Hultman, J., Paulin, L., Auvinen, P., and Kankaanpää, H. (2011). Spatially differing bacterial communities in water columns of the northern Baltic Sea. *FEMS Microbiol. Ecol.* 75, 99–110. doi: 10.1111/j.1574-6941.2010.00987.x

Kumar, S., Stecher, G., Li, M., Knyaz, C., and Tamura, K. (2018). MEGA X: molecular evolutionary genetics analysis across computing platforms. *Mol. Biol. Evol.* 35, 1547–1549. doi: 10.1093/molbev/msy096

Lami, R., Cottrell, M. T., Ras, J., Ulloa, O., Obernosterer, I., Claustre, H., et al. (2007). High abundances of aerobic anoxygenic photosynthetic bacteria in the South Pacific ocean. *Appl. Environ. Microbiol.* 73, 4198–4205. doi: 10.1128/AEM.02652-06

Lamy, D., De Carvalho-Maalouf, P., Cottrell, M. T., Lami, R., Catala, P., Oriol, L., et al. (2011). Seasonal dynamics of aerobic anoxygenic phototrophs in a Mediterranean coastal lagoon. *Aquat. Microb. Ecol.* 62, 153–163. doi: 10.3354/ame01467

Levin, L. A. (2018). Manifestation, drivers, and emergence of open ocean deoxygenation. *Ann. Rev. Mar. Sci.* 10, 229–260. doi: 10.1146/annurev-marine-121916-063359

Li, Q., Song, A., Peng, W., Jin, Z., Müller, W. E. G., and Wang, X. (2017). Contribution of aerobic anoxygenic phototrophic bacteria to total organic carbon pool in aquatic system of subtropical karst catchments, Southwest China: evidence from hydrochemical and microbiological study. *FEMS Microbiol. Ecol.* 93, 1–8. doi: 10.1093/femsec/fix065

Lindh, M. V., and Pinhassi, J. (2018). Sensitivity of bacterioplankton to environmental disturbance: a review of Baltic Sea field studies and experiments. *Front. Mar. Sci.* 5:361. doi: 10.3389/fmars.2018.00361

Linz, A. M., Aylward, F. O., Bertilsson, S., McMahon, K. D., Grossart, H. P., Massana, R., et al. (2020). Time-series metatranscriptomes reveal conserved patterns between phototrophic and heterotrophic microbes in diverse freshwater systems. *Limnol. Oceanogr.* 65, 101–112. doi: 10.1002/lno.11306

Liu, R., Zhang, Y., and Jiao, N. (2010). Diel variations in frequency of dividing cells and abundance of aerobic anoxygenic phototrophic bacteria in a coral reef system of the South China Sea. *Aquat. Microb. Ecol.* 58, 303–310. doi: 10.3354/ame01371

Liu, X., Hou, W., Dong, H., Wang, S., Jiang, H., Wu, G., et al. (2016). Distribution and diversity of Cyanobacteria and eukaryotic algae in Qinghai-Tibetan lakes. *Geomicrobiol. J.* 33, 860–869. doi: 10.1080/01490451.2015.1120368

Luuc, R. M., Olav, M. S., and Hans, U. (1999). "Cyanobacteria in the environment," in *Toxic Cyanobacteria in Water: A guide to Their Public Health Consequences, Monitoring and Management*, ed. J. Bartram (London: E&FN Spon), 15–40.

Mašín, M., Zdun, A., Stoń-Egiert, J., Nausch, M., Labrenz, M., Moulisová, V., et al. (2006). Seasonal changes and diversity of aerobic anoxygenic phototrophs in the Baltic Sea. *Aquat. Microb. Ecol.* 45, 247–254. doi: 10.3354/ame045247

Michelou, V. K., Cottrell, M. T., and Kirchman, D. L. (2007). Light-stimulated bacterial production and amino acid assimilation by Cyanobacteria and other microbes in the North Atlantic ocean. *Appl. Environ. Microbiol.* 73, 5539–5546. doi: 10.1128/AEM.00212-07

Montecchia, M. S., Pucheu, N. L., Kerber, N. L., and García, A. F. (2006). Oxygen and light effects on the expression of the photosynthetic apparatus in *Bradyrhizobium* sp. C7T1 strain. *Photosynth. Res.* 90, 215–222. doi: 10.1007/s11120-007-9129-5

Nishimura, K., Shimada, H., Ohta, H., Masuda, T., Shioi, Y., and Takamiya, K. I. (1996). Expression of the puf Operon in an aerobic photosynthetic bacterium, *Roseobacter denitrificans*. *Plant Cell Physiol.* 37, 153–159. doi: 10.1093/oxfordjournals.pcp.a028926

Norbent, W., and Steffen, U. (2003). Phytoplankton trends in the Baltic Sea. *ICES J. Mar. Sci.* 60, 177–186. doi: 10.1016/S1054

Oksanen, A. J., Blanchet, F. G., Friendly, M., Kindt, R., Legendre, P., Mcglinn, D., et al. (2013). *Package "vegan." Community Ecol. Packag.* Available online at: https://cran.r-project.org/web/packages/vegan/vegan.pdf (accessed November 28, 2020).

Paerl, H. W. (2012). "Marine plankton," in *Ecology of Cyanobacteria II: Their Diversity in Space and Time*, ed. B. A. Whitton (Dordrecht: Springer), 127–153. doi: 10.1007/978-94-007-3855-3_5

Pajares, S., Varona-Cordero, F., and Hernández-Becerril, D. U. (2020). Spatial distribution patterns of bacterioplankton in the oxygen minimum zone of the tropical Mexican Pacific. *Microb. Ecol.* 80, 519–536. doi: 10.1007/s00248-020-01508-7

Peiffer, J. A., Spor, A., Koren, O., Jin, Z., Tringe, S. G., Dangl, J. L., et al. (2013). Diversity and heritability of the maize rhizosphere microbiome under field conditions. *Proc. Natl. Acad. Sci. U.S.A.* 110, 6548–6553. doi: 10.1073/pnas.1302837110

Quast, C., Pruesse, E., Yilmaz, P., Gerken, J., Schweer, T., Yarza, P., et al. (2013). The SILVA ribosomal RNA gene database project: improved data processing and web-based tools. *Nucleic Acids Res.* 41, 590–596. doi: 10.1093/nar/gks1219

R Core Team (2020). *R: A Language and Environment for Statistical Computing*. Vienna: R Foundation Statistical Computing.

Raven, J. A. (2009). Contributions of anoxygenic and oxygenic phototrophy and chemolithotrophy to carbon and oxygen fluxes in aquatic environments. *Aquat. Microb. Ecol.* 56, 177–192. doi: 10.3354/ame01315

Reusch, T. B. H., Dierking, J., Andersson, H. C., Bonsdorff, E., Carstensen, J., Casini, M., et al. (2018). The Baltic Sea as a time machine for the future coastal ocean. *Sci. Adv.* 4:eaar8195. doi: 10.1126/sciadv.aar8195

Rutgersson, A., Jaagus, J., Schenk, F., and Stendel, M. (2014). Observed changes and variability of atmospheric parameters in the Baltic Sea region during the last 200 years. *Clim. Res.* 61, 177–190. doi: 10.3354/cr01244

Sala, M. M., Aparicio, F. L., Balague, V., Boras, J. A., Borrull, E., Cardelus, C., et al. (2016). Contrasting effects of ocean acidification on the microbial food web under different trophic conditions. *ICES J. Mar. Sci.* 73, 670–679. doi: 10.1093/icesjms/fsv130

Salka, I., Moulisová, V., Koblížek, M., Jost, G., Jürgens, K., and Labrenz, M. (2008). Abundance, depth distribution, and composition of aerobic bacteriochlorophyll a-producing bacteria in four basins of the central Baltic Sea. *Appl. Environ. Microbiol.* 74, 4398–4404. doi: 10.1128/AEM.02447-07

Šantić, D., Šestanović, S., Vrdoljak, A., Šolić, M., Kušpilić, G., Ninčević Gladan, Ž, et al. (2017). Distribution of aerobic anoxygenic phototrophs in the Eastern Adriatic Sea. *Mar. Environ. Res* 130, 134–141. doi: 10.1016/j.marenvres.2017.07.012

Sato-Takabe, Y., Hamasaki, K., and Suzuki, S. (2019). High temperature accelerates growth of aerobic anoxygenic phototrophic bacteria in seawater. *Microbiologyopen* 8:e00710. doi: 10.1002/mbo3.710

Sharon, I., Tzahor, S., Williamson, S., Shmoish, M., Man-Aharonovich, D., Rusch, D. B., et al. (2007). Viral photosynthetic reaction center genes and transcripts in the marine environment. *ISME J.* 1, 492–501. doi: 10.1038/ismej.2007.67

Sieracki, M. E., Gilg, I. C., Thier, E. C., Poulton, N. J., and Goericke, R. (2006). Distribution of planktonic aerobic anoxygenic photoheterotrophic bacteria in the northwest Atlantic. *Limnol. Oceanogr.* 51, 38–46. doi: 10.4319/lo.2006.51.1.0038

Sieradzki, E. T., Fuhrman, J. A., Rivero-Calle, S., and Gómez-Consarnau, L. (2018). Proteorhodopsins dominate the expression of phototrophic mechanisms in seasonal and dynamic marine picoplankton communities. *PeerJ* 6:e5798. doi: 10.7717/peerj.5798

Soo, R. M., Skennerton, C. T., Sekiguchi, Y., Imelfort, M., Paech, S. J., Dennis, P. G., et al. (2014). An expanded genomic representation of the phylum yanobacteria. *Genome Biol. Evol.* 6, 1031–1045. doi: 10.1093/gbe/evu073

Soo, R. M., Woodcroft, B. J., Parks, D. H., Tyson, G. W., and Hugenholtz, P. (2015). Back from the dead; the curious tale of the predatory cyanobacterium *Vampirovibrio chlorellavorus*. *PeerJ* 2015:e968. doi: 10.7717/peerj.968

Stevens, H., and Ulloa, O. (2008). Bacterial diversity in the oxygen minimum zone of the eastern tropical South Pacific. *Environ. Microbiol.* 10, 1244–1259. doi: 10.1111/j.1462-2920.2007.01539.x

Stoń, J., Kosakowska, A., Łotocka, M., and Łysiak-Pastuszak, E. (2002). Pigment composition in relation to phytoplankton community structure and nutrient content in the Baltic Sea. *Oceanologia* 44, 419–437.

Takolander, A., Cabeza, M., and Leskinen, E. (2017). Climate change can cause complex responses in Baltic Sea macroalgae: a systematic review. *J. Sea Res.* 123, 16–29. doi: 10.1016/j.seares.2017.03.007

Thureborn, P., Lundin, D., Plathan, J., Poole, A. M., Sjöberg, B. M., and Sjöling, S. (2013). A metagenomics transect into the deepest point of the Baltic Sea reveals clear stratification of microbial functional capacities. *PLoS One* 8:e74983. doi: 10.1371/journal.pone.0074983

Tomasch, J., Gohl, R., Bunk, B., Suarez Diez, M., and Wagner-Dö Bler, I. (2011). Transcriptional response of the photoheterotrophic marine bacterium *Dinoroseobacter shibae* to changing light regimes subject category: microbial ecosystem impacts. *ISME J.* 5, 1957–1968. doi: 10.1038/ismej.2011.68

Tsementzi, D., Wu, J., Deutsch, S., Nath, S., Rodriguez-R, L. M., Burns, A. S., et al. (2016). SAR11 bacteria linked to ocean anoxia and nitrogen loss. *Nature* 536, 179–183. doi: 10.1038/nature19068

Vahtera, E., Conley, D. J., Gustafsson, B. G., Kuosa, H., Pitkänen, H., Savchuk, O. P., et al. (2007). Internal ecosystem feedbacks enhance nitrogen-fixing cyanobacteria blooms and complicate management in the Baltic Sea. *Ambio* 36, 186–194. doi: 10.1579/0044-7447(2007)36[186:iefenc]2.0.co;2

Van Cappellen, P., Ingall, E. D., Paytan, A., Mclaughlin, K., Ruttenberg, K. C., Berner, R. A., et al. (2008). Expanding oxygen-minimum zones in the tropical oceans. *Science* 320, 655–658. doi: 10.1126/science.1153847

Vila-Costa, M., Sharma, S., Moran, M. A., and Casamayor, E. O. (2013). Diel gene expression profiles of a phosphorus limited mountain lake using metatranscriptomics. *Environ. Microbiol.* 15, 1190–1203. doi: 10.1111/1462-2920.12033

Voget, S., Wemheuer, B., Brinkhoff, T., Vollmers, J., Dietrich, S., Giebel, H. A., et al. (2015). Adaptation of an abundant Roseobacter RCA organism to pelagic systems revealed by genomic and transcriptomic analyses. *ISME J.* 9, 371–384. doi: 10.1038/ISMEJ.2014.134

Wasmund, N., and Siegel, H. (2008). "Phytoplankton," in *State and Evolution of the Baltic Sea 1952-2005*, eds R. Feistel, G. Nausch, and N. Wasmund (Hobokon, NJ: Wiley and Sons Inc), doi: 10.1002/9780470283134.ch15

Yurkov, V. V., and Beatty, J. T. (1998). Aerobic anoxygenic phototrophic bacteria. *Microbiol. Mol. Biol. Rev.* 62, 695–724. doi: 10.1128/mmbr.62.3.695-724.1998

Yutin, N., Béjà, O., Yutin, N., and Béjà, O. (2005). Putative novel photosynthetic reaction centre organizations in marine aerobic anoxygenic photosynthetic bacteria: insights from metagenomics and environmental genomics. *Environ. Microbiol.* 7, 2027–2033. doi: 10.1111/j.1462-2920.2005.00843.x

Yutin, N., Suzuki, M. T., Rosenberg, M., Rotem, D., Madigan, M. T., Süling, J., et al. (2009). BchY-based degenerate primers target all types of anoxygenic photosynthetic bacteria in a single PCR. *Appl. Environ. Microbiol.* 75, 7556–7559. doi: 10.1128/AEM.01014-09

Yutin, N., Suzuki, M. T., Teeling, H., Weber, M., Venter, J. C., Rusch, D. B., et al. (2007). Assessing diversity and biogeography of aerobic anoxygenic phototrophic bacteria in surface waters of the Atlantic and Pacific Oceans using the global ocean sampling expedition metagenomes. *Environ. Microbiol.* 9, 1464–1475. doi: 10.1111/j.1462-2920.2007.01265.x

Zhang, Y., and Jiao, N. (2007). Dynamics of aerobic anoxygenic phototrophic bacteria in the East China Sea. *FEMS Microbiol. Ecol.* 61, 459–469. doi: 10.1111/j.1574-6941.2007.00355.x

Conflict of Interest: The authors declare that the research was conducted in the absence of any commercial or financial relationships that could be construed as a potential conflict of interest.

Publisher's Note: All claims expressed in this article are solely those of the authors and do not necessarily represent those of their affiliated organizations, or those of the publisher, the editors and the reviewers. Any product that may be evaluated in this article, or claim that may be made by its manufacturer, is not guaranteed or endorsed by the publisher.

frontiers in Marine Science

ORIGINAL RESEARCH
published: 18 February 2022
doi: 10.3389/fmars.2022.850120

Proteins Are Well-Preserved in Shells Toasted at 300°C Revealed by Proteomics

*Xin Ji[1], Jingliang Huang[2], Zhenglu Wang[1], Zhiqiang Xu[3] and Chuang Liu[1]**

[1] College of Oceanography, Hohai University, Nanjing, China, [2] School of Chemical Engineering and Technology, Sun Yat-sen University, Zhuhai, China, [3] Freshwater Fisheries Research Institute of Jiangsu Province, Nanjing, China

The development of protein anti-degradation strategies is important for storage at ambient conditions, for example in vaccine storage. Despite that it is known that biominerals, typical inorganic-organic composites, can preserve proteins at room temperature for a long time, it is unclear the extent of protein degradation under high temperatures. In this study, we examined remaining proteins in the toasted abalone shell under high temperatures (200 and 300°C) by biomineral proteomics method. Surprisingly, 21 proteins including carbonic anhydrase, hemocyanin, actin can still be identified from shells even after toasting under 300°C, not much decreased compared to that in the 200°C-treated and the native shell. However, the microstructure and composition (both mineral and organic matrix) of shells were altered significantly revealed by scanning electron microscopy, infrared spectroscopy, and X-ray diffraction. The well-preserved proteins may be partially due to the sacrifice of mineral/organic interfaces and the formation of nanopores in the shell at high temperatures. Moreover, the extracted proteins from both groups were able to affect calcium carbonate *in vitro*, indicating certain remaining bioactivities of proteins. This study has potential implications in various fields such as protein storage at high temperatures and palaeoproteomics.

Keywords: biomineralization, proteomics, proteins-degradation, shells (structures), materials characterisation

OPEN ACCESS

Edited by:
Shiguo Li,
Research Center for Eco-Environmental Sciences, Chinese Academy of Sciences (CAS), China

Reviewed by:
Zhi Liao,
Zhejiang Ocean University, China
Zhaoyong Zou,
Wuhan University of Technology, China
Jorune Sakalauskaite,
University of Copenhagen, Denmark

****Correspondence:***
Chuang Liu
chuangliu2020@hhu.edu.cn

Specialty section:
This article was submitted to Marine Molecular Biology and Ecology, a section of the journal Frontiers in Marine Science

Received: *07 January 2022*
Accepted: *28 January 2022*
Published: *18 February 2022*

Citation:
Ji X, Huang J, Wang Z, Xu Z and Liu C (2022) Proteins Are Well-Preserved in Shells Toasted at 300°C Revealed by Proteomics. Front. Mar. Sci. 9:850120. doi: 10.3389/fmars.2022.850120

INTRODUCTION

Proteins are usually prone to be degraded under ambient temperatures let alone high temperatures (Bischof and He, 2006). The development of anti-degradation strategies is important for protein storage at ambient conditions, for example in vaccine storage (Zhang et al., 2012). Chemical modification of proteins such as crosslinking (Collins et al., 1992) and converting to polymers (Wiemann et al., 2018) may help to preserve proteins for a long time but these approaches will change the nature of proteins. Alternatively, proteins can be stabilized by organic macromolecules [e.g., glycerol (Vagenende et al., 2009) and arginine (Baynes et al., 2005)] that results from molecular interaction. In addition, minerals can also offer protection against degradation because of the isolation and stabilization effects (Demarchi et al., 2016).

Biominerals, typical inorganic-organic composite, are minerals formed by organisms (Addadi et al., 2006). In nature, commonly seen biominerals include bone, dental enamel, mollusk shell. Nacre, a typical mollusk shell biomineral, is composed of 95% calcium carbonate and 5% organics (proteins, polysaccharides, and lipids) (Addadi et al., 2006). In particular, proteins are found to

be key players in the formation of biominerals and they are occluded in the biominerals (Marin et al., 2007). In recent past two decades, by proteomic methods, dozens of proteins were identified in various mollusk biominerals (Marie et al., 2012; Liao et al., 2015; Liu et al., 2015; Marin, 2020; Liu and Zhang, 2021). Proteins associated with the minerals have high stability (Demarchi et al., 2016). In fact, proteins in bone or dental enamel fossils, which have been preserved for as long as thousands of years or even millions of years (Weiner et al., 1976), are employed to perform phylogenetic analysis (Welker et al., 2015) of humans or to reconstruct people's life in the past (Hendy et al., 2018; Cappellini et al., 2019; Sakalauskaite et al., 2019; Welker et al., 2019).

Despite that it is known that biominerals can preserve proteins at room temperature for a long time, it is unclear that the extent of protein degradation under high temperature. A recent study found that the shell proteins of the thorny oyster, *Spondylus gaederopus* can still be identified after heating the shell at 140°C (Sakalauskaite et al., 2021). In this study, to find out if proteins can be extracted and identified from seashells heated at even higher temperatures, we extracted proteins from toasted abalone shells (200, 300°C) and used liquid chromatography tandem-mass spectrometry (LC-MS/MS) to analyze their proteome. Scanning electron microscopy (SEM), fourier transform infrared spectroscopy (FTIR), X-ray diffraction (XRD), and thermogravimetric analysis (TGA) were complimentarily used for the characterization of mineral morphology, mineral composition, mineral crystallography, and thermal behavior, respectively (**Figure 1**).

MATERIALS AND METHODS

Materials

Native abalone (*Haliotis discus hannai*) were purchased from local markets from Fuzhou, Fujiang province, China. The shell was obtained by sacrificing the abalone and cleaned with deionized (DI) water. Toasted shells were obtained by toasting the whole abalone shell in an oven at 200°C, 300°C for 10 min and then cleaned with DI water. Untoasted shells were used as the control. Two replicates were performed. It is assumed that the temperature reached up to the same degree in all layers of shells.

Extraction of Shell Matrix Proteins From the Toasted Abalone Shells

The experiment was based on a well-established protocol for the extraction of SMPs in the pearl oyster shell (Liu et al., 2015). Two cleaned toasted abalone shells were immersed in 5% sodium hydroxide for 24 h and were subsequently rinsed in DI water to avoid possible contamination from soft tissues adhering to the shell. The fragments were pulverized (∼50 g) and were decalcified with 50 mL of 0.8 M ethylenediaminetetraacetic acid (EDTA, pH 8.0) for 48 h at 4 °C with continuous agitation. AEBSF (Sangon Biotech, Shanghai, China), an irreversible serine protease inhibitor, was added to prevent protein degradation. For the extraction of EDTA-soluble matrix, the supernatant was collected by centrifugation at 10,000 rpm for 30 min at 4 °C and was then desalted by dialysis and ultrafiltration (cutoff 3 K). For the extraction of EDTA-insoluble matrix, the above insoluble pellet was thoroughly rinsed with water and boiled with a denaturing solution (pH 8.0, 30 mM Tris-HCl, 1% sodium dodecyl sulfate, 10 mM dithiothreitol) for 10 min. The EDTA-insoluble matrix was desalted by dialysis against DI water and then was concentrated by Millipore tubes (cutoff 3 kDa). The samples were applied on 12% precast SDS-polyacrylamide gels (Sangon Biotech, Shanghai, China). The protein concentration was quantified by a BCA assay kit (Pierce).

Liquid Chromatography Tandem-Mass Spectrometry Analysis and Bioinformatic Analysis

This process was based on a previously established protocol for the pearl oyster shell (Liu et al., 2015) and was performed in the Biomedical Analysis Center of Tsinghua University. Proteins were stained with Coomassie Blue and the entire protein lane was excised in two pieces, which were completely destained by washing with 50 μL of 50 mM NH_4HCO_3/acetonitrile (50/50) mixture for 30 min at 37 °C. Reduction was conducted with 50 μL of 10 mM DTT in 50 mM NH_4HCO_3 for 1 h at 57 °C, followed by alkylation with 50 μL of 100 mM iodoacetamide for 30 min at room temperature in the dark. The cut gels were dried in acetonitrile and then treated with 0.4 μg trypsin (Proteomics Grade, Sigma) in 10 μL of 50 mM NH_4HCO_3 for 12 h at 37 °C. The suspension was treated with 50 μL of 1% formic acid at 30 °C for 30 min under agitation. The digests were then lyophilized and suspended in 30 μL of 0.1% trifluoroacetic acid and 4% acetonitrile for LC-MS/MS analysis. Five microliter of the samples were injected into the LTQ Orbitrap Velos mass spectrometer with Dionex U-3000 Rapid Separation nano-LC system (Thermo Fisher Scientific) for analysis. MS data were acquired automatically using Analyst QS 1.1 software (Applied Biosystems) following an MS survey scan over m/z 350–1,500 at a resolution of 60,000 for full scan and 2, 000 for MS/MS measurements.

The LC-MS/MS data were searched against the protein database downloaded from Mollusca category in the Uniprot database using a Mascot 2.1 search engine with oxidized methionine and tryptophan as variable modifications. No other post-translation modification has been performed. The peptide MS and MS/MS tolerances were set to 0.5 Da. Finally, sequences with mascot scores of at least 5.0 and with at least two matched peptide fragments were considered valid. Conserved domains of proteins were predicted using SMART.[1]

In vitro Calcium Carbonate Crystallization

Calcium carbonate crystallization experiment was performed by the slow diffusion of CO_2 vapor into six cell-culture dishes (Nest, China) from ∼10 g solid ammonium carbonate in a closed desiccator for about 24 h at room temperature. Each well contained 180 μL of 20 mM $CaCl_2$

[1]http://smart.embl-heidelberg.de/

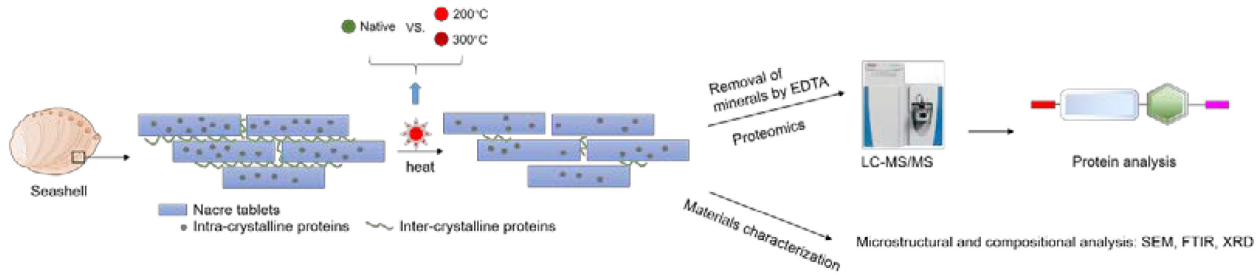

FIGURE 1 | The experimental process of toasting abalone shells. Shells were heated at 200 and 300°C for 10 min and native shells as the control. Then the shells were decalcified by EDTA and the remaining proteins were analyzed by LC-MS/MS. Additionally, the microstructure and composition of shells were examined by SEM, FTIR, and XRD.

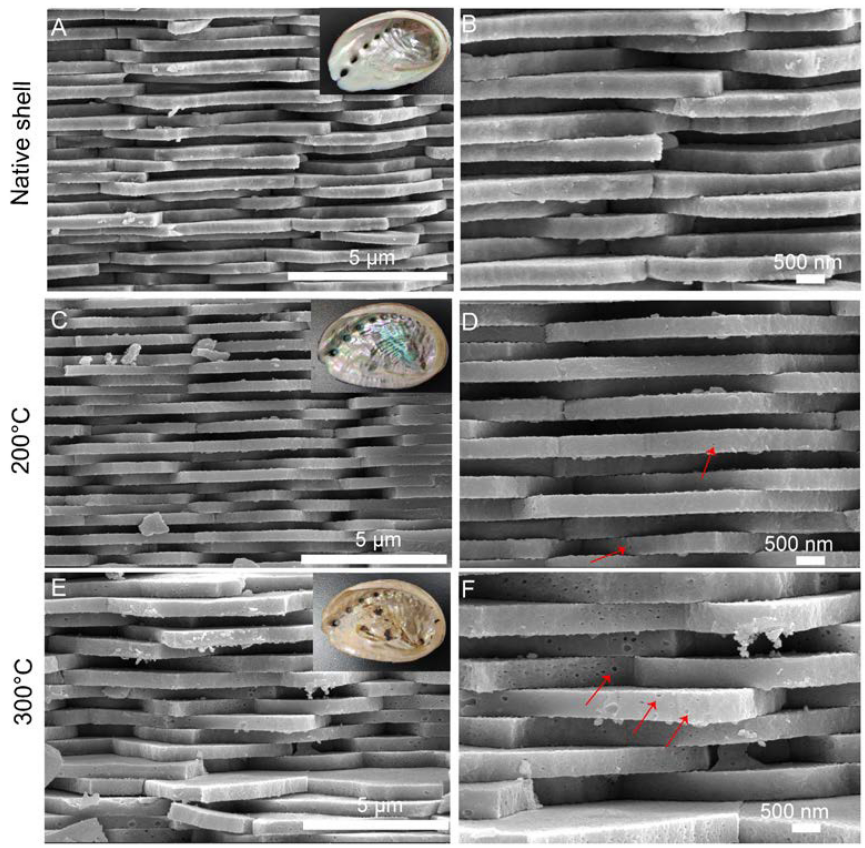

FIGURE 2 | Microstructure of the native and toasted abalone shell by SEM. **(A)** Native abalone shell and its magnification **(B)**; toasted abalone shells at 200°C **(C)** and 300°C **(E)** and their magnification **(D,F)** respectively. Red arrows indicate the nanoscale holes in the nacre tablets. The insets in **(A,C,E)** are the optical images of shells.

and 20 μL of EDTA-soluble proteins (free of SDS) with a final concentration of 150 μg mL^{-1} on a silica cover glass. For the control, no proteins were added. The final samples were rinsed twice with DI water and air-dried before further evaluation.

Characterization

The shells were fractured and the cross-sections were spurred with gold and then examined by SEM (Hitachi S4800, 5 kV). XRD of powdered shells was recorded on Bruker D8 ADVANCE diffractometer using CuKα radiation (λ = 0.154 nm) in the 2θ range 20–80°. FTIR of powdered shells was recorded at a resolution of 4 cm^{-1} with 64 scans with attenuated total reflectance (ATR) on a Thermo Scientific Nicolet IN10 instrument. TGA analysis of powdered shells (∼3 mg) was carried out using a TAQ 600 (TA Instruments, Inc., United States) in an air atmosphere with a temperature range from room temperature to 800°C.

Data Availability

Critical raw data of proteomics have been deposited into PRIDE, project accession: PXD030901.

RESULTS AND DISCUSSION

Shell Microstructural Change After Toasting

In the native abalone shell, the classical "brick-and-motor" structure composed of stacking nanoscale tablets (thickness, ∼350 nm) was observed by SEM (**Figures 2A,B**). Macroscopically, the inner shell surfaces were similar after the toasting treatment at 200°C (inset of **Figure 2C**). By contrast, the inner shell surfaces lost the iridescence after the toasting treatment at 300°C (inset of **Figure 2E**), indicating microstructural changes of nacre tablets. Microscopically, although the thickness of tablets remained almost unchanged in both conditions, broken pieces of tablets were observed (**Figures 2C–F**) and nanoscale holes (diameters of ca. 50 nm) were generated (**Figures 2D,F**) after toasting. In addition, the surfaces of tablets appeared rougher (**Figures 2D,F**), indicating altered mineral/organic matrices. The nanoscale pores may be due to the collapse of organics inside the minerals after toasting since organics were known to form nanoscale ellipse-shaped forms inside biominerals and synthetic $CaCO_3$ (Li et al., 2011; Rae Cho et al., 2016; Liu et al., 2017). Interestingly, these nanopores were also observed when sea urchin skeleton made of calcium carbonate was treated at high temperatures, in which the authors ascribed the pore formation to the transformation of amorphous calcium carbonate (ACC) to crystalline calcite (Albéric et al., 2018). It is also proposed that relatively thin ACC layers are adjacent to organic/inorganic interfaces, serving as buffer layers between intra-crystalline organics and crystalline calcite (Albéric et al., 2018). Given that ACC has been found in the abalone nacre tablets (Nassif et al., 2005) and other gastropod nacre (Macías-Sánchez et al., 2017), it is possible that ACC in the nacre tablets collapsed and pores formed when temperatures reached up to above 200°C, which might help to dissipate energy from the heat treatment.

Extraction and Proteomics Analysis of Shell Matrix Proteins From Toasted Shells

Next, we sought to check whether proteins can be preserved in the toasted shells. In agreement with previous studies, smear protein bands appeared in both the EDTA-soluble and EDTA-insoluble matrix. Interestingly, when shells were toasted at 200°C, protein bands from both matrices appeared in the entire gel lane, indicating the existence of proteins (**Figure 3A**). When shells were toasted at 300°C, very weak protein bands from both matrices appeared in the entire gel lane (**Figure 3A**). To analyze the SMP proteome, the entire gels of both matrices were cut and subjected to LC-MS/MS. To our surprise, many proteins can still be identified in both toasted groups, compared to the native shell. 49 and 21 proteins (**Table 1** and

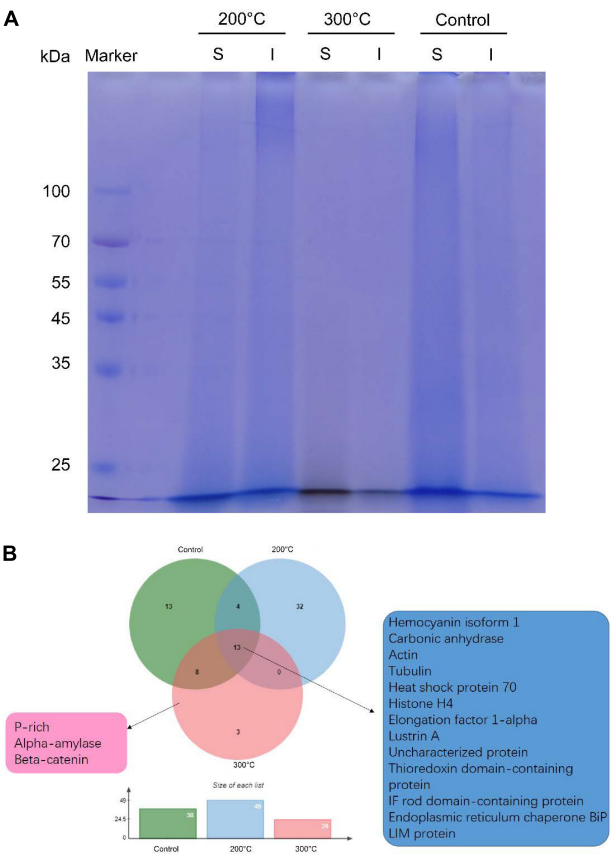

FIGURE 3 | Proteomic analysis of shell matrix proteins from the toasted shell. **(A)** SDS-PAGE of EDTA-soluble matrix and EDTA-insoluble matrix of toasted shells at 200, 300°C and the native shell (as the control). S: EDTA-soluble matrix; I: EDTA-insoluble matrix. **(B)** Venn diagram of identified proteins in the three groups by proteomics.

Supplementary Files) were found at the 200 and 300°C group, respectively, and in the control group, 38 proteins were identified. The three groups of abalone shells (200°C, 300°C, Control) shared 13 proteins, including Hemocyanin, Carbonic anhydrase, Lustrin A, Actin, and others (**Figure 3B**). In toasted shells at 300°C, there were three unique proteins, including proline-rich, Alpha-amylase, and Beta-catenin (**Figure 3B** and **Table 1**). Interestingly, the number of proteins in shells toasted at 200°C increased compared with the control group, which we speculated that it might be caused by the improved destabilization of proteins and/or the disruption of the peptide chains when the temperature increased.

One of the most abundant proteins was hemocyanin, which contains tyrosinase domains. Tyrosinase was commonly found in shells and was thought to be involved in the cross-linking of organic matrix (Liu and Zhang, 2021). Interestingly, hemocyanin has been found in cuttlebone before (Liu et al., 2021). Another abundant protein found was a secreted carbonic anhydrase (CA), which can converse CO_2 into HCO_3^- and therefore plays an important role in biomineralization (Cardoso et al., 2019). CA or proteins with similar functions have been found

TABLE 1 | Proteomic analysis of shell matrix proteins extracted from toasted abalone shells at 300°C for 10 min.

UniProt accession	Description	Score	Coverage, %	PSMs	Peptides	Unique peptides
C7FEG7	Hemocyanin isoform 1 (*Haliotis diversicolor*)	548.45	28.76	168	84	65
A0A7G7P0F1	Carbonic anhydrase (*Haliotis discus hannai)*	523.83	68.25	166	24	15
K1RA77	Ubiquitin (*Crassostrea gigas*)	80.81	74.32	23	8	8
B3TK83	Beta-actin 2 (*Haliotis diversicolor*)	80.44	56.80	27	15	2
V4A0D9	Histone H4 (*Lottia gigantea*)	49.36	33.80	17	9	6
A0A650A878	Lustrin A (*Haliotis discus hannai*)	26.16	6.86	10	6	6
A0A077D3S6	GAPDH (*Mytilus galloprovincialis*)	24.29	31.77	8	7	6
J9Z3 × 3	ATP synthase subunit beta (*Dreissena polymorpha*)	21.49	35.71	7	6	1
Q45Y88	Elongation factor 1-alpha (*Haliotis rufescens)*	16.07	13.63	5	4	1
A0A0B7B286	Tubulin alpha chain (*Arion vulgaris*)	14.40	20.05	7	5	1
Q8I6N2	Heat shock protein 70 (*Crassostrea gigas*)	13.20	11.02	5	5	1
B7U5G2	LIM protein (*Haliotis discus*)	12.53	17.48	3	2	2
G4V2C2	Fasciclin domain-containing protein (*Haliotis discus*)	7.97	17.16	3	3	3
B6RB16	Alginate lyase 2 (*Haliotis discus*)	7.03	6.75	2	2	2
A0A3S0ZWX4	P-rich (*Elysia chlorotica*)	6.46	5.86	3	1	1
L8AW48	Alpha-amylase (*Haliotis discus*)	6.09	4.70	2	2	2
A0A6P7SSE0	Proteasome subunit alpha type (*Octopus vulgaris*)	5.62	10.04	2	2	2
A0A141BGR0	Beta-catenin (*Pinctada fucata*)	5.32	2.30	2	2	2
A0A6J8DRP2	Fructose-bisphosphate aldolase (*Mytilus coruscus*)	5.24	6.89	2	2	2
A0A2C9K5L4	Thioredoxin domain-containing protein (*Biomphalaria glabrata*)	5.05	12.14	2	2	2
A0A6P7T1Z1	Endoplasmic reticulum chaperone BiP (*Octopus vulgaris*)	9.51	2.59	3	2	1

The 3rd column is the mascot score, which is the cumulative protein score based on summing the ion scores of the unique peptides identified for that protein. The 4th column is the peptide coverage found in the MS. The 5th column is PSMs (peptide spectrum matches), which display the total number of identified peptide sequences for the protein, including those redundantly identified.

in various biominerals such as the skeleton of sponges, corals and shells of pearl oysters, abalones, oysters, clams, etc. (Le Roy et al., 2014). CA is also homologous to nacrein, one of the first identified matrix proteins in the seashell (Miyamoto et al., 1996). Lustrin A was a known shell matrix protein found in the abalone shell, which contained cysteine-rich repeat interspersed by proline-rich domains (Shen et al., 1997). Together with other known SMPs such as LIM protein, Fasciclin domain-containing protein, Proline-rich protein, Thioredoxin domain-containing protein, Alpha-amylase, Alginate lyase 2, they indicated the well-preserved proteins in the shell after 300°C treatment. In addition to the above proteins, others are cellular proteins including actin, tubulin, ubiquitin, histone, transcription factor, and GAPDH. It has been proposed that exosomes or some other vesicles carrying these cellular proteins participated in the shell formation and finally occluded inside the minerals (Song et al., 2019).

Previously, in the native abalone (*Haliotis asinine*) shell proteome, 51 SMPs were found including Lustrin A, Perlucin, Perlustrin, AP24, Perlwapin, Ependymin related proteins, Kunitz domain-containing protein, glutamine-rich protein (Mann et al., 2018). Partially in agreement with their results, we found 38 proteins in our control. The difference in terms of protein number might be due to the species difference, treatment methods, or instrument sensitivity. In our study, compared with unroasted abalone shells, the number of proteins increased by around 30% at 200°C and decreased by around 45% at 300°C. CA and other proteins might be occluded inside the mineral crystals and therefore can withstand high temperatures. In contrast, other intercrystalline proteins or proteins located between nacreous building blocks (e.g., BPTI/Kunitz domain-containing protein, Calponin) may be susceptible to high temperatures.

The Compositional Analysis of Shell by Thermogravimetric Analysis, X-Ray Diffraction, and Fourier Transform Infrared Spectroscopy

To better understand the underlying mineral and matrix change after toasting treatment, materials characterization was conducted. First, TGA was employed to examine the thermal behavior of the native shells (**Figure 4A**). Particularly, the loss of organics and structural water occurred in samples below 300°C (**Figure 4B**). The weight percent of organics was around 2 wt.% and 3.7 wt.% if calculated until 300 and 550°C, respectively, close to the amount of organics in biominerals measured by TGA (Albéric et al., 2018). This result seems to indicate that some organics can withstand high temperatures at even above 300°C. At about 600°C, the weight percent dropped dramatically, which is caused by the transformation process of $CaCO_3$ to CaO (Balmain et al., 1999; **Figure 4A**). Further, to examine the potential compositional change during toasting treatment, XRD (for mineral crystallography) and FTIR (for mineral and organic matrix) were used. XRD showed similar peaks between the three samples (**Figure 4C**), which had all the characteristic diffraction lines of aragonite according to RRUFF ID R040078.1. In addition, the (104) peak of calcite was observed in all the group including the native shell. This indicates some prismatic layers made of calcite were in the

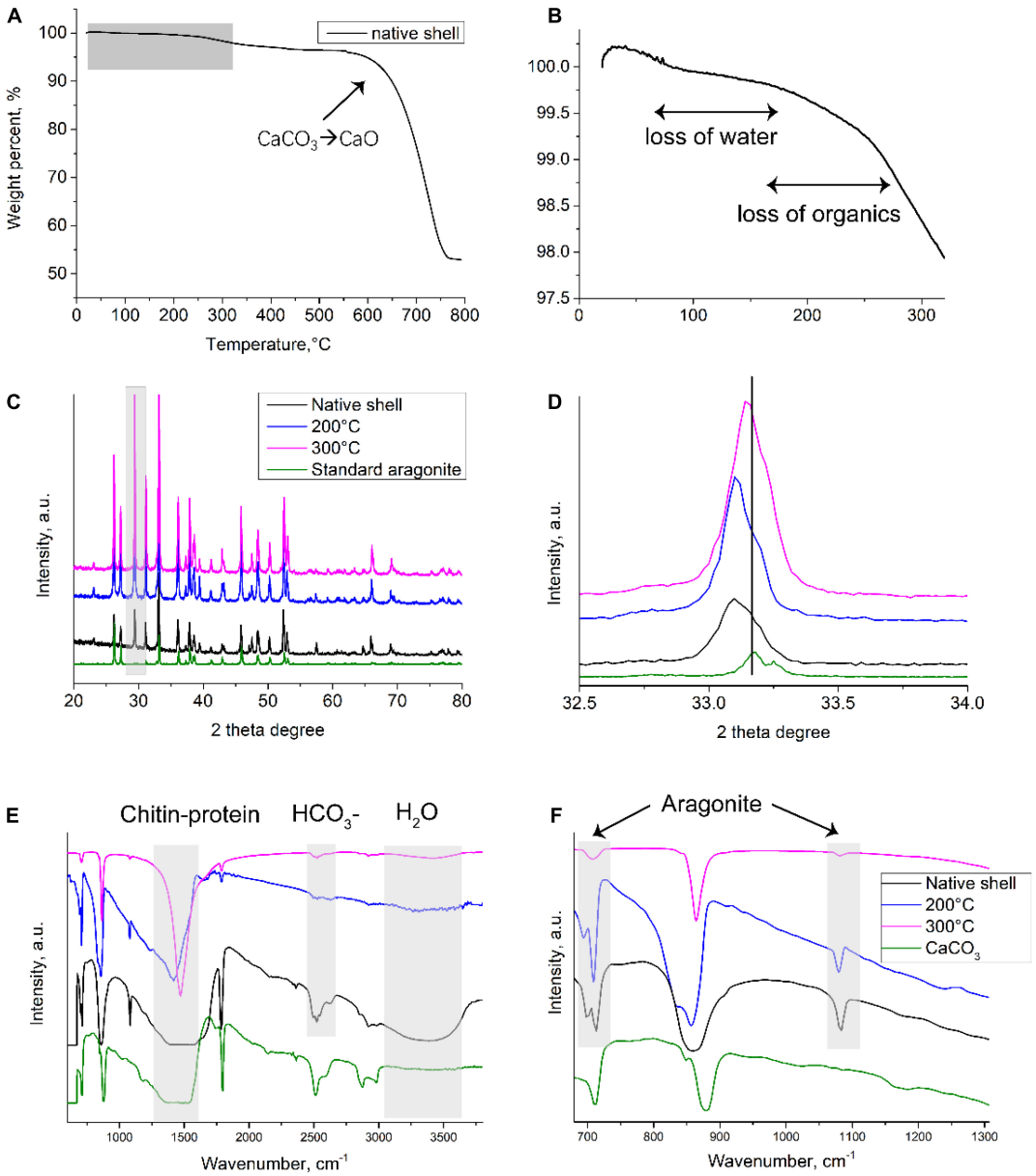

FIGURE 4 | Compositional analysis of native and toasted abalone shell. **(A)** TGA analysis of native shells and a close look at room temperature to 300°C **(B)**. XRD patterns **(C)** and a close exanimation of (012) peaks **(D)**; FTIR spectroscopy **(E)** and a close examination from wavenumbers at 650–1,300 cm^{-1} **(F)**.

samples. A close examination of (012) peaks at 33.2° of the toasted shell (200°C) indicated the left shift compared to the standard aragonite and native shell, but the (012) peak of toasted shells (300°C) just had a small shift and was close to the standard aragonite (**Figure 4D**). Previously, it is known that organics inside many biominerals cause the distortion of crystal lattice and heat treatment can eliminate this effect (Pokroy et al., 2004, 2006). The lattice distortion originates from strong atomic interactions at organic/inorganic interfaces (Pokroy et al., 2004). Thereby, it is possible that when proteins degraded with the increase of temperature to 300°C, some of the crystal deformation caused by occluded proteins disappeared. This assumption is supported by the above proteomics data, in which only 40% of proteins were lost. It is not hard to assume that when all proteins are degraded, the crystal lattice distortion caused by occluded proteins will disappear. The XRD results showed overall no change of crystal phase but suggested microscale changes of crystal domains caused by heat treatment. While XRD only reflected mineral phase, FTIR provides information on both the inorganic and organic compositional change between the two samples. Indeed, FTIR showed that the characteristic peaks of 700, 713, 864, 1,090, 1,490 cm^{-1} from aragonite (Balmain et al., 1999), 3,380 cm^{-1} from -OH bands of water, and 1,490–1,550 cm^{-1} from proteins and chitin in the native shell,

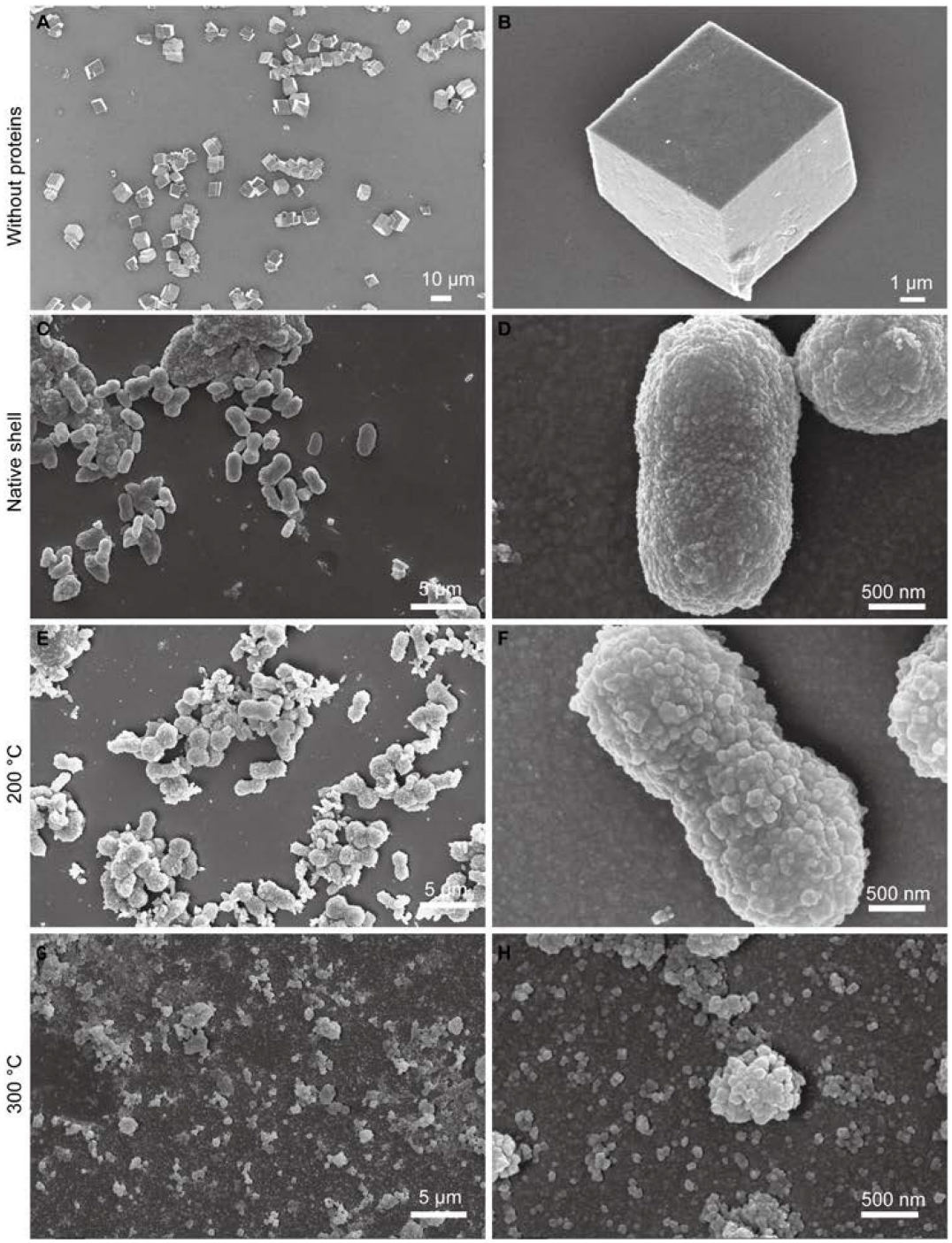

FIGURE 5 | Effects of SMPs of toasted shell on calcium carbonate crystallization. Representative SEM images of calcium carbonate crystals formed at different conditions. **(A,B)** Control condition without proteins; **(C,D)** SMPs extracted from native shells; **(E,F)** SMPs extracted from 200°C-toasted shells; **(G,H)** SMPs extracted from 300°C-toasted shells. All proteins are in the final concentration of 150 μg/mL.

however, with the increase of toasting temperature, many peaks were diminished. The right (blue) shift of wide bands around 1,490–1,550 cm^{-1} could be a result of changed interaction among chitin-proteins-$CaCO_3$ composite. After treatment at 200 and 300°C, the peak at 2,520 cm^{-1} from HCO_3^- at the mineral/organic interfaces (Balmain et al., 1999) and the peak at 3,500 cm^{-1} from OH^- of water (Balmain et al., 1999) were greatly diminished (**Figures 4E,F**), indicating the destruction of the mineral/organic interfaces and the loss of structural water, respectively. The destruction of the mineral/organic

interfaces supports the observation of nanopores formation by SEM (**Figures 2C–F**). It is speculated that heat energy was partially dissipated by the sacrifice of mineral/organic interfaces, and thereby protected the occluded proteins from high temperatures.

The Bioactivity of Remaining Proteins

To test whether the extracted SMPs still have certain bioactive abilities, the effects of SMPs on the crystallization of calcium carbonate *in vitro* were examined. In the control, when no proteins were added to the system, typical rhombohedral calcium carbonate crystals were formed (**Figures 5A,B**). In contrast, when proteins (150 μg/mL) extracted from native shells were added, dumbbell-shaped crystals with diameters of 2–5 μm were formed and small crystal units (diameters of ca. 30 nm) were found on the crystal surfaces (**Figures 5C,D**). Interestingly, in the 200°C-treated group, no dramatic change of crystal morphology has been observed although the small crystal units on the surfaces appeared to be slightly larger (diameters of ca. 90 nm) than that in the control group (**Figures 5E,F**). Moreover, in the 300°C-treated group, no dumbbell-shaped crystals but small crystals with diameters of 30–90 nm were formed (**Figures 5G,H**). It seems that crystal number and nucleation in the 200°C-treated group were similar to that in the native shell group. By contrast, the crystal number was higher in the 300°C-treated group compared to the 200°C-treated group and the native shell group. The crystal phase seems not affected by the proteins (data not shown). This data suggested that compared with untoasted shells, proteins in the 200°C-treated group still affect the crystallization of calcium carbonate *in vitro* and maintain similar bioactivities with that of control. Proteins in the 300°C-treated group lost certain abilities of control on crystal morphology but still can affect the calcium carbonate formation such as crystal nucleation and growth. This is also in agreement with our proteomic data.

Possible Indications, Limitations, and Outlook

The indications of this study are in four aspects:

1) Proteins or peptide-based drugs are growing drastically over the past few decades; however, they have low stability and high susceptibility to degradation during processing, storage, and distribution. The establishment and maintenance of a cold temperature environment from manufacturers to patients are therefore required, representing a significant economic burden and sometimes unrealistic in low-developed regions (Moreira et al., 2021). This study shows that proteins can be preserved in toasted seashells, indicating the potential application of protein storage in mineralized materials. In addition, it points out that proteins occluded inside the crystals are possibly more resistant to high temperatures, in agreement with previous concepts that amino acids are well preserved in shells or fossils (Abelson, 1957). Coincident with this idea, the encapsulation of organisms such as viruses, bacteria, yeast, and cells by biomineralized structures has been explored in the past 15 years (Liu et al., 2016; Wang et al., 2018). These studies have shown enhanced stability for preserving the encapsulated organisms (Liu et al., 2016; Wang et al., 2018).
2) Proteins can be preserved for a long time in biominerals such as teeth, bones, and shells. Extracting proteins and analyzing proteome from them (i.e., palaeoproteomics) are increasingly used as a powerful method in archeology and anthropology for the phylogenetic reconstruction of extinct species to the investigation of past human diets and ancient diseases (Hendy et al., 2018). Our study may inform that proteins can be identified in some fossils that are preserved in high-temperature regions, in agreement with previous studies that well-preserved protein sequences were found in ostrich (Struthionidae) eggshell, including from the paleontological sites of Laetoli (3.8 Ma) and Olduvai Gorge (1.3 Ma) in Tanzania (Demarchi et al., 2016).
3) Although shells of Mollusca are not commonly edible, this study indicated that the use of heated/cooked seashells as a food source may have some biomedical effects since the remaining proteins are inside the minerals. In fact, adding heated oyster shells to the diet of elderly patients appears to increase the bone quality (Fujita et al., 1996).
4) The temperature on Earth's surface ranges from -98.6 to 495°C (Merino et al., 2019) and the upper temperature limit for life is 130°C (microorganism *Geogemma barossii 121*) (Kashefi and Lovley, 2003). Current environmental and theoretical studies suggest that the upper limit of life might lay near 150°C, due primarily to the instability of macromolecules above this temperature (Merino et al., 2019). This study raises a hypothesis that proteins may sustain even higher temperatures when in certain local environment such as minerals. Further experiment is needed to test this hypothesis.

At last, several interesting questions remain to be explored. Are the proteins such as enzymes extracted from the biominerals still be active to catalyze reactions after the heat treatment? How extreme is the extent of proteins can be preserved in biominerals? Can this preservation effect be applied to other biominerals such as bone and teeth? What is the mechanism of protein protection in biominerals?

CONCLUSION

Although toasted abalone shells (200°C, 300°C for 10 min) have altered microstructure and composition in the nacre tablets, many proteins can still be extracted and identified from shells and maintain certain bioactivities. Nearly 60% of proteins (e.g., hemocyanin, carbonic anhydrase, Lustrin A, actin, tubulin) can still be identified from shells after 300°C treatment revealed by proteomics analysis. The well-preserved proteins may be due to the incorporation of proteins inside the crystal lattices of nacre tablets. This study has some implications in several aspects such as protein storage at high temperatures, palaeoproteomics in archeology, and food nutrients.

DATA AVAILABILITY STATEMENT

The datasets presented in this study can be found in online repositories. The names of the repository/repositories and accession number(s) can be found below: ProteomeXchange (accession: PXD030901).

AUTHOR CONTRIBUTIONS

CL conceived the project. XJ and CL performed the experiments. CL and JH analyzed the data and wrote the manuscript. All authors revised the manuscript.

FUNDING

CL gratefully acknowledges the support of Natural Science Foundation of Jiangsu Province BK20210363, the Fundamental Research Funds for the Central Universities B200201065, and the Jiangsu Innovation Talent Program JSSCBS20210250. JH gratefully acknowledges the National Natural Science Foundation of China Grant 42106091.

ACKNOWLEDGMENTS

We thank Dingfei Yan and Haiteng Deng in Center of Protein Analysis Technology, Tsinghua University, for MS analysis.

SUPPLEMENTARY MATERIAL

The Supplementary Material for this article can be found online at: https://www.frontiersin.org/articles/10.3389/fmars.2022.850120/full#supplementary-material

REFERENCES

Abelson, P. H. (1957). Some aspects of paleobiochemistry. *Ann. N.Y. Acad. Sci.* 69, 276–285. doi: 10.1111/j.1749-6632.1957.tb49663.x

Addadi, L., Joester, D., Nudelman, F., and Weiner, S. (2006). Mollusk shell formation: a source of new concepts for understanding biomineralization processes. *Chem. Eur. J.* 12, 980–987. doi: 10.1002/chem.200500980

Albéric, M., Caspi, E. N., Bennet, M., Ajili, W., Nassif, N., Azaïs, T., et al. (2018). Interplay between calcite, amorphous calcium carbonate, and intracrystalline organics in sea urchin skeletal elements. *Cryst. Grow. Des.* 18, 2189–2201. doi: 10.1021/acs.cgd.7b01622

Balmain, J., Hannoyer, B., and Lopez, E. (1999). Fourier transform infrared spectroscopy (FTIR) and X-ray diffraction analyses of mineral and organic matrix during heating of mother of pearl (nacre) from the shell of the mollusc Pinctada maxima. *J. Biomed. Mater. Res.* 48, 749–754. doi: 10.1002/(sici)1097-4636(1999)48:5<749::aid-jbm22>3.0.co;2-p

Baynes, B. M., Wang, D. I. C., and Trout, B. L. (2005). Role of arginine in the stabilization of proteins against aggregation. *Biochemistry* 44, 4919–4925. doi: 10.1021/bi047528r

Bischof, J. C., and He, X. (2006). Thermal stability of proteins. *Ann. N.Y. Acad. Sci.* 1066, 12–33.

Cappellini, E., Welker, F., Pandolfi, L., Ramos-Madrigal, J., Samodova, D., Ruther, P. L., et al. (2019). Early Pleistocene enamel proteome from Dmanisi resolves Stephanorhinus phylogeny. *Nature* 574, 103–107. doi: 10.1038/s41586-019-1555-y

Cardoso, J. C. R., Ferreira, V., Zhang, X., Anjos, L., Félix, R. C., Batista, F. M., et al. (2019). Evolution and diversity of alpha-carbonic anhydrases in the mantle of the Mediterranean mussel (Mytilus galloprovincialis). *Sci. Rep.* 9:10400. doi: 10.1038/s41598-019-46913-2

Collins, M. J., Westbroek, P., Muyzer, G., and De Leeuw, J. W. (1992). Experimental evidence for condensation reactions between sugars and proteins in carbonate skeletons. *Geochim. Cosmochim. Acta* 56, 1539–1544. doi: 10.1016/0016-7037(92)90223-6

Demarchi, B., Hall, S., Roncal-Herrero, T., Freeman, C. L., Woolley, J., Crisp, M. K., et al. (2016). Protein sequences bound to mineral surfaces persist into deep time. *eLife* 5:e17092. doi: 10.7554/eLife.17092

Fujita, T., Ohue, T., Fujii, Y., Miyauchi, A., and Takagi, Y. (1996). Heated oyster shell-seaweed calcium (AAA Ca) on osteoporosis. *Calcified Tissue Int.* 58, 226–230. doi: 10.1007/BF02508640

Hendy, J., Welker, F., Demarchi, B., Speller, C., Warinner, C., and Collins, M. J. (2018). A guide to ancient protein studies. *Nat. Ecol. Evol.* 2, 791–799.

Kashefi, K., and Lovley, D. R. (2003). Extending the upper temperature limit for life. *Science* 301, 934–934. doi: 10.1126/science.1086823

Le Roy, N., Jackson, D. J., Marie, B., Ramos-Silva, P., and Marin, F. (2014). The evolution of metazoan α-carbonic anhydrases and their roles in calcium carbonate biomineralization. *Front. Zool.* 11:75. doi: 10.1186/s12983-014-0075-8

Li, H., Xin, H. L., Kunitake, M. E., Keene, E. C., Muller, D. A., and Estroff, L. A. (2011). Calcite prisms from mollusk shells (Atrina Rigida): swiss-cheese-like organic–inorganic single-crystal composites. *Adv. Funct. Mater.* 21, 2028–2034.

Liao, Z., Bao, L.-F., Fan, M.-H., Gao, P., Wang, X.-X., Qin, C.-L., et al. (2015). In-depth proteomic analysis of nacre, prism, and myostracum of *Mytilus* shell. *J. Proteomics* 122, 26–40. doi: 10.1016/j.jprot.2015.03.027

Liu, C., and Zhang, R. (2021). Biomineral proteomics: a tool for multiple disciplinary studies. *J. Proteomics* 238:104171. doi: 10.1016/j.jprot.2021.104171

Liu, C., Du, J., Xie, L., and Zhang, R. (2017). Direct observation of nacre proteins in the whole calcite by super-resolution microscopy reveals diverse occlusion patterns. *Cryst. Grow Des.* 17, 1966–1976.

Liu, C., Ji, X., Huang, J., Wang, Z., Liu, Y., and Hincke, M. T. (2021). Proteomics of shell matrix proteins from the cuttlefish bone reveals unique evolution for cephalopod biomineralization. *ACS Biomater. Sci. Eng.* Online ahead of print, doi: 10.1021/acsbiomaterials.1c00693

Liu, C., Li, S., Kong, J., Liu, Y., Wang, T., Xie, L., et al. (2015). In-depth proteomic analysis of shell matrix proteins of Pinctada fucata. *Sci. Rep.* 5:17269. doi: 10.1038/srep17269

Liu, Z., Xu, X., and Tang, R. (2016). Improvement of biological organisms using functional material shells. *Adv. Funct. Mater.* 26, 1862–1880.

Macías-Sánchez, E., Willinger, M. G., Pina, C. M., and Checa, A. G. (2017). Transformation of ACC into aragonite and the origin of the nanogranular structure of nacre. *Sci. Rep.* 7:12728. doi: 10.1038/s41598-017-12673-0

Mann, K., Cerveau, N., Gummich, M., Fritz, M., Mann, M., and Jackson, D. J. (2018). In-depth proteomic analyses of Haliotis laevigata (greenlip abalone) nacre and prismatic organic shell matrix. *Proteome Sci.* 16:11. doi: 10.1186/s12953-018-0139-3

Marie, B., Joubert, C., Tayalé, A., Zanella-Cléon, I., Belliard, C., Piquemal, D., et al. (2012). Different secretory repertoires control the biomineralization processes of prism and nacre deposition of the pearl oyster shell. *Proc. Natl. Acad. Sci. U.S.A.* 109, 20986–20991. doi: 10.1073/pnas.1210552109

Marin, F. (2020). Mollusc shellomes: past, present and future. *J. Struct. Biol.* 212:107583. doi: 10.1016/j.jsb.2020.107583

Marin, F., Luquet, G., Marie, B., and Medakovic, D. (2007). Molluscan shell proteins: primary structure, origin, and evolution. *Curr. Top. Dev. Biol.* 80, 209–276. doi: 10.1016/S0070-2153(07)80006-8

Merino, N., Aronson, H. S., Bojanova, D. P., Feyhl-Buska, J., Wong, M. L., Zhang, S., et al. (2019). Living at the extremes: extremophiles and the limits of life in a planetary context. *Front. Microbiol.* 10:780. doi: 10.3389/fmicb.2019.00780

Miyamoto, H., Miyashita, T., Okushima, M., Nakano, S., Morita, T., and Matsushiro, A. (1996). A carbonic anhydrase from the nacreous layer in oyster pearls. *Proc. Natl. Acad. Sci. U.S.A.* 93, 9657–9660. doi: 10.1073/pnas.93.18.9657

Moreira, A., Lawson, D., Onyekuru, L., Dziemidowicz, K., Angkawinitwong, U., Costa, P. F., et al. (2021). Protein encapsulation by electrospinning and electrospraying. *J. Controlled Release* 329, 1172–1197. doi: 10.1016/j.jconrel.2020.10.046

Nassif, N., Pinna, N., Gehrke, N., Antonietti, M., Jäger, C., and Cölfen, H. (2005). Amorphous layer around aragonite platelets in nacre. *Proc. Natl. Acad. Sci. U.S.A.* 102, 12653–12655. doi: 10.1073/pnas.0502577102

Pokroy, B., Fitch, A. N., Marin, F., Kapon, M., Adir, N., and Zolotoyabko, E. (2006). Anisotropic lattice distortions in biogenic calcite induced by intra-crystalline organic molecules. *J. Struct. Biol.* 155, 96–103. doi: 10.1016/j.jsb.2006.03.008

Pokroy, B., Quintana, J. P., Caspi, E. A. N., Berner, A., and Zolotoyabko, E. (2004). Anisotropic lattice distortions in biogenic aragonite. *Nat. Mater.* 3, 900–902. doi: 10.1038/nmat1263

Rae Cho, K., Kim, Y.-Y., Yang, P., Cai, W., Pan, H., Kulak, A. N., et al. (2016). Direct observation of mineral–organic composite formation reveals occlusion mechanism. *Nat. Commun.* 7:10187. doi: 10.1038/ncomms10187

Sakalauskaite, J., Andersen, S. H., Biagi, P., Borrello, M. A., Cocquerez, T., Colonese, A. C., et al. (2019). 'Palaeoshellomics' reveals the use of freshwater mother-of-pearl in prehistory. *eLife* 8:e45644. doi: 10.7554/eLife.45644

Sakalauskaite, J., Mackie, M., Taurozzi, A. J., Collins, M. J., Marin, F., and Demarchi, B. (2021). The degradation of intracrystalline mollusc shell proteins: a proteomics study of Spondylus gaederopus. *BBA Proteins Proteom.* 1869:140718. doi: 10.1016/j.bbapap.2021.140718

Shen, X., Belcher, A. M., Hansma, P. K., Stucky, G. D., and Morse, D. E. (1997). Molecular cloning and characterization of Lustrin A, a matrix protein from shell and pearl nacre of Haliotis rufescens. *J. Biol. Chem.* 272, 32472–32481. doi: 10.1074/jbc.272.51.32472

Song, X., Liu, Z., Wang, L., and Song, L. (2019). Recent advances of shell matrix proteins and cellular orchestration in marine molluscan shell biomineralization. *Front. Mar. Sci.* 6:41. doi: 10.3389/fmars.2019.00041

Vagenende, V., Yap, M. G. S., and Trout, B. L. (2009). Mechanisms of protein stabilization and prevention of protein aggregation by glycerol. *Biochemistry* 48, 11084–11096. doi: 10.1021/bi900649t

Wang, X., Xiao, Y., Hao, H., Zhang, Y., Xu, X., and Tang, R. (2018). Therapeutic potential of biomineralization-based engineering. *Adv. Ther.* 1:1800079.

Weiner, S., Lowenstam, H. A., and Hood, L. (1976). Characterization of 80-million-year-old mollusk shell proteins. *Proc. Natl. Acad. Sci. U.S.A.* 73, 2541–2545. doi: 10.1073/pnas.73.8.2541

Welker, F., Collins, M. J., Thomas, J. A., Wadsley, M., Brace, S., Cappellini, E., et al. (2015). Ancient proteins resolve the evolutionary history of Darwin's South American ungulates. *Nature* 522, 81–84. doi: 10.1038/nature14249

Welker, F., Ramos-Madrigal, J., Kuhlwilm, M., Liao, W., Gutenbrunner, P., De Manuel, M., et al. (2019). Enamel proteome shows that Gigantopithecus was an early diverging pongine. *Nature* 576, 262–265. doi: 10.1038/s41586-019-1728-8

Wiemann, J., Fabbri, M., Yang, T.-R., Stein, K., Sander, P. M., Norell, M. A., et al. (2018). Fossilization transforms vertebrate hard tissue proteins into N-heterocyclic polymers. *Nat. Commun.* 9:4741. doi: 10.1038/s41467-018-07013-3

Zhang, J., Pritchard, E., Hu, X., Valentin, T., Panilaitis, B., Omenetto, F. G., et al. (2012). Stabilization of vaccines and antibiotics in silk and eliminating the cold chain. *Proc. Natl. Acad. Sci. U.S.A.* 109, 11981–11986. doi: 10.1073/pnas.1206210109

Conflict of Interest: The authors declare that the research was conducted in the absence of any commercial or financial relationships that could be construed as a potential conflict of interest.

Publisher's Note: All claims expressed in this article are solely those of the authors and do not necessarily represent those of their affiliated organizations, or those of the publisher, the editors and the reviewers. Any product that may be evaluated in this article, or claim that may be made by its manufacturer, is not guaranteed or endorsed by the publisher.

frontiers | Frontiers in Marine Science

ORIGINAL RESEARCH
published: 13 April 2022
doi: 10.3389/fmars.2022.850653

The Lysosome Origin of Biosilica Machinery in the Demospongiae Model *Petrosia ficiformis* (Poiret, 1789)

Marina Pozzolini[1], *Ivan Mikšík*[2], *Stefano Ghignone*[3], *Caterina Oliveri*[1], *Eleonora Tassara*[1] *and Marco Giovine*[1]*

[1] Department of Earth, Environment and Life Science, University of Genova, Genova, Italy, [2] Institute of Physiology of the Czech Academy of Sciences, Praha, Czechia, [3] Institute for Sustainable Plant Protection – SS Turin, CNR, Torino, Italy

The silicification mechanism in sponges is a biologically controlled process where the complex and amazing shape of spicules is the result of the hierarchical assembly of silicon particles to form a composite structure with organic compounds, mainly constituted by proteins. In this work, using an integrated approach of transcriptomic and proteomic analysis, we describe the protein content of sponge spicules in the marine demosponge *Petrosia ficiformis* (Poiret, 1789). Proteins from spicules were obtained *via* an ammonium fluoride extraction procedure to remove the inorganic silica followed by SDS-PAGE electrophoresis. The resulting data of LC-MS/MS analysis of the extracted SDS-PAGE bands were then processed with the MASCOT software to search against a database consisting of transcripts and predicted proteins of *P. ficiformis*. The results revealed a very heterogeneous group of 21 proteins, including silicatein beta, different isoforms of cathepsins, proteins with strong homologies with enzymes like sulphatases, glycosidases, lipid-related proteins, phosphatases, and some others with unknown function. Most of the proteins found here have structures and domains attributable to lysosomes enzymes and for this reason it could be related to these cellular structures the evolutionary origin of the biosilica machinery in sponges.

Keywords: marine sponges, *Petrosia ficiformis*, biosilica, spicules, lysosomes, silicatein, cathepsins

OPEN ACCESS

Edited by:
Rebecca Metzler,
Colgate University, United States

Reviewed by:
Manuel Maldonado,
Center for Advanced Studies of Blanes (CSIC), Spain
Maria Costantini,
Anton Dohrn Zoological Station, Italy
Katsuhiko Shimizu,
Tottori University, Japan

***Correspondence:**
Marco Giovine
mgiovine@unige.it

Specialty section:
This article was submitted to Marine Molecular Biology and Ecology, a section of the journal Frontiers in Marine Science

Received: *08 January 2022*
Accepted: *14 March 2022*
Published: *13 April 2022*

Citation:
Pozzolini M, Mikšík I, Ghignone S, Oliveri C, Tassara E and Giovine M (2022) The Lysosome Origin of Biosilica Machinery in the Demospongiae Model Petrosia ficiformis (Poiret, 1789). Front. Mar. Sci. 9:850653. doi: 10.3389/fmars.2022.850653

INTRODUCTION

Sponges are very simple and ancient animals, but they have a remarkably complex genetic and molecular organisation (Sebé-Pedrós et al., 2018; Musser et al., 2021). The presence of sponge fossils from more than 600 million years makes palaeontologists consider this phylum as the oldest animal group still living on the earth (Erwin et al., 2011). Sponges are pluricellular organisms with a simple body structure not organised in specialised tissues or organs (Simpson, 1984). Nevertheless, the evolution from unicellular to multi-cellular animals needed a relevant implementation of gene regulation mechanisms (Brunet and King, 2017). Amazingly, there are many molecular analogies between the highly evolved multi-cellular animals and the simple multi-cellular sponges. The presence of RNA based regulatory factors like long noncoding RNA (Gaiti et al., 2018), or signal

cascade translation systems based on inflammatory pathway response (Pozzolini et al., 2016; Pozzolini et al., 2017) and growth factors (Pozzolini et al., 2019) are examples showing the great molecular similitudes between sponges and other higher animals. The simplicity of sponges' body, the direct contact of their cells with the external environment (sponges filter water that permeates in all the body, through a very well organised channels system) and their sessile status induced on the other hand the need to protect from micro-organisms infections and from other animals' predation. This requirement is managed by the production of a great amount and variety of natural compounds, mainly supplied by symbiotic microorganisms (Brinkmann et al., 2017). All these features make sponges "unique" in the animal kingdom: a fascinating balancing of body simplicity and molecular complexity.

One of the most peculiar aspects of sponges is the structural organisation of their skeleton. The sponge body is supported by organic extracellular matrix (mainly collagen or/and "spongin" in some cases mixed with chitin) (Pozzolini et al., 2012; Ehrlich et al., 2018; Jesionowski et al., 2018) and in many species by inorganic structures called spicules, formed by amorphous silicon dioxide or, in Calcispongiae, calcium carbonate (Simpson, 1984; Ehrlich et al., 2011). Siliceous spicules have different shapes and dimensions with an extremely ordered organisation at a nanometre level (Şen et al., 2016). Biosilica is produced by Hexactinellida, by many Demospongiae and by some Homoscleromorpha (Simpson, 1984). There are many studies on the structural organisation and chemical composition of the biomaterial forming sponge spicules (see for overview Schoeppler et al., 2017; Wysokowski et al., 2018; Görlich et al., 2020; Pisera et al., 2021) and at present time, it seems clear that the features and the properties of biosilica depend on the composition of this material. Sponge biosilica is, in fact, a composite material where organic biomolecules contribute to its synthesis in environmental conditions, to the shape determination of spicules and to their technological properties (Khrunyk et al., 2020), but it is not easy at all to study the dynamics of spicule building. To satisfy this need, a multidisciplinary approach is necessary. Advanced material science technology to analyse in detail the structure and the properties of biosilica and good animal and cellular models to explain the molecular and genetic rules of spicule building are both necessary. At present, Hexactinellida have been mainly studied by material scientists: the production of large and long spicules (up to 2 meters long in *Monoraphis chuni*) (Müller et al., 2007; Ehrlich et al., 2008; Pisera et al., 2021) and their intriguing technological properties as optic fibre (Cattaneo-Vietti et al., 1996), were the main reasons for the choice of this class of animals. Demospongiae are instead approached by sponge cell biologists and molecular biologists, for the possibility to manage in controlled environment living animals and their sponge cell culture (Valisano et al., 2006; Pozzolini et al., 2014). It is also now clear that Hexactinellida and Demospongiae composite silica-based spicules apparently have common features but also very relevant differences in their composition (Müller et al., 2011; Shimizu et al., 2015). Definitively, many questions are still open to understand exhaustively the biological rules of biosilica production. Specifically, in Demospongiae, siliceous spicules are most commonly formed by monoaxonic or tetraxonic needle-like structures, from some μm to 1-2 mm long (Hooper and Van Soest, 2002). In the Demospongiae *Tethya aurantium* was for the first time sequenced and cloned silicatein, one key protein involved in the biosilicification process (Shimizu et al., 1998; Cha et al., 1999). In this last two decades, many studies approached from different points of view the role of silicatein in Demospongiae silica biosynthesis as well as its biotechnological applications (for an exhaustive and complete review see Shimizu and Morse, 2018) and animals and 3D cells models have been also developed to study the dynamics of spicule formation (Müller et al., 2006; Valisano et al., 2012; Müller et al., 2013a). In all these works, silicatein was indicated as the main molecular actor of biosilica formation. Silicatein is indeed a very peculiar protein: it has a remarkable sequence homology with the lysosomal protease family of cathepsins, but it is water-insoluble, and it has an enzymatic active site with serine in substitution to cysteine (Shimizu and Morse, 2018). Its insolubility, due to a higher number of hydrophobic regions and different post-translational modifications compared to cathepsins (Armirotti et al., 2009), determines its self-assemblage properties (Murr and Morse, 2005). This evidence clearly supports the assumption of the structural role of silicatein in the formation of the axial filament of spicules as well as its being a key component of biosilica composite structure. The enzymatic active site suggests, in the meantime, the catalytic role of this protein, even if there is not a definitive agreement among scientists on the mechanism. At present time, in fact, two main hypotheses are supported in literature: silicatein as an enzyme able to catalyse the biosilica precipitation from some organosilicon compound (Cha et al., 1999; Povarova et al., 2018a; Povarova et al., 2018b) and silicatein as enzyme able to catalyse the biosilica polymerisation from orthosilicic acid (Müller et al., 2013b). Both models are apparently sustainable and silicatein can be considered one of the major contributors for the biosilica condensation in environmental conditions. It is much more difficult to understand the molecular keys of spicule growth and spicule shape control. Silicatein probably is involved in growth control and shaping, mainly in Demospongiae (Müller et al., 2009), but many other components like collagen, chitin and actin seem to play some fundamental roles (Ehrlich, 2010; Ehrlich et al., 2010; Ehrlich et al., 2016; Ehrlich et al., 2022).

A recent work (Riesgo et al., 2015) further considered the scenario concerning silicatein: a comparative analysis of transcriptomes and genomes datasets puts clearly in evidence that not all biosilica forming sponges have/express silicatein genes. Mainly Hexactinellida and Homoscleromorpha sponges do have not this protein and some silica forming Demospongiae apparently do not have silicatein (*Chondrilla nucula*). In addition, sponges that do not produce biosilica seem to express silicatein genes. Another interesting and relevant aspect is the evidence of a remarkable expression of cathepsins (specifically cathepsins B and L) in biosilica forming sponges, whose functional role is to be better clarified (Riesgo et al., 2015). In this key work the authors, on the basis of transcriptome analysis

results, hypothesized a lysosomal origin of the "silica deposition vesicle" of Demospongiae (Riesgo et al., 2015). It is evident that the biosilicification mechanisms in sponges are far to be understood, and one of the major gaps of knowledge to be filled is to improve the description of the organic content of Demospongiae spicules.

To accomplish this objective, in the present work, an integrated transcriptome and proteome analysis is proposed as a strategy. Here, for the first time, using as experimental model the species *Petrosia ficiformis*, is described the protein content of Demospongiae spicules by a proteomics analysis followed with protein sequence identification based on the transcriptome dataset matching.

MATERIALS AND METHODS

Protein Extraction

The proteins contained inside the silica spicules were extracted accordingly to the previously described method (Armirotti et al., 2009). Briefly (**Scheme 1**), 5 g of dry of *P. ficiformis* collected in the Ligurian sea have been cut into small pieces of 1 cm^3 and dissolved in 500 mL of cold HNO_3/H_2SO_4 (1:4) over night. The cleaned spicules have been washed several times in distilled water until the pH was above 6, then once in 100% ethanol and finally air-dried. 1 g of clean spicules were dissolved into 100 ml of 2 M HF/8 M NH_4F (pH 5) at room temperature until the complete silica solubilization. The sample was then dialysed (10,000 MWCO Da) against 5 L of Milli-Q water for 4 hours at 4°C (five changes). At the end, the insoluble organic component was recovered by centrifugation for 30 minutes at 18,000 x *g* at 4°C, resuspended in 3 mL of Milli-Q water and stored at -20°C until use. To check the presence of proteins in the soluble fraction, the supernatant was ten-fold concentrated and analysed using the method of Bradford assay (Bradford, 1976).

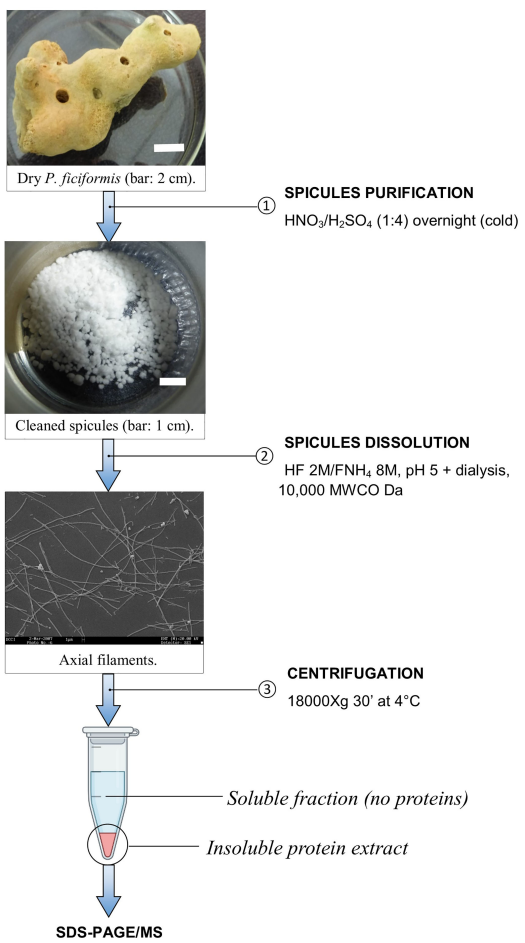

SCHEME 1 | Axial filament purification.

To evaluate the total protein concentration in the insoluble fraction, 0.5 mL of protein suspension were centrifuged for 5 minutes at 18,000 x *g* at room temperature. The supernatant was discarded, and the insoluble pellet was dissolved in 0.5 mL of 8 M urea. The protein content was evaluated by Bradford assay.

Electrophoretic Analysis

20 μg of silica spicule protein extract were separated by SDS-PAGE according to Laemmli (Laemmli, 1970) on 10 × 8 cm vertical 12% polyacrylamide gel at a constant amperage. After electrophoresis, proteins were fixed in 40% ethanol/10% acetic acid for 60 min, washed twice with Milli-Q water, stained over night with colloidal Coomassie blue (Neuhoff et al., 1988) and destained several hours in 5% acetic acid.

Band Cutting and Trypsin Digestion

Protein bands were manually excised from the gel and digested by trypsin at 37°C overnight (Shevchenko et al., 2006). Gel pieces were destained with acetonitrile, reduced in 10 mM DTT/100 mM ammonium bicarbonate and alkylated with 100 mM iodoacetamide/100 mM ammonium bicarbonate. The peptide samples were extracted after digestion by sonicating for 10 minutes, then vacuum dried.

Analysis of Tryptic Digests With LC-MS/MS

The LC-MS/MS method used was similar to the previously published one (Mikšík et al., 2018). The ultrahigh resolution MaXis Q-TOF (quadrupole – time of flight) mass spectrometer (Bruker Daltonics, Bremen, Germany) was coupled by nanoelectrosprayer to nano-HPLC system Proxeon Easy-nLC (Proxeon, Odense, Denmark). All controlled software was from Bruker Daltonics: HyStar (v. 3.2) micrOTOF-control (v. 3.0), ProteinScape (v. 3.0) and DataAnalysis (v. 4.0).

Three microliters of the peptide mixture were injected into trap column NS-MP-10 Biosphere C18 (particle size: 5 μm, pore size: 12 nm, length: 20 mm, inner diameter: 100 μm) and analysed by analytical column NS-AC-11-C18 Biosphere C18 column (particle size: 5 μm, pore size: 12 nm, length: 150 mm, inner diameter: 75 μm), both manufactured by NanoSeparations (Nieuwkoop, Holland).

The separation of peptides was achieved *via* a linear gradient between mobile phase A (water) and B (acetonitrile), both

containing 0.1% (v/v) formic acid. Separation was started by running the system with 5% mobile phase B, followed by a gradient elution to 30% B at 70 min. The next step was a gradient elution to 50% B in 10 min and then a gradient to 100% B in 10 min. Finally, the column was eluted with 100% B for 30 min. Equilibration between the runs was achieved by washing the column with 5% mobile phase B for 10 min. The flow rate was 0.25 µL/min, and the column was held at ambient temperature (25°C).

On-line nano-electrospray ionization (easy nano-ESI) was used in positive mode. The ESI voltage was set to +4.5 kV, scan time: 3 Hz. Operating conditions: drying gas (N_2): 4 L/min; drying gas temperature: 180°C; nebulizer pressure: 100 kPa. Experiments were performed by scanning from 50 to 2200 m/z. The reference ion used (internal mass lock) was a monocharged ion of C24H19F36N3O6P3 (m/z 1221.9906). Mass spectra corresponding to each signal from the total ion current chromatogram were averaged, enabling an accurate molecular mass determination. All LC-MS and LC-MS/MS analyses were done in duplicate.

Database Searching

Data were processed using ProteinScape software v. 3.0.0.446 (Bruker Daltonics, Bremen, Germany).

Proteins were identified by correlating tandem mass spectra to the putatively predicted proteins from *P. ficiformis* transcriptome, using the MASCOT searching engine v. 2.3.0 (http://www.matrixscience.com). Trypsin was chosen as the enzyme parameter. Extract likely coding regions and predicted candidate peptides from transcripts of *P. ficiformis* (Riesgo et al., 2014) were identified with TRANSDECODER V.5.2.0 (https://github.com/TransDecoder/TransDecoder), as previously described in Pozzolini et al., 2019. Three missed cleavages were allowed, and an initial peptide mass tolerance of ±15.0 ppm was used for MS and ±0.03 Da for MS/MS analysis. Variable modifications were set; proline and lysine were allowed to be hydroxylated, methionine oxidated, whereas asparagine and glutamine deamidated and cysteine carboxymethylated or carbamidomethylated. The monoisotopic peptide charge was set to 1+, 2+, and 3+. The Peptide Decoy option was selected during the data search process to remove false-positive results. Only significant hits were accepted (MASCOT score ≥80 for proteins and MASCOT score ≥20 for peptides), however, all peptides and proteins were additionally manually validated.

RESULTS

Analysis of the Proteins on Gel

The strategy of analysis of the proteins extracted from the biosilica was based on HF/NH_4F dissolution and dialysis against water (see **Scheme 1**). This approach allows the recovery of an insoluble fraction of organic material. Typically, 2 g of *P. ficiformis* clean silica spicules yielded 2 mg of total protein extract. The soluble fraction after dialysis (10,000 MWCO Da) was ten-fold concentrated and the total protein contents was assayed. No evident presence of protein was detected in the soluble fraction. The not-soluble organic residue was resuspended and 20 µg of proteins were run on a 12% polyacrylamide gel, coloured with colloidal Coomassie blue. **Figure 1** shows the results, protein separation was not easy, and a substantial swiping of proteins is evident. The scarce solubility of the protein mixture and, probably, the presence of some silica residues could be the cause. We cut anyway the gel into 9 small slices to perform MS analysis of the protein content inside it.

Identification and Characterisation of Proteins

The LC-MS/MS analysis raw data obtained from the organic components of *P. ficiformis* spicules were processed with the MASCOT software to search against a database consisting of transcript and predicted proteins of the above-mentioned sponge species here used as a study model.

To our knowledge, here we are showing the first case of description of the overall protein content of demosponge biosilica. In our experimental conditions, 21 proteins with a high level of confidence have been identified in their primary structure. The remarkable swiping of proteins in gel electrophoresis reflected its effects in the analytical results, where peptides of the same protein were found in different positions. In **Supplementary File 1**, the peptides and the related proteins found in the nine slices are listed. The main concentration of different proteins is present on slice 6. Some proteins are present in many or all slices (for example protein 1) while others are better distributed in the lower part of the gel.

All raw data are available on the following public repository: https://doi.org/10.5281/zenodo.6033766. **Table 1** summarizes

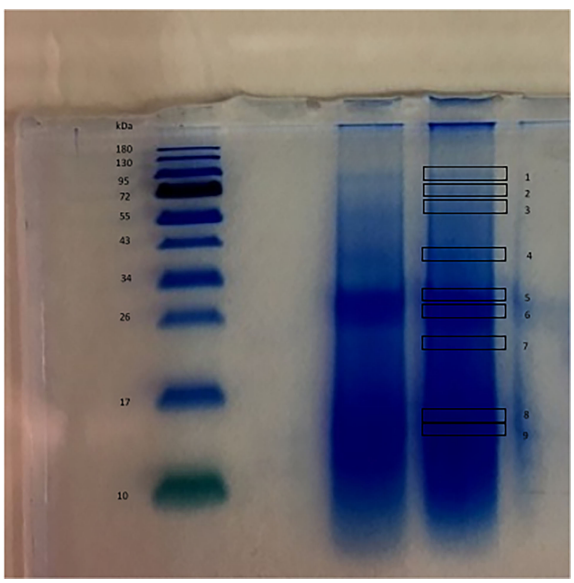

FIGURE 1 | SDS-PAGE of the 20 µg of proteins extracted from the spicules of *P. ficiformis*. MW standard (left) and two lines containing the proteins extracted (on the right). The numbers indicate the position of the slices cut for proteins extraction and MS analysis.

TABLE 1A | List of proteins extracted from siliceous spicules of *P. ficiformis*.

Protein	peptides found	Contig	Status	AA	Predicted MW	Predicted pI
1	8	contig_2646	internal	405	45572.15	5.85
2	4	contig_3602	5'-partial	463	50256.01	5.39
3	3	contig_5736	internal	254	28039.31	5.22
4	2	contig_7487	internal	436	48710.29	4.96
5	5	contig_3356	complete	340	37361.94	6.12
6	4	contig_6478	complete	334	37069.50	5.16
7	3	contig_910	complete	239	27596.48	4.65
8	2	contig_457	5'-partial	179	20405.85	4.98
9	1	contig_5079	3'-partial	155	17868.96	5.93
10	1	contig_6226	3'-partial	155	17960.19	5.93
11	4	contig_3070	5'-partial	146	16175.06	6.17
12	4	contig_313	5'-partial	338	37003.89	5.37
13	4	contig_183	complete	152	17240.88	7.10
14	4	contig_8334	5'-partial	720	not calculated	n.c.
15	4	contig_1552	complete	340	38075.11	5.49
16	4	contig_17524	3'-partial	171	19212.98	6.42
17	1	contig_9379	internal	120	12431.88	4.28
18	2	contig_2754	complete	362	40277.86	5.69
19	2	contig_7352	5'-partial	111	12782.54	7.77
20	1	contig_2762	5'-partial	418	45731.84	5.42
21	4	contig_3044	complete	165	17728.46	4.46

TABLE 1B | Main conserved domains.

Protein	Main domains/regions found	Signal peptide	Transmembran domains	Similar protein	Lisosome related
1	Pfam sulfatase	Y	N	Arylsulfatase A-like (E-value 1e-179). Acc. Num. XP_003387234.3	Y
2	SCOP d1iexa1 (E-value 2.00e-08), Pfam Glyco_hydro_3_C (E-value 1.4e-40), Fibronectin type III-like dom. (E-value 0.000822)	N	N	Probable beta-D-xylosidase 2 (E-value 1e-156), fam. Glycosil hydrolase. Acc.Num. XP_021231341.1	Y
3	Pfam Glyco_hydro_3 (E-value 4.1e-38)	N	N	Probable beta-D-xylosidase 6 (E-value 3e-126), fam. Glycosil hydrolase.Acc. Num. XP_028393522.1	Y
4	Pfam Glycohydro_20b2 (E-value 1.1e-17), Pfam Glyco_hydro_20 (E-value 3.1e-77)	N	N	Beta-hexosaminidase subunit alpha-like isoform X4 (E-value 0.0). Acc. Num. XP_019855835.1	Y
5	Inhibitor_I29 (E-value 7.58e-20), Pept_C1 (E-value 2.59e-93)	Y	N	Silicatein (E-value 0.0). Acc. Num. Q6YD92.1	Not known
6	Inhibitor_I29 (E-value 1.47e-17), Pept_C1 (E-value 1.59e-111)	Y	N	Cathepsin L1-like (E-value 1e-152). Acc.Num. XP_003383726.1	Y
7	PTPc_DSPc (E-value 1.84)	Y	N	Tyrosine phosphatase (E-value 1e-26). Acc. Num. KYR01243.1	Y
8	No domains predicted	N	N	UDP-N-acetylglucosamine–LPS N-acetylglucosamine transferase (E-value 2.4). Acc. Num. KYR01243.1	
9	Inhibitor_I29 (E-value 4e-19), Pfam Peptidase_C1 (E-value 2.7e-14)	Y	N	Cathepsin L1-like (E-value 2e-33). Acc. Num. XP_003385986.1	Y
10	Inhibitor_I29 (E-value1.6e-18), Pfam Peptidase_C1 (E-value 2.8e-13)	Y	N	Cathepsin L1-like (E-value5e-34). Acc. Num. XP_003385986.1	Y
11	No domains predicted	N	N	Cation-dependent mannose-6-phosphate receptor (E-value 0,75). Acc. Num. XP_011403525.2	Y
12	Pfam: Propeptide_C1 (E-value 2.4e-14), Pept_C1 (E-value 2.34e-91)	Y	N	Cathepsin B-like ((E-value 6e-166). Acc. Num. XP_003388842.1	Y
13	MD-2-related lipid-recognition (ML) (E-value 0.0000946)	N	N	NPC2-like protein (E-value 5e-06) Acc. Num. KOX75392.1	Y
14	Three PbH1 (E-values 4.11e+03, 2.02e+03, 2.46e+02)	N	N	Possible polysaccharide lyase.	Not known
15	Pfam Metallophos (E-value 1.2e-18)	N	Y	Tartrate-resistant acid phosphatase type 5-like isoform X3 (E-value 8e-153). Acc. Num. XP_019850709.1	Y
16	Pfam DUF547 (E-value 1.1e-06)	Y	N	Lipoprotein precursor (E-value 5e-15). Acc. Num. ARU54835.1	Not known
17	Pfam Aps (E-value 9.5e-26)	N	N	Lysosomal aspartic protease-like (E-value 1e-33), Cathepsin-D (E-value 8e-33)	Y

(Continued)

TABLE 1B | Continued

Protein	Main domains/regions found	Signal peptide	Transmembran domains	Similar protein	Lisosome related
18	Inhibitor_I29 (E-value 1.68e-12), Pept_C1 (E-value 2.73e-92)	N	N	Digestive cysteine proteinase 1-like (E-value 1e-153)	Y
19	No domains predicted	N	N	Mannose 6-phosphate receptor domain (Phyre2)	Y
20	Three PQQ (E-values 410, 41.9, 23.7)	Y	N	Pyrrolo-quinoline quinone (E-value 7e-05)	Not known
21	MD-2-related lipid-recognition (ML) (E-value 5.46e-19)	Y	N	Putative phosphatidylglycerol/phosphatidylinositol transfer protein (E-value 3e-34)	Y

Proteins extracted from the 9 gel slices. ***A****: number of peptides identified, the corresponding contig and relative status, number of Amino acids, predicted MW and PI. More details are reported in* ***Supplementary Files 1****,* ***3****.* ***B****: main conserved domains (see* ***Figure 3****), presence of signal peptide and/or transmembrane domains, similar proteins, and correlation with lysosome environment. More details are reported in* ***Supplementary File 3****.*

the structural features of the identified proteins and their theoretical functions based on the predicted primary structure and of the analysis of conserved domains. Spicule protein content in our findings can be divided into functional categories, as shown in **Figure 2**. Most proteins seem remarkably related to the lysosome environment (see **Table 1**) and only a few are of unknown origin. In **Figure 3** the specific domains of each protein characterized in this work are shown. A detailed overview of the results includes the presence of *P. ficiformis* silicatein beta, as expected (protein 5, **Table 1**). Silicatein peptides were detected from bands 4 to 9 with a typical swiping. With similar swiping behaviour, five different proteases of the cathepsin family (proteins 6, 9, 10, 12, 17) have been identified. The larger part of the other proteins in the list has remarkable similarity with lysosome-related polypeptides. Protein 1 shows strong homology with the aryl-sulphatase family enzymes, as in the predicted primary structure are present all the amino acids of the active site included the typical Cys residue normally modified in C-alpha-formyl-glycine by formyl-generating enzymes of rough endoplasmic reticulum. These enzymes are known to catalyse the cleavage of sulphate esters mainly in glycolipids and glycosaminoglycans inside lysosomes (Thompson and Daniel, 1988). Proteins 2, 3, and 4 have their primary structure remarkably homologs to glycosyl hydrolase family 3 (protein 2 and 3), and beta-hexosaminidase group (protein 4). All these proteins are involved in the catabolism of glycosphingolipids inside lysosomes (Ryckman et al., 2020). In mammalians, it is known that glycosyl hydrolases of family 3 are involved in the transxylosylation of cholesterol in lysosomes. Beta-hexosaminidases are involved in the hydrolysis of terminal N-acetyl-D-hexosamine residues in N-acetyl-β-D-hexosaminides and it is typically expressed inside lysosomes for glycosphingolipids catabolism. In the same "group" of proteins related to lipid catabolism it is included protein 13, whose primary sequence is remarkably related to cholesterol transporter from lysosomes as well as protein 21 whose lipid recognition domain is typically present in phosphatidylinositol/phosphatidylglycerol transfer protein, fundamentally found inside lysosomes. The 21 proteins list also includes proteins with possible mannose-6P receptor domain, characteristic of protein trafficking to lysosomes (proteins 11 and 19), in particular interacting with cathepsins and hexosaminidases (Staudt et al., 2017). Tyrosine phosphatases and tartrate-resistant phosphatases (proteins both present in the lysosome environment) are also represented in this very complex pattern of biomolecules found inside biosilica. The list includes

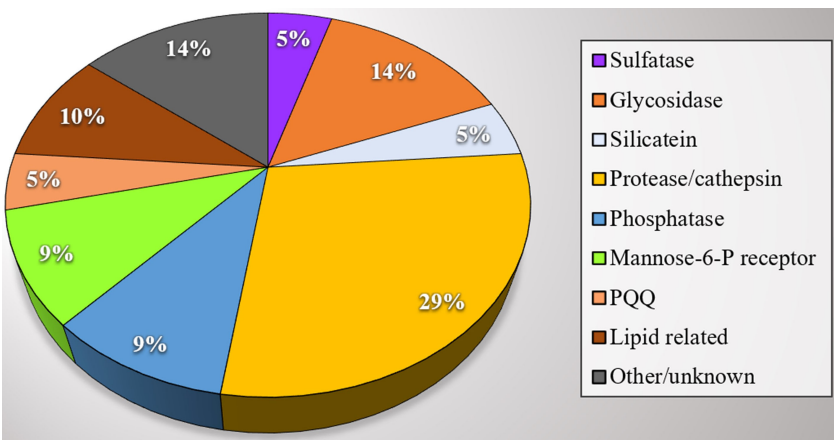

FIGURE 2 | Proteins extracted from *P. ficiformis* biosilica. Subdivision of proteins in activity categories. Each colour is representative of a category group and the numbers inside the circle areas indicate the numbers of proteins of the same category.

one protein with a domain corresponding to pyrrole quinoline quinone dehydrogenase. This protein is not typical of the lysosome environment. Finally, three unknown proteins are also represented.

DISCUSSION

The biomineralization process in Porifera still has several unsolved questions. Most of the scientists studying biosilicification in demosponges attribute to silicatein a key role in the skeleton forming process, (see the recent review, Shimizu and Morse, 2018). Indeed, silicatein is very abundant inside spicules and its distribution is intimately mixed with the inorganic part to form a composite (Müller et al., 2013; Shimizu and Morse, 2018). Nevertheless, at present, this peculiar protein, with its proposed double role (enzymatic and structural), in our opinion is not enough to fully explain all the aspects of the biosilicification mechanism in these animals. In biological controlled biomineralization, the molecular actors are very numerous, involving proteins and other biomacromolecules (polyamines for example), whose role in the process is often very difficult to identify (Wysokowski et al., 2018). Proteomic analysis in these cases give a relevant contribution to identify the various component of an organic compound and in the past, it has already been used to describe the post-translational modification of silicatein (Armirotti et al., 2009). In the present study we have improved the strategy looking again inside spicules using an integrated approach based on proteome and transcriptome analysis. Recently, similar methodologies were used to describe the organic matrix content of diatoms and corals (Kotzsch et al., 2016; Peled et al., 2020).

Using this technique, we have found together with silicatein a list of proteins until now never described before inside biosilica. The *P. ficiformis* transcriptome availability (Riesgo et al., 2014) allowed in the present work a fine identification of proteins inside spicules (**Figure 2** and **Table 1**) but, for many of them, it is not easy to attempt a possible explanation of their role in the process. Previous scientific publications demonstrate that the spicule formation in demosponges begins inside cells, but it continues outside, and the process pass through the production of biosilica building units inside cells successively secreted outside (Wang et al., 2011). A last century study (Lévi, 1963) and a more recent description of spicule formation by Schröder and co-workers (Schröder et al., 2007) show the formation of specific intracellular vesicles in which biosilica is precipitated. In accordance with what is described in many other biomineralization processes, the building blocks are organized intracellularly in appropriate compartments where the chemical conditions for mineral precipitation are created and maintained. The ultrastructural analysis reported in the work of Schröder and co-workers gives some explanation of the process: silica is released in extracellular granules outside the sclerocite; these granules are rich in silica, and they are named silicasomes. Morphological analysis showed that silicasomes positively react with antibodies against silicatein, and this reaction allowed to follow the intra- and extracellular evolution of these organelles (Schröder et al., 2007). This evidence suggests a subcellular process involving some systems related to endosome/exosome or microvesicles pathways. Furthermore, it is known that the acidic environment favours biosilica precipitation (Shimizu et al., 2001) and, for this reason, also lysosome or lysosome-related organelles may be involved in the formation of silicasomes. In this conceptual direction it is also placed the co-expression of silicatein and cathepsins recently described in sponge tissues by Riesgo and co-authors, suggesting some specific roles of these proteins in the biomineralisation process as well as clearly remarking the hypothesis of a silica deposition environment of lysosomal origin (Riesgo et al., 2015). In this study Riesgo and co-authors made an accurate analysis of the evolution of cathepsin genes among metazoan and many of them have been described in sponges. Specifically, in *P. ficiformis* transcriptome they documented the expression of Cathepsin B, L, and D as well as 4 different silicateins (Riesgo et al., 2015). This information derives from comparative transcriptomic analysis of sponges, without any further insights into protein localisation. Our findings demonstrate, for the first time, the presence of cathepsins and silicatein inside the biosilica, fully confirming the lysosome hypothesis. Additionally, in our research results many other proteins are for the first time identified inside *P. ficiformis* spicules after inorganic silica removal, almost half of them is provided with a signal peptide and shows a strong similarity with proteins normally found inside lysosomes (see **Table 1**). The scenario is however very complex: from one hand the common lysosomal origin of the majority of proteins listed in our work is something coherent and easy to discuss on the basis of the morphological evidence published (Schröder et al., 2007) and of the evolutionary study cited (Riesgo et al., 2015); on the other hand, it becomes very difficult to attribute a specific role in the process for many of the proteins here identified.

The first aspect emerging from the analysis of biosilica protein content shown in **Table 1** of our results is the demonstration of presence of some isoforms of cathepsin family together with silicateins, data strongly congruent with the previously published hypothesis of Riesgo (Riesgo et al., 2015). Riesgo and co-authors already suggested a possible role of cathepsins in the biosilification process (Riesgo et al., 2015). In particular, the fact that one silicatein cited by Riesgo has cysteine inside the active site is suggestive of a more complex scenario where some cathepsins can play some role (Riesgo et al., 2015). In addition, it also known that mutants of L cathepsin produced in recombinant systems confirm the existence of structural issues other than active sites in the biosilica biosynthesis in silicateins and cathepsins (Fairhead et al., 2008). On these bases, the changing of the active site from Cys to Ser is not the only molecular key of the mechanism, but also other regions of the protein can have a role in the catalysis and/or in the biosilica organisation and/or in other proteins assembling (Fairhead et al., 2008). Despite all these considerations, definitively it is not easy to define the exact role of various cathepsins in the biosilica precipitation environment: one additional possibility we suggest is that they can be involved in the specific activation of other proteins relevant in the process (*i.e.*, cleaving signal peptides and\or regulatory peptides) but more studies must be performed to better understand if these roles are related only to catalysis or also to structural organisation. Only future experimental

demonstrations based on selective enzymatic inhibition or gene silencing approach in cellular models can give a final answer.

In **Figure 3** and in **Supplementary File 2** are listed some details of domain and sequence homology also of the other proteins found and, in the results, we have underlined the enzymatic roles of the homologous polypeptides as described in other organisms. But, if it is difficult the possible explanation of cathepsins and silicateins roles, the discussion of other proteins here found in the biosilica matrix only on the basis of their structural similarity with other well-known proteins of lysosomal origin is much more speculative. A further interesting aspect is that many of these proteins have well defined enzymatic domains (see **Figure 3**), differently from other situations (corals and diatoms for example), where a considerable numbers of proteins with structural functions and apparently lacking catalytic domains have been found (Ramos-Silva et al., 2013; Kotzsch et al., 2016). In our research results we conversely identified aryl sulphatase, glycosyl hydrolase, beta-hexosaminidase, all typical proteins found inside lysosomes. Also, proteins involved in the lysosome cholesterol transport have been found (see **Table 1A** and **Figure 2**). Only three proteins are of unknown origin, (with some low similarities to acetylglucosamine transferase, polysaccharide lyase and one lipoprotein).

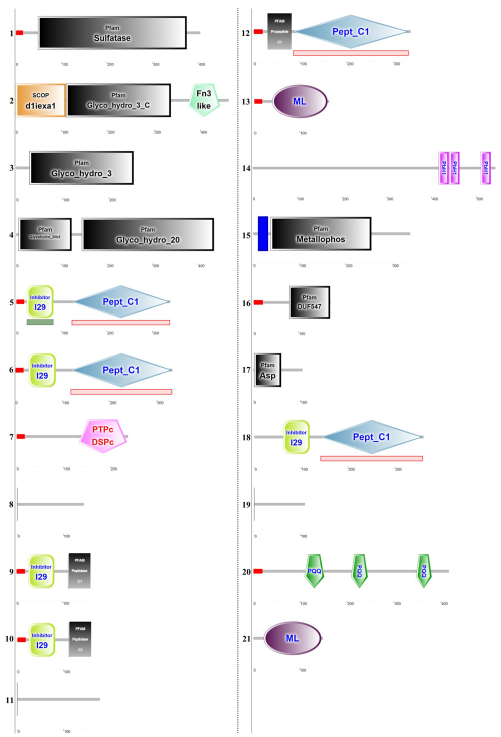

FIGURE 3 | Schematic conserved domain representation of the proteins extracted from the spicules. The analysis was performed using the deduced amino acids sequences obtained after *in silico* translation of contigs correspondent to MS-identified peptides. The conserved domain has been identified using the Simple Modular Architecture Research Tool (SMART) program (http://smart.embl-heidelberg.de/). The detailed legend is reported in **Supplementary File 2**. The domains list is reported in **Table 1**. The contig sequences identified are reported in **Supplementary File 3**.

The presence of enzymes related to glycosaminoglycans (GAGs) and polysaccharides catabolism inside biosilica is indeed intriguing. The sugars, the polyol and the GAGs interaction with silicon recently suggested by Nielsen (Nielsen, 2014) and the regulation of connective tissue formation in mammals influenced by silicon is suggestive of some biochemical mechanism involving silicon and GAGs and other polysaccharides in mammalians (Götz et al., 2019). The presence of these enzymes inside of silica sponge spicules suggest a possible sugars-silicon interaction originally involved in biomineralization. A future explanation of their role can give important answers not only in biosilicification process in sponges but also in cartilage and bone formation in mammalians and humans. The results here shown undoubtedly confirm the lysosome hypothesis since the list of proteins here found are in their majority clearly related to lysosomes, but at the same time opens the door to many unanswered questions, specifically on the metabolic management of silicon inside cells. The silicon uptake in sponges is under the control of specific transporters (Schröder et al., 2004; Maldonado et al., 2020), but the intracellular destiny of silicon is not clear. The hypothesis of one organosilicon compound already emerged from the beginning of studies of silicatein (see Shimizu et al., 1998) but, at the same time no specific ideas have already been confirmed. Bio-organic chemistry works suggested the general possibility to have silica derivatives with organic molecules of biological relevance (Kinrade et al., 1999; Vis et al., 2020). The presence of many enzymes related to sugar metabolism could be suggestive of silicon-organic compounds specifically involved in this process, while cathepsins and silicateins can play a role both in the enzymatic control of biosilica precipitation and in the structural organisation of spicules.

Much more difficult is to give some functional hypothesis of other proteins. Another finding is a protein with pyrrolo-quinoline quinone (PQQ) dehydrogenase domain. This family of proteins are normally present in prokaryotes but recently they have been described also in Eukaryotic, involved in sugars oxidoreductases process (Matsumura et al., 2014).

In this scenario, the apparent absence of silintaphins (Wiens et al., 2009) and galectins (Schröder et al., 2006) is surprising. In the first case, also inside the template transcriptome (Riesgo et al., 2014) we have not found silintaphins. We cannot currently confirm if this is due to incompleteness in transcriptome database used in this study or to some specific genetic differences that occurred in this sponge species. Different considerations should be made regarding galectins. In this second case, in the transcriptome database used, the presence of galectin transcript is confirmed, but any traces of these proteins in the proteomic analysis was not found, despite the presence of galectins in the biosilica matrix was proposed using specific antibodies in a previous work on *S. domuncula* (Schröder et al., 2006). In our experimental conditions, we performed a

strong acid spicules cleaning before silica dissolution. Differently, in the study of Schröder and co-workers the extraction procedure was completely different and milder (Schröder et al., 2006) and maybe some proteins involved in the biosilica building not intimately mixed inside biosilica in our approach can be missed. The methodological approach in the extraction procedure without doubt can affect the results. Here we have used this very strong cleaning process (cold HNO_3/H_2SO_4) of spicules in order to avoid contaminations. MS analysis, in fact, is highly sensitive and it is not easy to evaluate proteins at the quantitative level. This sensitivity on the other hand allows to identify many proteins not found before with different analytical approaches. Here we decide to focus our attention to those proteins very intimately mixed with the inorganic silica lattice.

CONCLUSIONS

Biomineralization in sponges is a process not completely explained. In this work, using a strong spicules cleaning procedure, we have extracted the organic proteinaceous material embedded inside biosilica spicules from the marine sponge *P. ficiformis* and analysed by MS analysis. The results obtained confirmed the hypothesis of lysosome origin of silicasomes, due to the identification of various cathepsins together with silicateins and surprisingly we found many proteins similar to lysosome enzymes, several of them related to polysaccharide and sugar metabolism. Taken together, these results open a new perspective in the study of biosilica forming in demosponges, suggesting a more complex scenario where sugars and maybe lipids can have key roles.

DATA AVAILABILITY STATEMENT

The original contributions presented in the study are publicly available. This data can be found here: https://doi.org/10.5281/zenodo.6033766.

AUTHOR CONTRIBUTIONS

Conceptualization: MP and MG. Methodology: MP, IM, SG, CO, ET, and MG. Investigation: MP, IM, SG, CO, and ET. Writing: MP and MG. Review and editing: MG and ET. Supervision: MP and MG. Funding acquisition: MP, IM, and MG. The manuscript was written through contributions of all authors. All authors have given approval to the final version of the manuscript.

FUNDING

This work was partially supported by University of Genova funds to MP and MG. IM acknowledges funding from the Czech Science Foundation (grant number 20-03899S).

ACKNOWLEDGMENTS

We thank Hermann Ehrlich for the critical reading of the manuscript.

SUPPLEMENTARY MATERIAL

The Supplementary Material for this article can be found online at: https://www.frontiersin.org/articles/10.3389/fmars.2022.850653/full#supplementary-material

REFERENCES

Armirotti, A., Damonte, G., Pozzolini, M., Mussino, F., Cerrano, C., Salis, A., et al. (2009). Primary Structure and Post-Translational Modifications of Silicatein Beta From the Marine Sponge *Petrosia Ficiformis* (Poiret 1789). *J. Proteome Res.* 8, 3995–4004. doi: 10.1021/pr900342y

Bradford, M. M. (1976). A Rapid and Sensitive Method for the Quantitation of Microgram Quantities of Protein Utilizing the Principle of Protein-Dye Binding. *Analytical Biochem.* 72, 248–254. doi: 10.1016/0003-2697(76)90527-3

Brinkmann, C. M., Marker, A., and Kurtböke, Dİ. (2017). An Overview on Marine Sponge-Symbiotic Bacteria as Unexhausted Sources for Natural Product Discovery. *Diversity* 9, 40. doi: 10.3390/d9040040

Brunet, T., and King, N. (2017). The Origin of Animal Multicellularity and Cell Differentiation. *Dev. Cell* 43, 124–140. doi: 10.1016/j.devcel.2017.09.016

Cattaneo-Vietti, R., Bavestrello, G., Cerrano, C., Sarà, M., Benatti, U., Giovine, M., et al. (1996). Optical Fibres in an Antarctic Sponge. *Nature* 383, 397–398. doi: 10.1038/383397b0

Cha, J. N., Shimizu, K., Zhou, Y., Christiansen, S. C., Chmelka, B. F., Stucky, G. D., et al. (1999). Silicatein Filaments and Subunits From a Marine Sponge Direct the Polymerization of Silica and Silicones *In Vitro*. *PNAS* 96, 361–365. doi: 10.1073/pnas.96.2.361

Ehrlich, H. (2010). Chitin and Collagen as Universal and Alternative Templates in Biomineralization. *Int. Geology Rev.* 52, 661–699. doi: 10.1080/00206811003679521

Ehrlich, H., Brunner, E., Simon, P., Bazhenov, V. V., Botting, J. P., Tabachnick, K. R., et al. (2011). Calcite Reinforced Silica–Silica Joints in the Biocomposite Skeleton of Deep-Sea Glass Sponges. *Advanced Funct. Mater.* 21, 3473–3481. doi: 10.1002/adfm.201100749

Ehrlich, H., Deutzmann, R., Brunner, E., Cappellini, E., Koon, H., Solazzo, C., et al. (2010). Mineralization of the Metre-Long Biosilica Structures of Glass Sponges Is Templated on Hydroxylated Collagen. *Nat. Chem.* 2, 1084–1088. doi: 10.1038/nchem.899

Ehrlich, H., Janussen, D., Simon, P., Bazhenov, V. V., Shapkin, N. P., Erler, C., et al. (2008). Nanostructural Organization of Naturally Occurring Composites–Part II: Silica-Chitin-Based Biocomposites. *J. Nanomater.* 2008, 670235. doi: 10.1155/2008/670235

Ehrlich, H., Luczak, M., Ziganshin, R., Mikšík, I., Wysokowski, M., Simon, P., et al. (2022). Arrested in Glass: Actin Within Sophisticated Architectures of Biosilica in Sponges. *Adv. Sci.* 2105059. doi: 10.1002/advs.202105059

Ehrlich, H., Maldonado, M., Parker, A. R., Kulchin, Y. N., Schilling, J., Köhler, B., et al. (2016). Supercontinuum Generation in Naturally Occurring Glass Sponges Spicules. *Advanced Optical Mater.* 4, 1608–1613. doi: 10.1002/adom.201600454

Ehrlich, H., Wysokowski, M., Żółtowska-Aksamitowska, S., Petrenko, I., and Jesionowski, T. (2018). Collagens of Poriferan Origin. *Marine Drugs* 16, 79. doi: 10.3390/md16030079

Erwin, D. H., Laflamme, M., Tweedt, S. M., Sperling, E. A., Pisani, D., and Peterson, K. J. (2011). The Cambrian Conundrum: Early Divergence and Later Ecological Success in the Early History of Animals. *Science* 334, 1091–1097. doi: 10.1126/science.1206375

Fairhead, M., Johnson, K. A., Kowatz, T., McMahon, S. A., Carter, L. G., Oke, M., et al. (2008). Crystal Structure and Silica Condensing Activities of Silicatein α–Cathepsin L Chimeras. *Chem. Commun.* 15, 1765–1767. doi: 10.1039/B718264C

Gaiti, F., Degnan, B. M., and Tanurdžić, M. (2018). Long Non-Coding Regulatory RNAs in Sponges and Insights into the Origin of Animal Multicellularity. *RNA Biol.* 15, 696–702. doi: 10.1080/15476286.2018.1460166

Görlich, S., Samuel, A. J., Best, R. J., Seidel, R., Vacelet, J., Leonarski, F. K., et al. (2020). Natural Hybrid Silica/Protein Superstructure at Atomic Resolution. *PNAS* 117, 31088–31093. doi: 10.1073/pnas.2019140117

Götz, W., Tobiasch, E., Witzleben, S., and Schulze, M. (2019). Effects of Silicon Compounds on Biomineralization, Osteogenesis, and Hard Tissue Formation. *Pharmaceutics* 11, 117. doi: 10.3390/pharmaceutics11030117

Hooper, J. N. A., and Van Soest, R. W. M. (2002). "Class Demospongiae Solla," in *In Systema Porifera: A Guide to the Classification of Sponges;*. Eds. J. N. A. Hooper, R. W. M. Van Soest and P. Willenz (Boston, MA: Springer US), pp 15–pp 51. doi: 10.1007/978-1-4615-0747-5_3

Jesionowski, T., Norman, M., Żółtowska-Aksamitowska, S., Petrenko, I., Joseph, Y., and Ehrlich, H. (2018). Marine Spongin: Naturally Prefabricated 3d Scaffold-Based Biomaterial. *Marine Drugs* 16, 88. doi: 10.3390/md16030088

Khrunyk, Y., Lach, S., Petrenko, I., and Ehrlich, H. (2020). Progress in Modern Marine Biomaterials Research. *Marine Drugs* 18, 589. doi: 10.3390/md18120589

Kinrade, S. D., Del Nin, J. W., Schach, A. S., Sloan, T. A., Wilson, K. L., and Knight, C. T. G. (1999). Stable Five- and Six-Coordinated Silicate Anions in Aqueous Solution. *Science* 285, 1542–1545. doi: 10.1126/science.285.5433.1542

Kotzsch, A., Pawolski, D., Milentyev, A., Shevchenko, A., Scheffel, A., Poulsen, N., et al. (2016). Biochemical Composition and Assembly of Biosilica-Associated Insoluble Organic Matrices From the Diatom Thalassiosira Pseudonana. *J. Biol. Chem.* 291, 4982–4997. doi: 10.1074/jbc.M115.706440

Laemmli, U. K. (1970). Cleavage of Structural Proteins During the Assembly of the Head of Bacteriophage T4. *Nature* 227, 680–685. doi: 10.1038/227680a0

Lévi, C. (1963). Cytologie-Scléroblastes Et Spiculogenèse Chez Une Éponge Siliceuse. *C. R. Hebd. Séances Acad. sci.* 256, 497–498.

Maldonado, M., López-Acosta, M., Beazley, L., Kenchington, E., Koutsouveli, V., and Riesgo, A. (2020). Cooperation Between Passive and Active Silicon Transporters Clarifies the Ecophysiology and Evolution of Biosilicification in Sponges. *Sci. Adv.* 6, 9322. doi: 10.1126/sciadv.aba9322

Matsumura, H., Umezawa, K., Takeda, K., Sugimoto, N., Ishida, T., Samejima, M., et al. (2014). Discovery of a Eukaryotic Pyrroloquinoline Quinone-Dependent Oxidoreductase Belonging to a New Auxiliary Activity Family in the Database of Carbohydrate-Active Enzymes. *PloS One* 9, e104851. doi: 10.1371/journal.pone.0104851.g002

Mikšík, I., Paradis, S., Eckhardt, A., and Sedmera, D. (2018). Analysis of Siamese Crocodile (Crocodylus Siamensis) Eggshell Proteome. *Protein J.* 37, 21–37. doi: 10.1007/s10930-017-9750-x

Müller, W. E. G., Belikov, S. I., Tremel, W., Perry, C. C., Gieskes, W. W. C., Boreiko, A., et al. (2006). Siliceous Spicules in Marine Demosponges (Example *Suberites Domuncula*). *Micron* 37, 107–120. doi: 10.1016/j.micron.2005.09.003

Müller, W. E. G., Eckert, C., Kropf, K., Wang, X., Schloßmacher, U., Seckert, C., et al. (2007). Formation of Giant Spicules in the Deep-Sea Hexactinellid Monorhaphis Chuni (Schulze 1904): Electron-Microscopic and Biochemical Studies. *Cell Tissue Res.* 329, 363–378. doi: 10.1007/s00441-007-0402-x

Müller, W. E. G., Mugnaioli, E., Schröder, H. C., Schloßmacher, U., Giovine, M., Kolb, U., et al. (2013a). Hierarchical Composition of the Axial Filament From Spicules of the Siliceous Sponge *Suberites Domuncula*: From Biosilica-Synthesizing Nanofibrils to Structure- and Morphology-Guiding Triangular Stems. *Cell Tissue Res.* 351, 49–58. doi: 10.1007/s00441-012-1519-0

Müller, W. E. G., Schröder, H. C., Burghard, Z., Pisignano, D., and Wang, X. (2013b). Silicateins-A Novel Paradigm in Bioinorganic Chemistry: Enzymatic Synthesis of Inorganic Polymeric Silica. *Chem. Eur. J.* 19, 5790–5804. doi: 10.1002/chem.201204412

Müller, W. E. G., Wang, X., Chen, A., Hu, S., Gan, L., Schröder, H. C., et al. (2011). "The Unique Invention of the Siliceous Sponges: Their Enzymatically Made Bio-Silica Skeleton," in *Molecular Biomineralization: Aquatic Organisms Forming Extraordinary Materials;*. Ed. W. E. G. Müller (Berlin, Heidelberg: Springer), pp 251–pp 281. doi: 10.1007/978-3-642-21230-7_9

Müller, W. E. G., Wang, X., Cui, F. Z., Jochum, K. P., Tremel, W., Bill, J., et al. (2009). Sponge Spicules as Blueprints for the Biofabrication of Inorganic–Organic Composites and Biomaterials. *Appl. Microbiol. Biotechnol.* 83, 397–413. doi: 10.1007/s00253-009-2014-8

Murr, M. M., and Morse, D. E. (2005). Fractal Intermediates in the Self-Assembly of Silicatein Filaments. *PNAS* 102, 11657–11662. doi: 10.1073/pnas.0503968102

Musser, J. M., Schippers, K. J., Nickel, M., Mizzon, G., Kohn, A. B., Pape, C., et al. (2021). Profiling Cellular Diversity in Sponges Informs Animal Cell Type and Nervous System Evolution. *Science* 374, 717–723. doi: 10.1126/science.abj2949

Neuhoff, V., Arold, N., Taube, D., and Ehrhardt, W. (1988). Improved Staining of Proteins in Polyacrylamide Gels Including Isoelectric Focusing Gels With Clear Background at Nanogram Sensitivity Using Coomassie Brilliant Blue G-250 and R-250. *Electrophoresis* 9, 255–262. doi: 10.1002/elps.1150090603

Nielsen, F. H. (2014). Update on the Possible Nutritional Importance of Silicon. *J. Trace. Elem. Med. Biol.* 28, 379–382.

Peled, Y., Drake, J. L., Malik, A., Almuly, R., Lalzar, M., Morgenstern, D., et al. (2020). Optimization of Skeletal Protein Preparation for LC–MS/MS Sequencing Yields Additional Coral Skeletal Proteins in Stylophora Pistillata. *BMC Mater.* 2, 8. doi: 10.1186/s42833-020-00014-x

Pisera, A., Łukowiak, M., Masse, S., Tabachnick, K., Fromont, J., Ehrlich, H., et al. (2021). Insights Into the Structure and Morphogenesis of the Giant Basal Spicule of the Glass Sponge Monorhaphis Chuni. *Front. Zool.* 18, 58. doi: 10.1186/s12983-021-00440-x

Povarova, N. V., Barinov, N. A., Baranov, M. S., Markina, N. M., Varizhuk, A. M., Pozmogova, G. E., et al. (2018b). Efficient Silica Synthesis From Tetra (Glycerol)Orthosilicate With Cathepsin- and Silicatein-Like Proteins. *Sci. Rep.* 8, 16759. doi: 10.1038/s41598-018-34965-9

Povarova, N. V., Markina, N. M., Baranov, M. S., Barinov, N. A., Klinov, D. V., Kozhemyako, V. B., et al. (2018a). A Water-Soluble Precursor for Efficient Silica Polymerization by Silicateins. *Biochem. Biophys. Res. Commun.* 495, 2066–2070. doi: 10.1016/j.bbrc.2017.12.075

Pozzolini, M., Bruzzone, F., Berilli, V., Mussino, F., Cerrano, C., Benatti, U., et al. (2012). Molecular Characterization of a Nonfibrillar Collagen From the Marine Sponge Chondrosia Reniformis Nardo 1847 and Positive Effects of Soluble Silicates on Its Expression. *Mar Biotechnol.* 14, 281–293. doi: 10.1007/s10126-011-9415-2

Pozzolini, M., Gallus, L., Ghignone, S., Ferrando, S., Candiani, S., Bozzo, M., et al. (2019). Insights Into the Evolution of Metazoan Regenerative Mechanisms: Roles of TGF Superfamily Members in Tissue Regeneration of the Marine Sponge Chondrosia Reniformis. *J. Exp. Biol.* 222, 207894. doi: 10.1242/jeb.207894

Pozzolini, M., Mussino, F., Cerrano, C., Scarfì, S., and Giovine, M. (2014). Sponge Cell Cultivation: Optimization of the Model Petrosia Ficiformis (Poiret 1789). *J. Exp. Marine Biol. Ecol.* 454, 70–77. doi: 10.1016/j.jembe.2014.02.004

Pozzolini, M., Scarfì, S., Gallus, L., Ferrando, S., Cerrano, C., and Giovine, M. (2017). Silica-Induced Fibrosis: An Ancient Response From the Early Metazoans. *J. Exp. Biol.* 220, 4007–4015. doi: 10.1242/jeb.166405

Pozzolini, M., Scarfì, S., Ghignone, S., Mussino, F., Vezzulli, L., Cerrano, C., et al. (2016). Molecular Characterization and Expression Analysis of the First Porifera Tumor Necrosis Factor Superfamily Member and of Its Putative Receptor in the Marine Sponge Chondrosia Reniformis. *Dev. Comp. Immunol.* 57, 88–98. doi: 10.1016/j.dci.2015.12.011

Ramos-Silva, P., Kaandorp, J., Huisman, L., Marie, B., Zanella-Cléon, I., Guichard, N., et al. (2013). The Skeletal Proteome of the Coral Acropora Millepora: The Evolution of Calcification by Co-Option and Domain Shuffling. *Mol. Biol. Evol.* 30, 2099–2112. doi: 10.1093/molbev/mst109

Riesgo, A., Farrar, N., Windsor, P. J., Giribet, G., and Leys, S. P. (2014). The Analysis of Eight Transcriptomes From All Poriferan Classes Reveals Surprising Genetic Complexity in Sponges. *Mol. Biol. Evol.* 31, 1102–1120. doi: 10.1093/molbev/msu057

Riesgo, A., Maldonado, M., López-Legentil, S., and Giribet, G. (2015). A Proposal for the Evolution of Cathepsin and Silicatein in Sponges. *J. Mol. Evol.* 80, 278–291. doi: 10.1007/s00239-015-9682-z

Ryckman, A. E., Brockhausen, I., and Walia, J. S. (2020). Metabolism of Glycosphingolipids and Their Role in the Pathophysiology of Lysosomal Storage Disorders. *Int. J. Mol. Sci.* 21, 6881. doi: 10.3390/ijms21186881

Schoeppler, V., Reich, E., Vacelet, J., Rosenthal, M., Pacureanu, A., Rack, A., et al. (2017). Shaping Highly Regular Glass Architectures: A Lesson From Nature. *Sci. Adv.* 3, 2047. doi: 10.1126/sciadv.aao2047

Schröder, H. C., Boreiko, A., Korzhev, M., Tahir, M. N., Tremel, W., Eckert, C., et al. (2006). Co-Expression and Functional Interaction of Silicatein With Galectin: Matrix-Guided Formation of Siliceous Spicules in the Marine Demosponge Suberites Domuncula. *J. Biol. Chem.* 281, 12001–12009. doi: 10.1074/jbc.M512677200

Schröder, H. C., Natalio, F., Shukoor, I., Tremel, W., Schloßmacher, U., Wang, X., et al. (2007). Apposition of Silica Lamellae During Growth of Spicules in the Demosponge Suberites Domuncula: Biological/Biochemical Studies and Chemical/Biomimetical Confirmation. *J. Struct. Biol.* 159, 325–334. doi: 10.1016/j.jsb.2007.01.007

Schröder, H. C., Perović-Ottstadt, S., Rothenberger, M., Wiens, M., Schwertner, H., Batel, R., et al. (2004). Silica Transport in the Demosponge Suberites Domuncula: Fluorescence Emission Analysis Using the PDMPO Probe and Cloning of a Potential Transporter. *Biochem. J.* 381, 665–673. doi: 10.1042/BJ20040463

Sebé-Pedrós, A., Chomsky, E., Pang, K., Lara-Astiaso, D., Gaiti, F., Mukamel, Z., et al. (2018). Early Metazoan Cell Type Diversity and the Evolution of Multicellular Gene Regulation. *Nat. Ecol. Evol.* 2, 1176–1188. doi: 10.1038/s41559-018-0575-6

Şen, E. H., Ide, S., Bayari, S. H., and Hill, M. (2016). Micro- and Nano-Structural Characterization of Six Marine Sponges of the Class Demospongiae. *Eur. Biophys. J.* 45, 831–842. doi: 10.1007/s00249-016-1127-0

Shevchenko, A., Tomas, H., Havli, J., Olsen, J. V., and Mann, M. (2006). In-Gel Digestion for Mass Spectrometric Characterization of Proteins and Proteomes. *Nat. Protoc.* 1, 2856–2860. doi: 10.1038/nprot.2006.468

Shimizu, K., Amano, T., Bari, M. R., Weaver, J. C., Arima, J., and Mori, N. (2015). Glassin, a Histidine-Rich Protein From the Siliceous Skeletal System of the Marine Sponge Euplectella, Directs Silica Polycondensation. *PNAS* 112, 11449–11454. doi: 10.1073/pnas.1506968112

Shimizu, K., Cha, J., Stucky, G. D., and Morse, D. E. (1998). Silicatein α: Cathepsin L-Like Protein in Sponge Biosilica. *PNAS* 95, 6234–6238. doi: 10.1073/pnas.95.11.6234

Shimizu, K., Del Amo, Y., Brzezinski, M. A., Stucky, G. D., and Morse, D. E. (2001). A Novel Fluorescent Silica Tracer for Biological Silicification Studies. *Chem. Biol.* 8, 1051–1060. doi: 10.1016/s1074-5521(01)00072-2

Shimizu, K., and Morse, D. E. (2018). "Chapter Fourteen - Silicatein: A Unique Silica-Synthesizing Catalytic Triad Hydrolase From Marine Sponge Skeletons and Its Multiple Applications," in *Methods in Enzymology*, vol. Vol. 605 . Ed. B. S. Moore. Cambridge. Massachussets USA: (Academic Press), pp 429–pp 455. Available at: http://doi.org/10.1016/bs.mie.2018.02.025.

Simpson, T. L. (1984). *The Cell Biology of Sponges*. Ed. T. L. Simpson (New York, NY: Springer), 216–254. Available at: https://doi.org/10.1007/978-1-4612-5214-6_5.

Staudt, C., Puissant, E., and Boonen, M. (2017). Subcellular Trafficking of Mammalian Lysosomal Proteins: An Extended View. *Int. J. Mol. Sci.* 18, 47. doi: 10.3390/ijms18010047

Thompson, D. B., and Daniel, W. L. (1988). Comparative Biochemistry of Mammalian Arylsulfatases A and B. *Comp. Biochem. Physiol. B* 90, 823–831. doi: 10.1016/0305-0491(88)90340-9

Valisano, L., Bavestrello, G., Giovine, M., Arillo, A., and Cerrano, C. (2006). Seasonal Production of Primmorphs From the Marine Sponge Petrosia Ficiformis (Poiret 1789) and New Culturing Approaches. *J. Exp. Marine Biol. Ecol.* 337, 171–177. doi: 10.1016/j.jembe.2006.06.030

Valisano, L., Pozzolini, M., Giovine, M., and Cerrano, C. (2012). "Biosilica Deposition in the Marine Sponge Petrosia Ficiformis (Poiret 1789): The Model of Primmorphs Reveals Time Dependence of Spiculogenesis," in *Ancient Animals, New Challenges: Developments in Sponge Research*. Eds. M. Maldonado, X. Turon, M. Becerro and M. J. Uriz (Dordrecht: Springer Netherlands), 259–273. doi: 10.1007/978-94-007-4688-6_22

Vis, B. M., Wen, J., Mellerup, S. K., Merchant, R. D., Mawhinney, R. C., and Kinrade, S. D. (2020). Silicon Forms a Rich Diversity of Aliphatic Polyol Complexes in Aqueous Solution. *J. Am. Chem. Soc.* 142, 9188–9202. doi: 10.1021/jacs.9b10701

Wang, X., Wiens, M., Schröder, H. C., Schloßmacher, U., Pisignano, D., Jochum, K. P., et al. (2011). Evagination of Cells Controls Bio-Silica Formation and Maturation During Spicule Formation in Sponges. *PloS One* 6 (6), e20523. doi: 10.1371/journal.pone.0020523

Wiens, M., Bausen, M., Natalio, F., Link, T., Schlossmacher, U., and Müller, W. E. G. (2009). The Role of the Silicatein-α Interactor Silintaphin-1 in Biomimetic Biomineralization. *Biomaterials* 30, 1648–1656. doi: 10.1016/j.biomaterials.2008.12.021

Wysokowski, M., Jesionowski, T., and Ehrlich, H. (2018). Biosilica as a Source for Inspiration in Biological Materials Science. *Am. Mineral* 103, 665–691. doi: 10.2138/am-2018-6429

Conflict of Interest: The authors declare that the research was conducted in the absence of any commercial or financial relationships that could be construed as a potential conflict of interest.

Publisher's Note: All claims expressed in this article are solely those of the authors and do not necessarily represent those of their affiliated organizations, or those of the publisher, the editors and the reviewers. Any product that may be evaluated in this article, or claim that may be made by its manufacturer, is not guaranteed or endorsed by the publisher.

frontiers | Frontiers in Marine Science

ORIGINAL RESEARCH
published: 10 May 2022
doi: 10.3389/fmars.2022.862929

Characterization of the Myostracum Layers in Molluscs Reveals a Conservative Shell Structure

Wentao Dong[1†], *Jingliang Huang*[1†], *Chuang Liu*[1], *Hongzhong Wang*[1], *Guiyou Zhang*[1], *Liping Xie*[1] *and Rongqing Zhang*[1,2*]

[1] Ministry of Education (MOE) Key Laboratory of Protein Sciences, School of Life Sciences, Tsinghua University, Beijing, China,
[2] Zhejiang Provincial Key Laboratory of Applied Enzymology, Yangtze Delta Region Institute of Tsinghua University, Jiaxing, China

Molluscs produce rigid shells to protect their soft bodies from predators and physiochemical violations. The soft tissues attach to shells *via* the myostracum layer (also called adductor muscle scar, AMS) which bears tremendous contract force and is of vital importance to the survival of the molluscs. Considering the prevalence of tissue-shell attachment in molluscs, we speculate that certain homology may be shared among varied species. To test this speculation, scanning electron microscopy and Raman spectrum were applied to analyze the microstructure and calcium carbonate polymorphs of the myostracum in most of the molluscan classes. It was found that all the tested molluscan classes and genera contain similar columnar prisms which aligned vertically and were composed of aragonite. Moreover, this structure was found in ammonoid fossils dating back to the Permian period. Such peculiar mineral structure may contribute to the loading contract force, thus being evolutionally conservative among varied species and for hundreds of millions of years. Our study underscores the vital impact of physiological functions on the evolution of the shell structure.

Keywords: molluscs, AMS, myostracum layer, microstructure, aragonite

OPEN ACCESS

Edited by:
Shiguo Li Research Center for Eco-environmental Sciences (CAS), China

Reviewed by:
Xiaotong Wang, Ludong University, China
Michio Suzuki, The University of Tokyo, Japan

****Correspondence:***
Rongqing Zhang
rqzhang@mail.tsinghua.edu.cn

[†]These authors have contributed equally to this work

Specialty section:
This article was submitted to Marine Molecular Biology and Ecology, a section of the journal Frontiers in Marine Science

Received: *26 January 2022*
Accepted: *25 March 2022*
Published: *10 May 2022*

Citation:
Dong W, Huang J, Liu C, Wang H, Zhang G, Xie L and Zhang R (2022) Characterization of the Myostracum Layers in Molluscs Reveals a Conservative Shell Structure. Front. Mar. Sci. 9:862929. doi: 10.3389/fmars.2022.862929

INTRODUCTION

Biominerals formed by living organisms exhibit excellent mechanical properties such as strength and stiffness (Raut et al., 2020). These organic-inorganic composites play a role in body supporting, protection, feeding, and directionality (Weaver et al., 2010; Addadi and Weiner, 2014; Guzman-Lastra et al., 2016; Deng et al., 2020). Characterizing biominerals with specific functions is fundamental for understanding how organisms make use of inorganic materials to orchestrate exquisite structures, and in return one can be inspired to build artificial analogous materials.

Molluscs can produce myriad shells with extraordinary morphology and microstructures. For example, one of the most adopted microstructures in Gastropoda is crossed-lamellar structure, and similar structure has been reprinted in plywood to improve its fracture resistance (Pramreiter et al., 2020). Nacre, also called mother of pearl, has been found in pearl oyster, mussel, abalone, and nautilus genera (Jackson et al., 1988; Sun and Bhushan, 2012). The salient feature of nacre is the mortar-and-brick arrangement consisting of stacking sheets of aragonite tablets separated by organic matrix, which leads to the dissipation of stress and results in extremely high toughness

(Jackson et al., 1988; Marin et al., 2008; Huang et al., 2019; Deng et al., 2020). Therefore, intensive efforts have been made to reproduce nacre-like biomaterials to gain strength (Mao et al., 2016; Raut et al., 2020). Other microstructures, such as prismatic layer and homogeneous fine grains have been found in various molluscan species (Bayerlein et al., 2014; Checa et al., 2016; Zhu et al., 2016).

Most molluscan shells form exoskeletons except that some Cephalopoda genera have evolved endoskeletons inside the soft tissue (Mao et al., 2021). For the exoskeleton, the soft tissue is attached to the mineral surface *via* the myostracum layer which is also called the adductor muscle scar. The adductor muscle is responsible for shell closure in the Bivalvia and retraction of the soft body (such as in the Gastropoda) (Gilman, 2007; Castro-Claros et al., 2021). Therefore, the myostracum layer mainly bears internal stress compared with the outer shell layers which withstand external damages. The microstructure of the myostracum has been reported in several bivalves (Nakahara and Bevelander, 1970; John and Taylor, 1973; Zhu et al., 2016) and Gastropoda (Suzuki et al., 2010). In previous studies, myostracum layers were usually described as "prismatic aragonite" (Weiner, 1989); however, exceptions were reported (Zhu et al., 2016). In addition, it remains unclear whether all molluscs share similar features in this particular shell layer.

Since all the molluscs with exoskeleton have myostracum layers of similar function, we speculate that some similarities may be shared among various species. In this study, shell samples from five classes (Polyplacophora, Bivalvia, Gastropoda, Cephalopoda, and Scaphopoda) were collected and examined using scanning electronic microscopy and Raman spectroscopy. It was found that myostracum layers in these classes share a striking similarity in both microstructure and mineralogy, indicating that these shell structures are evolutionarily conserved or resulted from convergent evolution for similar functions.

MATERIALS AND METHODS

Sample Collection

Abalone *Haliotis discus*, Arcoida *Tegillarca granosa*, mussels *Mytilus edulis* and *Pinna rudis*, scallop *Chlamys farreri,* Pacific oyster *Crassostrea gigas*, Unionoida *Cristaria plicata*, clams *Ruditapes philippinarum*, *Sinonovacula constricta* (Lamarck), *Dosinorbis japonica* and *Panopea abrupta* were purchased from a seafood market in Beijing City, China. Limpets *Cellana toreuma* were collected from the intertidal zone of Zhoushan Island in Zhejiang Province, China. Unionoida *Hyriopsis cumingii* was provided by Shanghai Ocean University in Shanghai City, China. Pearl oyster *Pinctada fucata* were purchased from Guangdong Ocean University in Guangdong Province, China. Mud snail *Bullacta exarata* (Philippi, 1848), chiton *Ischnochiton comptus* (Gould) and tusk shell *Pictodentalium vernerdi* were collected from the Eastern China Sea. Fresh water snails *Bradybaena ravida* (Benson) were collected in Zhuhai City of Guangdong Province, China. *Ammonoidea* sp. was collected in Pearl River Delta of Guangdong Province, China. All samples were living animals except the *P. vernerdi* and *Ammonoidea* sp. which were shell specimens. The soft tissues were removed by scalpel, the shells were thoroughly washed with deionized water, and air-dried.

Scanning Electronic Microscopy

The shell samples were cut into small pieces with scissors and a diamond cutter. The resultant shell samples were coated with gold in a vacuum sputtering apparatus and examined with a scanning electronic microscope (FEI Quanta 200) with an accelerating voltage of 30 kV in a high vacuum mode.

Raman Spectrum Analysis

Laser Raman Spectroscopy (Evolution, 111 HORIBA, France) was performed to determine the calcium carbonate polymorph with the detected wavenumber ranging from 100 cm^{-1} to 1200 cm^{-1}. For each shell sample tested, more than three sites were randomly selected in the myostracum layers or the shell layers underlying myostracum layers.

RESULTS

Living molluscs contain seven classes, namely Aplacophora, Polyplacophora, Monoplacophora, Gastropoda, Scaphopoda, Cephalopoda, and Bivalvia. Since most of the bivalves have adductor muscle for the shell closure, we first examined the myostracum layer in this class. Interestingly, all the studied species contained a similar microstructure at the muscle-shell attachment (**Figure 1** and **Supplementary Figure 1**). Though there exist some slight variations, the myostracum layers in bivalves consisted of simple regular prisms. Raman spectra showed that the mineral counterparts were all aragonite (**Table 1** and **Supplementary Figures 3**, **7**). Most of the species have a monolayer myostracum (**Figures 1A**–**T**). However, multilayered myostracum was observed in the Myoida *P. abrupta* (**Figures 1U, V**), thus forming regular alternate microstructure of prisms and fine granules. Usually, the height of the prismatic myostracum is 10-20 μm, except those in the *P. abrupta* and Arcoida *T. granosa* could reach more than 50 μm or even 200 μm in the latter (**Figures 1W, X**). Moreover, the myostracum in *T. granosa* differed from others in that the columns were much larger. The columns could reach 10 μm in diameter, while those in other species were only around 1 μm (e.g., in the *C. gigas* and *P. fucata*).

The marvelous similarity of the myostracum layers among various bivalves suggest that such microstructure might have evolved in the ancient bivalve ancestor and remained conservative once that occurred. When considering the vast diversity of the shell layers underlying the myostracum, such a scheme was more convincing. In mussels, pearl oyster, and Unionoida, the shell layer underlying the myostracum adopt a sheet nacreous microstructure, and in scallop and Pacific oyster, foliated sheets could be seen, while both fine-grained homogeneous structure and crossed lamellar were found in clams (**Table 1**). Moreover, the polymorphs of these shell

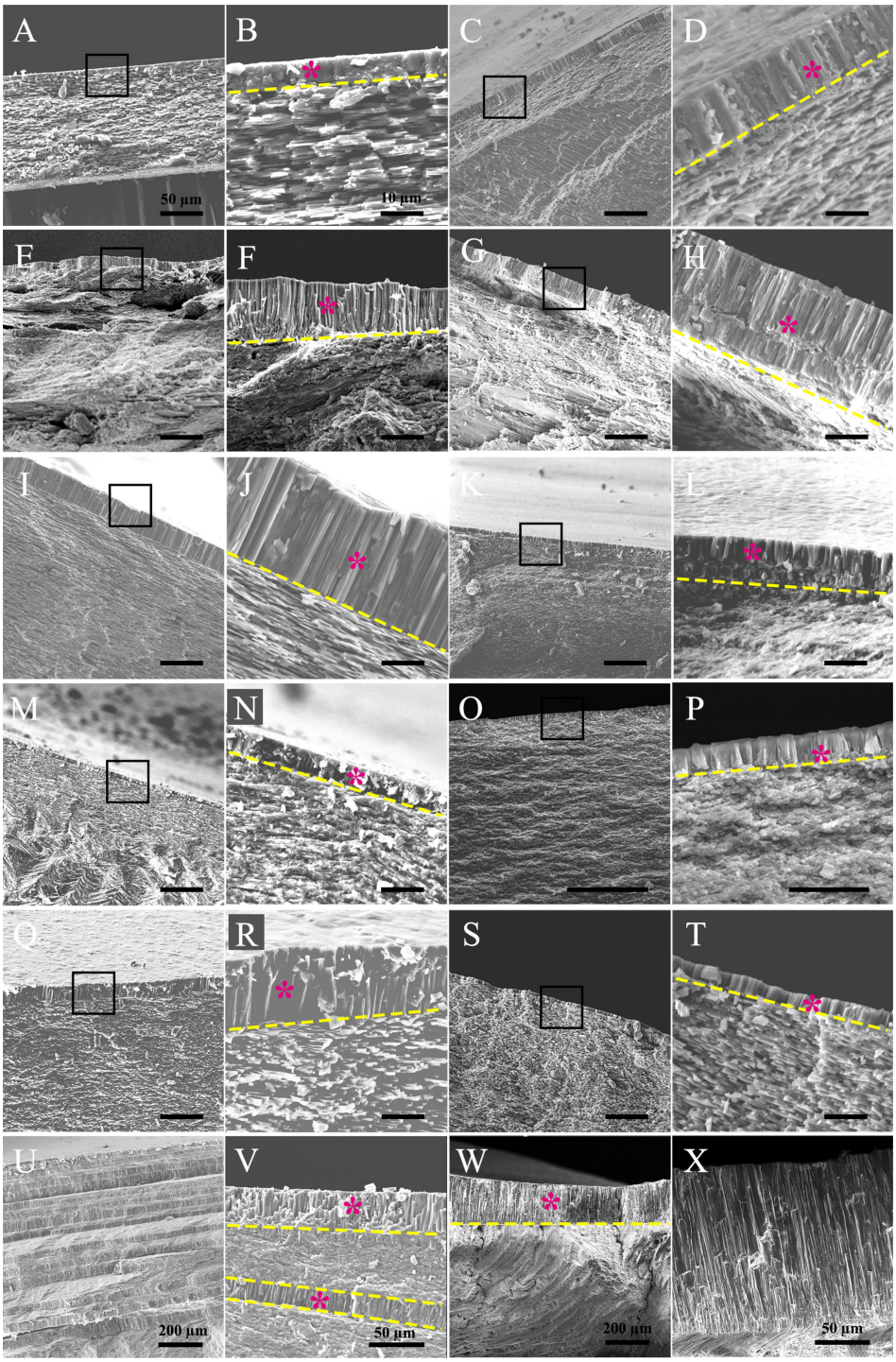

FIGURE 1 | Microstructure of the myostracum layer in bivalve molluscs. **(A, B)** pen shell *Pinna rudis*; **(C, D)** mussel *Mytilus edulis*; **(E, F)** Pacific oyster *Crassostrea gigas*; **(G, H)** scallop *Chlamys farreri*; **(I, J)** pearl oyster *Pinctada fucata*; **(K, L)** Dosiniinae *Dosinorbis japonica*; **(M, N)** solen *Sinonovacula constricta* (Lamarck); **(O, P)** clam *Ruditapes philippinarum*; **(Q, R)** freshwater mussel *Cristaria plicata*; **(S, T)** freshwater mussel *Hyriopsis cumingii*; **(U, V)** geoduck *Panopea abrupta*; **(W, X)** ark shell *Tegillarca granosa*. In each sample, the latter image is the magnification of the former (black boxes), except that in **(U–X)**, different positions of myostracum layers are shown. The myostracum layer is indicated by a purple star, and the boundary between the myostracum and the underlying shell layers is indicated by the yellow dashed line. The scale bar is 50 μm in the former image of each sample and 10 μm in the latter (magnification) as shown in **(A, B)**, except **(U–X)** which are marked in the images.

TABLE 1 | Summary of the microstructure and texture of tested shell layers in bivalves.

Species	Myostracum layer		Beneath the myostracum layer	
	Microstructure	Polymorph	Microstructure	Polymorph
Arcoida				
Tegillarca granosa	Radially elongate simple prismatic	Aragonite	Simple crossed lamellar	Aragonite
Mytioida				
Mytilus edulis	Regular simple prismatic	Aragonite	Sheet nacreous	Aragonite
Pinna rudis	Regular simple prismatic	Aragonite	Sheet nacreous	Aragonite
Pterioida				
Pinctada fucata	Regular simple prismatic	Aragonite	Sheet nacreous	Aragonite
Chlamys farreri	Regular simple prismatic	Aragonite	Foliated sheet	Calcite
Osteroida				
Crassostrea gigas	Regular simple prismatic	Aragonite	Foliated sheet/chalk	Calcite
Unionoida				
Cristaria plicata	Regular simple prismatic	Aragonite	Sheet nacreous	Aragonite
Hyriopsis cumingii	Regular simple prismatic	Aragonite	Sheet nacreous	Aragonite
Veneroida				
Ruditapes philippinarum	Regular simple prismatic	Aragonite	Fine-grained homogeneous	Aragonite
Sinonovacula constricta (Lamarck)	Regular simple prismatic	Aragonite	Cone canplex crossed lamellar	Aragonite
Dosinorbis japonica	Regular simple prismatic	Aragonite	Fine-grained homogeneous	Aragonite
Myoida				
Panopea abrupta	Multilayered regular simple prismatic	Aragonite	Fine-grained homogeneous	Aragonite

structures could be either aragonite or calcite (**Supplementary Figure 4**). For example, the nacreous layers in *P. fucata* were aragonite while foliated layers *C. farreri* were calcite, although both species belong to Pterioida. Therefore, the bulk shell structures in bivalves underwent divergent evolution which leads to the myriad microstructures. Oppositely, the myostracum layer might be under enormous evolutionary pressure and remain conservative in bivalves.

Then we wonder whether other molluscs have similar myostracum arrangement and when such shell structure evolved. Strikingly, prism columns were present in the innermost shell layer of the tested genera (**Figure 2** and **Supplementary Figure 2**), and the mineral counterparts were all aragonite (**Table 2** and **Supplementary Figure 3**). It should be noted that the fine structures were varied among different classes. In chiton, which belongs to Polyplacophora, the myostracum layer did not showcase regular prisms, instead, composite prisms were vertically aligned. The Gastropoda and Scaphopoda have more regular aligned prisms in the myostracum layer (**Figures 2C–J**) except that in the mud snail *B. exarata*, the prisms were irregular to some extent. Strikingly, a simple regular prismatic structure was found in the fossil specimen of ammonoid. Previous studies have proved that ammonoid fossils in south China dated back to the Permian period around 250 million years ago (Shen et al., 2019). The location was in the inner shell surface (**Supplementary Figures 2**, **8**), and this microstructure was supposed to be the adductor muscle scar according to previous studies (Kazushige Tanabe and Mapes, 1998; Zhu et al., 2016). Unfortunately, it was technically difficult to determine the polymorph of this myostracum layer. Nevertheless, the absence of magnesium implied that the aragonite was more likely the case (**Supplementary Figure 8**) because calcite in molluscan shell usually contained a certain amount of magnesium (Cuif et al., 2012). We also examined the Brachiopod *L. anatine* whose shells are similar to those of molluscs but consist of calcium phosphate. It was shown that, although they contain multilayers, the myostracum layer with columnar aragonitic prisms was absent in the *L. anatine* shells (**Figures 2O, P** and **Supplementary Figures 5**, **6**).

Similar to Bivalvia, shell structures underlying the myostracum layer in the Polyplacophora, Gastropoda, Scaphopoda, and Cephalopoda exhibited a diverse display. Columnar nacreous were present in both Gastropoda and Cephalopoda, while composite prismatic, crossed lamellar, and simple lamellar were also found as the bulk microstructure of tested shells. Moreover, both calcite and aragonite were found to be the composition of the main part of the shell layers.

DISCUSSION

Molluscs have elaborate rigid shells to protect the soft bodies, and when encountered with danger, the shells are closed or the soft bodies retract into the shell tube. Therefore, it would be of significant importance to control the shell movement and maintain the firm attachment of soft tissues and mineral organs. Our study showed that the myostracum layer in most molluscs adopt a conservative microstructure and crystal polymorphism, namely columnar prisms (or composite prisms in some individual cases) of aragonitic calcium carbonate. The result was consistent with previous studies in mussel, oyster, and scallop (Lee et al., 2011; Song et al., 2013; Zhu et al., 2016). Although myostracum is considered as prismatic aragonite in general in some archives (John and Taylor, 1973; Weiner, 1989; Zhu et al., 2016), most are focused on bivalves, and our present study extended this conception to most molluscs.

Zhu et al. (2016) reported that no distinguishable myostracum layer could be found in the clam *R. philippinarum*, at odds with our study (**Figures 1O, P**). Such

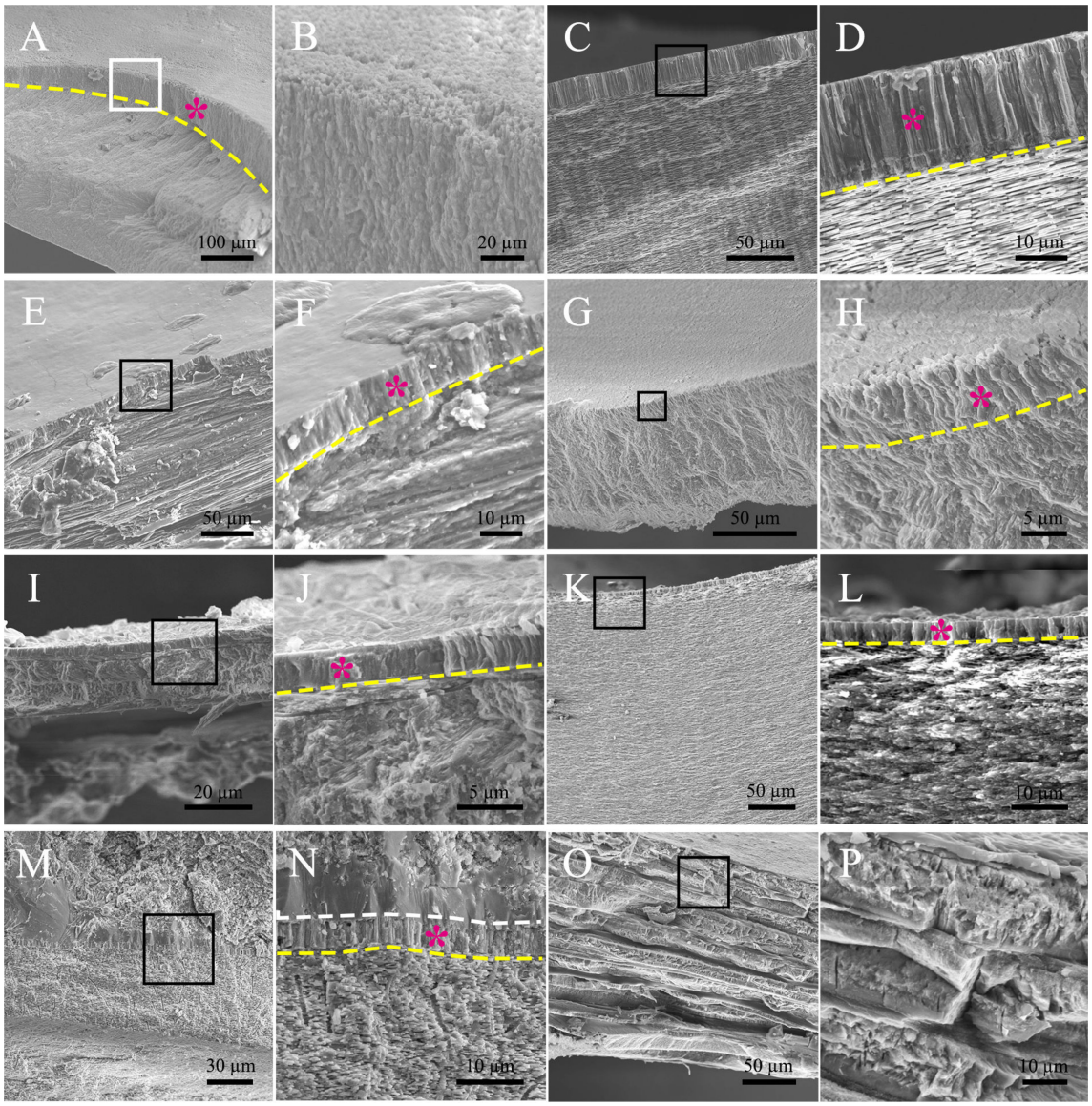

FIGURE 2 | Microstructure of the myostracum layer in some molluscan classes. **(A, B)** chiton *Ischnochiton comptus* (Gould); **(C, D)** abalone *Haliotis discus*; **(E, F)** Limpets *Cellana toreuma*; **(G, H)** mud snail *Bullacta exarata* (Philippi, 1848); **(I, J)** fresh water snail *Bradybaena ravida* (Benson); **(K, L)** Scaphopoda *Pictodentalium vernerdi*; **(M, N)** *Ammonoidea* sp.; **(O, P)** Brachiopod *Lingula anatine*, serving as a comparison. In each sample examined, the latter image is the magnification of the black box in the former image. The myostracum layer was indicated by a purple star, and the boundary between the myostracum and the underlying shell layers was indicated by the yellow dashed line. The white dashed line in **(N)** shows the boundary between the myostracum and the filled impurities in the shell lumen.

an inconsistency might be due to the different sampling methods. Because in Zhu's work, they examined the fracture surface perpendicular to the shell growth direction, which might lead to their missing the myostracum. Indeed, the myostracum in *R. philippinarum* was only 5 μm in height (**Figures 1O, P**), which was quite difficult to figure out. It would be much easier to image this structure in the fracture surface along the shell growth direction, as we did in the present study.

In all the selected living species, the myostracum layers adopted aragonite polymorphs, coincident with previous studies (Lee et al., 2011; Wang et al., 2014; Zhu et al., 2016), except the scallop. Reported data showed that myostracum in scallop *C. farreri* contained both aragonite and calcite (Zhu et al., 2016). The authors used FTIR to analyze the shell powder collected in myostracum, which might contain contaminated foliated layer (calcite) underlying the object. Because it was near impossible to completely separate the myostracum layer and the foliated layer, we applied *in situ* measurement (Raman spectrum) to analyze the mineral composition, and only aragonite was present.

The highly conserved myostracum in most molluscan classes suggested that such shell structure may be a primitive signature of their ancient ancestors. Indeed, evidence from this study (**Figure 2**

TABLE 2 | Summary of the microstructure and texture of tested shell layers in the species examined.

Species	Myostracum layer		Beneath the myostracum layer	
	Microstructure	Polymorph	Microstructure	Polymorph
Monoplacophora	nd	nd	nd	nd
Polyplacophora				
Ischnochiton comptus (Gould)	Composite prismatic	Aragonite	Composite prismatic	Aragonite
Gastropoda				
Haliotis discus	Regular simple prismatic	Aragonite	Columnar nacreous	Aragonite
Cellana toreuma	composite prismatic	Aragonite	Simple lamellar	Calcite
Bullacta exarata (Philippi,1848)	Irregular simple prismatic	Aragonite		Aragonite
Bradybaena ravida (Benson)	Irregular simple prismatic	Aragonite	Simple cross-lamellar	Aragonite
Scaphopoda				
Pictodentalium vernerdi	Regular simple prismatic	Aragonite	Intersected cross-acicular	Aragonite
Cephalopoda				
Carboniferous goniatite	Regular simple prismatic (Kazushige Tanabe and Mapes, 1998)	nd	Probably nacre (Landman et al., 2007)	nd
Ammonoidea sp.	Regular simple prismatic	nd	Columnar nacre	nd
Aplacophora	Shell-less			
Caudofoveata	Shell-less			

nd, not determined.

and **Supplementary Figure 8**) and archive [Figure 4Ain Reference (Kazushige Tanabe and Mapes, 1998)] revealed that prismatic myostracum structures already existed in molluscan shells dating back to the Permian and Jurassic periods. An interesting finding reported by Porter showed that calcite and aragonite seas have a strong influence on the mineralogy of carbonate skeletons at the time they first evolve (Porter, 2010). In that case, skeletons evolved in calcite sea would be composed of calcite, and skeletons evolved in aragonite sea would be composed of aragonite. Because there were two aragonite seas before the Permian period (Porter, 2010), unique myostracum structure might have evolved in early Cambrian or Carboniferous periods or both.

The prismatic microstructures of the myostracum seemed to be more advanced in Bivalvia class compared with other classes (**Figures 1**, **2**). Most of the bivalve genera have myostracum of simple regular prisms. In some particular samples, the myostracum layers could grow more than 200 μm in height (**Figures 1W, X**). This phenomenon may be due to the evolutionary pressure on closure of the two shell valves. As a result, the tissue-shell attachment in Bivalvia was one of the strongest ligaments in invertebrates (Castro-Claros et al., 2021). Nevertheless, Aplacophora completely lost their calcified shell, and some Gastropoda and Cephalopoda evolve endogenous skeletons or lose the shell. For example, slug *Agriolimax agrestis* (Linnaeus) is a terrestrial molluscs without a shell (Jiang et al., 2021). Some cuttlefish and squids have internal shells serving as buoyancy regulatory organs (Yang et al., 2020; Liu et al., 2021). We surmise that adductor muscle degenerated in these genera, although more studies are needed for verification.

CONCLUSION

In this study, we examined most of the molluscan genera to reveal the shell microstructure of the myostracum layers where the adductor muscle (soft tissue)-mineral attachment is located. The results showed that myostracum layers are composed of vertically aligned aragonitic prisms, and such microstructure is conserved among most molluscan classes and genera. Such evolution conservation implies pivotal functions of the unique myostracum layer with similar microstructure and mineralogy. How such shell structures are correlated with their physiological function remains elusive and deserves more in-depth studies.

DATA AVAILABILITY STATEMENT

The original contributions presented in the study are included in the article/**Supplementary Material**. Further inquiries can be directed to the corresponding author.

ETHICS STATEMENT

The animal study was reviewed and approved by the Animal Ethics Committee of Tsinghua University, Beijing, China.

AUTHOR CONTRIBUTIONS

WD carried out the lab work. JH conceived the project, participated in lab work and drafted the manuscript. CL helped with data analysis. HW and GZ revised the manuscript. LX and RZ provided financial supports and revised the manuscript. All authors gave final approval for publication.

FUNDING

This work was supported by National Natural Science Foundation of China Grants 31872543 and 32072951.

SUPPLEMENTARY MATERIAL

The Supplementary Material for this article can be found online at: https://www.frontiersin.org/articles/10.3389/fmars.2022.862929/full#supplementary-material

REFERENCES

Addadi, L., and Weiner, S. (2014). Biomineralization: Mineral Formation by Organisms. *Phys. Scripta* 89 (9). doi: 10.1088/0031-8949/89/9/098003

Bayerlein, B., Zaslansky, P., Dauphin, Y., Rack, A., Fratzl, P., and Zlotnikov, I. (2014). Self-Similar Mesostructure Evolution of the Growing Mollusc Shell Reminiscent of Thermodynamically Driven Grain Growth. *Nat. Mater.* 13 (12), 1102–1107. doi: 10.1038/nmat4110

Castro-Claros, J. D., Checa, A., Lucena, C., Pearson, J. R., and Salas, C. (2021). Shell-Adductor Muscle Attachment and Ca^{2+} Transport in the Bivalves Ostrea Stentina and Anomia Ephippium. *Acta Biomaterialia.* 120, 249–262. doi: 10.1016/j.actbio.2020.09.053

Checa, A. G., Macias-Sanchez, E., Harper, E. M., and Cartwright, J. H. (2016). Organic Membranes Determine the Pattern of the Columnar Prismatic Layer of Mollusc Shells. *Proc. Biol. Sci.* 283 (1830). doi: 10.1098/rspb.2016.0032

Cuif, J. P., Dauphin, Y., Nehrke, G., Nouet, J., and Perez-Huerta, A. (2012). Layered Growth and Crystallization in Calcareous Biominerals: Impact of Structural and Chemical Evidence on Two Major Concepts in Invertebrate Biomineralization Studies. *Minerals-Basel* 2 (1), 11–39. doi: 10.3390/min2010011

Deng, Z., Chen, H., Yang, T., Jia, Z., Weaver, J. C., Shevchenko, P. D., et al. (2020). Strategies for Simultaneous Strengthening and Toughening *via* Nanoscopic Intracrystalline Defects in a Biogenic Ceramic. *Nat. Commun.* 11 (1), 5678. doi: 10.1038/s41467-020-19416-2

Gilman, S. E. (2007). Shell Microstructure of the Patellid Gastropod Collisella Scabra (Gould): Ecological and Phylogenetic Implications. *Veliger* 48 (4), 235–242.

Guzman-Lastra, F., Kaiser, A., and Lowen, H. (2016). Fission and Fusion Scenarios for Magnetic Microswimmer Clusters. *Nat. Commun.* 7, 13519. doi: 10.1038/ncomms13519

Huang, W., Restrepo, D., Jung, J. Y., Su, F. Y., Liu, Z. Q., Ritchie, R. O., et al. (2019). Multiscale Toughening Mechanisms in Biological Materials and Bioinspired Designs. *Adv. Mater.* 31 (43). doi: 10.1002/adma.201901561

Jackson, A. P., Vincent, J. F. V., and Turner, R. M. (1988). The Mechanical Design of Nacre. *Proc. R. Soc. London Ser. B Biol. Sci.* 234 (1277), 415–440. doi: 10.1098/rspb.1988.0056

Jiang, L., Zhao, R. N., Tian, H., Wu, X. S., Guo, F., and Chen, W. L. (2021). Functional Response and Predation Potential of Carabus Elysii Adults Against the Terrestrial Slug Agriolimax Agrestis. *Insects* 12 (12). doi: 10.3390/insects12121135

John, D., and Taylor, W. J. K. (1973). The Shell Structure and Mineralogy of the Bivalvia II. Lucinacea-Clavagellacea, Conclusions: Bulletin of the British Museum (Natural History) 253–294. doi: 10.5962/p.314199

Kazushige Tanabe, N. H. L., and Mapes, R. H. (1998). Muscle Attachment Scars in a Carboniferous Goniatite. *Paleontol. Res.* 2 (2), 130–136. doi: 10.2517/prpsj.2.130

Landman, N. H., Davis, R. A., and Mapes, R. H. (2007). *Cephalopods Present and Past: New Insights and Fresh Perspectives* (The Nitherlands: Springer Press.).

Lee, S.-W., Jang, Y.-N., and Kim, J.-C. (2011). Characteristics of the Aragonitic Layer in Adult Oyster Shells,Crassostrea Gigas: Structural Study of Myostracum Including the Adductor Muscle Scar. *Evidence-Based Complement. Altern. Med.* 2011, 1–10. doi: 10.1155/2011/742963

Liu, C., Ji, X., Huang, J., Wang, Z., Liu, Y., and Hincke, M. T. (2021). Proteomics of Shell Matrix Proteins From the Cuttlefish Bone Reveals Unique Evolution for Cephalopod Biomineralization. *ACS Biomater. Sci. Eng.* doi: 10.1021/acsbiomaterials.1c00693

Mao, L. B., Gao, H. L., Yao, H. B., Liu, L., Colfen, H., Liu, G., et al. (2016). Synthetic Nacre by Predesigned Matrix-Directed Mineralization. *Science* 354 (6308), 107–110. doi: 10.1126/science.aaf8991

Mao, A. R., Zhao, N. F., Liang, Y. H., and Bai, H. (2021). Mechanically Efficient Cellular Materials Inspired by Cuttlebone. *Adv. Mater.* 33 (15). doi: 10.1002/adma.202007348

Marin, F., Luquet, G., Marie, B., and Medakovic, D. (2008). Molluscan Shell Proteins: Primary Structure, Origin, and Evolution. *Curr. Top. Dev. Biol.* 80, 209–276. doi: 10.1016/S0070-2153(07)80006-8

Nakahara, H., and Bevelander, G. (1970). An Electron Microscope Study of the Muscle Attachment in the Mollusc Pinctada Radiata. *Tex. Rep. Biol. Med.* 28 (3), 279–286. doi: 10.1080/01459740.1984.9965887

Porter, S. M. (2010). Calcite and Aragonite Seas and the *De Novo* Acquisition of Carbonate Skeletons. *Geobiology* 8 (4), 256–277. doi: 10.1111/j.1472-4669.2010.00246.x

Pramreiter, M., Rohner, M., Kumpenza, C., Ungerer, B., Stadlmann, A., Keckes, J., et al. (2020). Energy-Absorbing Wood Composite for Improved Damage Tolerance Inspired by Mollusc Shells. *Mater. Res. Express* 7 (9). doi: 10.1088/2053-1591/abb1f3

Raut, H. K., Schwartzman, A. F., Das, R., Liu, F., Wang, L., Ross, C. A., et al. (2020). Tough and Strong: Cross-Lamella Design Imparts Multifunctionality to Biomimetic Nacre. *ACS Nano*. 14 (8), 9771–9779. doi: 10.1021/acsnano.0c01511

Shen, S. Z., Zhang, H., Zhang, Y. C., Yuan, D. X., Chen, B., He, W. H., et al. (2019). Permian Integrative Stratigraphy and Timescale of China. *Sci. China Earth Sci.* 62 (1), 154–188. doi: 10.1007/s11430-017-9228-4

Song, Y., Lu, Y., Ding, H., Lv, H., Gao, G., and Sun, C. (2013). Structural Characteristics at the Adductor Muscle and Shell Interface in Mussel. *Appl. Biochem. Biotechnol.* 171 (5), 1203–1211. doi: 10.1007/s12010-013-0194-2

Sun, J. Y., and Bhushan, B. (2012). Hierarchical Structure and Mechanical Properties of Nacre: A Review. *Rsc Adv.* 2 (20), 7617–7632. doi: 10.1039/c2ra20218b

Suzuki, M., Kameda, J., Sasaki, T., Saruwatari, K., Nagasawa, H., and Kogure, T. (2010). Characterization of the Multilayered Shell of a Limpet, Lottia Kogamogai (Mollusca: Patellogastropoda), Using SEM-EBSD and FIB-TEM Techniques. *J. Struct. Biol.* 171 (2), 223–230. doi: 10.1016/j.jsb.2010.04.008

Wang, X. T., Li, L., Zhu, Y. B., Song, X. R., Fang, X. D., Huang, R. L., et al. (2014). Aragonite Shells are More Ancient Than Calcite Ones in Bivalves: New Evidence Based on Omics. *Mol. Biol. Rep.* 41 (11), 7067–7071. doi: 10.1007/s11033-014-3620-9

Weaver, J. C., Wang, Q. Q., Miserez, A., Tantuccio, A., Stromberg, R., Bozhilov, K. N., et al. (2010). Analysis of an Ultra Hard Magnetic Biomineral in Chiton Radular Teeth. *Mater. Today* 13 (1-2), 42–52. doi: 10.1016/S1369-7021(10)70016-X

Weiner, H. L. S. (1989). *On Biomineralization* (New York: Oxford University Press).

Yang, T., Jia, Z., Chen, H. S., Deng, Z. F., Liu, W. K., Chen, L. N., et al. (2020). Mechanical Design of the Highly Porous Cuttlebone: A Bioceramic Hard Buoyancy Tank for Cuttlefish. *P Natl. Acad. Sci. U.S.A.* 117 (38), 23450–23459. doi: 10.1073/pnas.2009531117

Zhu, Y., Sun, C., Song, Y., Jiang, F., Yin, X., Tang, M., et al. (2016). The Study of the Adductor Muscle-Shell Interface Structure in Three Mollusc Species. *Acta Oceanol. Sinica* 35 (8), 57–64. doi: 10.1007/s13131-016-0878-x

Conflict of Interest: The authors declare that the research was conducted in the absence of any commercial or financial relationships that could be construed as a potential conflict of interest.

frontiers | Frontiers in Marine Science

REVIEW
published: 27 June 2022
doi: 10.3389/fmars.2022.874534

The Mineralization of Molluscan Shells: Some Unsolved Problems and Special Considerations

Jingliang Huang[1*] *and Rongqing Zhang*[2,3*]

[1] School Chemical Engineering and Technology, Sun Yat-sen University, Zhuhai, China, [2] Ministry of Education (MOE) Key Laboratory of Protein Sciences, School of Life Sciences, Tsinghua University, Beijing, China, [3] Zhejiang Provincial Key Laboratory of Applied Enzymology, Yangtze Delta Region Institute of Tsinghua University, Jiaxing, China

The field of biomineralization is an inspiration for human design across disciplines, e.g. biomimetic materials, environmental and biomedical treatments, etc. Having a coherent understanding of the basic science sets the pillars for these fields that will impact human welfare. Intensive studies lead to great progress in unraveling the molecular mechanism underlying molluscan shell formation, especially in the past three decades. However, some problems remain, and discrepancy exists in varied studies. In this review, we pay attention to some issues which have been overlooked and warranted more in-depth studies, and pointed out that considerations should be seriously taken when looking into the cellular and molecular events in shell formation. We first consider the evolution of shell mineralogy and organic matrix by emphasizing the great impact of sea water chemistry. Secondly, we discussed the recent progress on the shell matrix protein (SMP) characterization and pointed out environmental and physiological conditions should be taken into account when studying the SMP functions. Finally, we highlighted some ambiguous issues in the less studied mineralizing tissues and cells, and the underlying cellular control on shell formation. New researchers in this field should keep in mind that early geochemistry *in vitro* research has mostly failed to address the *in vivo* context of biomineralization in cells and tissues. Therefore, the more biologically relevant experiments are still needed for future research.

Keywords: mollusk, mineralogy, organic matrix, shell matrix protein (SMPs), evolution

OPEN ACCESS

Edited by:
Gary H. Dickinson, The College of New Jersey, United States

Reviewed by:
Frederic Marin, Délégation Centre-Est (CNRS), France
Vera Bin San Chan, Clemson University, United States

***Correspondence:**
Jingliang Huang
huangjliang3@mail.sysu.edu.cn
Rongqing Zhang
rqzhang@mail.tsinghua.edu.cn

Specialty section:
This article was submitted to Marine Molecular Biology and Ecology, a section of the journal Frontiers in Marine Science

Received: *12 February 2022*
Accepted: *18 May 2022*
Published: *27 June 2022*

Citation:
Huang J and Zhang R (2022) The Mineralization of Molluscan Shells: Some Unsolved Problems and Special Considerations. Front. Mar. Sci. 9:874534. doi: 10.3389/fmars.2022.874534

INTRODUCTION

In nature, biominerals are synthesized by myriads of living organisms for body support, protection, feeding and perception (Addadi and Weiner, 2014; Clark, 2020). Molluscs are among the most exceptional for their ability to fabricate tremendous shells, leading molluscs to be the second largest phylum in invertebrates with more than 70, 000 living species (Rosenberg, 2014). The field of biomineralization is an inspiration for human design across disciplines, e.g. biomimetic materials, tissue engineering in medicine, energy production, environmental treatments, etc. Having a coherent understanding of the basic science sets the pillars for these fields that will impact human welfare.

The primary role of the shell is to protect the soft tissues, and in particular cases, the shell may serve as a buoyancy regulator in squids (Yang et al., 2020) or burrowing tool in shipworms (Distel et al., 2017). Some classes and genera completely lost their shells, such as slugs and sea hares in Gastropoda and octopus in Cephalopoda. The shells are composed of more than 95% inorganic minerals and a small amount of organic matrix (Marin et al., 2012; Checa, 2018). $CaCO_3$ in shells is commonly found as calcite and aragonite in adult individuals and often amorphous calcium carbonate (ACC) in juvenile animals (Lowenstam and Weiner, 1989; Weiss et al., 2002; McDougall and Degnan, 2018). In contrast to the limited forms of inorganic constituents, the organic matrix exhibits vast diversity and contains polysaccharides, lipids and proteins. Shell proteins play a central role in regulating $CaCO_3$ precipitation, including nucleation, polymorph selection, and morphology modification by self-assembly and bind to the polysaccharide framework (Marin et al., 2008; Marin et al., 2012). Since the pioneering work of identifying Lustrin A, MSI60 and MSI30 in the 1990s (Shen et al., 1997; Sudo et al., 1997), hundreds of shell matrix proteins (SMPs) have been characterized. Recombinant SMPs expressed and purified in *Escherichia coli* further shed light on their vital role and location in the shell layers (Pan et al., 2014; Bahn et al., 2017; Kong et al., 2018), although they may not fully reveal the exact role of the corresponding natural matrix proteins due to their lack of post-translational modifications and the absence of other SMPs.

Both inorganic constituents and organic matrix are secreted by the mineralizing cells lining the outer surface of the mantle which is a compartmentalized membrane-shape tissue. Typically, the mantle edge has three folds (**Figure 1**): inner fold for muscular movement, middle fold for sensing, and outer fold for shell secreting (Taylor and Kennedy, 1969). The groove between the middle and outer folds is responsible for synthesizing periostracum which is a tanned organic membrane covering the inner calcified shell layers (Checa, 2000; Yue et al., 2019). The mineralized shells usually have several layers with dramatically different morphologies and textures. The multilayers may be ascribed to the compartmentalization of the mantle tissue (**Figure 1**). For example, in the pearl oyster Pterioida, the mantle edge and submarginal zone are responsible for the prismatic layer secretion, while the pallial zone and central zone secrete the nacreous layer (Marie et al., 2012; Liu et al., 2015). In addition, hemocytes in bivalves have been found to participate in shell formation (Mount et al., 2004; Li et al., 2016).

More and more evidence shows that the shell biomineralization is a complex process involving exquisite regulation on cellular and molecular levels. And there are some overlooked aspects in recent studies. *In vitro* $CaCO_3$ crystallization experiment on SMPs could lead to misleading conclusions as these reactions were not properly set under physiologically relevant conditions. In this comment, we summarize some unsolved issues which warrant more in-depth research in the future, and make the community aware that there are some problems which should be carefully appreciated.

SHELL MICROSTRUCTURE AND TEXTURE

Mineralogy Determined by Mg/Ca Ratio

Calcite and aragonite are the two most used calcium carbonate polymorphs in mollusk shells. In natural environment and inorganic chemical reaction under abiotic conditions, the formation of calcite or aragonite is mainly controlled by Mg/Ca

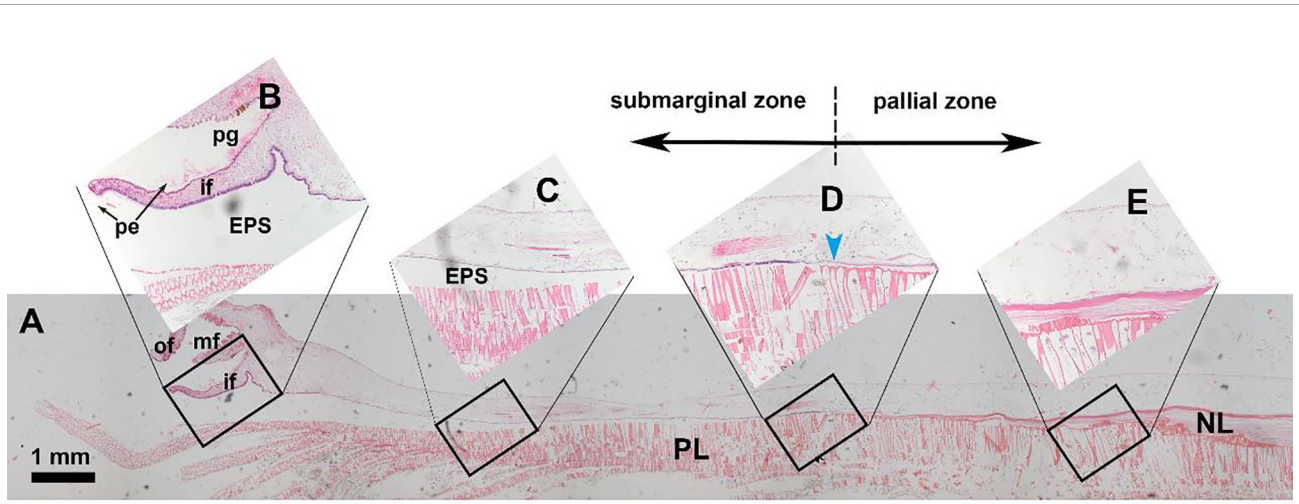

FIGURE 1 | Hematoxylin-eosin staining of the mantle tissue and decalcified shell in the pearl oyster *Pinctada fucata*. **(A)** holistic view of the mantle and the underlying shell layers. **(B-E)** magnifications of the black frames. **(B)** the mantle edge and shell edge. Note that the periostracum membrane (pe) secreted in the periostracum groove is visible. **(C)** submarginal zone of the mantle and prismatic layer. **(D)** transition zone of the prismatic layer and nacreous layer. **(E)** pallial zone of the mantle and nacreous layer. pe, periostracum; pg, periostracum groove; of, outer fold; mf, middle fold; if, inner fold; EPS, extrapallial space; PL, prismatic layer; NL, nacreous layer. The blue arrowhead indicates the growth front of the nacreous layer.

ratio of the solution and the reaction temperature (Balthasar and Cusack, 2015). As shown in **Figure 2**, relatively higher content of magnesium ions can strongly promote the formation of aragonite. The current seawater has a high Mg/Ca ratio (~ 5.2), so the naturally formed calcium carbonate at mild temperature would have been 100% aragonite. In addition, modern seawater contains a large amount of SO_4^{2-} which can also promote aragonite precipitation (Vavouraki et al., 2008). Therefore, the modern ocean belongs to the aragonite sea. In this case, the deposition of aragonite such as nacreous shell layer in mollusks or exoskeleton in scleractinian corals is thermodynamically favored.

However, most $CaCO_3$ produced by living organisms is definitely under biologically controlled. It has been found that organic matrices extracted from aragonite shells promote aragonite formation, while those extracted from calcite shells promote the precipitation of calcite (Falini et al., 1996; Takeuchi et al., 2008; Ponce and Evans, 2011; Fang et al., 2012; Rivera-Perez and Hernandez-Saavedra, 2021). It should be noted that most of the studies were based on results from *in vitro* $CaCO_3$ crystallization experiments, and these results do not necessarily reflect the exact physiological functions of SMPs *in vivo*. For example, PfN44 localized in both prismatic and nacreous layers, and could promote deposition of high Mg calcite at high Mg/Ca ratio (Pan et al., 2014). Clearly, this is unlikely the role PfN44 plays in the aragonitic nacre. Moreover, many SMPs were found to promote aragonite deposition *in vitro* (Suzuki et al., 2009; Ponce and Evans, 2011; Fang et al., 2012), but synthesizing proteins to facilitate aragonite deposition in modern aragonite sea is energetically costly and evolutionarily unfavorable. Therefore, the function of some SMPs should be carefully reconsidered. Moreover, relatively high level of Ca^{2+} solutions (mostly 10 mM) are used indiscriminatingly in most crystallization experiments, but that is quite different from the physiological context of freshwater molluscs, which may alter the experimental output.

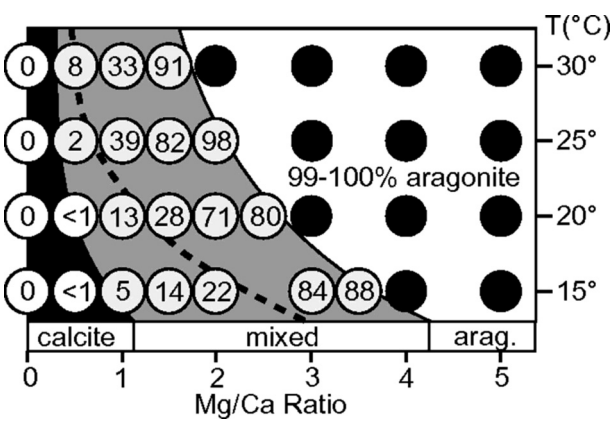

FIGURE 2 | Influence of temperature and Mg/Ca ratio on aragonite deposition [Taken from Balthasar & Cusack (Balthasar and Cusack, 2015), with permission of GSA]. The Mg/Ca ratio and temperature in the reaction system affect the content of aragonite in $CaCO_3$ crystals. The number in the white circle indicates the proportion of aragonite in the total $CaCO_3$ sediment, and the black circle indicates that more than 99% of the formed $CaCO_3$ is aragonite. Note that the Mg/Ca ratio of current sea water is around 5.2 (corresponding to the right of the graph).

Study of the mollusk exoskeleton evolution has shown that calcite and aragonite seas do have a strong influence on carbonate skeletal mineralogy at the time mineralized skeletons first evolve (Porter, 2010). In that case, the carbonate skeletons evolved in the aragonite seas were primarily aragonite, while those evolved in the calcite seas were primarily calcite (**Figure 3**). Interestingly, the mineralogy of most calcified shell layers appeared to remain unchanged once determined evolutionarily, even in the face of dramatic seawater chemistry changes (Porter, 2010). This may be due to the high energy cost of changing the shell mineralogy, so maintaining the original mineralogy was energetically more favorable.

We speculate that the aragonite-promoting or calcite-promoting SMPs evolved as the mineralized skeletons first appeared, and their primary functions remain unchanged across Phanerozoic times. For example, when a mollusk species evolved a calcified skeleton in a calcite sea, calcite rather than aragonite would stochastically precipitate due to thermodynamics. Simultaneously, those calcite-promoting extracellular organic matrices rapidly evolved under evolutionary pressure. Very likely, these calcite-promoting extracellular organic matrices could specifically bind and interact with calcite, and ultimately be integrated into the calcite crystals (Addadi et al., 1987). In this situation, the mineralogy may serve as the main effector that determined the evolution of organic matrices. In turn, the matrices, such as Asp-rich matrix proteins further promote calcite deposition (Politi et al., 2007; Takeuchi et al., 2008). When the seawater chemistry changed (into an aragonite sea), the cost might have been too high to evolve an aragonite formation secretome. Instead, the species retained the calcite formation secretome, although it cost much energy to overcome the inhibitory effect of high Mg/Ca ratio. Occasionally, some species have lost their original shell layers during the long history of evolution (Hautmann, 2001).

In addition to the regulation of shell matrices, molluscs may determine the $CaCO_3$ mineralogy by regulating the ion concentrations *in vivo* (Robert and Lorens, 1980). This strategy has been found to be used by foraminifera to deposit calcite (de Nooijer et al., 2009). In addition to actively removing Mg from vacuolized seawater, some foraminifera are able to elevate the pH at the calcification site, thus overcoming inhibitory effect of ambient Mg concentrations (de Nooijer et al., 2009). However, the cellular and molecular mechanisms by which they operate is not fully understood, nor it is clear that the molluscs use a similar mechanism. New techniques such as cryo-SEM-EDS and *in situ* atomic force microscopy are helpful for us to further understand the regulation mechanism. These techniques can be used to elucidate the cellular processes involved in biomineralization and examine the sample *in situ* (Hendley et al., 2015; Sviben et al., 2016; Choudhary et al., 2020).

Evolution of the Prismatic Layers in Bivalve Molluscs

Prismatic layers are frequently found in Palaeoheterodonta and Pteriomorphia. They are the outer most mineral layers and composed of polygonal prisms. Although the morphologies are

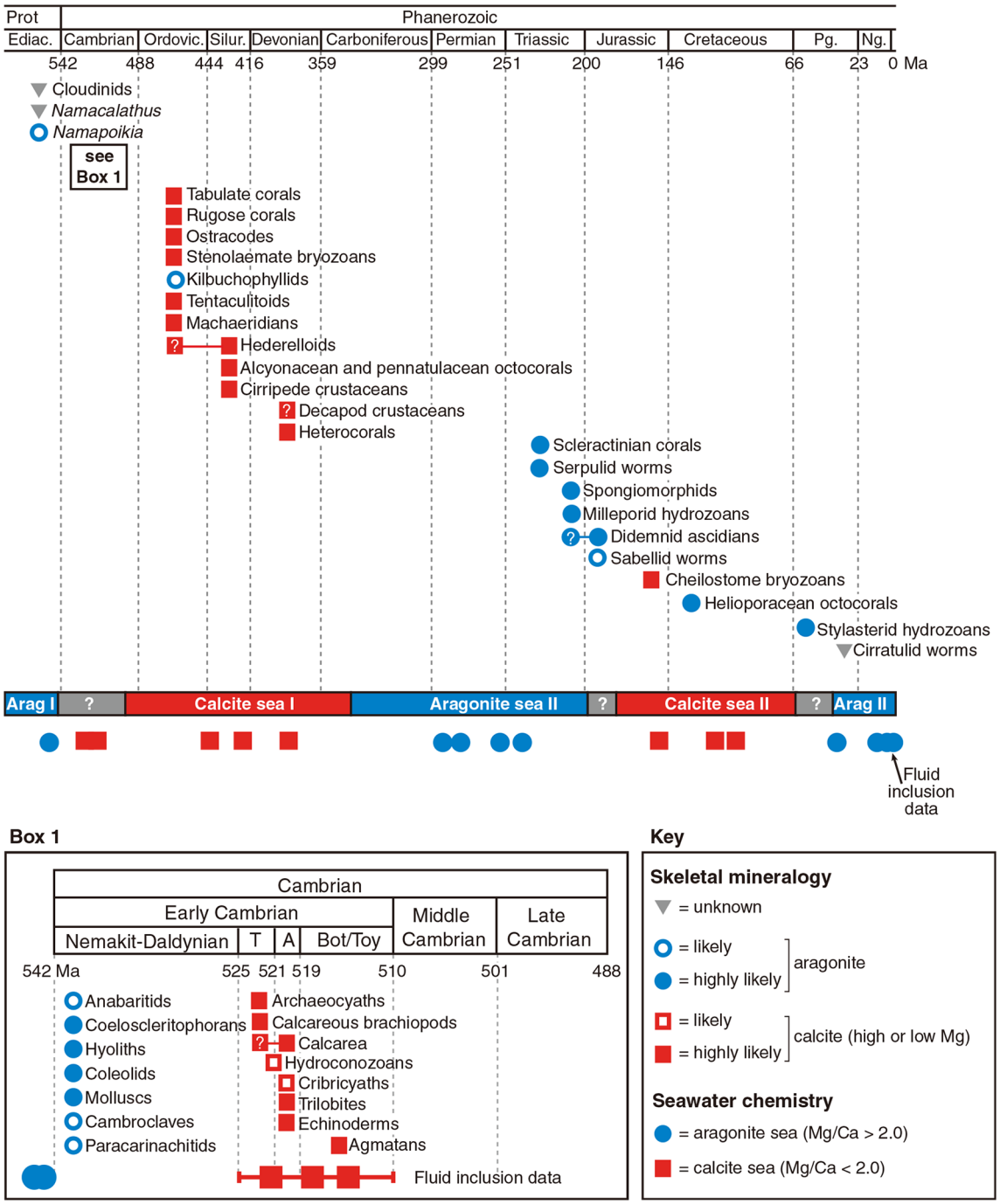

FIGURE 3 | Effect of seawater chemistry on calcium carbonate mineralogy in calcified skeleton evolution [Taken from S. Porter (2010), with permission of Wiley]. The first emergence time and predicted primary biomineral of the carbonate-mineralizing clades. Calcite seas and aragonite seas reconstructed from Mg/Ca ratios in non-skeletal carbonates and fluid inclusions. T, Tommotian Stage; A, Atdabanian Stage; Bot / Toy, Botomian and Toyonian stages.

quite similar, prismatic layers in Palaeoheterodonta (freshwater bivalves) are all composed of aragonite, whereas those in Pteriomorphia (seawater bivalves) are exclusive calcite (Lowenstam and Weiner, 1989; Dauphin, 2003; Marie et al., 2007; Okumura et al., 2010). This scenario is puzzling, considering the high Mg/Ca ratio in the seawater and low Mg/Ca ratio in the freshwater (**Table 1**). Such contradictory results may be ascribed to the different ambient environments where freshwater bivalves and marine bivalves first evolved prismatic layers. It is likely that freshwater bivalve ancestors evolved the

TABLE 1 | Comparison of the shell layers in freshwater bivalve *Hyriopsis Cumingii* and marine bivalve *Pinctada fucata* and the corresponding ambient environment.

Parameters	*H. Cumingii*	*P. fucata*
Prismatic layer	aragonite	calcite
Nacreous layer	aragonite	aragonite
Ambient calcium	1.33 ± 0.23 mM	9.25 ± 0.40 mM
Ambient magnesium	0.61 ± 0.07 mM	53.00 ± 2.50 mM
Mg/Ca ratio	~ 0.46	~ 5.2
Osmotic pressure	< 10 osm	~ 1100 osm

outer prismatic layer in the aragonite sea before they moved into freshwater systems. Indeed, in the 'living fossil' bivalve Neotrigonia, which belongs to marine palaeoheterodont, the shell contained prismatic layer and nacreous layer of aragonite (Checa et al., 2014), suggesting that the ancestor of Neotrigonia and Unionoida have already evolved the aragonite prismatic layer. And the evolution of prismatic layers in marine bivalves should have occurred in calcite sea. In that case, the prismatic layers were independently evolved in the ancestors of current freshwater and marine bivalves.

The exact time when bivalve prismatic layers evolved is not clear. Until now, the earliest known freshwater bivalve is *Archanodon catskillensis*, presumed to be Unionoida genus of Devonian age, according to the fossil record found in New York (Friedman and Chamberlain, 1995). However, there is no evidence showing the fine microstructure of the shell layer of this species, leading to the uncertainty of the existence of its prismatic layer. Because the prismatic layers of modern Unionidae are all aragonite, their ancestor might have evolved prismatic layer in aragonite sea before entering the freshwater habitats. Moreover, within the Unionidae, *Hyriopsis cumingii* F and *Anodonta woodiana* F split in early Permian (**Figure 4**), and both of them have aragonitic prisms (Liu and Li, 2015; Zhang et al., 2021). Therefore, the acquisition of prismatic layer in the Unionidae likely occurred during the early Mississippian to the early Permian, corresponding to the aragonite sea II period (**Figure 3**). As for the marine bivalves, typical columnar prismatic layers are present in the Ostreoida and Pteriida of Pteriomorphia (Checa et al., 2009; Okumura et al., 2010), but not in Pectinoidea and Mytilidae (Grefsrud et al., 2008; Gao et al., 2015). Therefore, the time when the Ostreoida and Pteriida evolved prismatic layer might be between the late Cambrian and early Devonian, right after the radiation of the Pteriomorphia (**Figure 4**). Alternatively, the prismatic microstructure might represent a convergent evolution during the Jurassic and Cretaceous, which is less likely. Comprehensive studies on the mantle transcriptome and shell protein proteome may provide insight into the evolution of the prismatic layers, both in the freshwater Unionidae and marine Pteriomorphia.

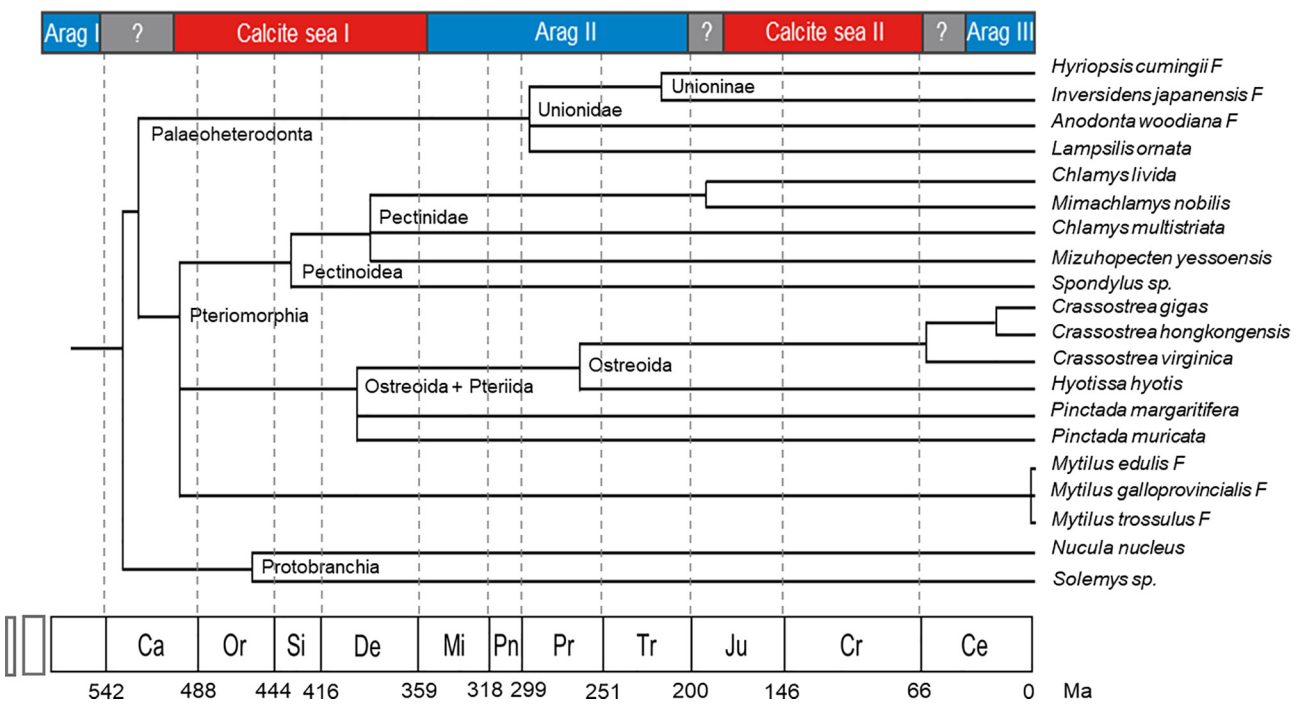

FIGURE 4 | Bivalve phylogeny coupled with the geologic time scale showing the evolution of the selected bivalve genera (Modified from Plazzi and Passamonti (2010), with permission of Elsevier). Ca, Cambrian; Or, Ordovician; Si, Silurian; De, Devonian; Mi, Mississippian; Pn, Pennsylvanian; Pr, Permian; Tr, Triassic; Ju, Jurassic; Cr, Cretaceous; Ce, Cenozoic; Ma, million years.

ORGANIC MATRICES

Shell Matrix Proteins Versus Shell Proteins

Molluscan shells are composed of more than 95% $CaCO_3$ and 1-5% organic matrices (Marin et al., 2008; Checa et al., 2016). The organic matrices contain polysaccharides, lipids and proteins and play a crucial role in regulating shell formation. The functions of polysaccharides and lipids are not understood at all. Most studies focused on the protein components which have been shown to control $CaCO_3$ precipitation, including nucleation, morphological modification, mineralogy selection, crystal growth and inhibition (Weiner and Dove, 2003; Marin et al., 2012; Checa, 2018). Hundreds of shell matrix proteins have been identified in the past three decades, especially after the application of high through-put omics methods (Liu and Zhang, 2021). However, attention should be taken to the contamination of residual proteins from soft tissues, as suggested by Marie *et al.* (Marie et al., 2013). Moreover, the extrapallial fluids contain large amounts of cellular proteins and immune components (Hattan et al., 2001) which may be adsorbed to the inner shell surface and lead to false detection if the samples were not carefully prepared.

Although most cellular proteins in shell matrix proteomic studies are regarded as contamination of residual proteins from attached tissues, their presence in the shell layers has been shown by some robust evidence. Drake *et al.* (Drake et al., 2013) show that the cell-free skeleton of the hermatypic coral *Stylophora pistillata* has some cellular components such as Actin and Glyceraldehyde 3-phosphatase dehydrogenase. In our recent work, prismatic layers from pearl oyster *P. fucata* were completely digested with HClO (Liu et al., 2021), resulting in removal of cellular components and extraction of mineral-occluded organic matrix. Although cellular proteins commonly found in other studies such as Actin and Paramyosin were absent, certain cellular proteins were found in the intra-mineral matrix (such Isocitrate lyase and Toll-like receptor 6) (Liu et al., 2021). In this case, we speculate that some cellular proteins are indeed incorporated into the mineral phase of the shell, but this does not necessarily lead to their indispensable function in shell formation. Take it a step further, some proteins previously identified in the shell may not be true shell matrix proteins even though they have been characterized to some certain extent. We suggest that these proteins should be regarded as shell proteins which integrate into the shell minerals but actually do not participate in shell mineralization, such as the immune components and some commonly found cellular proteins.

Nevertheless, it should be noted that there are some biomineralization-related proteins which are not incorporated into the shell layers. Amorphous calcium carbonate binding protein (ACCBP) was identified by our group from the extrapallial fluids of *P. fucata* (Ma et al., 2007). ACCBP is secreted by mantle epithelial cells and can stabilize ACC *in vitro*, suggesting its important role in shell formation. Strikingly, ACCBP has never been found in any shell layers. The way by which it participates in biomineralization remains unclear. Similarly, EP28, the most abundant EPF protein (account for half of the total EPF proteins) in *Mytilus edulis* is absent in the mussel shell, although it has calcium binding affinity and is supposed to participate in shell mineralization (Hattan et al., 2001). Very likely, these components, together with other biomineralization-related proteins such as Calmodulin (Li et al., 2005), Calcineurin (Buddawong et al., 2021) and ferritin (Varney et al., 2021) are involved in the metabolism of calcium and/or other ions. Alternatively, EPF proteins ACCBP and EP28 may inhibit undesired mineralization in the hemolymph and other body fluids considering their broad tissue distributions (Hattan et al., 2001; Ma et al., 2007).

Functional Studies of the SMPs

Although hundreds of SMPs have been identified in molluscan shells, only a small part of them are characterized with full-length amino acid sequence and known function. Because the genomes of most molluscs have not been sequenced, except several species including the pearl oyster *P. fucata* (Takeuchi et al., 2012), Pacific oyster *Crassostrea gigas* (Zhang et al., 2012), blue mussel *Mytilus* spp (Murgarella et al., 2016; Yang et al., 2021)., and scallops (Wang et al., 2017; Li et al., 2018). For those without available genome information, the full-length amino acid sequence of an SMP is deduced from its coding cDNA obtained by routine RACE (rapid-amplification of cDNA ends) (Fang et al., 2012; Jia et al., 2015). Their involvement in shell formation can be speculated from the tissue distribution of the gene expression and localization of the mature protein. In this case, if the coding gene of a protein is specifically expressed in the mantle epithelia and/or the mature protein is detected in the shell layer, for example by gold particle labeling (Suzuki et al., 2009), this protein would be considered to participate in shell formation. Moreover, the potential function of the protein can be speculated from its amino acid sequence *via* homologous blast search against public database (Finn et al., 2014). But a large number of SMPs are unique in molluscs and have no homologs in other animals. In some cases, the predicted SMPs are heterogeneously expressed in *E. coli*, and the recombinant SMPs are purified and studied *via in vitro* $CaCO_3$ crystallization. Until now, dozens of recombinant SMPs have been published and found to fulfill important roles in shell formation (Rivera-Perez and Hernandez-Saavedra, 2021).

However, due to the lack of cell lines, traditional and advanced techniques in cell biology are seldom used in studying the exact physiological function of the SMPs. Moreover, *in situ* observation of shell mineralization is rather difficult, especially in adult animals. These situations greatly hinder the unraveling of cellular and molecular processes in shell mineralization and lead to some principle perspectives largely uncertain and under debate. Moreover, the functions of SMPs are usually not explored under physiological conditions. For example, some SMPs from marine molluscs are found to promote aragonite precipitation in the absence of magnesium (calcite-promoting condition) (Suzuki et al., 2009; Fang et al., 2012). Because the ion composition in marine molluscs is similar

to the ambient sea water, aragonite deposition would be favored under physiological conditions (Crenshaw, 1972; Nair and Robinson, 1998; Balthasar and Cusack, 2015). In this scenario, aragonite-promoting would be redundant for marine molluscs. We surmise that the results of *in vitro* $CaCO_3$ crystallization do not necessarily link to the exact physiological role of the SMPs.

Another problem of the *in vitro* $CaCO_3$ crystallization experiment is the effects of impurity. Most of the characterized SMPs are found to inhibit $CaCO_3$ growth *in vitro* (Miyamoto et al., 2005; Samata et al., 2008; Pan et al., 2014; Liang et al., 2015; Rivera-Perez and Hernandez-Saavedra, 2021), regardless of their chemical properties. Even the carbonic anhydrase domain-containing Nacrein was found to be a negative regulator in $CaCO_3$ crystallization according to the *in vitro* experiments (Miyamoto et al., 2005). Considering the hypersaturation in $CaCO_3$ crystallization system, the effect of impurity may greatly influence the results, and lead to the observed inhibitory effect of SMPs. Therefore, new criteria are urgently needed in assessing SMPs functions.

The Evolution of SMPs

As aforementioned, seawater chemistry had a great impact on the evolved marine shells when they first emerged (Porter, 2010). But the evolution of SMPs and their relations to shell evolution remain elusive. We propose that the SMPs evolution coordinate with the shell evolution: the mineralogy of the evolved shell may serve as the main effector that determines the corresponding SMPs, rather than the specific SMPs determining the shell mineralogy (**Figure 5**). For example, when the calcified shell evolved in an aragonite sea, aragonite-promoting SMPs would rapidly evolve and further accelerate aragonite precipitation in the shell. These aragonite-promoting SMPs (such nacre proteins Pif, N16 and PfN23) have strong binding ability to aragonite and may have special domains or motifs (e.g. Gln-Gly-Gln tandem repeats) which can be inserted into the lattice of aragonite crystal (Ponce and Evans, 2011; Fang et al., 2012; Bahn et al., 2017), thus facilitating aragonite nucleation. When the sea water chemistry changes, the aragonite-promoting SMPs (together with other organic matrices) are conserved under unknown evolutionary pressure, and in turn determine the unchanged shell mineralogy (**Figure 5**, lower panel). It is the same case for calcite-promoting proteins (**Figure 5**, upper panel).

Extrapallial Fluids

Extrapallial fluids (EPF) are the body fluids in the extrapallial space enclosed by the mantle tissue and the forming shell. The chemical composition of the EPF is similar to the hemolymph (Crenshaw, 1972), indicating the close relationship between

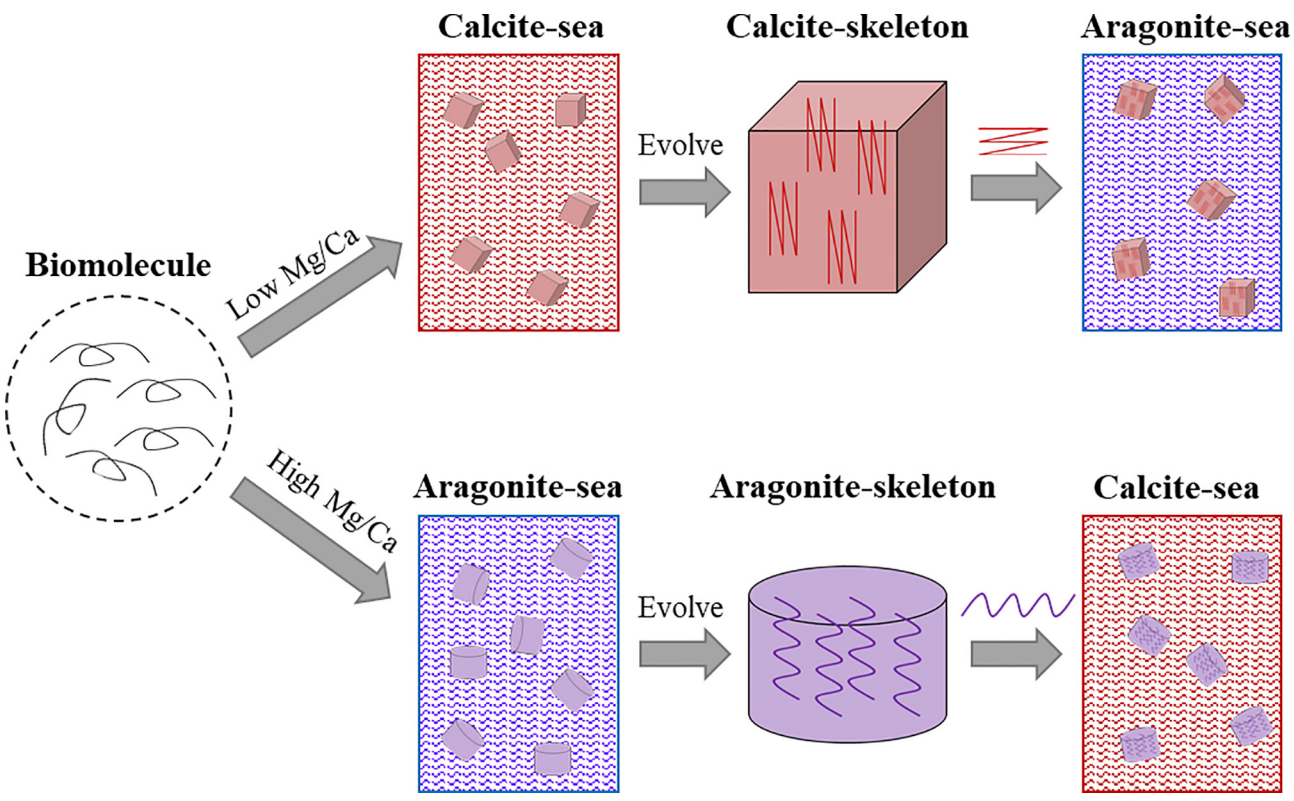

FIGURE 5 | Schematic illustration of proposed shell matrix evolution in molluscs. The progenitor of the shell matrix evolved in accordance with the seawater chemistry when the calcified skeleton first emerged. When the seawater chemistry changed, for example from calcite sea to aragonite sea, the evolved calcite-associated shell matrices promote calcite deposition in the aragonite sea.

them. In marine molluscs, the concentration of inorganic ions in EPF is consistent with those in the ambient environment, while in freshwater molluscs, calcium and carbonates of the EPF have higher content (>110 ppm) than the ambient environment (around 30 ppm) (Pietrzak et al., 1976), suggesting that an active uptake and retention of calcium in the EPF in these animals.

The primary role of the EPF is supposed to maintain the microenvironment for shell mineralization. Any disturbance in the EPF might lead to abnormal $CaCO_3$ deposition. Xie *et al.* (Xie et al., 2016) found that when the protein content of the EPF was reduced, the nacreous layers were disordered, and calcite was randomly deposited. Moreover, some pathogenic microbes may invade the extrapallial space and cause serious infection. Indeed, the EPF was found to exert immune reaction to clear the pathogens, thus ensuring the biomineralization process (Allam et al., 2000; Huang et al., 2018). In addition, EPF is believed to contain the precursor of shell matrices. Liu *et al.* (Liu et al., 2018) used pearl nucleus (same as those in pearl aquaculture) as a template and found that EPF of *P. fucata* could promote the growth of nacre-like multilayer structures, suggesting that EPF might directly participate in shell formation. However, in-depth analysis of the EPF composition turned out to be quite confusing. Only a few SMPs were identified by LC/MS-MS, and when the EPF were incubated with aragonite crystals, the eluate did not contain aragonite-binding SMPs such as Pif and N16 (Xie, 2016). These puzzling results made us revisit the exact role of EPF.

More than a decade ago, Steve Werner and his colleagues (Addadi et al., 2006) questioned the role of EPF and proposed that epithelial cells deposit calcium carbonate directly on the shell surface and that EPF plays a very limited role in shell formation. Although ACCBP and another calcium-binding protein have been identified in mollusk EPF, these proteins were not SMPs (see discussion in *Shell Matrix Proteins Versus Shell Proteins*). Considering that the majority of EPF proteins were cellular components and immune factors, the primary function of EPF may be exerting immune reaction, together with the hemocytes in the extrapallial space (Huang et al., 2018).

Nevertheless, it is important to note that the role of EPF may be different for various molluscs. For example, in freshwater mussels, the extrapallial space is filled with a large amount of EPF (personal observation), so the mantle (central region) is unlikely to contact the nacreous layer for direct mineralization. Therefore, the nacre of freshwater mussels should be directed by EPF. Unfortunately, information about the EPF composition in the freshwater molluscs is scarce, which warrants more studies in the future.

Self-Assembly of the Shell Matrices

Because the mineral assembly and growth appear to occur extracellularly, the shell matrices secreted by the mantle cells should undergo self-assembly and guide the $CaCO_3$ precipitation independently. However, up to now, how these events happen remains largely unknown. Levi-Kalisman *et al.* (Levi-Kalisman et al., 2001) proposed that the shell matrix forms a hydrogel where the chitin fibers are arranged as the main framework which is bound by silk-like matrix proteins. More and more evidence supports the principle idea of this model. Indeed, many SMPs have modular arrangement in their amino acid sequences. For example, the nacre protein Pif of *P. fucata*, which plays a vital role in nacreous layer deposition, has a typical arrangement of a chitin binding domain and an acidic domain which can bind calcium ion (Suzuki et al., 2009). Other shell matrix proteins may have VWA domain mediating protein-protein interaction with each other (McDougall and Degnan, 2018; Liu and Zhang, 2021).

One of the most impressive features of SMPs is the presence of low complexity regions (LCR) in their sequence (Marin et al., 2008). LCR usually forms random coil and does not have secondary structure, which makes it difficult to predict their functions. Moreover, the LCRs in SMPs are unique in that they have hardly any homologies with known proteins and are clade-specific (McDougall et al., 2013). It should be noted that SMPs from similar shell microstructures (such as nacre tablets in the pearl oyster and *Mytilus* spp.) may vary dramatically in their LCRs (Liu et al., 2015; Gao et al., 2015). Stephen Weiner and Leroy Hood's pioneering work revealed that the soluble proteins in the mollusk shell matrix were enriched in Asp, Gly and Ser (Weiner and Hood, 1975). However, the insoluble fractions of the shell matrix from many genera contained proteins enriched in Gly and basic amino acids such as Lys and Arg (Zhang et al., 2006), indicating that the shell matrices undergo self-assembly through intermolecular interactions. Indeed, our group recently found that electrostatic interaction and hydrophobicity play a key role in the shell matrix organization of the prismatic layers in pearl oyster *P. fucata* (**Figure 6**) (Huang et al., 2021). Furthermore, the lipids (very likely derived from secreted vesicles) fused with the hydrophobic fraction of the matrix and in return increase the hydrophobicity of the organic mixture.

Liquid-liquid phase separation (LLPS) of the shell matrix may add to another driving force of self-assembly. LLPS of proteins is crucial for the formation of membrane-less organelles, as well as some pathological progresses (Brangwynne et al., 2015; Boeynaems et al., 2017; Kanaan et al., 2020). The proteins undergo LLPS *via* intra-chain interaction (such as charge-charge and hydrogen bonding), hydrophobic effect (especially *via* aromatic groups), and multivalent interaction *via* folded domains (Alberti et al., 2019; Dzuricky et al., 2020). Interestingly, many SMPs share similar features in amino acid sequences. Indeed, Pif80 and Pif97 from nacreous layers of *P. fucata* formed liquid droplets under high concentration of salt (Bahn et al., 2015; Bahn et al., 2017). We proposed that many SMPs would undergo LLPS, and SMPs with LCRs comprising similar amino acid compositions or interactive domains may fuse *via* LLPS.

MINERALIZING CELLS

Transportation of Shell Constituents

As seawater is rich in Ca^{2+}, and $CaCO_3$ is in a supersaturated state, calcium transportation may not be a limiting factor for shell deposition in marine molluscs (Sillanpaa et al., 1891). Moreover, seawater bivalves balance calcium ions between hemolymph and EPF through channels in the mantle cells

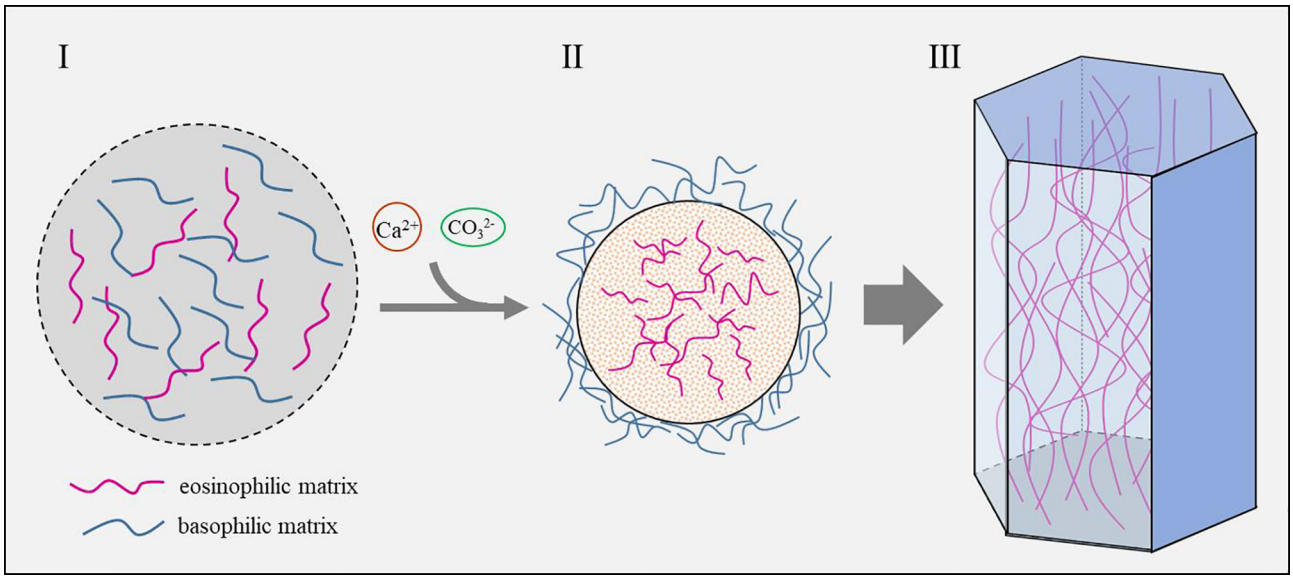

FIGURE 6 | Schematic model of the prismatic column formation controlled by shell matrix (Huang et al., 2021). I. Shell matrices secreted by the mantle cells contain both eosinophilic matrix and basophilic matrix. II. Calcium and carbonate are recruited by the shell matrix and concentrated until saturation state is reached. Eosinophilic matrix which contains more acidic amino acids and sulfonate serves as nucleation sites and crystallizes with calcium carbonate, while the basophilic matrix which contains numerous hydrophobic amino acids is excluded outside the mineral. III. As the crystals grow, the excluded basophilic matrix is squeezed and hardened, thus forming the polygonal framework.

(Bleher and Machado, 2004). Given that $CaCO_3$ is continuously deposited on the shell surface, calcium from the hemolymph can reach the EPF by simple diffusion or passive transport (**Figure 7**). It should be noted that, in the cultured mantle cells, Xiang Liang *et al.* (Xiang et al., 2014) found that the mantle cells could *de novo* synthesize ACC in the cytosol. ACC has been proposed to be the precursor of shell minerals and has been found in the larval and adult shells (Weiss et al., 2002; Gal et al., 2014). Is the ACC precursor synthesized by the mantle cells and then secreted to the shell growth front? Moreover, hemocytes bearing $CaCO_3$ crystals have been reported in several bivalves (Li et al., 2016), and particularly in the eastern oyster *C. virginica*, $CaCO_3$ crystals were secreted onto the shell surface by the hemocytes (Silverman. et al., 1988; Mount et al., 2004). However, how crystalline calcium carbonate is transported across the cell membrane is unclear.

Despite the intensive studies on the characterization of the shell matrix, especially the SMPs, there is limited information on the way shell matrices are secreted (**Figure 7**). Most of the identified SMPs have signal peptides, suggesting their secretion *via* classical endoplasmic reticulum-Golgi complex pathway (Davis and Tai, 1980). However, as we mentioned in Section 3.3, SMPs were not the main components in the EPF and could hardly be detected in the EPF, making their secreting pathway a mystery. Moreover, some shell proteins (not classical matrix proteins) have no signal peptides, indicating that non-classical secretion pathways are involved (Huang et al., 2022). In fact, Xiaotong Wang *et al.* (Wang et al., 2013) proposed diverse origins of shell proteins from mantle cells, hemocytes and other organs.

Control on the Shell Microstructure

The microstructures of the molluscan shells display dramatic diversity, including cross-lamella, polygonal prisms, sheets, granules, *etc* (Marin et al., 2012). Although the shell microstructures in various genera have been explored and characterized for decades, the mechanism by which these microstructures are determined is still under debate. Take the prismatic layer in bivalves as an example. Both cellular control and physical control were thought to serve as the determinant for the polygonal arrangement. Bayerlein *et al.* (Bayerlein et al., 2014) used synchrotron-radiation-based micro-CT to reveal the evolution process of polygon domains in *Pinna nobilis*, and found that the domain evolution can be well predicted by using grain growth theory, indicating a passive adaptation of the organic matrix to the mineral domains. On the other hand, Checa *et al.* (Checa et al., 2016) reported in some bivalves, the prism domain pattern could not be explained by the grain growth theory, but was rather controlled, as the authors argued, by the membranes (organic matrix). How to reconcile these contradictory mechanisms is tough and challenging.

SMPs are believed to play central roles in regulating $CaCO_3$ precipitation, including crystal morphology. Indeed, dozens of extracted or recombinant SMPs could modify the appearance of calcite or aragonite *in vitro*, which may be due to the specific binding of the SMPs to the lattice plane or crystal axis

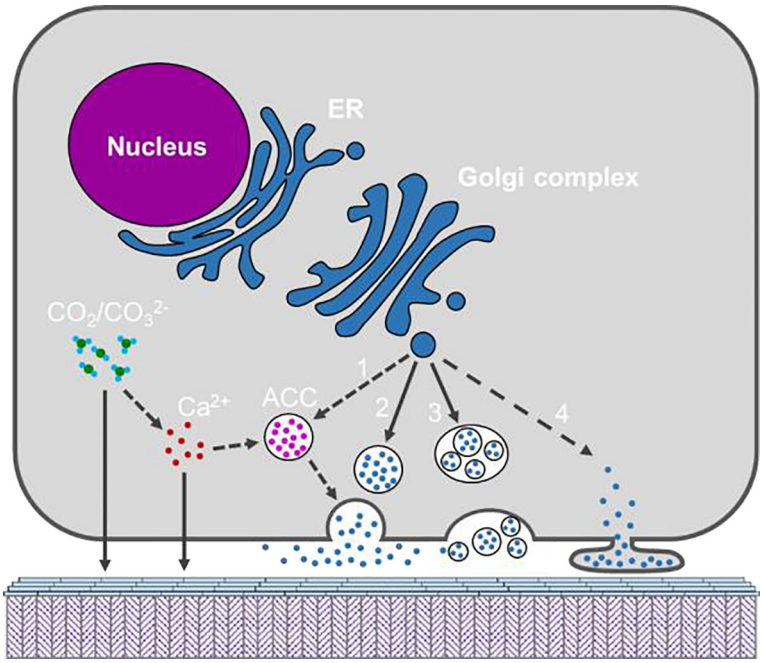

FIGURE 7 | Schematic model showing the possible secretary pathways of the organic materials and inorganic constituents by the mantle cell. Calcium and CO_2/CO_3^{2-} may be secreted directly or *via* ACC formed in the cytosol. Organic materials are shown as blue dots and maybe secreted *via* diverse pathways, namely (1) ACC binding matrix, (2) exocytosis; (3) multivesicular body; (4) shedding microvesicle. The solid arrow indicates pathway which is supported by published work, and dotted arrow indicates potential pathway which warrant more evidence.

(Rivera-Perez and Hernandez-Saavedra, 2021). Furthermore, inhibition of these SMPs by neutralizing antibodies or RNAi knock-down showed disturbance on the shell microstructures (Suzuki et al., 2009). These results pointed to the important role of SMPs in regulating microstructure. However, due to the lack of direct *in vivo* evidence, seldom did any study come to an unequivocal conclusion that a certain SMP plays a designated role in shell deposition. For example, until now, no SMP has been found to be responsible for the formation of hexagonal tablets in nacre. Moreover, helical arrangements of nacre tablets have been found in some genera and ascribed to helical dislocations in crystallography (Yao et al., 2006). It is worth paying more attention to applying classical theories of thermodynamics and crystallography in shell biomineralization.

Nevertheless, the mineralizing cells themselves have been proposed to control shell microstructure directly. M.B. Johnstone *et al.* (Johnstone et al., 2015) examined the metal alloy surfaces implanted under the outer mantle epithelial cells (OME) of *Crassostrea virginica* and found the extracellular matrix walls appeared to be originated from the OME surface, indicating direct orchestration of the shell microstructure by the OME. Furthermore, Checa *et al.* suggested that direct subcellular activity in the formation of the helical fibrous microstructure in cavolinioidean gastropods (Checa et al., 2016), where the mantle cells dynamically recognize the positions of the fiber tips and secrete shell constituents. However, in this scenario, the mantle cells have to displace the fiber tips along circular routes to achieve a spiral path. Direct observation of the matrix secretion across the outer cell membrane would underpin this innovative idea, although it may be technically difficult.

Special Roles of Hemocytes

After the pioneering work published by Andrew Mount' group showing that hemocytes (granulocytes in particular) might mediate a special mineralization pathway in the eastern oyster *C. virginica* (**Figures 8A, B**) (Mount et al., 2004), the exact role of types of hemocytes in shell formation is still poorly studied. In the previous study, granulocytes were found to deliver calcium, in $CaCO_3$ crystalline form, to the shell growth front during shell repair (Mount et al., 2004). Later, two hemocyte-secreted matrix proteins (48kDa and 55kDa phosphoproteins) were identified and localized in the circulatory system using immuno-fluorescent probe (Johnstone et al., 2008). Moreover, hemocytes' participation in shell formation (especially in calcium supply) has been reported in several bivalves (**Figure 8**) (Silverman. et al., 1988; Kádár, 2008; Trinkler et al., 2011; Li et al., 2016). However, there is no robust evidence showing that the hemocytes are indispensable for shell formation. Meanwhile, it is difficult to rule out the participation of hemocytes, because hemocytes are commonly present in the shell growth front, and we could not block the migration of hemocytes into the mantle tissue.

The presence of hemocytes in the EPF has been reported in many bivalves. Considering their large numbers, the exact way they get into the extrapallial space is not fully understood. In a

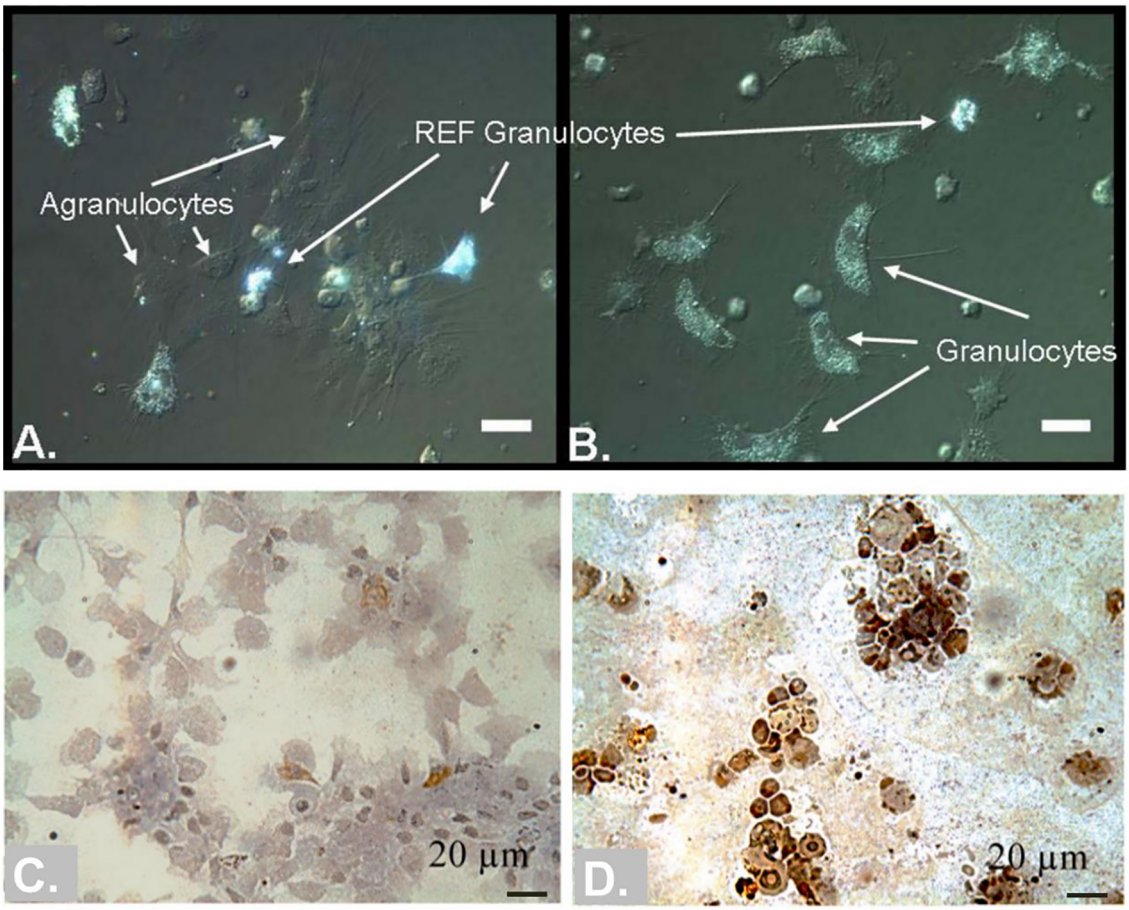

FIGURE 8 | Hemocytes in bivalve molluscs may participate in shell calcification. **(A, B)** comparison of agranulocytes, granulocytes and REF granulocytes in the eastern oyster *C. virginica* [Taken from Mount *et al.* (Mount et al., 2004), with permission of Science]. Note that the REF granulocytes were highly refractive under DIC microscopy. **(C, D)** hemocytes colored with Von Kossa stain in the clam *Venerupis philippinarum* during shell repair [Taken from Trinkler *et al.* (Trinkler et al., 2011), ©Inter-Research 2011, with permission of Inter-Research]. Hemocytes in **(C)** were collected from hemolymph, and hemocytes in **(D)** were collected from central extrapallial fluid. The insoluble calcium carbonate salts are dark (brown) colored.

previous study, we found that there were many pore structures on the outer surface of mantle tissue, and some hemocytes were observed nearby (Li et al., 2016). However, when using a milder fixation method, we could not observe these pore structures, which was further supported by histochemical staining and transmission electron microscopy of the mantle tissues. Moreover, P. S. Nair and W. E. Robinson (Nair and Robinson, 1998) examined the material interchange between the EPF and hemolymph in *Mercenaria mercenaria*. It was found that small molecules, such as tyrosine, can quickly reach equilibrium between the two body fluids, while macromolecules, such as proteins (bovine serum albumin) can never reach equilibrium, but are confined in EPF. Therefore, it is unlikely that the hemocytes migrate into the EPF *via* holes on the mantle epithelium, and the exact way remains to be further explored.

Nevertheless, the presence of calcium carbonate crystals inside the hemocytes is fascinating. Although most molluscs appeared to assemble and grow calcified shells extracellularly, many other non molluscan species have been shown to produce intracellular compartment for crystals nucleation to overcome the thermodynamic barrier of Ca supersaturation states required (Hayes and Goreau, 1977; Sorrosa et al., 2005). In bivalves, intracellular calcium carbonate is often supposed to serve as a temporary storage for calcium (Silverman et al., 1983), but its formation remains a great mystery. Our group found that in *P. fucata*, crystal-bearing hemocytes have numerous calcium-rich particles (Li et al., 2016; Huang et al., 2018), consistent with the granulocytes reported in the eastern oyster and clam (Mount et al., 2004; Trinkler et al., 2011). Moreover, many genes related to calcium metabolism and carbonic anhydrase gene were highly expressed in the hemocytes, indicating that some hemocytes may accumulate calcium in the form of calcium carbonate and ultimately produce $CaCO_3$ crystals (Huang et al., 2018). If these hemocytes are responsible for calcium storage and transportation, there should be a reverse process for the release of calcium (or calcium carbonate), which is largely unknown.

FINAL REMARKS

Great progress has been made to elucidate cellular and molecular events which lead to the final delicate shells. In this review, we underscored some specific considerations that should be taken seriously when studying shell biomineralization. Due to the lack of proper research models for *in situ* observation, a large part of the knowledge was obtained from indirect evidence. *In vitro* $CaCO_3$ crystallization experiments facilitate elucidation of SMP functions, which, however, would lead to misleading conclusions if the reaction conditions were not properly set. Moreover, studies resolving biomineralization mechanism are limited within only a few model species. More representative species should be included to fulfill the whole map of shell formation and evolution.

AUTHOR CONTRIBUTIONS

JH contributed to the design of the study, drafted the manuscript and provided financial support; RZ provided financial support and revised the manuscript. All authors gave final approval for publication.

FUNDING

This work was supported by the National Natural Science Foundation of China Grants 32072951 and 42106091, and the Fundamental Research Funds for the Central Universities, Sun Yat-sen University, 2021qntd13.

REFERENCES

Addadi, L., Joester, D., Nudelman, F., and Weiner, S. (2006). Mollusk Shell Formation: A Source of New Concepts for Understanding Biomineralization Processes. *Chem-Eur. J.* 12 (4), 981–987. doi: 10.1002/chem.200500980

Addadi, L., Moradian, J., Shay, E., Maroudas, N. G., and Weiner, S. (1987). A Chemical Model for the Cooperation of Sulfates and Carboxylates in Calcite Crystal Nucleation: Relevance to Biomineralization. *Proc. Natl. Acad. Sci. U. S. A.* 84 (9), 2732–2736. doi: 10.1073/pnas.84.9.2732

Addadi, L., and Weiner, S. (2014). Biomineralization: Mineral Formation by Organisms. *Phys. Scripta.* 89 (9). doi: 10.1088/0031-8949/89/9/098003

Alberti, S., Gladfelter, A., and Mittag, T. (2019). Considerations and Challenges in Studying Liquid-Liquid Phase Separation and Biomolecular Condensates. *Cell* 176 (3), 419–434. doi: 10.1016/j.cell.2018.12.035

Allam, B., Paillard, C., and Auffret, M. (2000). Alterations in Hemolymph and Extrapallial Fluid Parameters in the Manila Clam, *Ruditapes Philippinarum*, Challenged With the Pathogen Vibrio Tapetis. *J. Invertebr. Pathol.* 76 (1), 63–69. doi: 10.1006/jipa.2000.4940

Bahn, S. Y., Jo, B. H., Choi, Y. S., and Cha, H. J. (2017). Control of Nacre Biomineralization by Pif80 in Pearl Oyster. *Sci. Adv.* 3 (8). doi: 10.1126/sciadv.1700765

Bahn, S. Y., Jo, B. H., Hwang, B. H., Choi, Y. S., and Cha, H. J. (2015). Role of Pif97 in Nacre Biomineralization: *In Vitro* Characterization of Recombinant Pif97 as a Framework Protein for the Association of Organic-Inorganic Layers in Nacre. *Cryst. Growth Des.* 15 (8), 3666–3673. doi: 10.1021/acs.cgd.5b00275

Balthasar, U., and Cusack, M. (2015). Aragonite-Calcite Seas-Quantifying the Gray Area. *Geology* 43 (2), 99–102. doi: 10.1130/G36293.1

Bayerlein, B., Zaslansky, P., Dauphin, Y., Rack, A., Fratzl, P., and Zlotnikov, I. (2014). Self-Similar Mesostructure Evolution of the Growing Mollusc Shell Reminiscent of Thermodynamically Driven Grain Growth. *Nat. Mat.* 13 (12), 1102–1107. doi: 10.1038/Nmat4110

Bleher, R., and Machado, J. (2004). Paracellular Pathway in the Shell Epithelium of Anodonta Cygnea. *J. Exp. Zool. Part A.* 301a (5), 419–427. doi: 10.1002/jez.a.20065

Boeynaems, S., Bogaert, E., Kovacs, D., Konijnenberg, A., Timmerman, E., Volkov, A., et al. (2017). Phase Separation of C9orf72 Dipeptide Repeats Perturbs Stress Granule Dynamics. *Mol. Cell.* 65 (6), 1044–1055. doi: 10.1016/j.molcel.2017.02.013

Brangwynne, C. P., Tompa, P., and Pappu, R. V. (2015). Polymer Physics of Intracellular Phase Transitions. *Nat. Phys.* 11 (11), 899–904. doi: 10.1038/Nphys3532

Buddawong, T., Asuvapongpatana, S., Suwannasing, C., Habuddha, V., Sukonset, C., Sombutkayasith, C., et al. (2021). Calcineurin Subunit B is Involved in Shell Regeneration in *Haliotis Diversicolor*. *Peerj* 9. doi: 10.7717/peerj.10662

Checa, A. (2000). A New Model for Periostracum and Shell Formation in Unionidae (Bivalvia, Mollusca). *Tissue Cell.* 32 (5), 405–416. doi: 10.1054/tice.2000.0129

Checa, A. G. (2018). Physical and Biological Determinants of the Fabrication of Molluscan Shell Microstructures. *Front. Mar. Sci.* 5. doi: 10.3389/fmars.2018.00353

Checa, A. G., Esteban-Delgado, F. J., Ramirez-Rico, J., and Rodriguez-Navarro, A. B. (2009). Crystallographic Reorganization of the Calcitic Prismatic Layer of Oysters. *J. Struct. Biol.* 167 (3), 261–270. doi: 10.1016/j.jsb.2009.06.009

Checa, A. G., Macias-Sanchez, E., Harper, E. M., and Cartwright, J. H. (2016). Organic Membranes Determine the Pattern of the Columnar Prismatic Layer of Mollusc Shells. *Proc. Biol. Sci.* 283 (1830). doi: 10.1098/rspb.2016.0032

Checa, A. G., Macias-Sanchez, E., and Ramirez-Rico, J. (2016). Biological Strategy for the Fabrication of Highly Ordered Aragonite Helices: The Microstructure of the Cavolinioidean Gastropods. *Sci. Rep.* 6. doi: 10.1038/srep25989

Checa, A. G., Salas, C., Harper, E. M., and Bueno-Perez, J. D. (2014). Early Stage Biomineralization in the Periostracum of the 'Living Fossil' Bivalve Neotrigonia. *PloS One* 9 (2). doi: 10.1371/journal.pone.0090033

Choudhary, M. K., Jain, R., and Rimer, J. D. (2020). *In Situ* Imaging of Two-Dimensional Surface Growth Reveals the Prevalence and Role of Defects in Zeolite Crystallization. *P. Natl. Acad. Sci. U.S.A.* 117 (46), 28632–28639. doi: 10.1073/pnas.2011806117

Clark, M. S. (2020). Molecular Mechanisms of Biomineralization in Marine Invertebrates. *J. Exp. Biol.* 223 (Pt 11). doi: 10.1242/jeb.206961

Crenshaw, M. A. (1972). The Inorganic Composition of Molluscan Extrapallial Fluid. *Biol. Bull.* 143 (3), 506–512. doi: 10.2307/1540180

Dauphin, Y. (2003). Soluble Organic Matrices of the Calcitic Prismatic Shell Layers of Two Pteriomorphid Bivalves - *Pinna Nobilis* and Pinctada Margaritifera. *J. Biol. Chem.* 278 (17), 15168–15177. doi: 10.1074/jbc.M204375200

Davis, B. D., and Tai, P. C. (1980). The Mechanism of Protein Secretion Across Membranes. *Nature* 283 (5746), 433–438. doi: 10.1038/283433a0

de Nooijer, L. J., Toyofuku, T., and Kitazato, H. (2009). Foraminifera Promote Calcification by Elevating Their Intracellular Ph. *P. Natl. Acad. Sci. U.S.A.* 106 (36), 15374–15378. doi: 10.1073/pnas.0904306106

Distel, D. L., Altamia, M. A., Lin, Z. J., Shipway, J. R., Han, A., Forteza, I., et al. (2017). Discovery of Chemoautotrophic Symbiosis in the Giant Shipworm *Kuphus Polythalamia* (Bivalvia: Teredinidae) Extends Wooden-Steps Theory. *P. Natl. Acad. Sci. U.S.A.* 114 (18), E3652–E36E8. doi: 10.1073/pnas.1620470114

Drake, J. L., Mass, T., Haramaty, L., Zelzion, E., Bhattacharya, D., and Falkowski, P. G. (2013). Proteomic Analysis of Skeletal Organic Matrix From the Stony Coral Stylophora Pistillata. *P. Natl. Acad. Sci. U.S.A.* 110 (10), 3788–3793. doi: 10.1073/pnas.1301419110

Dzuricky, M., Rogers, B. A., Shahid, A., Cremer, P. S., and Chilkoti, A. (2020). *De Novo* Engineering of Intracellular Condensates Using Artificial Disordered Proteins. *Nat. Chem.* 12 (9), 814–825. doi: 10.1038/s41557-020-0511-7

Falini, G., Albeck, S., Weiner, S., and Addadi, L. (1996). Control of Aragonite or Calcite Polymorphism by Mollusk Shell Macromolecules. *Science* 271 (5245), 67–69. doi: 10.1126/science.271.5245.67

Fang, D., Pan, C., Lin, H., Lin, Y., Zhang, G., Wang, H., et al. (2012). Novel Basic Protein, PfN23, Functions as Key Macromolecule During Nacre Formation. *J. Biol. Chem.* 287 (19), 15776–15785. doi: 10.1074/jbc.M112.341594

Finn, R. D., Bateman, A., Clements, J., Coggill, P., Eberhardt, R. Y., Eddy, S. R., et al. (2014). Pfam: The Protein Families Database. *Nucleic Acids Res.* 42 (D1), D222–DD30. doi: 10.1093/nar/gkt1223

Friedman, G. M., and Chamberlain, J. A.Jr. (1995). Archanodon Catskillensis (Vanuxem): Fresh-Water Clams From One of the Oldest Back-Swamp Fluvial Facies (Upper Middle Devonian), Catskill Mountains, New York. *Northeastern. Geol. Environ. Sci.* 17 (4), 431–443.

Gal, A., Kahil, K., Vidavsky, N., DeVol, R. T., Gilbert, P. U. P. A., Fratzl, P., et al. (2014). Particle Accretion Mechanism Underlies Biological Crystal Growth From an Amorphous Precursor Phase. *Adv. Funct. Mater.* 24 (34), 5420–5426. doi: 10.1002/adfm.201400676

Gao, P., Liao, Z., Wang, X. X., Bao, L. F., Fan, M. H., Li, X. M., et al. (2015). Layer-By-Layer Proteomic Analysis of Mytilus Galloprovincialis Shell. *PloS One* 10 (7). doi: 10.1371/journal.pone.0133913

Grefsrud, E. S., Dauphin, Y., Cuif, J. P., Denis, A., and Strand, O. (2008). Modifications in Microstructure of Cultured and Wild Scallop Shells (*Pecten Maximus*). *J. Shellfish. Res.* 27 (4), 633–641. doi: 10.2983/0730-8000(2008)27[633:Mimoca]2.0.Co;2

Hattan, S. J., Laue, T. M., and Chasteen, N. D. (2001). Purification and Characterization of a Novel Calcium-Binding Protein From the Extrapallial Fluid of the Mollusc, Mytilus Edulis. *J. Biol. Chem.* 276 (6), 4461–4468. doi: 10.1074/jbc.M006803200

Hautmann, M. (2001). Taxonomy and Phylogeny of Cementing Triassic Bivalves (Families Prospondylidae, Plicatulidae, Dimyidae and Ostreidae). *Palaeontology* 44, 339–373. doi: 10.1111/1475-4983.00183

Hayes, R. L., and Goreau, N. I. (1977). Intracellular Crystal-Bearing Vesicles in the Epidermis of Scleractinian Corals, Astrangia Danae (Agassiz) and Porites Porites (Pallas). *Biol. Bull.* 152 (1), 26–40. doi: 10.2307/1540724

Hendley, C. T., Tao, J. H., Kunitake, J. A. M. R., De Yoreo, J. J., and Estroff, L. A. (2015). Microscopy Techniques for Investigating the Control of Organic Constituents on Biomineralization. *Mrs. Bulletin.* 40 (6), 480–489. doi: 10.1557/mrs.2015.98

Huang, J., Li, L., Jiang, T., Xie, L., and Zhang, R. (2022). Mantle Tissue in the Pearl Oyster *Pinctada Fucata* Secretes Immune Components *via* Vesicle Transportation. *Fish. Shellfish. Immunol.* 121, 116–123. doi: 10.1016/j.fsi.2022.01.001

Huang, J., Li, S., Liu, Y., Liu, C., Xie, L., and Zhang, R. (2018). Hemocytes in the Extrapallial Space of *Pinctada Fucata* are Involved in Immunity and Biomineralization. *Sci. Rep.* 8 (1), 4657. doi: 10.1038/s41598-018-22961-y

Huang, J., Liu, Y., Liu, C., Xie, L., and Zhang, R. (2021). Heterogeneous Distribution of Shell Matrix Proteins in the Pearl Oyster Prismatic Layer. *Int. J. Biol. Macromol.* 189, 641–648. doi: 10.1016/j.ijbiomac.2021.08.075

Jia, G., Liang, J., Xie, J., Wang, J., Bao, Z., Xie, L., et al. (2015). cfMSP-1, an Extremely Acidic Matrix Protein Involved in Shell Formation of the Scallop Chlamys Farreri. *Comp. Biochem. Physiol. B. Biochem. Mol. Biol.* 185, 34–41. doi: 10.1016/j.cbpb.2015.03.004

Johnstone, M. B., Ellis, S., and Mount, A. S. (2008). Visualization of Shell Matrix Proteins in Hemocytes and Tissues of the Eastern Oyster, Crassostrea Virginica. *J. Exp. Zool. Part B.* 310b (3), 227–239. doi: 10.1002/jez.b.21206

Johnstone, M. B., Gohad, N. V., Falwell, E. P., Hansen, D. C., Hansen, K. M., and Mount, A. S. (2015). Cellular Orchestrated Biomineralization of Crystalline Composites on Implant Surfaces by the Eastern Oyster, *Crassostrea Virginica* (Gmelin, 1791). *J. Exp. Mar. Biol. Ecol.* 463, 8–16. doi: 10.1016/j.jembe.2014.10.014

Kádár, E. (2008). Haemocyte Response Associated With Induction of Shell Regeneration in the Deep-Sea Vent Mussel *Bathymodiolus Azoricus* (Bivalvia: Mytilidae). *J. Exp. Mar. Biol. Ecol.* 362 (2), 71–78. doi: 10.1016/j.jembe.2008.05.014

Kanaan, N. M., Hamel, C., Grabinski, T., and Combs, B. (2020). Liquid-Liquid Phase Separation Induces Pathogenic Tau Conformations In Vitro. *Nat. Commun.* 11 (1). doi: 10.1038/s41467-020-16580-3

Kong, J. J., Liu, C., Yang, D., Yan, Y., Chen, Y., Huang, J. L., et al. (2018). Alv Protein Plays Opposite Roles in the Transition of Amorphous Calcium Carbonate to Calcite and Aragonite During Shell Formation. *Cryst. Growth Des.* 18 (7), 3794–3804. doi: 10.1021/acs.cgd.8b00025

Levi-Kalisman, Y., Falini, G., Addadi, L., and Weiner, S. (2001). Structure of the Nacreous Organic Matrix of a Bivalve Mollusk Shell Examined in the Hydrated State Using Cryo-TEM. *J. Struct. Biol.* 135 (1), 8–17. doi: 10.1006/jsbi.2001.4372

Liang, J., Xu, G., Xie, J., Lee, I., Xiang, L., Wang, H., et al. (2015). Dual Roles of the Lysine-Rich Matrix Protein (KRMP)-3 in Shell Formation of Pearl Oyster, Pinctada Fucata. *PloS One* 10 (7), e0131868. doi: 10.1371/journal.pone.0131868

Li, S., Liu, Y., Liu, C., Huang, J., Zheng, G., Xie, L., et al. (2016). Hemocytes Participate in Calcium Carbonate Crystal Formation, Transportation and Shell Regeneration in the Pearl Oyster Pinctada Fucata. *Fish. Shellfish. Immunol.* 51, 263–270. doi: 10.1016/j.fsi.2016.02.027

Li, C., Liu, X., Liu, B., Ma, B., Liu, F. Q., Liu, G. L., et al. (2018). Draft Genome of the Peruvian Scallop *Argopecten Purpuratus*. *Gigascience* 7 (4). doi: 10.1093/gigascience/giy031

Liu, C., Ji, X., Huang, J., Wang, Z., Liu, Y., and Hincke, M. T. (2021). Proteomics of Shell Matrix Proteins From the Cuttlefish Bone Reveals Unique Evolution for Cephalopod Biomineralization. *ACS Biomat. Sci. Eng.* doi: 10.1021/acsbiomaterials.1c00693

Liu, X. J., and Li, J. L. (2015). Formation of the Prismatic Layer in the Freshwater Bivalve *Hyriopsis Curninqii*: The Feedback of Crystal Growth on Organic Matrix. *Acta Zool-Stockholm.* 96 (1), 30–36. doi: 10.1111/azo.12048

Liu, C., Li, S. G., Kong, J. J., Liu, Y. J., Wang, T. P., Xie, L. P., et al. (2015). In-Depth Proteomic Analysis of Shell Matrix Proteins of Pinctada Fucata. *Sci. Rep.* 5. doi: 10.1038/srep17269

Liu, C., Xu, G. R., Du, J. Z., Sun, J., Wan, X., Liu, X. J., et al. (2018). Mineralization of Nacre-Like Structures Mediated by Extrapallial Fluid on Pearl Nucleus. *Cryst. Growth Des.* 18 (1), 32–36. doi: 10.1021/acs.cgd.7b01316

Liu, C., and Zhang, R. Q. (2021). Biomineral Proteomics: A Tool for Multiple Disciplinary Studies. *J. Proteomics* 238. doi: 10.1016/j.jprot.2021.104171

Li, S., Xie, L. P., Ma, Z. J., and Zhang, R. Q. (2005). cDNA Cloning and Characterization of a Novel Calmodulin-Like Protein From Pearl Oyster Pinctada Fucata. *FEBS J.* 272 (19), 4899–4910. doi: 10.1111/j.1742-4658.2005.04899.x

Lowenstam, H., and Weiner, S. (1989). *On Biomineralization* (New York: Oxford University Press).

Ma, Z., Huang, J., Sun, J., Wang, G., Li, C., Xie, L., et al. (2007). A Novel Extrapallial Fluid Protein Controls the Morphology of Nacre Lamellae in the Pearl Oyster, Pinctada Fucata. *J. Biol. Chem.* 282 (32), 23253–23263. doi: 10.1074/jbc.M700001200

Marie, B., Joubert, C., Tayale, A., Zanella-Cleon, I., Belliard, C., Piquemal, D., et al. (2012). Different Secretory Repertoires Control the Biomineralization Processes of Prism and Nacre Deposition of the Pearl Oyster Shell. *Proc. Natl. Acad. Sci. U. S. A.* 109 (51), 20986–20991. doi: 10.1073/pnas.1210552109

Marie, B., Luquet, G., De Barros, J. P. P., Guichard, N., Morel, S., Alcaraz, G., et al. (2007). The Shell Matrix of the Freshwater Mussel *Unio Pictorum* (Paleoheterodonta, Unionoida). *FEBS J.* 274 (11), 2933–2945. doi: 10.1111/j.1742-4658.2007.05825.x

Marie, B., Ramos-Silva, P., Marin, F., and Marie, A. (2013). Proteomics of $CaCO_3$ Biomineral-Associated Proteins: How to Properly Address Their Analysis. *Proteomics* 13 (21), 3109–3116. doi: 10.1002/pmic.201300162

Marin, F., Luquet, G., Marie, B., and Medakovic, D. (2008). Molluscan Shell Proteins: Primary Structure, Origin, and Evolution. *Curr. Top. Dev. Biol.* 80, 209–276. doi: 10.1016/S0070-2153(07)80006-8

Marin, F., Roy, N. L., and Marie, B. (2012). The Formation and Mineralization of Mollusk Shell. *Front. Biosci.* S4, 1099–1125. doi: 10.2741/321

McDougall, C., Aguilera, F., and Degnan, B. M. (2013). Rapid Evolution of Pearl Oyster Shell Matrix Proteins With Repetitive, Low-Complexity Domains. *J. R. Soc. Interface.* 10 (82). doi: 10.1098/rsif.2013.0041

McDougall, C., and Degnan, B. M. (2018). The Evolution of Mollusc Shells. *Wire. Dev. Biol.* 7 (3). doi: 10.1002/wdev.313

Miyamoto, H., Miyoshi, F., and Kohno, J. (2005). The Carbonic Anhydrase Domain Protein Nacrein is Expressed in the Epithelial Cells of the Mantle and Acts as a Negative Regulator in Calcification in the Mollusc Pinctada Fucata. *Zool. Sci.* 22 (3), 311–315. doi: 10.2108/zsj.22.311

Mount, A. S., Wheeler, A. P., Paradkar, R. P., and Snider, D. (2004). Hemocyte-Mediated Shell Mineralization in the Eastern Oyster. *Science* 304 (5668), 297–300. doi: 10.1126/science.1090506

Murgarella, M., Puiu, D., Novoa, B., Figueras, A., Posada, D., and Canchaya, C. (2016). A First Insight Into the Genome of the Filter-Feeder Mussel *Mytilus Galloprovincialis*. *PloS One* 11 (3). doi: 10.1371/journal.pone.0151561

Nair, P. S., and Robinson, W. E. (1998). Calcium Speciation and Exchange Between Blood and Extrapallial Fluid of the Quahog *Mercenaria Mercenaria* (L.). *Biol. Bull.* 195 (1), 43–51. doi: 10.2307/1542774

Okumura, T., Suzuki, M., Nagasawa, H., and Kogure, T. (2010). Characteristics of Biogenic Calcite in the Prismatic Layer of a Pearl Oyster, Pinctada Fucata. *Micron* 41 (7), 821–826. doi: 10.1016/j.micron.2010.05.004

Pan, C., Fang, D., Xu, G., Liang, J., Zhang, G., Wang, H., et al. (2014). A Novel Acidic Matrix Protein, PfN44, Stabilizes Magnesium Calcite to Inhibit the Crystallization of Aragonite. *J. Biol. Chem.* 289 (5), 2776–2787. doi: 10.1074/jbc.M113.504027

Pietrzak, J. E., Bates, J. M., and Scott, R. M. (1976). Constituents of Unionid Extrapallial Fluid. Ii Ph and Metal Ion Composition. *Hydrobiologia* 50, 89–93. doi: 10.1007/BF00016846

Plazzi, F., and Passamonti, M. (2010). Towards a Molecular Phylogeny of Mollusks: Bivalves' Early Evolution as Revealed by Mitochondrial Genes. *Mol. Phylogenet. Evol.* 57 (2), 641–657. doi: 10.1016/j.ympev.2010.08.032

Politi, Y., Mahamid, J., Goldberg, H., Weiner, S., and Addadi, L. (2007). Asprich Mollusk Shell Protein: *In Vitro* Experiments Aimed at Elucidating Function in $CaCO_3$ Crystallization. *Crystengcomm* 9 (12), 1171–1177. doi: 10.1039/b709749b

Ponce, C. B., and Evans, J. S. (2011). Polymorph Crystal Selection by N16, an Intrinsically Disordered Nacre Framework Protein. *Cryst. Growth Des.* 11 (10), 4690–4696. doi: 10.1021/cg201015w

Porter, S. M. (2010). Calcite and Aragonite Seas and the *De Novo* Acquisition of Carbonate Skeletons. *Geobiology* 8 (4), 256–277. doi: 10.1111/j.1472-4669.2010.00246.x

Rivera-Perez, C., and Hernandez-Saavedra, N. Y. (2021). Review: Post-Translational Modifications of Marine Shell Matrix Proteins. *Comp. Biochem. Phys. B.* 256. doi: 10.1016/j.cbpb.2021.110641

Robert, B., and Lorens, M. L. B. (1980). The Impact of Solution Chemistry on *Mytilus Edulis* Calcite and Aragonite. *Geochim. Cosmochim. Ac.* 44 (9), 1265–1278. doi: 10.1016/0016-7037(80)90087-3

Rosenberg, G. (2014). A New Critical Estimate of Named Species-Level Diversity of the Recent Mollusca. *Am. Malacol. Bull.* 32 (2), 308–322. doi: 10.4003/006.032.0204

Samata, T., Ikeda, D., Kajikawa, A., Sato, H., Nogawa, C., Yamada, D., et al. (2008). A Novel Phosphorylated Glycoprotein in the Shell Matrix of the Oyster Crassostrea Nippona. *FEBS J.* 275 (11), 2977–2989. doi: 10.1111/j.1742-4658.2008.06453.x

Shen, X., Belcher, A. M., Hansma, P. K., Stucky, G. D., and Morse, D. E. (1997). Molecular Cloning and Characterization of Lustrin A, a Matrix Protein From Shell and Pearl Nacre of Haliotis Rufescens. *J. Biol. Chem.* 272 (51), 32472–32481. doi: 10.1074/jbc.272.51.32472

Sillanpaa, J. K., Sundh, H., and Sundell, K. S. (1891). Calcium Transfer Across the Outer Mantle Epithelium in the Pacific Oyster, Crassostrea Gigas. *P. Roy. Soc. B-Biol. Sci.* 2018, 285. doi: 10.1098/rspb.2018.1676

Silverman, H., Richard, P. E., Goddard, R. H., and Dietz, T. H. (1988). Intracellular Formation of Calcium Concretions by Phagocytic Cells in Freshwater Mussels. *Can. J. Zool.* 67 (1), 198–207. doi: 10.1139/z89-027

Silverman, H., Steffens, W. L., and Dietz, T. H. (1983). Calcium Concretions in the Gills of a Freshwater Mussel Serve as a Calcium Reservoir During Periods of Hypoxia. *J. Exp. Zool.* 227 (2), 177–189. doi: 10.1002/jez.1402270203

Sorrosa, J. M., Satoh, M., and Shiraiwa, Y. (2005). Low Temperature Stimulates Cell Enlargement and Intracellular Calcification of Coccolithophorids. *Mar. Biotechnol.* 7 (2), 128–133. doi: 10.1007/s10126-004-0478-1

Sudo, S., Fujikawa, T., Nagakura, T., Ohkubo, T., Sakaguchi, K., Tanaka, M., et al. (1997). Structures of Mollusc Shell Framework Proteins. *Nature* 387 (6633), 563–564. doi: 10.1038/42391

Suzuki, M., Saruwatari, K., Kogure, T., Yamamoto, Y., Nishimura, T., Kato, T., et al. (2009). An Acidic Matrix Protein, Pif, is a Key Macromolecule for Nacre Formation. *Science* 325 (5946), 1388–1390. doi: 10.1126/science.1173793

Sviben, S., Gal, A., Hood, M. A., Bertinetti, L., Politi, Y., Bennet, M., et al. (2016). A Vacuole-Like Compartment Concentrates a Disordered Calcium Phase in a Key Coccolithophorid Alga. *Nat. Commun.* 7. doi: 10.1038/ncomms11228

Takeuchi, T., Kawashima, T., Koyanagi, R., Gyoja, F., Tanaka, M., Ikuta, T., et al. (2012). Draft Genome of the Pearl Oyster *Pinctada Fucata*: A Platform for Understanding Bivalve Biology. *DNA Res.* 19 (2), 117–130. doi: 10.1093/dnares/dss005

Takeuchi, T., Sarashina, I., Iijima, M., and Endo, K. (2008). *In Vitro* Regulation of $CaCO_3$ Crystal Polymorphism by the Highly Acidic Molluscan Shell Protein Aspein. *FEBS Lett.* 582 (5), 591–596. doi: 10.1016/j.febslet.2008.01.026

Taylor, J. D., and Kennedy, W. J. (1969). The Influence of the Periostracum on the Shell Structure of Bivalve Molluscs. *Calcif. Tissue Res.* 3 (3), 274–283. doi: 10.1007/BF02058669

Trinkler, N., Bardeau, J. F., Marin, F., Labonne, M., Jolivet, A., Crassous, P., et al. (2011). Mineral Phase in Shell Repair of Manila Clam *Venerupis Philippinarum* Affected by Brown Ring Disease. *Dis. Aquat. Organ.* 93 (2), 149–162. doi: 10.3354/dao02288

Varney, R. M., Speiser, D. I., McDougall, C., Degnan, B. M., and Kocot, K. M. (2021). The Iron-Responsive Genome of the Chiton *Acanthopleura Granulata*. *Genome Biol. Evol.* 13 (1). doi: 10.1093/gbe/evaa263

Vavouraki, A. I., Putnis, C. V., Putnis, A., and Koutsoukos, P. G. (2008). An Atomic Force Microscopy Study of the Growth of Calcite in the Presence of Sodium Sulfate. *Chem. Geol.* 253 (3-4), 243–251. doi: 10.1016/j.chemgeo.2008.05.013

Wang, X. T., Li, L., Zhu, Y. B., Du, Y. S., Song, X. R., Chen, Y. X., et al. (2013). Oyster Shell Proteins Originate From Multiple Organs and Their Probable Transport Pathway to the Shell Formation Front. *PloS One* 8 (6). doi: 10.1371/journal.pone.0066522

Wang, S., Zhang, J. B., Jiao, W. Q., Li, J., Xun, X. G., Sun, Y., et al. (2017). Scallop Genome Provides Insights Into Evolution of Bilaterian Karyotype and Development. *Nat. Ecol. Evol.* 1 (5). doi: 10.1038/s41559-017-0120

Weiner, S., and Dove, P. M. (2003). An Overview of Biomineralization Processes and the Problem of the Vital Effect. *Rev. Mineral. Geochem.* 54, 1–29. doi: 10.2113/0540001

Weiner, S., and Hood, L. (1975). Soluble Protein of the Organic Matrix of Mollusk Shells: A Potential Template for Shell Formation. *Science* 190 (4218), 987–989. doi: 10.1126/science.1188379

Weiss, I. M., Tuross, N., Addadi, L., and Weiner, S. (2002). Mollusc Larval Shell Formation: Amorphous Calcium Carbonate is a Precursor Phase for Aragonite. *J. Exp. Zool.* 293 (5), 478–491. doi: 10.1002/jez.90004

Xiang, L., Kong, W., Su, J. T., Liang, J., Zhang, G. Y., Xie, L. P., et al. (2014). Amorphous Calcium Carbonate Precipitation by Cellular Biomineralization in Mantle Cell Cultures of *Pinctada Fucata*. *PloS One* 9 (11). doi: 10.1371/journal.pone.0113150

Xie, J. (2016). *The Mechanism Study of Extrapallial Fluid Protein in the Shell Formation of Pinctada Fucata* (Beijing: Tsinghua University).

Xie, J., Liang, J., Sun, J., Gao, J., Zhang, S. R., Liu, Y. J., et al. (2016). Influence of the Extrapallial Fluid of *Pinctada Fucata* on the Crystallization of Calcium Carbonate and Shell Biomineralization. *Cryst. Growth Des.* 16 (2), 672–680. doi: 10.1021/acs.cgd.5b01203

Yang, J. L., Feng, D. D., Liu, J., Xu, J. K., Chen, K., Li, Y. F., et al. (2021). Chromosome-Level Genome Assembly of the Hard-Shelled Mussel Mytilus Coruscus, a Widely Distributed Species From the Temperate Areas of East Asia. *Gigascience* 10 (4). doi: 10.1093/gigascience/giab024

Yang, T., Jia, Z., Chen, H. S., Deng, Z. F., Liu, W. K., Chen, L. N., et al. (2020). Mechanical Design of the Highly Porous Cuttlebone: A Bioceramic Hard Buoyancy Tank for Cuttlefish. *P. Natl. Acad. Sci. U.S.A.* 117 (38), 23450–23459. doi: 10.1073/pnas.2009531117

Yao, N., Epstein, A., and Akey, A. (2006). Crystal Growth *via* Spiral Motion in Abalone Shell Nacre. *J. Mat. Res.* 21 (8), 1939–1946. doi: 10.1557/Jmr.2006.0252

Yue, X., Zhang, S. J., Yu, J. J., and Liu, B. Z. (2019). Identification of a Laccase Gene Involved in Shell Periostracal Tanning of the Clam Meretrix Petechialis. *Aquat. Biol.* 28, 55–65. doi: 10.3354/ab00709

Zhang, G., Fang, X., Guo, X., Li, L., Luo, R., Xu, F., et al. (2012). The Oyster Genome Reveals Stress Adaptation and Complexity of Shell Formation. *Nature* 490 (7418), 49–54. doi: 10.1038/nature11413

Zhang, X., Xia, Z. H., Liu, X. J., and Li, J. L. (2021). The Novel Matrix Protein Hic7 of Hyriopsis Cumingii Participates in the Formation of the Shell and Pearl. *Comp. Biochem. Phys. B.* 256. doi: 10.1016/j.cbpb.2021.110640

Zhang, C., Xie, L., Huang, J., Liu, X., and Zhang, R. (2006). A Novel Matrix Protein Family Participating in the Prismatic Layer Framework Formation of Pearl Oyster, Pinctada Fucata. *Biochem. Biophys. Res. Commun.* 344 (3), 735–740. doi: 10.1016/j.bbrc.2006.03.179

Conflict of Interest: The authors declare that the research was conducted in the absence of any commercial or financial relationships that could be construed as a potential conflict of interest.

Publisher's Note: All claims expressed in this article are solely those of the authors and do not necessarily represent those of their affiliated organizations, or those of the publisher, the editors and the reviewers. Any product that may be evaluated in this article, or claim that may be made by its manufacturer, is not guaranteed or endorsed by the publisher.

frontiers | Frontiers in Marine Science

BRIEF RESEARCH REPORT
published: 30 June 2022
doi: 10.3389/fmars.2022.904835

Proteomic Profiling of Black Coral (Antipatharia) Skeleton Reveals Hundreds of Skeleton-Associated Proteins Across Two Taxa

Jeana L. Drake[1†] *and Tali Mass*[1,2*]

[1] Department of Marine Biology, Leon H. Charney School of Marine Sciences, University of Haifa, Mount Carmel, Haifa, Israel,
[2] Morris Kahn Research Station, Leon H. Charney School of Marine Sciences, University of Haifa, Sdot Yam, Israel

OPEN ACCESS

Edited by:
Rebecca Metzler,
Colgate University, United States

Reviewed by:
Anderson B. Mayfield,
Coral Reef Diagnostics, United States
Xinguo Zhao,
Chinese Academy of Fishery Sciences (CAFS), China

***Correspondence:**
Tali Mass
tmass@univ.haifa.edu

†Present address:
Jeana L. Drake,
Earth, Planetary, and Space Sciences Department, University of California, Los Angeles, United States

Specialty section:
This article was submitted to Marine Molecular Biology and Ecology, a section of the journal Frontiers in Marine Science

Received: 25 March 2022
Accepted: 30 May 2022
Published: 30 June 2022

Citation:
Drake JL and Mass T (2022) Proteomic Profiling of Black Coral (Antipatharia) Skeleton Reveals Hundreds of Skeleton-Associated Proteins Across Two Taxa. Front. Mar. Sci. 9:904835. doi: 10.3389/fmars.2022.904835

Black corals, ecologically important cnidarians found from shallow to deep ocean depths, form a strong yet flexible skeleton of sclerotized chitin and other biomolecules including proteins. The structure and mechanical properties of the chitin component of the skeleton have been well-characterized. However, the protein component has remained a mystery. Here we used liquid chromatography-tandem mass spectrometry to sequence proteins extracted from two species of common Red Sea black corals following either one or two cleaning steps. We detected hundreds of proteins between the two corals, nearly 70 of which are each other's reciprocal best BLAST hit. Unlike stony corals, only a few of the detected proteins were moderately acidic (biased toward aspartic and/or glutamic acid residues) suggesting less of a role for these types of proteins in black coral skeleton formation as compared to stony corals. No distinct chitin binding domains were found in the proteins, but proteins annotated as having a role in protein and chitin modifications were detected. Our results support the integral role of proteins in black coral skeleton formation, structure, and function.

Keywords: antipatharians, chitin, chitinase, skeletal proteins, LC-MS/MS protein sequencing

INTRODUCTION

Antipatharians (black corals) are colonial cnidarians easily recognized by their black or golden brown chitinous skeletons. They are found from shallow to deep depths and in all oceans as well as the Mediterranean and Red Seas (Opresko, 2001; Wagner et al., 2012; Morgulis et al., 2022), although they face increasing pressure from harvesting (legal and illegal), invasive species, and contaminant introductions (Grigg, 2004; Todinanahary et al., 2016; Ruiz-Ramos et al., 2017). Their flexible skeletons, typically displaying small protrusions (spines), are covered by animal tissue with each polyp displaying six-fold symmetry (Opresko, 2001). At photic depths, they tend to grow in low light locations and are most frequently observed in locations with strong currents (Wagner et al., 2012; Morgulis et al., 2022).

Black corals are ecologically important as food, habitat/protection, and camouflage for a variety of invertebrates, fish, and mammals, particularly where the corals grow in high density (e.g., Parrish et al., 2002; Boland and Parrish, 2005; De Clippele et al., 2019), although they are not reef builders. Black corals can be home to a high density of organisms; in one study in the Philippines some black

coral forests were associated with over 8,000 individual invertebrates per m^2 (Suarez et al., 2015). Further, in areas with black coral forests, some fish taxa are found only within the colonies (e.g., Boland and Parrish, 2005). However, colonies can be damaged by a variety of human activities including bottom fishing and climate change (Deidun et al., 2015; Godefroid et al., 2022), and at least one species of black coral is considered endangered (IUCN, 2021).

While they have historically been used by humans as money (Tescione, 1973), jewelry (Gress and Andradi-Brown, 2018), and curios (Grigg, 1993), black corals also display a variety of medicinal properties. As suggested by their name (antipathes is Greek for "against diseases") black corals and their extracts have historically been used in medical treatments including antibacterial activity, reducing fever, pain, and swelling, treating ulcers, and curing lung conditions (Narchi et al., 2015; Peña Moreno, 2017). From a pharmacological perspective, chitin can be deacetylated in alkaline conditions or enzymatically converted to chitosan, a stable non-toxic polymer; this chitosan and its derivatives then displays antibacterial, antifungal, and antiviral properties (review by Nuc and Dobrzycka-Krahel, 2021). Laboratory studies have supported that several of these historical medicinal uses are biochemically founded. For example, mice exposed to cigarette smoke and black coral extract displayed higher superoxide dismutase and malondialdehyde activity and lower lung tissue inflammation than mice exposed to cigarette smoke alone (Bai et al., 2011).

The skeletons of black corals are formed of chitin and other biomolecules (Goldberg, 1976). No minerals are present in the sclerotized skeleton (Goldberg et al., 1994), although the anions iodine and bromine are abundant (Juárez-de la Rosa et al., 2007). Epithelial cells secrete the chitin and other biomolecules that form the extracellular skeleton as concentric layers with a hollow core within the skeleton stalk (Daly et al., 2007). While the chitinous component of the skeleton has been well-characterized in a number of black coral taxa (e.g., Kim et al., 1992; Nowak et al., 2009; Bo et al., 2012; Juárez-de la Rosa et al., 2012), much less is known about the proteinaceous component. Proteins make up around 50% of the skeleton (Goldberg et al., 1994). Glycine, alanine, and histidine are the most abundant amino acids, and treating skeletons with alkaline solutions results in protein loss and shifts in the relative abundance of amino acids (Goldberg et al., 1994).

It has been suggested that chitin provides a viscous-elastic response while the protein component provides a plastic response, yielding the high degree of flexibility of the skeleton (Juárez-de la Rosa et al., 2012). The arrangement of the chitin fibrils in a helical pattern layer by layer may also contribute to the flexibility and reduced buckling under stresses induced by the high water flow environments in which black corals are frequently found (Kim et al., 1992). Further, the spines on the skeleton are cemented to the skeleton creating fixed points to reduce delamination as the skeletons bend and twist in the current (Kim et al., 1992). These mechanical properties may be useful in industry when synthesizing new structural materials. Additional bio-inspiration to be taken from black coral skeleton could focus on the chitin and protein content of black corals, yielding nanocomposites with industrial and medicinal uses (João et al., 2017; Zheng et al., 2019).

To address the gaps in knowledge about particular biomolecules involved in formation of their chitinous skeleton, we use liquid chromatography-tandem mass spectrometry to characterize the protein composition of ground skeleton from two black coral species, *Antipathes griggi* and *Stichopathes* sp., two commonly occurring black corals in the northern Red Sea (**Figures 1A, B**) (Morgulis et al., 2022). We detected hundreds of proteins in the chitin skeleton of both species. Unlike stony corals, there are few proteins strongly biased toward the acidic amino acids. Gene ontology analysis and domain searching did not reveal any proteins with known chitin binding domains, although several proteins contained an abundance of amino acids associated with chitin binding. Nearly 70 proteins that are each other's reciprocal best BLAST hit were observed in both species, suggesting that, like stony corals, black corals may share a consensus skeletal 'toolkit' with a long evolutionary history (Zaquin et al., 2021). Our findings will be important in conservation, pharmaceutical development, and synthesizing materials inspired by strong yet flexible black coral skeletons.

METHODS

Specimen Collection

Several specimens of *Antipathes griggi* and *Stichopathes* sp. were collected at 40-60 m depth from the reef adjacent to the Interuniversity Institute in Eilat, Israel under a permit issued by the Israel Nature and Parks Authority (**Figures 1A, B**). Branches or coils of each species were clipped from colonies using underwater shears, segmented into 2-3 cm sections, and immediately transported to the laboratory for preservation in RNA/DNA Shield (Zymo) or 100% ethanol for protein extraction at 4°C. The next day, specimens were transported to the laboratory for processing.

Samples for Proteomics

Black coral segments of each species were combined and washed copiously in MilliQ water to remove the ethanol, soaked in a 10% bleach solution for 30 minutes at room temperature and for 1 hour with sonication, and then rinsed again with MilliQ and dried at 60°C. The bleaching process was repeated with 50% bleach and the sections were rinsed and re-dried. While the first wash removed most of the tissue, some tentacles of the polyps were still observed at low magnification light microscopy. The second higher concentration bleaching step appeared to remove all tissue by visual inspection. Dried skeletons were ground with a mortar and pestle; *Antipathes* skeletons ground to a finer powder than did *Stichopathes* skeletons. Ground powder was divided; half was used is-as while half was cleaned again in 50% bleach while sonicating for 2 hours, rinsed five times with MilliQ water, and dried at 60°C.

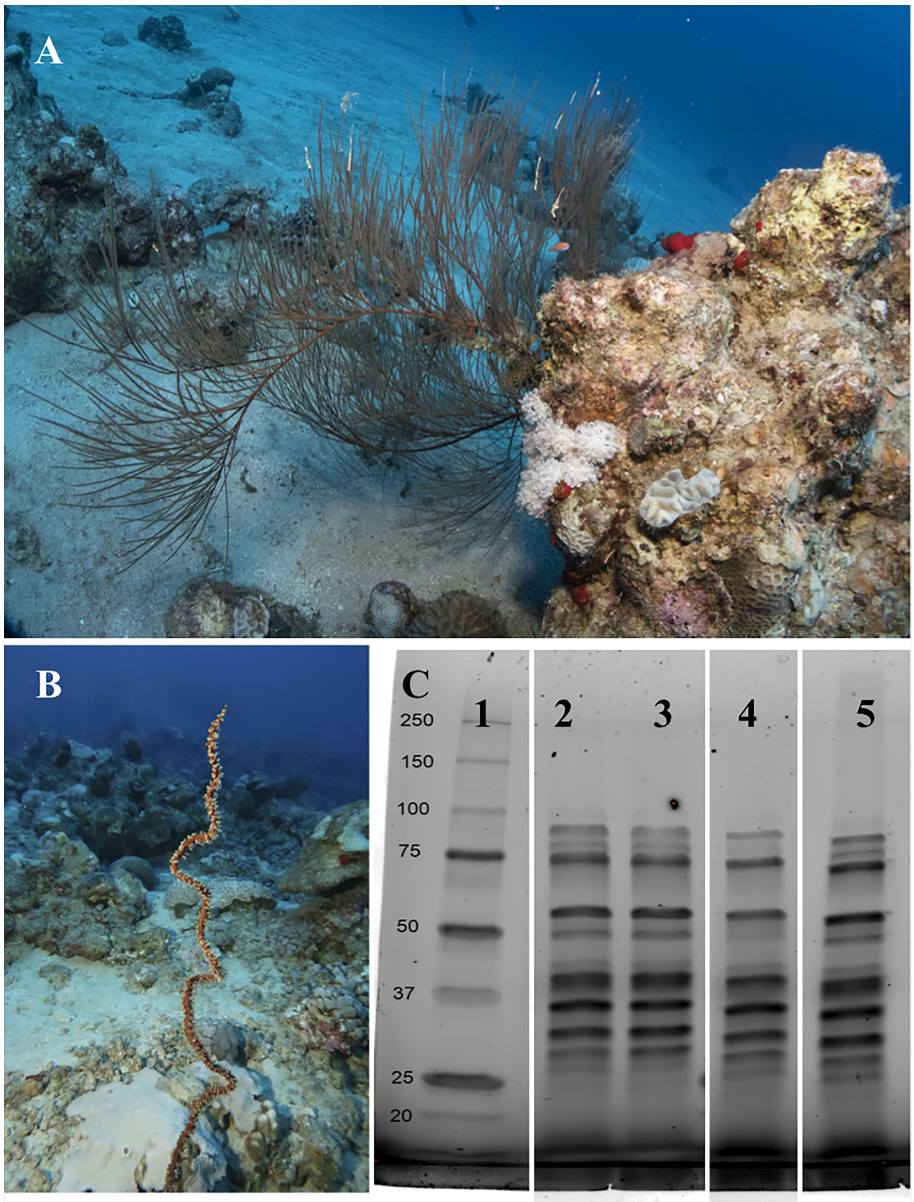

FIGURE 1 | *Antipathes griggi* **(A)** and *Stichopathes* sp. **(B)** collected from the Red Sea adjacent to the Interuniversity Institute in Eilat, Israel, at 40-60 m depth, for proteomic sequencing of the chitinous skeleton. **(C)** Imaging of SDS-PAGE separation of proteins extracted by chitinase from chitinous black coral skeleton cleaned both before and after grinding. MW marker (lane 1); *Antipathes* cleaned only before grinding (lane 2); *Stichopathes* cleaned only before grinding (lane 3); *Antipathes* cleaned before and after grinding (lane 4); *Stichopathes* cleaned before and after grinding (lane 5). Photos: Hagai Nativ.

Samples for Transcriptomics

One sample of fresh black coral tissue from each species was flash frozen and then RNA was extracted using the CTAB method (Wang and Stegemann, 2010), followed by use of a Purelink RNA Mini Kit following the manufacturer's instructions. RNA quality was examined by TapeStation (Agilent). Libraries were prepared using the INCPM-mRNA-seq (an internal protocol G-INCPM). The polyA fraction (mRNA) was purified from 500 ng of total RNA followed by fragmentation and generation of double-stranded cDNA. Then, end repair, A base addition, adapter ligation and PCR amplification steps were performed. Libraries were evaluated by Qubit (Thermo Fisher Scientific) and TapeStation (Agilent). Sequencing libraries were constructed with barcodes to allow multiplexing of samples. Around 140 million paired-end 150X2-bp reads were sequenced on an Illumina NovaSeq SP300 cyc. Poly-A/T stretches and Illumina adapters were trimmed from the reads using cutadapt; resulting reads shorter than 30 bp were discarded. Trimmed reads were used for assembly using Trinity (Trinity-v2.11.0) and likely bacterial contaminant sequences were filtered out. Highly

similar sequences were clustered with CD-hit (CD-HIT version 4.5.4). Completeness was assessed (BUSCO 4.1.4), with BUSCO scores of 73.8% and 77.2% for *Antipathes* and *Stichopathes*, respectively. Sequence reads were aligned using bowtie2 (version 2.3.4.1), with alignment rates of 97.5% and 95.3% for *Antipathes* and *Stichopathes*, respectively. ORF prediction was performed in TransDecoder-v3.0.1 based on blastp-v2.7.1. Finally, sequences were characterized by InterProScan and annotated in OmicsBox. Transcriptome information and sequences are available in NCBI BioProject PRJNA809900.

Protein Extraction

Four methods were tested for protein extraction from black coral skeleton powders: Soak in 1 ml each (1) 1 M HCl at room temperature for 1 hour (modified from Shimahara and Takiguchi, 1988); (2) 6 M guanidinium hydrochloride in 8 mM imidazole, 50 mM sodium phosphate monobasic, 50 mM Tris HCl at 30°C for 1 hour (modified from Gildemeister et al., 1994); (3) 50 mM dithiothreitol (DTT) at 100°C for 15 minutes (modified from Mathys et al., 1999); or (4) 1 mg/ml chitinase in PBS 37°C for 2 hours. At the end of the incubation periods all samples were pelleted at 500 xg for 5 minutes at room temperature. Protein concentration of supernatants was quantified by bicinchoninic acid (BCA) assay (**Supplementary Material Table 1**), proteins in 10 µg quantified total protein were visualized by SDS-PAGE separation on Mini-Protean TGX Stain-Free precast gels (BioRad) with 5-minute UV activation, and fractions were stored separately at -80°C until further analysis. Chitinase yielded the darkest bands on UV-activated Stain-Free gels (**Figure 1C**); therefore, only chitinase fractions were submitted for sequencing. HCl also yielded faint bands by SDS-PAGE that were observable after computationally increasing the image contrast (**Supplementary Material Figure 1A**); however, these samples were not submitted for sequencing due to the low protein yield. Guanidinium hydrochloride and DTT extracts did not show any protein bands by SDS-PAGE (**Supplementary Material Figures 1A, B**).

Protein Sequencing

Proteins extracted by chitinase from ground black coral skeleton cleaned only pre-grinding as well as skeleton cleaned again post-grinding were dissolved in 5% SDS and digested with trypsin using the S-trap method overnight at room temperature. Single samples of each species for each cleaning fraction were processed. The resulting peptides were analyzed using a nanoflow ultra-performance liquid chromatograph (nanoAcquity) coupled to a high resolution, high mass accuracy mass spectrometer (Fusion Lumos) fitted with a Symmetry C18 0.18*20mm trap column (Waters, Inc) for peptide trapping and then a HSS T3 0.075*250 mm column (Waters, Inc.) for peptide separation using a gradient of 4-28% (80% acetonitrile, 0.1% Formic acid) for 150 minutes. Spray voltage was set to +2kV. The data were acquired in a Fusion Lumos by a Top Speed Data-Dependent Acquisition method with a cycle time of 3 s. An MS1 scan was performed in the Orbitrap at 120,000 resolution with a maximum injection time of 60 ms and the data were scanned between 300-1800 m/z. MS2 was selected using a monoisotopic precursor selection set to peptides, peptide charge states set to +2-+8 and dynamic exclusion set to 30 s. MS2 was performed using HCD fragmentation scanning in the Orbitrap, with the first mass set to 130 m/z at a resolution of 15,000. Maximum injection time was set to 60 ms with automatic gain control of $5x10^{-4}$ ions as a fill target. The resulting data were searched against the protein databases derived from our *de novo* black coral transcriptomes described above using the Byonic search engine (Protein Metrics Inc.). A first search was carried out without any false discovery rate (FDR) filtering, to generate a focused database for a second search. The second search was set to 1% FDR, allowing fixed carbamidomethylation on C and variable oxidation on MW, deamidation on NQ and protein N-terminal acetylation. The mass spectrometry proteomics data have been deposited to the ProteomeXchange Consortium *via* the Pride partner repository (Perez-Riverol et al., 2019), under the dataset identifier PXD032043.

Data Sorting

The *de novo* transcriptomes described above for *Antipathes griggi* and *Stichopathes* sp. were used as reference peptide databases for the mass spectrometry analysis. A common contaminants database was also included. Only proteins with at least two significant peptides or at least one significant peptide with at least 10 spectra and an identification score of 250 or greater were retained. To further filter out potential human proteins inadvertently introduced during sample preparation, all sequences were BLASTed against the 'Primates' database in NCBI using Blast2GO 6.0 (Conesa et al., 2005). NCBI-generated sequence alignments of black coral versus Homo sapiens proteins with Blast2GO e-values lower than e^{-50} and percent mean similarity greater than 50%, e-values lower than e^{-100}, and percent similarity greater than 80% were removed from our final list of proteins if manual visual examination showed that likely tryptic peptides could have been human, rather than black coral, derived (Peled et al., 2020).

For each taxon, likely coral-specific skeleton proteins were divided into those which were found in skeleton that had only been cleaned pre-grinding (cleaned once), those which were found in skeleton that were cleaned again post-grinding (cleaned twice), and those that were found in both fractions (both). Proteins in each group were then characterized for amino acid composition using SubsetDF in the CHNOSZ package in RStudio (Team, 2019), presence of a signal peptide using the Signal P-5.0 server (Armenteros et al., 2019), and completeness of predicted sequence using the annotations described above. Proteins were further examined for strong bias toward cysteine, aspartic and/or glutamic acid, or tryptophan, lysine, and/or phenylalanine. Domains for completely predicted proteins with a strong amino acid bias were predicted in the PROSITE server (Sigrist et al., 2012) and domain visualizations were created in the PROSITE MyDomains Image Creator (Hulo et al., 2007). Clustering at 30, 50, and 90% sequence similarity of black coral and scleractinian (Drake et al., 2013; Ramos-Silva et al., 2013; Takeuchi et al., 2016; Peled et al., 2020) proteins plus proteins extracted from chitinous cuticles of the mosquito *Anopheles*

gambiae (He et al., 2007; Mastrobuoni et al., 2013; Champion et al., 2016; Zhou et al., 2016) was conducted in CD-HIT with default settings (Huang et al., 2010). Gene ontology term enrichment was performed using a two-tailed Enrichment Analysis in Blast2GO with $p<0.05$ (Conesa et al., 2005), which integrates the FatiGO package (Al-Shahrour et al., 2004) using the Fisher's Exact Test. Reciprocal BLASTing was performed in the BLAST+ command line application.

RESULTS AND DISCUSSION

Of the four protein extraction methods tested for the two black coral species - HCl, guanidine hydrochloride, DTT, and chitinase - chitinase yielded the highest amount of protein separated by SDS-PAGE with subsequent imaging (**Figure 1C**). While BCA assays suggested that HCl, DTT, and guanidine hydrochloride resulted in protein extraction from the chitin skeletons (**Supplementary Material Table 1**), it appears more likely that these treatments released chitosan, an amide derivative of chitin that can react with the BCA reagents (Kasaai et al., 2013; Gao et al., 2019). Cleaned and uncleaned fractions of black coral skeletal proteins extracted by chitinase were therefore submitted for protein sequencing.

All samples contained at least 100 returned proteins above the designated cutoffs and that were not likely human contaminants (**Supplementary Material Table 2).** *Antipathes* skeleton yielded 167 proteins that were only in the twice-cleaned fraction, 105 proteins that were only in the once-cleaned fraction, and 99 proteins in both fractions (**Figure 2A**). From *Stichopathes* skeleton, 93 proteins were only in the twice-cleaned fraction, 62 were in the once-cleaned fraction, and 73 were in both fractions (**Figure 2B**). Some of the proteins from the singly cleaned fractions were likely not bound to the chitinous skeleton and as such were removed during the second cleaning step as has been shown for removal of non-intracrystalline stony coral skeletal organic matter (Hendy et al., 2012). However, we cannot exclude them from the list of potential proteins involved in the chitinous black coral skeleton as they may still serve a role in skeleton strength as has been shown in squid pen which is also a composite of chitin plus proteins, lipids, and other polysaccharides (Montroni et al., 2021).

Of the total 371 proteins from *Antipathes* skeleton and 228 proteins from *Stichopathes* skeleton (Additional Files S1 and S2, respectively), 112 were found in the transcriptomes of both species and 68 were each other's reciprocal best BLAST hit (**Figure 2C**, **Supplementary Material Table 3**). Distribution of reciprocal best BLAST hit proteins between cleaning fractions between the two taxa is non-random (Fisher's exact test, $p<0.05$, **Supplementary Material Table 4**). Orthologous proteins found in the same cleaning fractions of both species include a MAM and LDL receptor domain containing protein, three coadhesin/hemicentin/mucin proteins, and four collagen alpha proteins among others. Interestingly, these protein types are also known from stony coral skeleton, as are several protein types that were detected in both black coral skeletons but in different cleaning fractions including an EGF and laminin G domain-containing protein, a potential protocadherin, and uncharacterized skeletal organic matrix protein 5 (Drake et al., 2013; Ramos-Silva et al., 2013; Takeuchi et al., 2016; Peled et al., 2020). Only *Antipathes* skeleton contained a carbonic anhydrase, which is known from stony coral skeleton from multiple species (Drake et al., 2013; Ramos-Silva et al., 2013; Peled et al., 2020), where it likely supplies bicarbonate for the eventual production of the calcium carbonate exoskeleton of scleractinians (Bertucci et al., 2013; Comeau et al., 2017).

Not all proteins were completely predicted (**Supplementary Material Table 2**). Of 84 proteins in the twice-cleaned fraction extracted from *Antipathes* that were completely predicted, two displayed a disproportionate amount of aspartic and glutamic acids ('disproportionate' defined as >20% of total amino acids) and four had >10% cysteine; three of those with excess cysteine had signal peptides. Nearly half the number of completely predicted proteins (47) were found only in the once-cleaned fraction from *Antipathes*, and 20 of these displayed a signal peptide with two of this subset also showing excess aspartic and glutamic acids. Eighteen proteins observed in both fractions were both completely predicted and displayed a signal peptide; two of these were >10% cysteine.

Fewer proteins were completely predicted in *Stichopathes* (**Supplementary Material Table 2**). In the twice-cleaned fraction for this taxon, 16 of 42 completely predicted proteins have signal peptides and only one is >10% C. Similarly, 23 of 44 complete proteins found in both fractions have signal peptides and only one is >10% cysteine. No completely predicted proteins in these two fractions were biased toward acidic amino acids. The once-cleaned fraction also showed a similar breakdown of completeness and signal peptides, with 34 proteins being complete and 12 of these having a signal peptide; however, none of these were biased toward any amino acids of interest.

Bias of skeletal proteins toward acidic amino acids (aspartic and glutamic acids) is well-documented in organisms that produce biocarbonates (e.g., Nocente-McGrath et al., 1989; Gotliv et al., 2005; Mass et al., 2013) and biophosphates (He et al., 2003), and even in collagen-dominated biophosphates there are several known acidic non-collagenous proteins (Gorski, 2011). Unlike either stony coral skeletons or vertebrate bone, however, black corals' skeletons are constructed of sclerotized chitin, a long-chained polysaccharide (Goldberg, 1976). Chitin displays a similar hierarchical organization to biocarbonates (Ehrlich, 2010), and acidic chitinases (e.g., Samac et al., 1990) have been characterized from a number of organisms. Further, an acidic chitin binding protein appears to be involved in the precipitation of calcium phosphate and then calcium carbonate in crustacean teeth (Tynyakov et al., 2015). Our results suggest that acidic proteins may be involved in black coral chitinous skeleton development; however, despite likely sharing conserved biomineralization-related genes with stony corals (review by Gilbert et al., 2022), black coral acidic proteins are perhaps not as central to the process as they appear to be in allowing stony corals

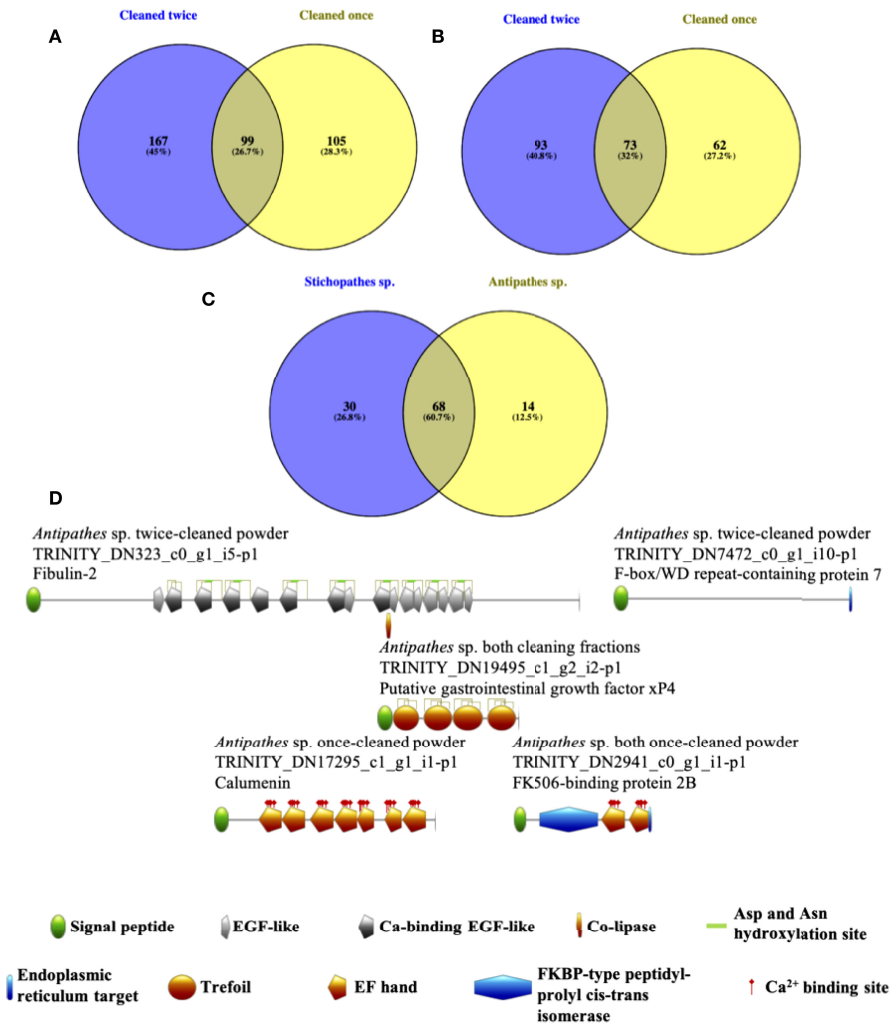

FIGURE 2 | For both *Antipathes* **(A)** and *Stichopathes* **(B)** we observed ~30% overlap in protein detection between skeleton cleaned only before grinding (yellow) and skeleton clean both before and after grinding (purple). Unique proteins were also found in both fractions. Further, for both species, the largest number of proteins were found in the twice-cleaned fractions (purple, a & b). 60.7% of detected proteins with reciprocal best BLAST hits between the two species were observed in both species **(C)** across the various cleaning fractions. **(D)** Predicted domains in proteins extracted from black coral skeleton using chitinase. Only proteins that were completely predicted, display a proposed signal peptide, and are biased toward key amino acids were considered. Although several *Stichopathes* skeletal proteins meet these criteria, none are predicted to have any domains.

biomineralize (Mass et al., 2013) and to counter the effects of ocean acidification (e.g., Drake et al., 2017).

Several amino acids are associated with chitin binding domains, including cysteine, phenylalanine, tryptophan, and tyrosine (Shen and Jacobs-Lorena, 1999). Invertebrate and plant chitin binding proteins typically display several conserved cysteines that are likely involved in disulfide bonds related to protein secondary and tertiary structure (Shen and Jacobs-Lorena, 1999). Tyrosine and phenylalanine are conserved components of the R&R consensus motif of chitin binding cuticle proteins (Rebers and Willis, 2001), and tyrosine and tryptophan are crucial conserved amino acids in the binding cleft of *Bascillus* chitinase. Despite a small number of completely predicted detected proteins being biased toward cysteine, and none toward phenylalanine, tryptophan, or tyrosine, some of the proteins may have chitin binding capabilities and should be tested in the future.

We also considered only those full proteins that are proposed to have a signal peptide for export to the cell membrane or extracellular space (review by von Heijne, 1990), and then queried this final group for those with predicted domains. Out of nine proteins between the two species that meet the above criteria, five are predicted to have known domains, although none are explicitly chitin binding, and no such proteins from *Stichopathes* were found to have predicted domains (**Figure 2D**). A protein annotated as fibulin-2 contains several EGF-like domains, some of which can be Ca^{2+} binding. EGF-like domains are found in extracellular matrix proteins and can be

TABLE 1 | Black coral, stony coral, and mosquito exoskeleton proteins clustered by sequence similarity in CD-Hit.

50% Similarity			
Cluster Number	**Annotation**	**Sequence ID**	**% Sequence similarity**
1	MAM and LDL-receptor class A domain-containing protein 2-like	XP_022794736.1	
	MAM and LDL-receptor class A domain-containing protein 2	Antipathes_TRINITY_DN90165_c0_g1_i1.p1	64.3%
	MAM and LDL-receptor class A domain-containing protein 2-like	Stichopathes_TRINITY_DN24487_c0_g1_TRINITY_DN24487_c0_g1_i1_g.57476	64.6%
	MAM and LDL-receptor class A domain-containing protein 2-like	Stichopathes_TRINITY_DN45621_c1_g1_TRINITY_DN45621_c1_g1_i1_g.64725	62.6%
	MAM and LDL-receptor class A domain-containing protein 2-like	Stichopathes_TRINITY_DN6745_c0_g1_TRINITY_DN6745_c0_g1_i1_g.29670	64.4%
	MAM and LDL-receptor class A domain-containing protein 2-like	Stichopathes_TRINITY_DN8568_c0_g1_TRINITY_DN8568_c0_g1_i3_g.28233	71.6%
	MAM and LDL-receptor class A domain-containing protein 2-like	JT011118.1	55.9%
	MAM and LDL-receptor domain- containing protein 2	JR994474.1	50.8%
	MAM and LDL-receptor class A domain-containing protein 2-like	g6066	56.4%
	MAM and LDL-receptor class A domain-containing protein 2-like	g1714	72.0%
	MAM and LDL-receptor class A domain-containing protein 2-like	g13890	96.3%
	MAM and LDL-receptor class A domain-containing protein 2-like	g1647	55.5%
	MAM and LDL-receptor class A domain-containing protein 2-like	g15955	50.1%
2	MAM and LDL-receptor class A domain-containing protein 2	Stichopathes_TRINITY_DN1603_c0_g1_TRINITY_DN1603_c0_g1_i7_g.121738	
	MAM and LDL-receptor class A domain-containing protein 2	Antipathes_TRINITY_DN10485_c0_g1_i1.p1	96.7%
	MAM and LDL-receptor class A domain-containing protein 2	Antipathes_TRINITY_DN1203_c0_g1_i1.p1	96.7%
	MAM and LDL-receptor class A domain-containing protein 2-like	aug_v2a.09969.t1	59.6%
3	protein lingerer-like	XP_022806664.1	
	NA	Antipathes_TRINITY_DN2417_c0_g1_i1.p1	53.3%
	collagen alpha-1(II) chain-like	Stichopathes_TRINITY_DN47849_c2_g1_TRINITY_DN47849_c2_g1_i1_g.74739	53.3%
4	collagen alpha-2(V) chain-like	Stichopathes_TRINITY_DN7187_c0_g1_TRINITY_DN7187_c0_g1_i4_g.116238	
	NA	Antipathes_TRINITY_DN60847_c0_g1_i2.p1	90.7%
	collagen alpha chain-like	JR991083.1	54.7%
5	MAM and LDL-receptor class A domain-containing protein 1-like isoform X1	Stichopathes_TRINITY_DN26_c0_g1_TRINITY_DN26_c0_g1_i3_g.3085	
	CUB and peptidase domain-containing protein 1 {ECO:0000303|PubMed:23765379}	Antipathes_TRINITY_DN6910_c0_g1_i2.p1	76.9%
	CUB and peptidase domain-containing protein 2-like	XP_022780694.1	50.8%
6	MAM and LDL-receptor class A domain-containing protein 2-like	aug_v2a.09968.t1	
	MAM and LDL-receptor class A domain-containing protein 1	Antipathes_TRINITY_DN5167_c0_g1_i1.p1	63.3%
7	NA	Antipathes_TRINITY_DN20198_c0_g1_i1.p1	
	uncharacterized	g8985	72.4%
30% Similarity			
Cluster Number	**Annotation**	**Sequence ID**	**% Sequence similarity**
1	MAM and LDL-receptor class A domain-containing protein 2-like	XP_022794736.1	
	MAM and LDL-receptor class A domain-containing protein 2-like	JR994474.1	61.4%
	MAM and LDL-receptor class A domain-containing protein 2-like	JT011118.1	62.3%
	MAM and LDL-receptor class A domain-containing protein 2-like	aug_v2a.09968.t1	50.3%

(Continued)

TABLE 1 | Continued

30% Similarity

Cluster Number	Annotation	Sequence ID	% Sequence similarity
	MAM and LDL-receptor class A domain-containing protein 2	Stichopathes_TRINITY_DN1603_c0_g1_TRINITY_DN1603_c0_g1_i7_g.121738	37.7%
	MAM and LDL-receptor class A domain-containing protein 2-like	aug_v2a.09969.t1	38.1%
	MAM and LDL-receptor class A domain-containing protein 2-like	g15955	65.4%
	MAM and LDL-receptor class A domain-containing protein 2-like	g1647	84.8%
	MAM and LDL-receptor class A domain-containing protein 2-like	Stichopathes_TRINITY_DN8568_c0_g1_TRINITY_DN8568_c0_g1_i3_g.28233	71.2%
	MAM and LDL-receptor class A domain-containing protein 2-like	Stichopathes_TRINITY_DN6745_c0_g1_TRINITY_DN6745_c0_g1_i1_g.29670	63.0%
	MAM and LDL-receptor class A domain-containing protein 2-like	Stichopathes_TRINITY_DN24487_c0_g1_TRINITY_DN24487_c0_g1_i1_g.57476	64.1%
	MAM and LDL-receptor class A domain-containing protein 2-like	g1714	95.5%
	MAM and LDL-receptor class A domain-containing protein 2-like	g6066	71.4%
	MAM and LDL-receptor class A domain-containing protein 1	Antipathes_TRINITY_DN5167_c0_g1_i1.p1	58.2%
	MAM and LDL-receptor class A domain-containing protein 2-like	g13890	95.9%
	MAM and LDL-receptor class A domain-containing protein 2	Antipathes_TRINITY_DN10485_c0_g1_i1.p1	62.7%
	MAM and LDL-receptor class A domain-containing protein 2-like	Stichopathes_TRINITY_DN45621_c1_g1_TRINITY_DN45621_c1_g1_i1_g.64725	62.6%
	MAM and LDL-receptor class A domain-containing protein 2	Antipathes_TRINITY_DN90165_c0_g1_i1.p1	63.6%
2	EGF and laminin G domain-containing protein-like	XP_022804012.1	
	EGF and laminin G domain-containing protein-like	Stichopathes_TRINITY_DN2042_c0_g1_TRINITY_DN2042_c0_g1_i2_g.8370	41.3%
	EGF and laminin G domain-containing protein-like	JR980881.1	47.4%
	EGF and laminin G domain-containing protein-like	aug_v2a.06122.t1	43.1%
	EGF and laminin G domain-containing protein	Antipathes_TRINITY_DN21208_c0_g1_i1.p1	43.9%
	EGF and laminin G domain-containing protein-like	g7086	86.2%
	EGF and laminin G domain-containing protein-like	g34749	85.1%
	EGF and laminin G domain-containing protein-like	g20420	82.3%
	EGF and laminin G domain-containing protein-like	g20041	82.9%
3	MAM and LDL-receptor class A domain-containing protein 1-like isoform X1	Stichopathes_TRINITY_DN26_c0_g1_TRINITY_DN26_c0_g1_i14_g.3080	
	MAM and LDL-receptor class A domain-containing protein 2	Antipathes_TRINITY_DN507_c0_g1_i17.p1	52.1%
	MAM and LDL-receptor class A domain-containing protein 1-like isoform X1	Stichopathes_TRINITY_DN26_c0_g1_TRINITY_DN26_c0_g1_i3_g.3085	55.0%
	MAM and LDL-receptor class A domain-containing protein 1-like isoform X1	Stichopathes_TRINITY_DN26_c0_g1_TRINITY_DN26_c0_g1_i4_g.3083	73.6%
	Zinc metalloproteinase nas-15	Antipathes_TRINITY_DN385_c0_g1_i12.p1	53.6%
	meprin A subunit beta-like	Stichopathes_TRINITY_DN3619_c0_g1_TRINITY_DN3619_c0_g1_i1_g.25688	41.7%
	CUB and peptidase domain-containing protein 1	Antipathes_TRINITY_DN6910_c0_g1_i2.p1	66.0%
	CUB and peptidase domain-containing protein 2-like	XP_022780694.1	47.9%
4	ZP domain-containing protein-like	JN631095.1	
	ZP domain-containing protein-like	XP_022806326.1	57.9%
	ZP domain-containing protein-like	aug_v2a.07627.t1	91.9%
	ZP domain-containing protein	Antipathes_TRINITY_DN41751_c1_g1_i1.p1	47.1%
	ZP domain-containing protein-like	g907	62.2%
	ZP domain-containing protein-like	g18277	62.1%
5	fibronectin type III domain-containing protein-like	JR993827.1	
	fibronectin type III domain-containing protein-like	Stichopathes_TRINITY_DN1772_c0_g1_TRINITY_DN1772_c0_g1_i9_g.72338	43.8%
	Fibronectin type III domain-containing protein	Antipathes_TRINITY_DN1513_c0_g1_i5.p1	47.2%
	fibronectin type III domain-containing protein-like	g22569	49.6%
	Fibronectin type III domain-containing protein	Antipathes_TRINITY_DN1513_c0_g1_i7.p1	48.7%

(Continued)

TABLE 1 | Continued

30% Similarity			
Cluster Number	**Annotation**	**Sequence ID**	**% Sequence similarity**
6	Uncharacterized skeletal organic matrix protein 5	Antipathes_TRINITY_DN6046_c0_g1_i1.p1	
	uncharacterized skeletal organic matrix protein 5-like	Stichopathes_TRINITY_DN648_c1_g1_TRINITY_DN648_c1_g1_i10_g.36676	73.9%
	uncharacterized skeletal organic matrix protein 5-like	JR973117.1	36.3%
	uncharacterized skeletal organic matrix protein 5-like	aug_v2a.22918.t1	35.5%
	NA	Stichopathes_TRINITY_DN4778_c0_g2_TRINITY_DN4778_c0_g2_i1_g.1379	79.2%
7	NA	Antipathes_TRINITY_DN3769_c0_g1_i7.p1	
	golgin subfamily A member 4-like	Stichopathes_TRINITY_DN2366_c0_g1_TRINITY_DN2366_c0_g1_i2_g.62183	97.8%
	protein MLP1-like	g9861	48.5%
8	Matrix metalloproteinase-24	Antipathes_TRINITY_DN2668_c0_g2_i1.p1	
	matrix metalloproteinase-25-like	Stichopathes_TRINITY_DN70_c0_g1_TRINITY_DN70_c0_g1_i3_g.3376	91.3%
	collagenase 3-like	XP_022783952.1	32.5%
9	kielin/chordin-like protein	g5540	
	Fibroblast growth factor 20	Antipathes_TRINITY_DN22734_c0_g1_i4.p1	32.9%
	kielin/chordin-like protein	g39770	57.1%
10	NA	Antipathes_TRINITY_DN20198_c0_g1_i1.p1	
	uncharacterized	g8985	72.4%
11	digestive cysteine proteinase 1-like	XP_022803524.1	
	Cathepsin L	Antipathes_TRINITY_DN1770_c0_g1_i11.p1	35.3%

While sequence similarity was observed between black and stony corals at 30% and 50% similarity, none was observed between any corals and mosquitos.

involved in protein-protein interactions (review by Engel, 1989; Rao et al., 1995). Trefoil domains have also been found in extracellular matrix proteins; the domain typically contains six cysteines that form disulfide bridges; these proteins may interact with mucin (Thim, 1997), which has been found in the skeleton-associated extracellular matrix of stony corals (Ramos-Silva et al., 2013; Takeuchi et al., 2016; Peled et al., 2020) and which associates with chitin in arthropod guts (Dias et al., 2018), although mucin has not been sequenced from arthropod cuticle.

To determine if invertebrates that produce a chitinous skeleton display skeletal proteome similarities across divergent phyla, we compared the black coral skeletal proteome with that of mosquito cuticle. No clustering of black coral and *Anopheles gambiae* cuticular proteins was observed at 30, 50, or 90% sequence similarity. While no clustering of black and stony coral skeletal proteins was observed at 90% similarity, several clusters were observed at 50 (7 clusters) and 30% (11 clusters) similarity. Clustered black and stony coral proteins are annotated as collagenase like, CUB and peptidase domain containing, digestive cysteine proteins like, EGF and laminin G domain containing, fibronectin type III domain containing, kielin/chordin like, MAM and LDL receptor domain containing, protein MLP like, uncharacterized skeletal organic matrix

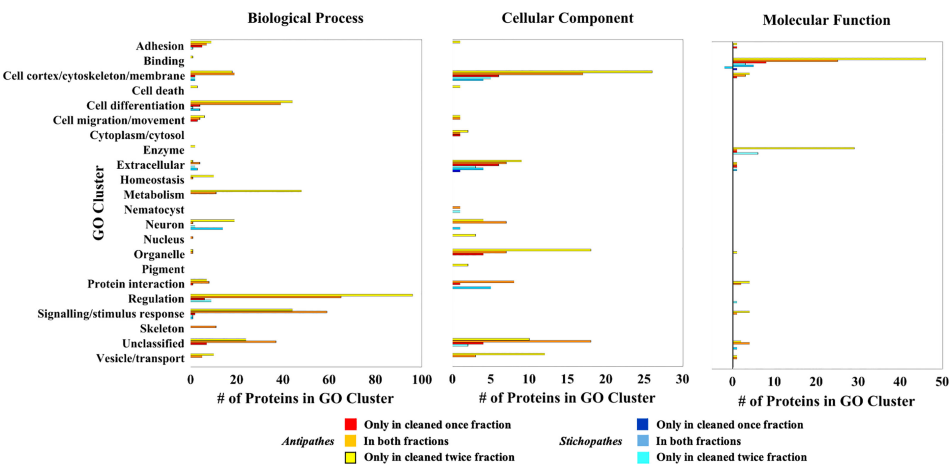

FIGURE 3 | Clustered skeletal proteins with enriched GO terms relative to each species' transcriptome. Bars greater than zero are the number of proteins with over-enriched GO terms in the skeletal proteomes whereas those less than zero have under-enriched GO terms. Note the different ranges in the numbers of proteins in each GO cluster.

protein 5, ZP domain containing, and uncharacterized in stony corals (**Table 1**).

Antipathes skeletal proteins sequenced in this work are over-enriched in GO terms related to binding, the cell cortex/cytoskeleton/membrane, cell differentiation, enzymes, extracellular location, metabolism, organelles, regulation, signaling/stimulus response, and vesicles/transport (**Figure 3**). Similarly, *Stichopathes* skeletal proteins are over-enriched in GO terms for binding, enzymes, extracellular location, and regulation; additionally, they are enriched for neurons and protein interaction (**Figure 3**). The only GO term cluster that was under-enriched was observed for *Stichopathes* and included terms related to binding: organic cyclic compound binding [GO:0097159] and heterocyclic compound binding [GO:1901363]. Proteins with extracellular location and membrane GO terms may be important as black coral chitin formation and sclerotization are extracellular processes (Wagner et al., 2012). As vesicular transport of ions and organic molecules that form the skeleton appears to be important in stony corals (Schmidt et al., 2022), vesicle and transport proteins may also play a role in black coral skeleton formation. Proteins which function as enzymes may also be important to the formation and modification of the chitinous skeleton; these include a carbonic anhydrase in *Antipathes*, a calmodulin in *Stichopathes*, and several proteases and chitinases in both species.

CONCLUSIONS

While the structure and mechanical properties of black coral skeleton chitin have been well-characterized, to date, their protein composition has received less attention. To address this research gap, we sequenced the skeletal proteome of two species of common Red Sea black corals under two steps of strong oxidative cleaning. Our analyses reveal hundreds of proteins in the skeletons of each species, with ~70 being each other's reciprocal best BLAST hit, potentially representing a conserved toolkit. A small number of proteins can be considered moderately acidic and only a few are biased toward amino acids known to be involved in chitin binding. Instead, our GO analysis shows that terms related to vesicles and transport, membrane structure, and enzymatic functionality are enriched. This initial work suggests that more research is required to fully comprehend the functions of black coral skeletal proteins and their interactions with chitin.

DATA AVAILABILITY STATEMENT

The datasets generated for this study can be found in the following online repositories: (1) Transcriptome data are available under NCBI BioProject PRJNA809900. (2) The mass spectrometry proteomics data have been deposited to the ProteomeXchange Consortium via the PRIDE (Perez-Riverol et al.) partner repository with the dataset identifier PXD032043 and 10.6019/PXD032043.

AUTHOR CONTRIBUTIONS

Conceptualization, investigation, writing—original draft preparation, JD and TM. Formal analysis, data curation, visualization, JD. Resources, supervision, funding acquisition, TM. All authors have read and agreed to the published version of the manuscript. All authors contributed to the article and approved the submitted version.

FUNDING

This project has received funding from GIF, the German-Israeli Foundation for Scientific Research and Development by the Israeli Science Foundation (Award #Grant I-1496-302.8) to TM. JD was supported by the Zuckerman STEM Leadership Postdoctoral program.

ACKNOWLEDGMENTS

We thank the InterUniversity Institute in Eilat, Israel for accommodations during sampling; Hagai Nativ for photography; the Morris Khan Research Station diving team for SCUBA assistance; David Morgenstern at the de Botton Institute for Protein Profiling at Nancy and Stephen Grand Israel National Center for Personalized Medicine at the Weizmann Institute of Science for proteomic sequencing and analysis; the Nancy and Stephen Grand Israel National Center for Personalized Medicine at the Weizmann Institute of Science for transcriptome sequencing and analysis; and Tal Zaquin and Ricardo Almuly at the University of Haifa for laboratory assistance.

SUPPLEMENTARY MATERIAL

The Supplementary Material for this article can be found online at: https://www.frontiersin.org/articles/10.3389/fmars.2022.904835/full#supplementary-material

REFERENCES

Al-Shahrour, F., Díaz-Uriarte, R., and Dopazo, J. (2004). FatiGO: A Web Tool for Finding Significant Associations of Gene Ontology Terms With Groups of Genes. *Bioinformatics* 20, 578–580. doi: 10.1093/bioinformatics/btg455

Armenteros, J. J. A., Tsirigos, K. D., Sønderby, C. K., Petersen, T. N., Winther, O., Brunak, S., et al. (2019). SignalP 5.0 Improves Signal Peptide Predictions Using Deep Neural Networks. *Nat. Biotechnol.* 37, 420. doi: 10.1038/s41587-019-0036-z

Bai, X., Chen, Y., Chen, W., Lei, H., Gao, F., Qin, Y., et al. (2011). The Effect of Black Coral Extraction on Acute Lung Inflammation Induced by Cigarette

Smoke in Mice. *Exp. Lung Res.* 37, 627–632. doi: 10.3109/01902148.2011.627084

Bertucci, A., Moya, A., Tambutté, S., Allemand, D., Supuran, C. T., and Zoccola, D. (2013). Carbonic Anhydrases in Anthozoan Corals—A Review. *Bioorganic Medicinal Chem.* 21, 1437–1450. doi: 10.1016/j.bmc.2012.10.024

Bo, M., Bavestrello, G., Kurek, D., Paasch, S., Brunner, E., Born, R., et al. (2012). Isolation and Identification of Chitin in the Black Coral *Parantipathes Larix* (Anthozoa: Cnidaria). *Int. J. Biol. Macromolecules* 51, 129–137. doi: 10.1016/j.ijbiomac.2012.04.016

Boland, R. C., and Parrish, F. A. (2005). A Description of Fish Assemblages in the Black Coral Beds Off Lahaina, Maui, Hawai 'I. *Pacific Sci.* 59, 411–420. doi: 10.1353/psc.2005.0032

Champion, M. M., Sheppard, A. D., Rund, S. S., Freed, S. A., O'Tousa, J. E., and Duffield, G. E. (2016). ""Qualitative and Quantitative Proteomics Methods for the Analysis of the Anopheles Gambiae Mosquito Proteome,"," in *Short Views on Insect Genomics and Proteomics* (Springer) Berlin, Germany, 37–62.

Comeau, S., Tambutté, E., Carpenter, R., Edmunds, P., Evensen, N., Allemand, D., et al. (2017). Coral Calcifying Fluid pH is Modulated by Seawater Carbonate Chemistry Not Solely Seawater pH. Proc. *R. Soc B* 284, 20161669. doi: 10.1098/rspb.2016.1669

Conesa, A., Götz, S., García-Gómez, J. M., Terol, J., Talón, M., and Robles, M. (2005). Blast2GO: A Universal Tool for Annotation, Visualization and Analysis in Functional Genomics Research. *Bioinformatics* 21, 3674–3676. doi: 10.1093/bioinformatics/bti610

Daly, M.arymegan, M. R. Brugler, P. Cartwright, A. G. Collins, M. N. Dawson, D. G. Fautin, et al. (2007). The Phylum Cnidaria: A Review of Phylogenetic Patterns and Diversity 300 Years After Linnaeus. In *Linnaeus Tercentenary: Progress in Invertebrate Taxonomy*, Z.-Q. Zhang and W. A. Shear, editors. Zootaxa 1668:127–182.

De Clippele, L. H., Huvenne, V. A., Molodtsova, T. N., and Roberts, J. M. (2019). The Diversity and Ecological Role of non-Scleractinian Corals (Antipatharia and Alcyonacea) on Scleractinian Cold-Water Coral Mounds. *Front. Mar. Sci.* 6, 184. doi: 10.3389/fmars.2019.00184

Deidun, A., Andaloro, F., Bavestrello, G., Canese, S., Consoli, P., Micallef, A., et al. (2015). First Characterisation of a *Leiopathes Glaberrima* (Cnidaria: Anthozoa: Antipatharia) Forest in Maltese Exploited Fishing Grounds. *Ital. J. Zoology* 82, 271–280. doi: 10.1080/11250003.2014.986544

Dias, R., Cardoso, C., Pimentel, A., Damasceno, T., Ferreira, C., and Terra, W. (2018). The Roles of Mucus-Forming Mucins, Peritrophins and Peritrophins With Mucin Domains in the Insect Midgut. *Insect Mol. Biol.* 27, 46–60. doi: 10.1111/imb.12340

Drake, J. L., Mass, T., Haramaty, L., Zelzion, E., Bhattacharya, D., and Falkowski, P. G. (2013). Proteomic Analysis of Skeletal Organic Matrix From the Stony Coral *Stylophora Pistillata*. *Proc. Natl. Acad. Sci.* 110, 3788–3793. doi: 10.1073/pnas.1301419110

Drake, J. L., Schaller, M. F., Mass, T., Godfrey, L., Fu, A., Sherrell, R. M., et al. (2017) 63(1):107–121. Molecular and Geochemical Perspectives on the Influence of CO_2 on Calcification in Coral Cell Cultures. *Limnol. Oceanog.* doi: 10.1002/lno.10617

Ehrlich, H. (2010). Chitin and Collagen as Universal and Alternative Templates in Biomineralization. *Int. Geology Rev.* 52, 661–699. doi: 10.1080/00206811003679521

Engel, J. (1989). EGF-Like Domains in Extracellular Matrix Proteins: Localized Signals for Growth and Differentiation? *FEBS Lett.* 251, 1–7. doi: 10.1016/0014-5793(89)81417-6

Gao, C., Fisher, Z. B., and Edgar, K. J. (2019). Azide Reduction by DTT or Thioacetic Acid Provides Access to Amino and Amido Polysaccharides. *Cellulose* 26, 445–462. doi: 10.1007/s10570-018-2195-3

Gilbert, P. U., Bergmann, K. D., Boekelheide, N., Tambutté, S., Mass, T., Marin, F., et al. (2022). Biomineralization: Integrating Mechanism and Evolutionary History. *Sci. Adv.* 8, eabl9653. doi: 10.1126/sciadv.abl9653

Gildemeister, O. S., Zhu, B. C., and Laine, R. A. (1994). Chitovibrin: A Chitin-Binding Lectin From *Vibrio Parahemolyticus*. *Glycoconjugate J.* 11, 518–526. doi: 10.1007/BF00731302

Godefroid, M., Hédouin, L., Mercière, A., Dubois, P., and Consortium, U. T. P. (2022). Thermal Stress Responses of the Antipatharian *Stichopathes* Sp. From the Mesophotic Reef of Mo'orea, French Polynesia. *Sci. Total Environ.*, 820 153094. doi: 10.1016/j.scitotenv.2022.153094

Goldberg, W. M. (1976). Comparative Study of the Chemistry and Structure of Gorgonian and Antipatharian Coral Skeletons. *Mar. Biol.* 35, 253–267. doi: 10.1007/BF00396873

Goldberg, W. M., Hopkins, T. L., Holl, S. M., Schaefer, J., Kramer, K. J., Morgan, T. D., et al. (1994). Chemical Composition of the Sclerotized Black Coral Skeleton (Coelenterata: Antipatharia): A Comparison of Two Species. *Comp. Biochem. Physiol. Part B: Comp. Biochem.* 107, 633–643. doi: 10.1016/0305-0491(94)90197-X

Gorski, J. P. (2011). Biomineralization of Bone: A Fresh View of the Roles of non-Collagenous Proteins. *Front. Biosci. (Landmark edition)* 16, 2598. doi: 10.2741/3875

Gotliv, B.-A., Kessler, N., Sumerel, J. L., Morse, D. E., Tuross, N., Addadi, L., et al. (2005). Asprich: A Novel Aspartic Acid-Rich Protein Family From the Prismatic Shell Matrix of the Bivalve *Atrina Rigida*. *ChemBioChem* 6, 304–314. doi: 10.1002/cbic.200400221

Gress, E., and Andradi-Brown, D. A. (2018). Assessing Population Changes of Historically Overexploited Black Corals (Order: Antipatharia) in Cozumel, Mexico. *PeerJ* 6, e5129. doi: 10.7717/peerj.5129

Grigg, R. W. (1993). Precious Coral Fisheries of Hawaii and the US Pacific Islands. *Mar. Fish. Rev.* 55, 50–60.

Grigg, R. W. (2004). Harvesting Impacts and Invasion by an Alien Species Decrease Estimates of Black Coral Yield Off Maui, Hawai'i. *Pacific Sci.* 58, 1–6. doi: 10.1353/psc.2004.0006

He, N., Botelho, J. M., McNall, R. J., Belozerov, V., Dunn, W. A., Mize, T., et al. (2007). Proteomic Analysis of Cast Cuticles From *Anopheles Gambiae* by Tandem Mass Spectrometry. *Insect Biochem. Mol. Biol.* 37, 135–146. doi: 10.1016/j.ibmb.2006.10.011

He, G., Dahl, T., Veis, A., and George, A. (2003). Dentin Matrix Protein 1 Initiates Hydroxyapatite Formation *In Vitro*. *Connective Tissue Res.* 44, 240–245. doi: 10.1080/03008200390181726

Hendy, E. J., Tomiak, P. J., Collins, M. J., Hellstrom, J., Tudhope, A. W., Lough, J. M., et al. (2012). Assessing Amino Acid Racemization Variability in Coral Intra-Crystalline Protein for Geochronological Applications. *Geochimica cosmochimica Acta* 86, 338–353. doi: 10.1016/j.gca.2012.02.020

Huang, Y., Niu, B., Gao, Y., Fu, L., and Li, W. (2010). CD-HIT Suite: A Web Server for Clustering and Comparing Biological Sequences. *Bioinformatics*. 26 (5):680–682. doi: 10.1093/bioinformatics/btq003

Hulo, N., Bairoch, A., Bulliard, V., Cerutti, L., Cuche, B. A., De Castro, E., et al. (2007). The 20 Years of PROSITE. *Nucleic Acids Res.* 36, D245–D249. doi: 10.1093/nar/gkm977

IUCN (2021). *The IUCN Red List of Threatened Species. Version 2021-3*. https://www.iucnredlist.org. Accessed May 2022

João, C. F., Echeverria, C., Velhinho, A., Silva, J. C., Godinho, M. H., and Borges, J. P. (2017). Bio-Inspired Production of Chitosan/Chitin Films From Liquid Crystalline Suspensions. *Carbohydr. Polymers* 155, 372–381. doi: 10.1016/j.carbpol.2016.08.039

Juárez-de la Rosa, B., Ardisson, P.-L., Azamar-Barrios, J., Quintana, P., and Alvarado-Gil, J. (2007). Optical, Thermal, and Structural Characterization of the Sclerotized Skeleton of Two Antipatharian Coral Species. *Materials Sci. Engineering: C* 27, 880–885. doi: 10.1016/j.msec.2006.10.006

Juárez-de la Rosa, B., Munoz-Saldana, J., Torres-Torres, D., Ardisson, P.-L., and Alvarado-Gil, J. (2012). Nanoindentation Characterization of the Micro-Lamellar Arrangement of Black Coral Skeleton. *J. Struct. Biol.* 177, 349–357. doi: 10.1016/j.jsb.2011.12.009

Kasaai, M. R., Arul, J., and Charlet, G. (2013). Fragmentation of Chitosan by Acids. *Sci. World J.* 11. doi: 10.1155/2013/508540

Kim, K., Goldberg, W. M., and Taylor, G. T. (1992). Architectural and Mechanical Properties of the Black Coral Skeleton (Coelenterata: Antipatharia): A Comparison of Two Species. *Biol. Bull.* 182, 195–209. doi: 10.2307/1542113

Mass, T., Jeana, L., Haramaty, L., Kim, J. D., Zelzion, E., Bhattacharya, D., et al. (2013). Cloning and Characterization of Four Novel Coral Acid-Rich Proteins That Precipitate Carbonates *In Vitro*. *Curr. Biol.* 23, 1126–1131. doi: 10.1016/j.cub.2013.05.007

Mastrobuoni, G., Qiao, H., Iovinella, I., Sagona, S., Niccolini, A., Boscaro, F., et al. (2013). A Proteomic Investigation of Soluble Olfactory Proteins in Anopheles Gambiae. *PloS One* 8, e75162. doi: 10.1371/journal.pone.0075162

Mathys, S., Evans, T. C.Jr., Chute, I. C., Wu, H., Chong, S., Benner, J., et al. (1999). Characterization of a Self-Splicing Mini-Intein and its Conversion Into Autocatalytic N-And C-Terminal Cleavage Elements: Facile Production of

Protein Building Blocks for Protein Ligation. *Gene* 231, 1–13. doi: 10.1016/S0378-1119(99)00103-1

Montroni, D., Sparla, F., Fermani, S., and Falini, G. (2021). Influence of Proteins on Mechanical Properties of a Natural Chitin-Protein Composite. *Acta Biomaterialia* 120, 81–90. doi: 10.1016/j.actbio.2020.04.039

Morgulis, M., Martinez, S., Almuly, R., Einbinder, S., Zaslansky, P., and Mass, T. (2022). Black Corals (Antipatharia) of the Northern Red Sea: Ancient Predators of the Mesophotic Reef. *Mar. Ecol. Prog. Ser.* 688, 33–47. doi: 10.3354/meps14022

Narchi, N. E., Marlett, C. M., and Bertsch, H. (2015). ""Corals and Coralline Organisms in Seri Culture: Traditional and Modern Uses,"," in *Ethnobiology of Corals and Coral Reefs* (Springer) Switzerland, 87–102.

Nocente-McGrath, C., Brenner, C. A., and Ernst, S. G. (1989). Endo16, a Lineage-Specific Protein of the Sea Urchin Embryo, is First Expressed Just Prior to Gastrulation. *Dev. Biol.* 136, 264–272. doi: 10.1016/0012-1606(89)90147-4

Nowak, D., Florek, M., Nowak, J., Kwiatek, W., Lekki, J., Chevallier, P., et al. (2009). Morphology and the Chemical Make-Up of the Inorganic Components of Black Corals. *Materials Sci. Engineering: C* 29, 1029–1038. doi: 10.1016/j.msec.2008.08.028

Nuc, Z., and Dobrzycka-Krahel, A. (2021). From Chitin to Chitosan - a Potential Natural Antimicrobial Agent. *Prog. Chem. Appl. Chitin its Derivatives* 26, 23–40. doi: 10.15259/PCACD.26.003

Opresko, D. M. (2001). Revision of the Antipatharia (Cnidaria: Anthozoa). Part I. Establishment of a New Family, Myriopathidae. *Zoologische Mededelingen* 75, 343–370. urn:nbn:nl:ui:19-217449

Parrish, F. A., Abernathy, K., Marshall, G. J., and Buhleier, B. M. (2002). Hawaiian Monk Seals (*Monachus Schauinslandi*) Foraging in Deep-Water Coral Beds. *Mar. Mammal Sci.* 18, 244–258. doi: 10.1111/j.1748-7692.2002.tb01031.x

Peled, Y., Drake, J. L., Malik, A., Almuly, R., Lalzar, M., Morgenstern, D., et al. (2020). Optimization of Skeletal Protein Preparation for LC–MS/MS Sequencing Yields Additional Coral Skeletal Proteins in *Stylophora Pistillata*. *BMC Materials* 2, 8. doi: 10.1186/s42833-020-00014-x

Peña Moreno, D. V. (2017). *Antimicrobial Activity of Culturable Microorganisms Associated With Caribbean Black Corals (Antipatharia)* ('Universidad de los Andes, Bogota, Colombia).

Perez-Riverol, Y., Csordas, A., Bai, J., Bernal-Llinares, M., Hewapathirana, S., Kundu, D. J., et al. (2019). The PRIDE Database and Related Tools and Resources in 2019: Improving Support for Quantification Data. *Nucleic Acids Res.* 47, D442–D450. doi: 10.1093/nar/gky1106

Ramos-Silva, P., Kaandorp, J., Huisman, L., Marie, B., Zanella-Cleon, I., Guichard, N., et al. (2013). The Skeletal Proteome of the Coral *Acropora Millepora*: The Evolution of Calcification by Cooption and Domain Shuffling. *Mol. Biol. Evol.* 30(9):2099–2112. doi: 10.1093/molbev/mst109

Rao, Z., Handford, P., Mayhew, M., Knott, V., Brownlee, G. G., and StuartZ, D. (1995). The Structure of a Ca^{2+}-Binding Epidermal Growth Factor-Like Domain: Its Role in Protein-Protein Interactions. *Cell* 82, 131–141. doi: 10.1016/0092-8674(95)90059-4

Rebers, J. E., and Willis, J. H. (2001). A Conserved Domain in Arthropod Cuticular Proteins Binds Chitin. *Insect Biochem. Mol. Biol.* 31, 1083–1093. doi: 10.1016/S0965-1748(01)00056-X

Ruiz-Ramos, D. V., Fisher, C. R., Baums, I. B., and Thomsen, L. (2017). Stress Response of the Black Coral *Leiopathes Glaberrima* When Exposed to Sub-Lethal Amounts of Crude Oil and Dispersant. *Elementa: Sci. Anthropocene* 5. doi: 10.1525/elementa.261

Samac, D. A., Hironaka, C. M., Yallaly, P. E., and Shah, D. M. (1990). Isolation and Characterization of the Genes Encoding Basic and Acidic Chitinase in *Arabidopsis Thaliana*. *Plant Physiol.* 93, 907–914. doi: 10.1104/pp.93.3.907

Schmidt, C. A., Stifler, C. A., Luffey, E. L., Fordyce, B. I., Ahmed, A., Barreiro Pujol, G., et al. (2022). Faster Crystallization During Coral Skeleton Formation Correlates With Resilience to Ocean Acidification. *J. Am. Chem. Soc.* 144 (3):1332–1341. doi: 10.1021/jacs.1c11434

Shen, Z., and Jacobs-Lorena, M. (1999). Evolution of Chitin-Binding Proteins in Invertebrates. *J. Mol. Evol.* 48, 341–347. doi: 10.1007/PL00006478

Shimahara, K., and Takiguchi, Y. (1988). ""Preparation of Crustacean Chitin,"," in *Methods in Enzymology* (Elsevier), 417–423. Academic Press. New York, NY

Sigrist, C. J., De Castro, E., Cerutti, L., Cuche, B. A., Hulo, N., Bridge, A., et al. (2012). New and Continuing Developments at PROSITE. *Nucleic Acids Res.* 41, D344–D347. doi: 10.1093/nar/gks1067

Suarez, H. N., Dy, D. T., and Violanda, R. R. (2015). Density of Associated Macrofauna of Black Corals (Anthozoa: Antipatharia) in Jagna, Bohol, Central Philippines. *Philipp J. Sci.* 144, 107–115.

Takeuchi, T., Yamada, L., Shinzato, C., Sawada, H., and Satoh, N. (2016). Stepwise Evolution of Coral Biomineralization Revealed With Genome-Wide Proteomics and Transcriptomics. *PloS One* 11, e0156424. doi: 10.1371/journal.pone.0156424

Team, R (2019). *"RStudio: Integrated Development for R"* (Boston, MA: RStudio, Inc).

Tescione, G. (1973). *The Italians and Their Coral Fishing* (Fausto Fiorentino) Naples, Italy.

Thim, L. (1997). Trefoil Peptides: From Structure to Function. *Cell. Mol. Life Sci. CMLS* 53, 888–903. doi: 10.1007/s000180050108

Todinanahary, G., Terrana, L., Lavitra, T., and Eeckhaut, I. (2016). First Records of Illegal Harvesting and Trading of Black Corals (Antipatharia) in Madagascar. *Madagascar Conserv. Dev.* 11:1–6. doi: 10.4314/mcd.v11i1.5

Tynyakov, J., Bentov, S., Abehsera, S., Yehezkel, G., Roth, Z., Khalaila, I., et al. (2015). A Crayfish Molar Tooth Protein With Putative Mineralized Exoskeletal Chitinous Matrix Properties. *J. Exp. Biol.* 218, 3487–3498. doi: 10.1242/jeb.123539

von Heijne, G. (1990). The Signal Peptide. *J. Membrane Biol.* 115, 195–201. doi: 10.1007/BF01868635

Wagner, D., Luck, D. G., and Toonen, R. J. (2012). The Biology and Ecology of Black Corals (Cnidaria: Anthozoa: Hexacorallia: Antipatharia). *Adv. Mar. Biol.* 63, 67–132. doi: 10.1016/B978-0-12-394282-1.00002-8

Wang, L., and Stegemann, J. P. (2010). Extraction of High Quality RNA From Polysaccharide Matrices Using Cetlytrimethylammonium Bromide. *Biomaterials* 31, 1612–1618. doi: 10.1016/j.biomaterials.2009.11.024

Zaquin, T., Malik, A., Drake, J. L., Putnam, H. M., and Mass, T. (2021). Evolution of Protein-Mediated Biomineralization in Scleractinian Corals. *Front. Genet.* 12, 52. doi: 10.3389/fgene.2021.618517

Zheng, C., Liu, X., Luo, X., Zheng, M., Wang, X., Dan, W., et al. (2019). Development of a Novel Bio-Inspired "Cotton-Like" Collagen Aggregate/Chitin Based Biomaterial With a Biomimetic 3D Microstructure for Efficient Hemostasis and Tissue Repair. *J. Materials Chem. B* 7, 7338–7350. doi: 10.1039/C9TB02028D

Zhou, Y., Badgett, M. J., Bowen, J. H., Vannini, L., Orlando, R., and Willis, J. H. (2016). Distribution of Cuticular Proteins in Different Structures of Adult *Anopheles Gambiae*. *Insect Biochem. Mol. Biol.* 75, 45–57. doi: 10.1016/j.ibmb.2016.05.001

Conflict of Interest: The authors declare that the research was conducted in the absence of any commercial or financial relationships that could be construed as a potential conflict of interest.

Publisher's Note: All claims expressed in this article are solely those of the authors and do not necessarily represent those of their affiliated organizations, or those of the publisher, the editors and the reviewers. Any product that may be evaluated in this article, or claim that may be made by its manufacturer, is not guaranteed or endorsed by the publisher.

frontiers | Frontiers in Marine Science

TYPE Original Research
PUBLISHED 04 August 2022
DOI 10.3389/fmars.2022.909017

OPEN ACCESS

EDITED BY:
Gary H. Dickinson,
The College of New Jersey,
United States

REVIEWED BY:
Joseph Kunkel,
University of Massachusetts Amherst,
United States
Aaron Ninokawa,
Friday Harbor Laboratories, College of the Environment, University of Washington, United States

*CORRESPONDENCE:
Kaitlyn B. Lowder
kaitlyn.b.lowder@gmail.com
Jennifer R. A. Taylor
j3taylor@ucsd.edu

†PRESENT ADDRESS:
Kaitlyn B. Lowder,
The Ocean Foundation, Washington, DC, United States

SPECIALTY SECTION:
This article was submitted to Marine Molecular Biology and Ecology, a section of the journal Frontiers in Marine Science

RECEIVED: 31 March 2022
ACCEPTED: 28 June 2022
PUBLISHED: 04 August 2022

CITATION:
Lowder KB, deVries MS, Hattingh R, Day JMD, Andersson AJ, Zerofski PJ and Taylor JRA (2022) Exoskeletal predator defenses of juvenile California spiny lobsters (*Panulirus interruptus*) are affected by fluctuating ocean acidification-like conditions. *Front. Mar. Sci.* 9:909017. 10.3389/fmars.2022.909017

Exoskeletal predator defenses of juvenile California spiny lobsters (*Panulirus interruptus*) are affected by fluctuating ocean acidification-like conditions

Kaitlyn B. Lowder[1*†], Maya S. deVries[2], Ruan Hattingh[3], James M. D. Day[3], Andreas J. Andersson[3], Phillip J. Zerofski[1] and Jennifer R. A. Taylor[1*]

[1]Marine Biology Research Division, Scripps Institution of Oceanography, University of California, San Diego, La Jolla, CA, United States, [2]Department of Biological Sciences, San José State University, San Jose, CA, United States, [3]Geosciences Research Division, Scripps Institution of Oceanography, University of California, San Diego, La Jolla, CA, United States

Spiny lobsters rely on multiple biomineralized exoskeletal predator defenses that may be sensitive to ocean acidification (OA). Compromised mechanical integrity of these defensive structures may tilt predator-prey outcomes, leading to increased mortality in the lobsters' environment. Here, we tested the effects of OA-like conditions on the mechanical integrity of selected exoskeletal defenses of juvenile California spiny lobster, *Panulirus interruptus*. Young spiny lobsters reside in kelp forests with dynamic carbonate chemistry due to local metabolism and photosynthesis as well as seasonal upwelling, yielding daily and seasonal fluctuations in pH. Lobsters were exposed to a series of stable and diurnally fluctuating reduced pH conditions for three months (ambient pH/stable, 7.97; reduced pH/stable 7.67; reduced pH with low fluctuations, 7.67 ± 0.05; reduced pH with high fluctuations, 7.67 ± 0.10), after which we examined the intermolt composition (Ca and Mg content), ultrastructure (cuticle and layer thickness), and mechanical properties (hardness and stiffness) of selected exoskeletal predator defenses. Cuticle ultrastructure was consistently robust to pH conditions, while mineralization and mechanical properties were variable. Notably, the carapace was less mineralized under both reduced pH treatments with fluctuations, but with no effect on material properties, and the rostral horn had lower hardness in reduced/high fluctuating conditions without a corresponding difference in mineralization. Antennal flexural stiffness was lower in reduced, stable pH conditions compared to the reduced pH treatment with high fluctuations and not correlated with changes in cuticle structure or mineralization. These results demonstrate a complex relationship between mineralization and mechanical properties of the exoskeleton under changing ocean chemistry, and that fluctuating reduced pH conditions can induce responses not observed under the stable reduced pH conditions often used in OA research. Furthermore, this study shows that some juvenile California spiny lobster exoskeletal defenses are responsive to changes in

ocean carbonate chemistry, even during the intermolt period, in ways that can potentially increase susceptibility to predation among this critical life stage.

KEYWORDS

crustacean, ocean acidification, predator defense, mechanical properties, exoskeleton, decapod

Introduction

Marine invertebrates possess a diverse array of weapons and defense structures that use biomineralization to confer sufficient hardness and stiffness for optimal function. Structures spanning spines, plates, claws, mandibles, antennae, raptorial appendages, shells, and exoskeletons all have hierarchical structural design elements fortified with minerals, such as calcium carbonates and calcium phosphates, that help produce the material properties for a specific function. Yet, biomineralization, particularly calcification, in marine organisms is demonstrably sensitive to ocean acidification-like reduced pH/high pCO_2 conditions (Kroeker et al., 2010). Most invertebrates with calcified structures experience reductions in mineral content (Chan and Connolly, 2013; Kroeker et al., 2013; Davis et al., 2021) under reduced pH/high pCO_2 exposure due to lowered carbonate ion concentration and carbonate mineral saturation state. In contrast, some crustacean species experience increases in calcification (McDonald et al., 2009; Long et al., 2013; Taylor et al., 2015; deVries et al., 2016; Glandon et al., 2018), which is potentially accomplished by drawing upon bicarbonate accumulated for acid-base regulation (Truchot, 1979; Pane and Barry, 2007; Spicer et al., 2007; Knapp et al., 2015; Whiteley et al., 2018). The degree of mineralization is strongly linked with material properties, whereby greater mineral content corresponds to greater stiffness and brittleness (Currey, 1984). Thus, disruptions to the biomineralization process under ocean acidification (OA) conditions, resulting in either decreases or increases to calcification, have the potential to alter the mechanical integrity of defense structures and ultimately the potential outcomes of predator-prey interactions in future ocean conditions.

OA research often targets biomineralization responses, but rarely are the effects on material properties and mechanical functioning, which are consequential for survival during predator-prey interactions, studied concurrently. Reduced calcification is generally purported to have negative consequences on material properties and mechanical efficiency. This is exemplified by reduced calcification corresponding with lower stem stiffness in a calcified green alga and decreased shell elasticity in a Mediterranean top snail, both studied at CO_2 seep sites (Newcomb et al., 2015; Duquette et al., 2017), and decreased abalone shell fracture toughness concurrent with reductions in shell mineralization and thickness under reduced pH conditions (Auzoux-Bordenave et al., 2020; Avignon et al., 2020). Increased calcification, however, can also create weaker barnacle shell wall plates (McDonald et al., 2009) due to increased brittleness. In mantis shrimp, exoskeletal hardness and stiffness remained the same despite increases to Mg content (deVries et al., 2016). Altered mineralization, either through increases or decreases, has the potential to disrupt the material properties and mechanical efficiency of organism structures, but the thresholds for these effects are likely specific to structures and species (Siegel et al., 2022). As such, there is still much to learn about the relationship between changes to material composition and the degree to which the material is compromised. Unraveling this relationship will help inform how single-species responses can be inferred to impact species interactions, such as predator-prey encounters.

A better understanding of potential impacts is especially needed for crustaceans, which have generally garnered less OA research attention than other marine calcifiers (Whiteley, 2011; Siegel et al., 2022), but have an exoskeleton that is complex, multifunctional, and highly variable within a single individual. The decapod crustacean exoskeleton is heterogenous and comprised of mineral, usually in the form of calcite, magnesian calcite, amorphous calcium carbonate, and sometimes calcium phosphate, that is embedded among lamellae of sugars and protein, which stack to form the distinct layers of the epicuticle, exocuticle, and endocuticle (Travis, 1963; Huner et al., 1979; Vigh and Dendinger, 1982; Addadi et al., 2003; Dillaman et al., 2005; Boßelmann et al., 2007; Kunkel et al., 2012). Within the exocuticle and endocuticle, layer thickness, lamellae stacking density, and mineral composition can all be adjusted to produce a spectrum of material properties that support a range of exoskeleton functions (Raabe et al., 2005; Chen et al., 2008). Crustaceans can construct exoskeletal regions with specificity to meet functional demands (Melnick et al., 1996; Dutil et al., 2000; Chen et al., 2008) and likely have complex responses to OA-like conditions (Siegel et al., 2022).

Exoskeleton versatility is exemplified in the California spiny lobster, *Panulirus interruptus*, which begin living in coastal kelp forests as juveniles and use their exoskeleton in a suite of defenses against predators such as octopus, eels, and large fish, particularly the California sheephead, *Semicossyphus pulcher* (Lindberg, 1955; Loflen and Hovel, 2010; Higgins et al., 2018). One of the first strategies that spiny lobsters can employ to avoid harm is using the rostral horns to lock onto the roof of a rocky

shelter to avoid expulsion (Lindberg, 1955). Another option is to use their long, spiny antennae to push against predators, keeping the bulk of their body a safe distance away (Barshaw et al., 2003; Briones-Fourzán et al., 2006). As a last line of defense, the carapace is coated in flattened spines that likely enhance pierce-resistance (Tarsitano et al., 2006). Each of these defense behaviors are dependent on the exoskeleton being sufficiently stiff, hard, and strong under their different loading regimes, and their distinct composition and structure affords them the proper mechanical properties to achieve their function (Lowder, 2019). These defense structures, however, may be differentially vulnerable to the impacts of changing carbonate chemistry and therefore yield greater insight into the variable effects of OA on the structure-property relationships of calcified materials.

Understanding the impacts on spiny lobsters is not only complicated by the variability in their exoskeleton, but also by the variability in their environment. Spiny lobsters, like a number of other coastal organisms, live in dynamic environments that may shape their response to changing ocean conditions. Juvenile *P. interruptus* spend two to three years in shallow eelgrass or kelp environments (Engle, 1979), where they must be able to successfully exercise their full range of predator defense strategies while contending with diurnal changes in their environment (Frieder et al., 2012). In coastal environments, carbonate chemistry fluctuates diurnally, tidally, and seasonally (Johnson et al., 2013), producing variable conditions to which organisms in these habitats are subjected. In environments dominated by a large biomass of photosynthetic organisms, such as kelp forests or seagrass meadows, daily ranges of pH may be as great as the decrease in pH expected over the next century, 0.3-0.4 units (Frieder et al., 2012; Challener et al., 2015; James et al., 2019) driven in part by the uptake of CO_2 *via* photosynthesis during the day and organismal respiration at night. These ranges can be even greater than 1 unit (Semesi et al., 2009) depending on currents, tides, depth, and community composition (Hofmann et al., 2011; Page et al., 2016; Silbiger and Sorte, 2018). In addition, in coastal regions where seasonal upwelling is prominent, such as the U.S. West Coast, further decreases in near-shore pH may occur owing to intrusion of deep seawater with high CO_2 and low pH (Takeshita et al., 2015; Chan et al., 2017; Kekuewa et al., 2020).

For organisms that inhabit dynamic environments, the exposure to a range of conditions has potentially led to a degree of adaptation that may be beneficial as ocean carbonate chemistry continues to change. A growing, but still limited, number of studies have imposed fluctuations around low and high pH setpoints and discovered varied responses. For example, fluctuating pH conditions may ameliorate some or all of the negative growth and sensory impacts observed at stable reduced pH in pink salmon (Ou et al., 2015) and coral reef fish, where it is hypothesized to help prevent physiological changes in the brain (Jarrold et al., 2017). *Mytilus edulis* mussels take advantage of higher pH during the day to increase calcification rates, lessening the overall negative impact to calcification (Wahl et al., 2018), while *Mytilus galloprovincialis* veligers experiencing fluctuating reduced pH did not experience the same reductions in shell length that those in stable reduced pH did (Frieder et al., 2014). Yet, in some organisms, fluctuating pH conditions either have no discernable effect from stable reduced pH conditions (Clark and Gobler, 2016), or they appear to increase stress, producing more negative responses than stable reduced pH conditions alone (Alenius and Munguia, 2012; Mangan et al., 2017; Onitsuka et al., 2017; Johnson et al., 2019). Thus, to establish realistic impacts on organisms like the California spiny lobster, it is important to incorporate the natural fluctuating conditions of their habitat into OA experiments (Andersson and Mackenzie, 2012; McElhany and Busch, 2013; Andersson et al., 2015).

In this study, we exposed juvenile California spiny lobsters, *Panulirus interruptus*, to stable and fluctuating high pCO_2/reduced pH conditions that mimic their current and future habitat and examined the integrity of their predator defenses. Specifically, we examined the rostral horns, antennae, and carapace for elemental composition (Ca and Mg content), structure (cuticle and layer thickness), and material properties (hardness and stiffness) (Figure 1). We hypothesized that lobsters under low, stable pH conditions would have relatively higher exoskeleton mineralization than those in ambient conditions, resulting in altered mechanical properties, while these effects would be lessened in the fluctuating reduced pH conditions due to a respite from constant reduced pH conditions. Alternatively, the fluctuating reduced pH conditions may exceed potential pH thresholds, eliciting the same or exacerbated responses. We also hypothesized that the magnitude of response would vary across defensive structures due to localized control and functional specificity.

Methods

Animal collection

Sixty-four juvenile lobsters were collected from offshore La Jolla, San Diego, CA over the course of six days in October 2016. Commercial lobster traps were modified with smaller mesh and set at depths of 8.5 to 15.2 m. Lobsters were transported to the experimental aquarium at Scripps Institution of Oceanography (SIO) within 2.5 hours of collection and placed in flow-through seawater pumped from the Scripps Pier, approximately 2 km northeast from the site of collection.

Experimental design

The experimental ocean acidification system consisted of four 81 L header tanks that each received filtered seawater pumped from the SIO pier (3-4 m depth, 300 m offshore) at ambient pH (7.97 ± 0.03), pCO_2 (464 ± 39 µatm), and salinity (33.4 ± 0.2 PSU) (mean ± s.d. during the experimental period). A mix of chilled

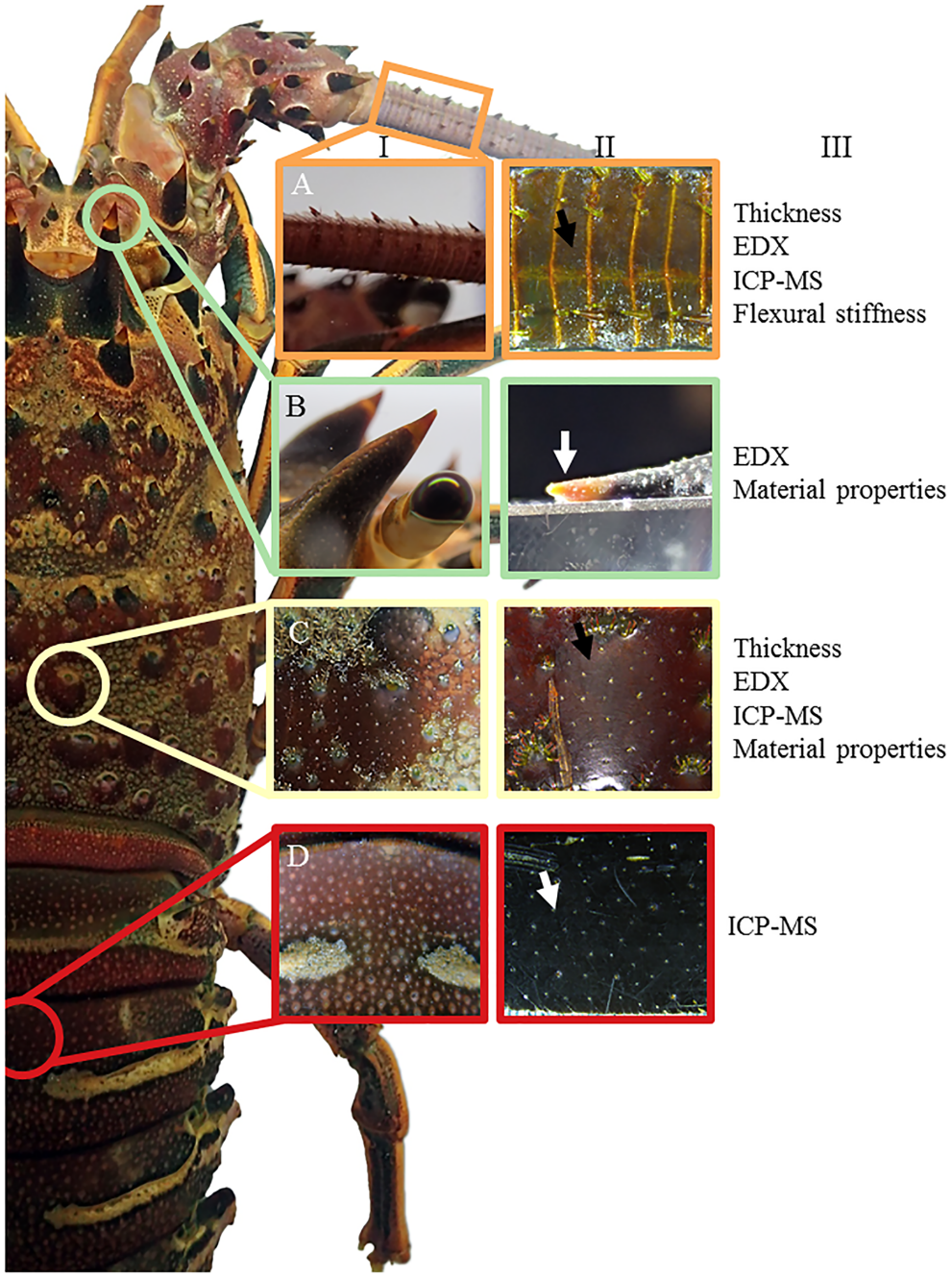

FIGURE 1
Exoskeletal defense structures of *Panulirus interruptus*. **(A)** antenna, **(B)** horn tip, **(C)** carapace spine, **(D)** abdominal segment in image columns I and II. The analyses performed for each structure are listed in column III. Arrows indicate areas where nanoindentation was performed normal to the surface. The horn tip in B-II is affixed to an aluminum block for nanoindentation.

and ambient temperature seawater was fed into the header tanks, which were maintained at a stable 16.5 ± 0.6°C with the aid of heaters. Two 1585 GPH aquarium powerheads were placed in each header tank to ensure adequate mixing.

One header tank was kept at ambient pH to provide the control treatment while the three others were adjusted for high pCO_2/low pH treatments. One treatment was adjusted to a stable pH of 7.7, congruent with current predictions for decreases in global ocean surface pH values of 0.3 pH units by the year 2100 (IPCC, 2014). pH levels as low as 7.77 have been observed at 10 m in the habitat of spiny lobsters during upwelling seasons (Kekuewa et al., 2020). In the kelp forest less than 1000 m from

the site of lobster collection, pH was found to average 8.05 units at 7 m depth with minima around 7.8 during a springtime period of observation (Frieder et al., 2012). The two other treatments were set to fluctuate around this reduced pH, but to different degrees. The reduced/low fluctuating pH treatment was set to 7.7 ± 0.05 (total range: 7.65-7.75) pH units based on published measurements of southern California kelp forest diurnal pH variations, which depend upon tide, season, and weather conditions, and which are approximately 0.1 pH units on average (Frieder et al., 2012; Kapsenberg and Hofmann, 2016). The reduced/high fluctuating pH treatment was set to 7.7 ± 0.10 (total range: 7.6-7.8) pH units, which mimics future diurnal fluctuations, calculated in CO_2Sys for decreases in buffering capacity associated with higher anthropogenic pCO_2 values and thus larger pH swings assuming the same autotrophic forcing of DIC (Pierrot et al., 2006). For both of the fluctuating treatments, high pH values were held stable for approximately 10 hours to match daylight (and photosynthesis) hours at the time of the experiment. Nighttime low pH values were held stable for 12 hours. pH was set at a midpoint value for one hour between each of these highs and lows as a transition period.

Experimental pH conditions were achieved by bubbling 100% CO_2 into the three treatment header tanks and were controlled by an Apex Lite aquarium controller with Apex Neptune pH and temperature probes (0.01 pH accuracy; temperature accuracy 0.1°C, Neptune Systems, Morgan Hill, CA, USA). pH and temperature of the header tanks were logged every 10 minutes throughout the duration of the experiment. The Apex pH probes were calibrated prior to the experimental period, but because stability and not accuracy was desired, they were not calibrated again.

Each header tank supplied flow-through seawater separately to 16 experimental tanks (8.4 L) that were randomly intermixed in the experimental area. Each experimental tank contained a single lobster, for a combined total of 64 individuals. Experimental water parameters were gradually altered over the course of three days to minimize potential acute stress. Once the targeted water parameters were reached, the experiment was run for 102 days.

Water chemistry

Daily readings of pH and temperature were taken from each lobster tank using a portable probe (HQ40d, probe PHC201, precision 0.01 pH, 0.1 temperature, Hach, Loveland, CO, USA) as a method of high-frequency measurements in between discrete carbonate chemistry water sample measurements (Figure S1). This probe was calibrated with NBS buffer solutions (Fisher Scientific, Fair Lawn, NJ, USA) approximately every three weeks to control its slow drift. Daily readings were taken at consistent times during the daytime to capture the high value in the fluctuating treatments. Calculated pH from discrete water samples (see below) was averaged for each sampling period and used to correct the portable probe values to pH_{total}. Each water sampling round corresponded to one calibration period of the portable probe.

Nighttime pH was checked using two methods to confirm that stable treatments were constant and that target fluctuations were achieved and consistent. In addition to four probes constantly monitoring and logging header tank pH, two additional Neptune Apex electrodes were rotated between random lobster tanks once per day and recorded pH every 10 minutes over the course of each 24-hour period. Nighttime pH in the fluctuating treatments was recorded to be 0.11 ± 0.02 (n = 54) and 0.21 ± 0.03 (n = 46) pH units lower than daytime pH, consistent with our targeted values. Periodic measurements of nighttime pH with the handheld probe (n=8) were in agreement with the readings of the Apex probes.

Discrete samples were collected for water chemistry analysis four times from three randomized lobster tanks per treatment over the experimental period (48 samples total). Samples were collected in 500 mL Pyrex glass bottles and poisoned with 120 µL of a saturated solution of $HgCl_2$ in accordance with standard operating procedures (Dickson et al., 2007). Each water sample was analyzed for total alkalinity (A_T) by potentiometric acid titration (0.1 N HCl) using an 876 Dosimat (Metrohm, Riverview, Florida, USA) and pH electrode (Ecotrode Plus, Metrohm, Riverview, Florida, USA) and for dissolved inorganic carbon (DIC) using an AIRICA system (Marianda, Kiel, Germany) with integrated infrared CO_2 analyzer (Li-COR 7000, Li-COR, Lincoln, Nebraska, USA). Certified reference material (CRM) provided by the Dickson laboratory at SIO were used to verify the accuracy and precision, both to ± 1–4 µmol kg^{-1}, before and after measuring samples as well as between every five samples for DIC and ten for A_T. Other parameters of the carbonate system were calculated using CO_2Sys 25.06 (Pierrot et al., 2006) (**Table 1**). For calculations, dissociation constants of K_1, K_2 were from Mehrbach et al., 1973, refit by Dickson and Millero, 1987. The HSO_4^- constant was from Dickson, 1990 and the [B]T value was from Uppström, 1974.

Survival, molting, and growth

Lobsters were fed equal amounts of squid five days per week in excess, with remaining food removed daily. Tanks were checked daily for deaths and molting events; exuviae were promptly removed to prevent fouling and consumption. Growth was recorded at the start and end of the experiment by weighing damp lobsters in air after removal from tanks and allowing excess water to run off. Carapace length was measured from the notch at the base of the rostral horns to the posterior edge of the carapace at the dorsal midline. Initial size ranged from 43.5 to 58.5 mm carapace length (CL) and 75.4 to 198.2 g. Of the 64 lobsters, 20 were male and 44 were female, and 30% showed at least some physical indications of sexual maturity (e.g., softened sternal plates and enlarged testes identified during dissection). Carapace

TABLE 1 Water parameters during the experimental period as mean ± sd.

Treatment	Daytime pH (total)	Daily range of pH	Mean pH (total)	Temp (°C)	DIC (µmol/kg SW)	TA (µmol/kg SW)	pCO_2 (µatm)	HCO_3^- (µmol/kg SW)	Ω Calcite
Ambient/ stable (7.97)	7.97 ± 0.03 [1329]	0.01 ± 0.01 [49]	7.97	16.5 ± 0.6 [1560]	2030 ± 16 [12]	2219 ± 10 [12]	464 ± 39 [12]	1873 ± 30 [12]	3.37 ± 0.32 [12]
Reduced/ stable (7.67)	7.67 ± 0.04 [1350]	0.01 ± 0.02 [50]	7.67	16.6 ± 0.6 [1569]	2136 ± 11 [12]	2218 ± 9 [12]	978 ± 53 [12]	2023 ± 13 [12]	1.90 ± 0.15 [12]
Reduced/ low fluctuating (7.67 ± 0.05)	7.72 ± 0.03 [1317]	0.11 ± 0.02 [54]	7.67	16.4 ± 0.5 [1662]	2124 ± 11 [12]	2219 ± 8 [12]	863 ± 71 [12]	2008 ± 14 [12]	2.06 ± 0.14 [12]
Reduced/ high fluctuating (7.67 ± 0.10)	7.77 ± 0.03 [1333]	0.21 ± 0.03 [46]	7.67	16.4 ± 0.7 [1667]	2103 ± 12 [12]	2219 ± 8 [12]	751 ± 52 [12]	1979 ± 17 [12]	2.34 ± 0.20 [12]

Values in brackets indicate the sample size. pH is calculated by applying the offset between discrete water samples and portable probe readings to the daily probe readings. Daily ranges of pH are calculated from two Apex probes that were rotated between lobster tanks daily. The mean pH for each treatment was determined as the midpoint between mean daytime and nighttime pH. Temperature is from daily portable probe readings. DIC and TA are directly measured from discrete water samples, while pCO_2, HCO_3^-, and calcite saturation state are all calculated from discrete water samples using CO_2Sys; these values reflect daytime conditions. Nighttime pH values may be inferred from the difference between the daytime pH and the daily range.

length and sex were used to assign individuals to each treatment so that these factors were evenly distributed.

Cuticle structure and elemental composition

At the end of the experiment, lobsters were anesthetized by brief placement in a -20°C freezer and then sacrificed by piercing the exoskeleton and tissue between the rostral horns with a ceramic knife. Samples of cuticle were dissected by cutting ~ 0.75 x 0.75 cm^2 around a consistent carapace spine located below the cephalothorax line, a 0.5 x 1.5 cm^2 section of the antennae 1 cm above the posterior base on the dorsal side, and around the base of the rostral horn. Each cuticle sample was rinsed with DI water and allowed to air dry. Samples were then freeze-fractured with liquid nitrogen so that an orthogonal cross-section was produced and critical-point dried (AutoSamdri 815 Series A, Tousimis, Rockville, MD, USA) before being mounted on a 90-degree SEM tip and sputter-coated with iridium.

Cross-sections of these cuticle samples were examined with ultra-high-resolution scanning electron microscopy under high vacuum (XL30 SFEG with Sirion column and Apreo LoVac, FEI, Hillsboro, OR, USA with Oxford X-MAX 80 EDS detector, Concord, MA, USA) at 10 or 20 kV. One to two samples each of the carapace spine and antenna from individual lobsters were imaged and measured for the total cuticle thickness (epicuticle, exocuticle, and endocuticle), as well as thickness of the individual exo- and endocuticle layers, which were differentiated by the abrupt change in lamellae stacking density (Figure S3). The rostral horn has an unusual structure, consisting of only two layers: an inner region, that we will refer to as the core, and an outer layer that we will refer to as the outer ring (Lowder, 2019). Layer thickness (and the total thickness) for which the sample did not produce a clean cross section, most commonly observed as a flaky and uneven endocuticle, were not included in analyses (n=0-2 per layer per treatment).

Elemental composition of cuticle samples was quantified using both energy-dispersive x-ray spectroscopy (EDX) and inductively coupled plasma mass spectrometry (ICP-MS). The spatial resolution of EDX enabled elemental sampling of the surface of exocuticle and endocuticle layers separately, whereas ICP-MS provided precise quantification of elements present in the whole volume of cuticle sample. EDX was measured with two machines (XL30 SFEG with Sirion column and Apreo LoVac, FEI, Hillsboro, OR, USA with Oxford X-MAX 80 EDS detector, Concord, MA, USA) at 20 kV acceleration voltage. Spectra were taken on the cross-sectional surface of the exocuticle and the endocuticle layers of the carapace spine and antenna base and the core and outer ring of the horn tip. Eleven elements were consistently present in varying amounts: C, N, O, Ca, Mg, Na, Al, P, Si, S, and Cl. The amount of Ca and Mg were expressed as weight percent (% wt) relative to the other nine elements.

Inductively-coupled plasma mass spectrometry (ICP-MS) was performed on cuticle samples at the Scripps Isotope Geochemistry Laboratory (SIGL) for a precise quantification of elements. The carapace spine was air-dried and then trimmed so only the spine remained with no setae, and the abdominal segment was cut as a 1 x 1 cm^2 from the center of the second abdominal segment and air-dried. Samples were weighed and placed in Teflon vials for digestion with 0.5 ml of concentrated Teflon-distilled (TD) nitric acid (HNO_3) on a hotplate at 100°C for >24 h. Samples were dried down and diluted by a factor of 4000 with 2% TD HNO_3 before being transferred to pre-cleaned centrifuge tubes for analysis. Samples were doped with an indium

solution to monitor instrumental drift. Measurements were done using a ThermoScientific iCAPq c ICP-MS (Thermo Fisher Scientific GmbH, Bremen, Germany) in standard mode. Masses of Mg and Ca were sequentially measured for 30 ratios, resulting in internal precision of <2% (2 s.d.). Elements were corrected for total mole fraction. Total procedural blanks represented <0.3% of the measurement for Mg and Ca. Raw data were corrected offline for instrument background and drift. Samples were bracketed by internal standards of crab carapace (n=3), which allowed for calculation of absolute values. The standards yielded external precision of 2% and 3% for Mg and Ca, respectively. We targeted the following isotopes: ^{10}B, ^{25}Mg, ^{26}Mg, ^{27}Al, ^{29}Si, ^{31}P, ^{43}Ca, ^{48}Ca, ^{54}Fe, ^{57}Fe, ^{65}Cu, ^{66}Zn, ^{86}Sr, ^{111}Cd, ^{137}Ba, ^{208}Pb, and ^{238}U (Figures S4, S5). A weighted average based on the natural abundance of isotopes was calculated for Ca and Mg and used in analyses.

Material properties

The carapace spine and rostral horn tip were tested for hardness and stiffness using a nanoindentation materials testing machine (Nano Hardness Tester, Nanovea, Irvine, CA, USA) equipped with a Berkovich tip. Fresh samples (<12 hours, except for two samples tested within 24 hours) were kept hydrated in seawater until testing. Samples were secured to an aluminum block with cyanoacrylate glue such that the outer surface was facing up. Indentations were performed by applying a load of 40 mN to the outer surface of the sample at loading and unloading rates of 80 mN/min with a 30 sec hold for creep. At least three indents were taken and averaged per sample.

Antenna stiffness

One antenna was removed from each lobster at the base (first segment above the antennae knuckle). The proximal 5 mm of the antennal base was embedded in epoxy (EpoxiCure, Buehler, Lake Bluff, IL, USA) and allowed to cure overnight. Antennae were covered with seawater-soaked paper towels to remain hydrated until testing. The embedded ends of the antennae were clamped in a universal materials testing machine (E1000, 250N load cell, Instron, Norwood, MA, USA) such that the antennae extended laterally. A force was applied at a rate of 20 mm/min to two locations on the antennae, one at 1/3 of the total antenna length ("proximal") and one at 2/3 of the total antenna length ("distal"), until a displacement of 10% of antenna length was reached. The stiffer proximal region of the antenna has a thicker ovular cross section than the distal location, and it lies directly over the carapace when the lobster raises its antennae in a defensive position, so it is believed to be the primary location where force is applied by predators (Lowder, pers. obs.). The tapering of the antennae imbues more flexibility towards the distal end, perhaps to avoid breakage. Flexural stiffness, *EI*, was calculated as:

$$EI = \frac{F_{max} \times antennal\,length^3}{3 \times deflection_{max} \times 0.001}$$

Statistics

All analyses were carried out in R version 3.5.1 (R Core Team, 2019) and associated packages (Wickham, 2016a, 2016b, 2017). We tested survival, growth, cuticle measurements (elemental composition, thickness, material properties), and antennae flexural stiffness data for normality and homogeneity of variances with the Shapiro-Wilk and Bartlett's tests (after the removal of outliers, see below). If data met these conditions, we compared metrics across treatments using one-way ANOVAs and followed with Tukey's Honest Significant Difference test if appropriate. Otherwise, the Kruskal-Wallis with Dunn's test or Welch's corrected ANOVA with Games-Howell *post-hoc* test was used for instances of non-normality and heteroscedasticity, respectively. Carapace length ANOVA residuals were checked for test assumptions visually and with the Shapiro-Wilks test, then log-transformed to meet assumptions. $\alpha = 0.05$ with the exception of elemental data, where we used a Bonferroni correction for repeated measures.

Some cuticle samples had one or two material properties tests that resulted in unusually high values for crustacean cuticle. In many of these instances, the indent was misshapen (stretched in one direction), indicating that the force was not applied perpendicularly to the surface in the manner that is required for accurate measurements. As such, material property outliers of each treatment were calculated and removed *via* the Tukey "fence" or "boxplot rules" method of Q_3 + 1.5 x IQR, where Q_3 is the third quartile and IQR is the interquartile range from the first to the third quartile (Tukey, 1977). The lower "fence" was also calculated, but was always below zero. This method identified outliers ≥ 13.4 GPA in stiffness for the horn and ≥13.1 GPa for the carapace spine. Hardness outliers were ≥ 0.49 GPa for the horn and ≥ 0.52 GPa for the carapace spine.

Results

Survival and molting

All lobsters survived the experimental period and appeared healthy at its conclusion. Molting only occurred in nine out of the sixty-four animals (n=4 in ambient/stable; n=1 in reduced/stable pH; n=3 in reduced/low fluctuating; n=1 in reduced/high fluctuating treatment) and were not included in subsequent analyses. Growth results are included in the supplementary material. The remaining lobsters were molt-staged based on exoskeleton hardness and evidence of apolysis (Travis, 1954; Lyle and MacDonald, 1983) and were determined to be in intermolt, excluding two lobsters that showed signs of apolysis (one from

10.3389/fmars.2022.909017

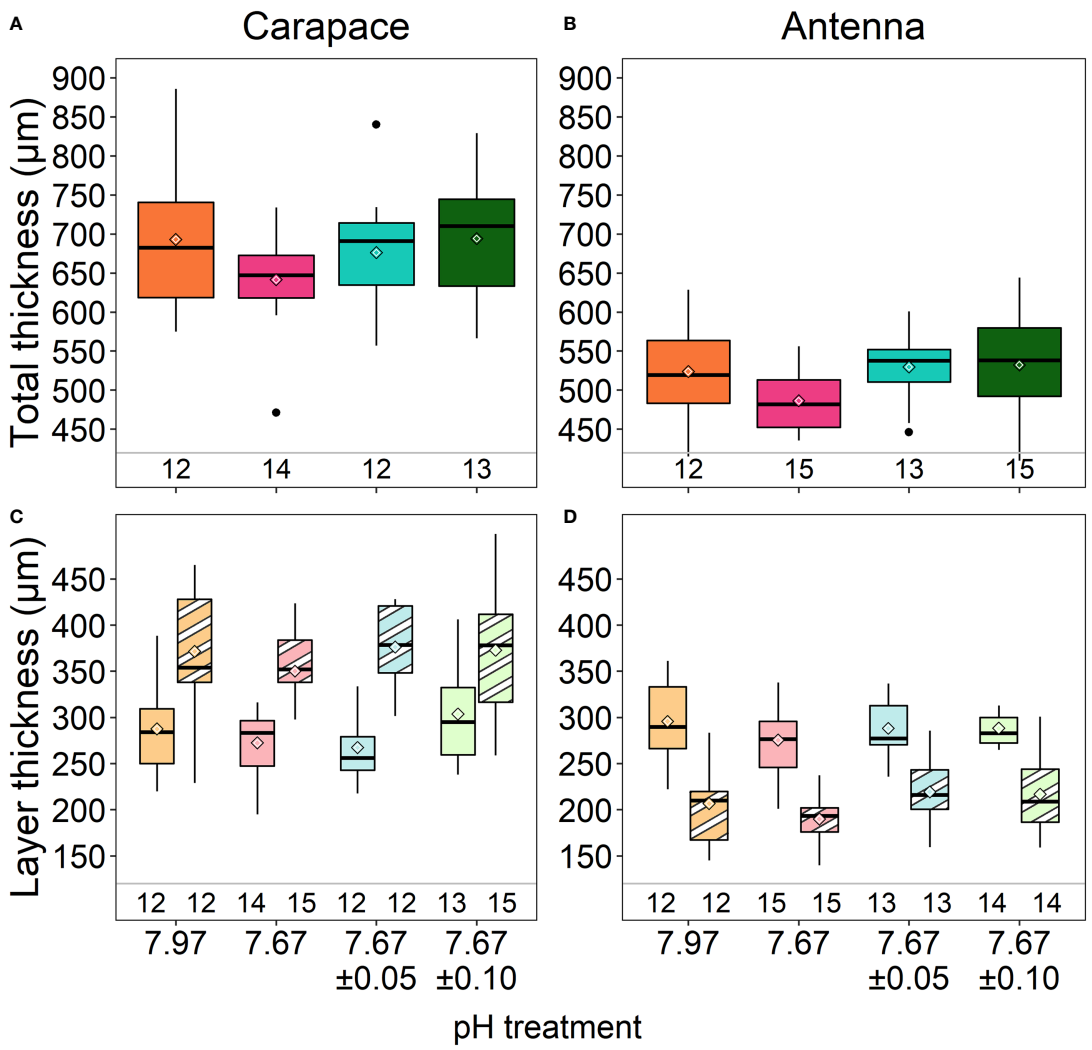

FIGURE 2
Total cuticle thickness of the carapace **(A)** and antennae **(B)** and cuticle layer thickness of the carapace **(C)** and antennae **(D)**. Exocuticle layers are right boxes of each treatment (stripes in **C, D**) and endocuticle layers are left boxes of each treatment (solids in C, D). There were no differences in total thickness or layer thickness of the carapace or antennae among treatments. Box boundaries are the first and third quartiles, whiskers are 1.5 times the interquartile range, the center line is the median, black and white diamonds are the mean, and outliers are solid dots. Values on the bottom of panels denote sample size.

the reduced/stable pH treatment and one from the reduced/high fluctuating pH treatment).

Cuticle structure

There were no significant differences in total cuticle thickness of the carapace (ANOVA: $F_{3,47} = 1.283$, p=0.291) and antennae (ANOVA: $F_{3,51} = 2.006$, p=0.125) among treatments (Figures 2A, B; Table 2; Lowder et al., 2022). Additionally, there were no significant differences in thickness of either the exocuticle or endocuticle layers of either structure (Figures 2C, D; ANOVA, carapace exocuticle: $F_{3,50} = 0.522$, p=0.669; endocuticle: $F_{3,47} = 1.874$, p=0.147; antenna exocuticle: ANOVA: $F_{3,50} = 1.675$, p=0.184; endocuticle: ANOVA: $F_{3,50} = 0.562$, p=0.642).

Cuticle elemental composition

Elemental data from the XL30 SFEG EDX were inconsistent with that of the other EDX instrument and with previous data on lobster cuticle (Lowder, 2019), and were thus excluded from analysis. Analyses carried out with the full set of data did not result in different conclusions. The remaining data (n=5-9 samples per treatment) revealed no significant differences in % wt Ca in either of the carapace layers (Figure 3A; exocuticle: Kruskal-Wallis,

TABLE 2 Mineralization (μmol/mg from ICP-MS measurements; % wt from EDX measurements), ultrastructure (μm from SEM measurements), and mechanical properties (GPa from nanoindentation tests) for the four studied structures across treatments.

Measurement	Structure	Treatment			
		Ambient/stable	Reduced/stable	Reduced/low fluctuating	Reduced/ high fluctuating
Thickness (μm)					
Total cuticle	Abdominal segment	–	–	–	–
	Antenna	524 ± 68	487 ± 40	530 ± 46	532 ± 71
	Carapace	693 ± 92	641 ± 64	676 ± 78	694± 85
	Horn	–	–	–	–
Exocuticle	Abdominal segment	–	–	–	–
	Antenna	207 ± 52	190 ± 26	219 ± 36	217 ± 41
	Carapace	372 ± 67	350 ± 63	376 ± 46	373± 68
	Horn	–	–	–	–
Endocuticle	Abdominal segment	–	–	–	–
	Antenna	296 ± 47	275 ± 40	288 ± 29	288 ± 48
	Carapace	288 ± 50	272 ± 35	267 ± 40	304 ± 47
	Horn	–	–	–	–
Ca					
Total cuticle (μmol/mg)	Abdominal segment	4.65 ± 0.13	4.57 ± 0.18	4.48 ± 0.1	4.59 ± 0.21
	Antenna	–	–	–	–
	Carapace	6.04 ± 0.36	5.95 ± 0.39	5.78 ± 0.31	**5.62 ± 0.25**
	Horn	–	–	–	–
Exocuticle/	Abdominal segment	–	–	–	–
outer ring (% wt)	Antenna	19.3 ± 5.9	15.3 ± 8.4	20.1 ± 10.1	22.7 ± 6.5
	Carapace	20.6 ± 10.5	25.1 ± 6.4	21.6 ± 8.8	20.6 ± 5.1
	Horn	1.3 ± 1.6	0.6 ± 0.2	0.7 ± 0.5	2.6 ± 5.5
Endocuticle/	Abdominal segment	–	–	–	–
core (% wt)	Antenna	27 ± 9.4	21.4 ± 6.3	25.3 ± 11.9	28.2 ± 11
	Carapace	25.2 ± 7.2	30.4 ± 10.9	23 ± 5.3	25.5 ± 6.9
	Horn	18.1 ± 5.8	17.3 ± 5.8	17.9 ± 4.1	17.1 ± 7.6
Mg					
Total cuticle (μmol/mg)	Abdominal segment	0.44 ± 0.02	0.42 ± 0.03	0.44 ± 0.03	0.42 ± 0.03
	Antenna	–	–	–	–
	Carapace	0.47 ± 0.04	0.44 ± 0.04	**0.43 ± 0.04**	**0.41 ± 0.02**
	Horn	–	–	–	–
Exocuticle/	Abdominal segment	–	–	–	–
outer ring (% wt)	Antenna	1.4 ± 0.3	1.1 ± 0.3	1.4 ± 0.1	1.4 ± 0.3
	Carapace	1.6 ± 0.1	1.8 ± 0.3	1.7 ± 0.2	1.7 ± 0.3
	Horn	0.3 ± 0.1	0.2 ± 0.0	0.3 ± 0.2	0.5 ± 0.5
Endocuticle/	Abdominal segment	–	–	–	–
core (% wt)	Antenna	1.1 ± 0.4	1.1 ± 0.2	1.2 ± 0.2	1.2 ± 0.3
	Carapace	1.5 ± 0.2	1.5 ± 0.3	1.6 ± 0.1	1.6 ± 0.3
	Horn	1.1 ± 0.2	1 ± 0.2	1 ± 0.2	0.9 ± 0.4
Material properties					
Stiffness (GPa)	Carapace	15.3 ± 5.3	14.6 ± 5.8	11.9 ± 5.4	11.5 ± 4.1
	Horn	7.0 ± 1.9	7.3 ± 1.9	6.9 ± 2.4	7.2 ± 2
Hardness (GPa)	Carapace	0.32 ± 0.12	0.34 ± 0.13	0.22 ± 0.12	0.24 ± 0.09
	Horn	0.34 ± 0.05	0.36 ± 0.05	0.28 ± 0.03	**0.28 ± 0.05**

Values are mean ± s.d. Bold values are significantly different from values of lobsters in ambient conditions.

χ^2 = 2.154, df=3, p = 0.541; endocuticle: ANOVA, $F_{3,25}$ = 1.081, p = 0.375), horn layers (Figure 3C; outer ring: Kruskal-Wallis, χ^2 = 0.453, df=3, p = 0.929; core: ANOVA, $F_{3,21}$ = 0.04, p = 0.989), and antenna layers (Figure 3B; exocuticle: ANOVA, $F_{3,25}$ = 1.873, p = 0.160; endocuticle: ANOVA, $F_{3,25}$ = 0.658, p = 0.585; Table 2).

There were also no significant differences in % wt Mg in either of the carapace layers (Figure 3D; exocuticle: Welch's ANOVA, $F_{3,11.80}$ = 2.389, p = 0.121; endocuticle: Kruskal-Wallis, χ^2 = 1.266, df=3, p = 0.737), horn layers (Figure 3F); outer ring: Kruskal-Wallis, χ^2 = 0.754, df=3, p = 0.861; core: Kruskal-Wallis, χ^2 = 2.559, df=3, p = 0.465), and antenna layers (Figure 3E; exocuticle: Kruskal-Wallis, χ^2 = 6.061, df=3, p = 0.109; endocuticle: Kruskal-Wallis, χ^2 = 0.968, df=3, p = 0.809; Table 2).

Elemental analysis of the carapace using ICP-MS contrasted with the results obtained from the EDX analysis; the former measured elements over whole volume cuticle whereas the latter measured elements over a surface area whose features can influence electron scattering and thus element quantification. There were significant differences in calcium and magnesium content in the carapace across treatments (calcium: ANOVA,

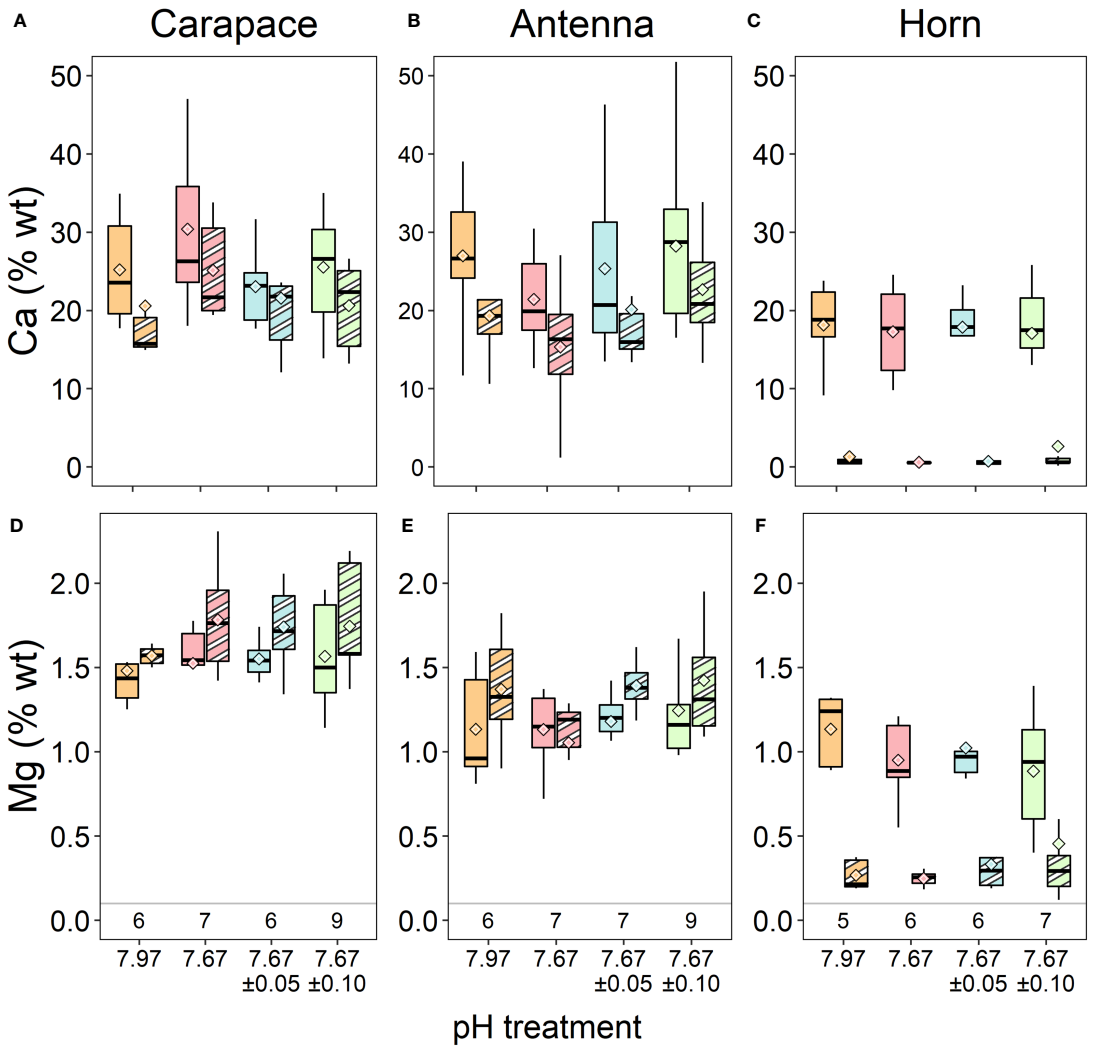

FIGURE 3
Calcium and **(A-C)** Mg **(D-F)** % wt of three exoskeletal structures from EDX measurements. There were no significant differences in either element across treatment conditions. Each structure's exocuticle, or the outer layer in the case of the horn, is represented as the right boxes of each treatment (striped shades), and the endocuticle layers or core of the horn are the left boxes of each treatment (solid shades). Box boundaries are the first and third quartiles, whiskers are 1.5 times the interquartile range, the center line is the median, and black and white diamonds are the mean. Values on the bottom of panels **(D-F)** denote sample size for each structure.

$F_{3,51}$ = 4.313, p = 0.009; magnesium: Kruskal-Wallis, χ^2 = 15.184, df=3, p = 0.002; Figures 4A, C; Table 2). Calcium was 6% lower in the reduced/high fluctuating treatment than the reduced/stable treatment (Tukey HSD, p = 0.043) and 7% lower than the ambient/stable conditions (Tukey HSD, p = 0.010).

Carapace magnesium was significantly lower, by 13%, in the reduced/high fluctuating treatment in comparison to both ambient/stable and the reduced/stable treatments (Tukey HSD, $p \leq 0.006$; Figure 4C; Table 2). The reduced/low fluctuating treatment was also significantly decreased by 8% compared to the ambient/stable treatment (Dunn's test, p = 0.011). Magnesium tended to be lower in the reduced/stable treatment than in ambient/stable (Dunn's test, p = 0.047), and the two fluctuating treatments showed slightly different concentrations (Dunn's test, p = 0.042), although these trends were not statistically significant, as the Bonferroni correction for repeated measures was applied.

In the abdominal segment, there were no significant differences in the calcium (ANOVA: $F_{3,51}$ = 2.21, p=0.098; Figure 4B), and magnesium (ANOVA: $F_{3,51}$ = 1.36, p=0.266; Figure 4D) concentrations between treatments (Table 2).

Cuticle material properties

The carapace spine and rostral horn responded differently to treatment conditions. The carapace spine did not show a significant difference in hardness (ANOVA: $F_{3,37}$ = 2.708, p=0.06; Figure 5A), although the carapaces that were exposed to reduced

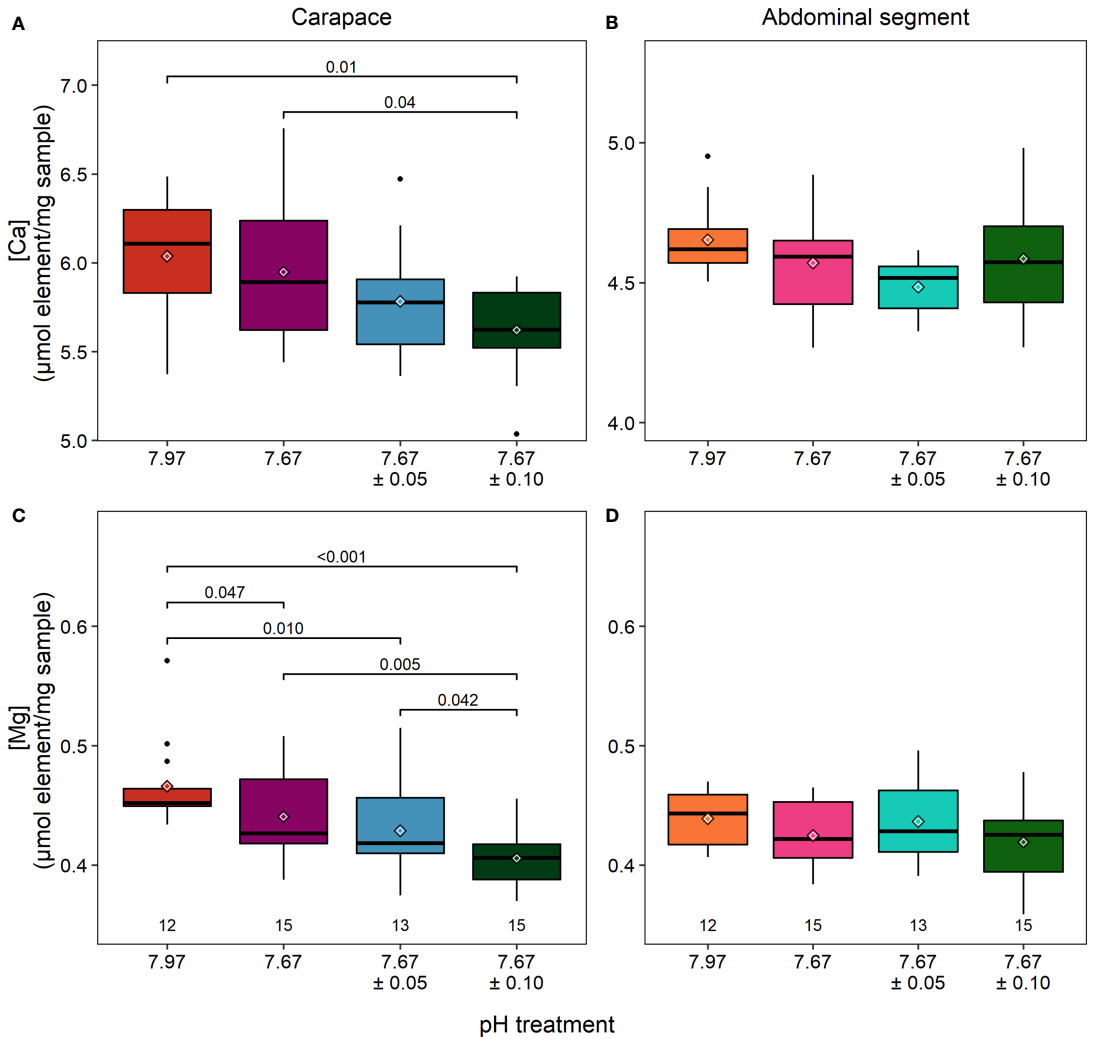

FIGURE 4
Calcium **(A, B)** and magnesium **(C, D)** concentrations measured with ICP-MS. In the carapace of lobsters in the reduced/high fluctuating treatment (7.67 ± 0.10), there was significantly less calcium **(A)** present than in lobsters in ambient/stable conditions. Lobsters in both fluctuating treatments had significantly less magnesium than those in ambient/stable treatments. There were no differences found in the cuticle of the abdominal segment, which had lower and less variable amounts of calcium but similar amounts of Mg to the carapace. Note different axes for panels **(A, B)** α=0.025 after a Bonferroni correction. Box boundaries are the first and third quartiles, whiskers are 1.5 times the interquartile range, the center line is the median, black and white diamonds are the mean, and outliers are solid dots. Values on the bottom of panels denote sample size.

fluctuating pH treatments tended to show lower hardness than those in stable pH treatment, averaging 28% lower. Stiffness was not significantly different across treatments (ANOVA: $F_{3,37}$ = 1.376, p =0.27; Figure 5C; Table 2).

The horns differed significantly in hardness among treatments (ANOVA: $F_{3,36}$ = 7.307, p<0.001) (Figure 5B; Table 2). Horns from lobsters exposed to the two stable pH treatments were statistically the same. However, horn samples from the reduced/high fluctuating treatment were significantly less hard than those from either of the stable pH treatments by 15 - 22% ($p \leq 0.045$). The reduced/low fluctuating treatment horns were lower, but not significantly different, from those in the ambient/stable pH treatment (p=0.050), although they were significantly lower than those in reduced/stable pH treatment (p=0.004). There were no significant differences in horn stiffness among the treatments (ANOVA: $F_{3,36}$ = 0.077, p=0.972; Figure 5D; Table 2).

Antenna stiffness

Mean antennal flexural stiffness (*EI*) at the more flexible distal location did not differ among lobsters in any treatments (Kruskal-Wallis rank sum test, χ^2 = 3.52, df=3, p=0.318) (ambient/stable: 0.004 ± 0.002 Nm^2; reduced/stable: 0.003 ± 0.002 Nm^2; reduced/low fluctuating: 0.003 ± 0.001 Nm^2; reduced/high fluctuating: 0.004 ± 0.002 Nm^2) (Figure 6). At the stiffer proximal location, *EI* was significantly lower in lobsters exposed to reduced/stable pH

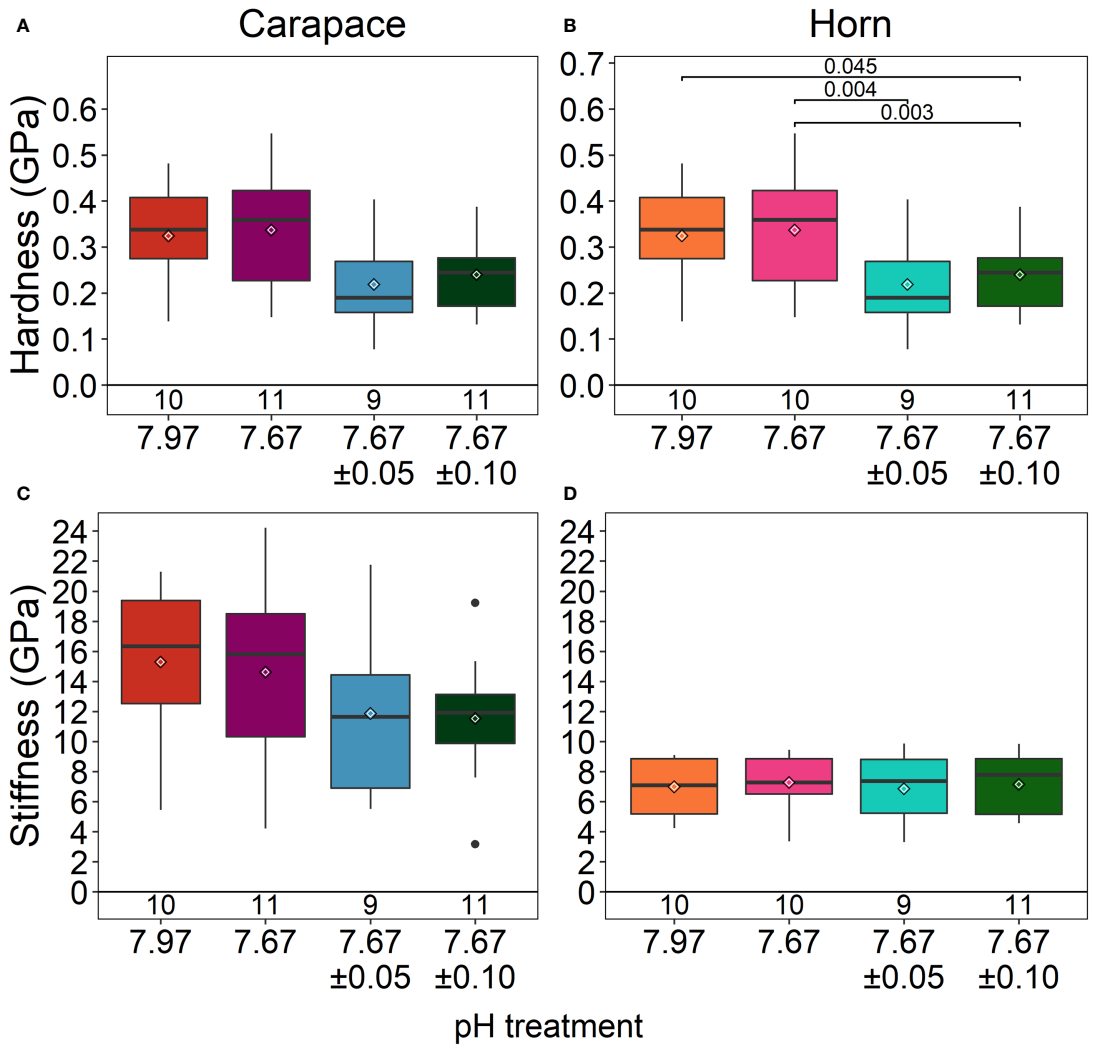

FIGURE 5
Material properties of the carapace spine **(A, C)** and rostral horn **(B, D)**. The carapace spine did not show any differences in material properties among treatments. The horn significantly differed in hardness. Lobsters exposed to reduced/high fluctuating pH conditions had horns that were less hard than those exposed to stable pH conditions (both ambient and reduced pH). Box boundaries are the first and third quartiles, whiskers are 1.5 times the interquartile range, the center line is the median, black and white diamonds are the mean, and outliers are solid dots. Values on the bottom of panels denote sample size.

treatments than lobsters exposed to reduced/high fluctuating pH (Welch's ANOVA: $F_{3,22.55} = 3.15$, p=0.045; Games-Howell posthoc p=0.035). There were no significant differences among the other treatments ($p \geq 0.20$), although *EI* was slightly lower in antennae from the reduced/stable and reduced/low fluctuating treatment than those in ambient conditions (ambient/stable: 0.023 ± 0.012 Nm^2; reduced/stable: 0.018 ± 0.004 Nm^2; reduced/low fluctuating: 0.020 ± 0.004 Nm^2; reduced/high fluctuating: 0.026 ± 0.010 Nm^2).

Discussion

Predation is thought to be the largest source of mortality for juvenile California spiny lobster, *P. interruptus*, until they reach a size refuge against most predators at four to five years of age (Engle, 1979). Mortality rates during this critical life stage could be exacerbated if anti-predation strategies and defenses are compromised by changing ocean carbonate chemistry. OA-like conditions are known to affect the composition of calcified materials (Chan and Connolly, 2013; Kroeker et al., 2013; Davis et al., 2021), potentially disrupting the mechanical properties, though this link is not often studied in crustaceans (Taylor et al., 2015). Furthermore, mineralization effects are generally measured on one or two crustacean body regions, typically the carapace and chelae (Dutil et al., 2000; Boßelmann et al., 2007; Amato et al., 2008), but the strong localization of mineralization and specialization of different structures can lead to differential responses to OA. Lastly, exposure to stable reduced pH experimental conditions does not adequately assess the vulnerability of animals

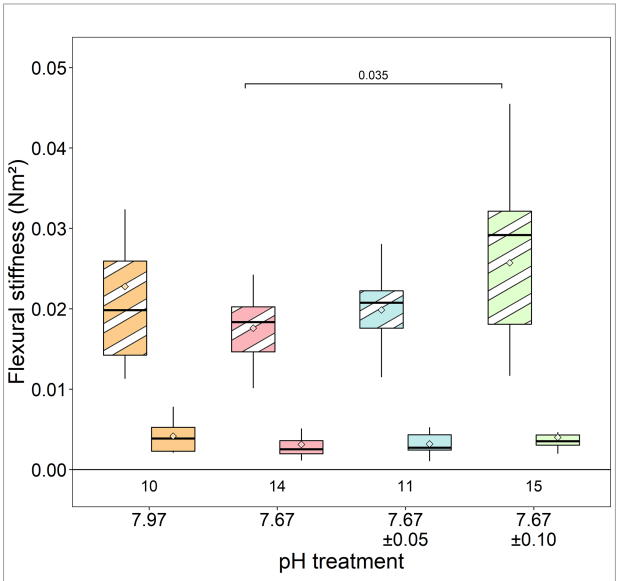

FIGURE 6
Flexural stiffness of the antennae at proximal (striped shades) and distal (solid shades) locations. The low stiffness at the distal location was similar across all treatments. While antennae from the reduced/high fluctuating treatment were stiffer at the proximal base than lobsters in the reduced/stable pH treatment, there were no significant differences in flexural stiffness from the ambient/stable treatment. Box boundaries are the first and third quartiles, whiskers are 1.5 times the interquartile range, the center line is the median, and black and white diamonds are the mean. Values on the bottom of panels denote sample size.

that live in dynamic pH environments (Wahl et al., 2015). Here, we tested the hypotheses that reduced stable pH conditions would affect the mineralization and mechanical properties of exoskeletal defense structures, that the effects would differ in magnitude across structures, and that fluctuating reduced pH conditions would mitigate these effects. After exposing juvenile *P. interruptus* to diurnal conditions that mimic their natural environment under near-future seasonal upwelling and/or OA, we found that most exoskeletal properties were unaffected by the treatment conditions, but that the integrity of some important exoskeletal defenses were compromised in variable ways and not as hypothesized. In particular, changes in mineralization or material properties were observed across key defensive structures (i.e., carapace, rostral horns, and antennae) in ways that were site specific, but absent of typical mineral-mechanical properties relationships. These effects were induced primarily by fluctuating reduced pH conditions and, to a limited extent, stable reduced pH conditions.

Exoskeletal defense integrity

Rostral horns

Spiny lobster rostral horns must be sufficiently hard and stiff to anchor animals in their dens when predators attempt to expel them. The spine-like shape of the horns is effective at locking into the interstices of hard substrate, while high hardness and stiffness limit deformation and yield stress. Structurally, rostral horns differ from the typical cuticle template by having only two layers, an outer and inner core (Lowder, 2019). The outer layer of the horn is poorly mineralized in comparison to typical crustacean cuticle, with just 1.4% Ca and 0.3% Mg. Neither Ca or Mg percentages were affected by reduced pH conditions in either layer, but hardness of the horn tips was lower in the reduced pH fluctuating conditions (both low and high fluctuating). The magnitude of this change in hardness is slight (<0.1 GPa, or 15%) compared to the decrease in microhardness observed in the chelae of juvenile blue and red king crabs (~44 VHN, or 46%) (Coffey et al., 2017). While red king crabs exhibited this decrease after exposure to pH 7.8, blue king crabs did so under a more extreme pH of 7.5; however, both species were exposed for a longer period of time (1 year) during which these effects manifested. It is unknown if the magnitude of change observed in spiny lobsters after three months of exposure would result in notable effects on lobster anchoring ability, but it is possible that longer exposure encompassing exoskeleton regeneration through one or more molt cycles could result in more dramatic effects.

We could not separate the horn layers for analysis of Ca and Mg content using the ICP-MS method, though EDX is sufficient for documenting differences in elemental composition (Fabritius et al., 2012; Taylor et al., 2015). The rostral horns have high amounts of halogens, such as chlorine, in the outer ring (Lowder, 2019), similar to the dactyl tips of crabs that scrape algae from rocks (Cribb et al., 2009). The replacement of calcium carbonate with halogenated compounds provides structures with greater toughness rather than hardness, which is beneficial for avoiding wear and breakage on rocky surfaces (Cribb et al., 2009; Schofield et al., 2009). This would be functionally important for the rostral horns that must lodge into the rocky underhangs of their shelter. It is interesting though that horn hardness was affected by reduced, fluctuating pH conditions despite its uncalcified state, hinting at a potentially complex interplay of elements under different ocean carbon chemistry parameters.

Antenna

Lobsters use their antennae as cantilevers to push away animals and maintain their distance (Kanciruk, 1980; Spanier and Zimmer-Faust, 1988). Sufficient flexural stiffness of the antennae is necessary to produce and maintain forces that hold predators at bay. In general, antennal cuticle has a thinner exocuticle layer compared to carapace cuticle, but both have similar Ca and Mg content. Flexural stiffness of the antenna is derived by the greater second moment of area associated with its hollow, tubular design, but it is also dependent on cuticle thickness and stiffness. Neither cuticle thickness nor mineral content of the antennae were affected by reduced pH conditions, unlike the carapace. Though there were no detectable changes in structure and composition, stiffness at the proximal base of the antennae in reduced/stable pH conditions was significantly reduced, by 31%, relative to

the reduced pH/high fluctuating conditions. The mechanism underlying this change in bending stiffness is unclear, but may stem from weakened articulations between antennal annuli. Antennae breakage tends to occur in these regions (Lowder, pers. obs.), which warrants detailed morphological analysis.

Carapace

Should lobsters fail to keep predators at bay, their last line of exoskeletal defense is their armored carapace. The spiny lobster carapace is covered with thick, flattened spines and is more heavily mineralized than the abdominal segments (Lowder, 2019). These attributes enhance hardness and stiffness, consequently providing greater resistance to the piercing and crushing forces of predator attacks, such as by the California sheephead. The abdomen, in contrast, facilitates the tail flip escape response and is not exposed to predators when the animal is sheltering. While there was no change to material properties after medium-term exposure to reduced pH/fluctuating conditions, carapace mineralization (both Ca and Mg) decreased and there was no change within the abdominal segment. The higher concentration of mineral as calcium carbonate and magnesian calcite in the carapace may have made it more favorable to draw from for potential hemolymph buffering under reduced pH conditions (Henry et al., 1981; Spicer et al., 2007). Thus, structures with greater mineral availability, and which benefit the most from the hardness that mineralization provides, may be more vulnerable to losing it in reduced pH/high pCO_2 conditions.

Discrepancies between elemental composition measured with ICP-MS and EDX are likely due to differences in the sensitivities of the techniques and/or in the cuticle regions sampled. Here, ICP-MS analysis revealed decreases to mineralization in reduced pH/fluctuating conditions, whereas no decrease was identified by EDX. Measuring elements over a 2-dimensional surface with EDX, compared to a volume of material with ICP-MS, captures more variation within and between cuticle samples, introducing greater variability, as observed in our data. EDX is also sensitive to surface morphology and sample preparation, which affects electron scattering and element detection. Furthermore, using EDX we only measured elements across regions of the endo- and exo-cuticle layers, whereas with ICP-MS we measured all layers, including the epicuticle. The distribution of mineral across cuticle layers in spiny lobsters is not well-documented, but the American lobster cuticle exhibits a defined calcitic layer near the outermost region of the exocuticle, bordering the epicuticle (Al-Sawalmih et al., 2008; Kunkel, 2013). If spiny lobster cuticles are similar, then changes to the mineralization of this layer would more likely be detected through our ICP-MS measurements of the whole cuticle, rather than our EDX sampling that did not capture this particular region.

Tangled links between composition and properties

Among mineralized organisms, changes to Ca and Mg content after exposure to reduced pH are assumed to belie changes to the mechanical function of calcified structures, but the limited studies testing this link so far defy expectations. In one study, increases in Mg content in the raptorial appendage of mantis shrimp exposed to ocean acidification-like conditions did not result in significant changes to the hardness or stiffness of the cuticle (deVries et al., 2016). In another study, Ca content increased in the carapace and chela of blue king crabs and red king crabs, respectively, but only the chela mechanical properties in both species changed (Coffey et al., 2017). For tanner crabs, an increase in carapace Mg and decrease in Ca did not result in any changes to microhardness, but chelae without significant alterations in mineralization experienced reductions in microhardness (Dickinson et al., 2021). In the present study, both Ca and Mg content decreased in the carapace of California spiny lobsters, but there was no significant change in cuticle hardness or stiffness. In all of these studies of crustaceans, changes in mineral content were less than 20%, which may not be of sufficient magnitude to induce measurable changes in nanomechanical properties. Several studies have established coarse correlations between the degree of mineralization and mechanical properties in crustacean cuticle (Currey at al., 1982; Raabe et al., 2005; Taylor and Kier 2006; Sachs et al., 2006; Fabritius et al., 2012; Weaver et al., 2012; Rosen et al., 2020), but its complex structure and variation among species make it difficult to parse out fine-scale relationships and potential thresholds.

In contrast, cuticle mechanical properties may change independently from adjustments to mineral content, as observed here in the rostral horns of the spiny lobster that decreased in hardness without any corresponding changes to mineral content. Both cuticle structure (i.e., total thickness, layer thickness and stacking density) and mineral phase contribute to cuticle mechanical properties (Raabe et al., 2005). Changes to the former have not been observed in most crustaceans exposed to reduced pH conditions (Taylor et al., 2015; deVries et al., 2016; Lowder et al., 2017; Coffey et al., 2017), including species whose mechanical integrity was compromised (Coffey et al., 2017). Structural level changes, thus, are unlikely to be the mechanism driving observable effects in mechanical properties. The present study, as well as other crustacean OA studies, implicitly assume that the protein-chitin matrix of the cuticle remains unchanged, so that changes to the mineral:matrix ratios governing stiffness are driven by mineral content alone. What has yet to be widely observed in OA research are potential changes to the mineral phase in crustaceans. Crustaceans can manipulate calcium carbonate forms and use amorphous calcium carbonate, magnesian calcite, and calcite (Huner et al., 1979; Vigh and Dendinger, 1982; Addadi

et al., 2003; Dillaman et al., 2005; Boßelmann et al., 2007), which may allow species to compensate for mineralization changes due to OA while maintaining structural function. Indeed, Tanner crabs that were post terminal molt appeared to shift amorphous calcium carbonate to calcite after two years of exposure to reduced pH conditions (Dickinson et al., 2021).

Crustacean cuticle is built with multiple levels of hierarchical structure (Raabe et al., 2005) that adds complexity to the large-scale link between structure, composition, and mechanical function under OA-like conditions. This link becomes clouded in other marine calcifiers as well, including mussels that develop more brittle and less stiff shell regions without any direct change in structure or composition (Fitzer et al., 2015). Consequently, direct relationships between compositional changes under OA-like conditions and material properties have not been consistently identified, and the perceived implications of observed changes to mineralization should be tested when possible.

Reduced pH affects intermolt exoskeleton

The effects of OA-like conditions on crustacean mineralization should be maximally expressed during molting, when animals shed and rapidly build a new exoskeleton. Mineral deposition peaks during the early postmolt period, but is otherwise considered stable throughout the duration of intermolt, except when mineral is potentially drawn away to be stored in gastroliths prior to the next molt (Shechter et al., 2008). As only two individuals (one from the reduced/stable pH treatment and one from the reduced/high fluctuating pH treatment) showed indications of entering the premolt stage (softened exoskeleton and apolysis) at the conclusion of the experiment, variations in molt stage do not likely explain variation in measurements. Juvenile California spiny lobsters of the size used in this study molt annually (California Department of Fish and Wildlife, 2004), and only a few lobsters from each treatment molted over the three month duration of this experiment. Yet, significant changes in mineralization and material properties occurred in the absence of molting, which has also been observed in Tanner crabs past their terminal molt (Dickinson et al., 2021). We found significant decreases in both Ca and Mg in the carapace, hardness in the rostral horns, and flexural stiffness in the antennae of intermolt lobsters, demonstrating that the fully-formed exoskeleton of intermolt animals is sensitive to reduced pH conditions.

Crustaceans use bicarbonate to regulate internal acid-base chemistry under external high pCO_2 conditions and the carbonate minerals in the cuticle can be one source of the ion (Henry et al., 1981). A significant decrease in calcium concentration in the carapace was only found in the reduced/high fluctuating treatment, potentially indicating that the lowest pH values of the experiment reached in that treatment at night (7.57) may have triggered calcium carbonate dissolution from the carapace to use for buffering. Magnesium concentration showed significant decreases from ambient conditions in all three reduced pH treatments. Magnesium is likely in the form of magnesian calcite, a more soluble form of calcite, and may have been drawn out first (Davis et al., 2000).

In other juvenile crustaceans, mineralization is often not affected by exposure to pH conditions expected within the next century. For example, there was no change in either [Mg] or [Ca] at moderate (0.25 pH unit) decreases in pH for the early juvenile stage of the American lobster, *H. americanus*, after five weeks of exposure (Menu-Courey et al., 2018). Juvenile blue swimming crabs and hermit crabs exposed to reduced pH conditions incurred no changes in Ca content, but hermit crabs exhibited small increases in Mg (Glandon et al., 2018; Ragagnin et al., 2018). The above results were all found in animals that had molted during the experiment. In *Homarus gammarus* that didn't molt, there was no change in Mg and Ca after five weeks of exposure to a 0.4 unit decrease in pH (Small et al., 2016), although longer-term exposure might induce detectable changes.

Fluctuating pH conditions may exacerbate effects of reduced pH

Our results indicate that future scenarios of fluctuating pH conditions are not beneficial to *P. interruptus*, despite the current natural fluctuations they experience in kelp forests on diurnal and seasonal scales (Frieder et al., 2012; Kapsenberg and Hofmann, 2016; Kekuewa et al., 2020). While each reduced pH treatment had the same mean pH value, fluctuations above this value were hypothesized to provide a short, daily refuge period when processes like calcification can mainly be carried out (Wahl et al., 2018). Indeed, we found distinct differences in exoskeletal defenses between fluctuating and stable reduced pH conditions, but they were contrary to expectations. Mineralization (e.g., carapace Mg concentration) and material properties (e.g., rostral horn hardness) were significantly reduced in fluctuating conditions, but were unaffected by stable pH exposure. At the same time, antennae flexural stiffness was significantly lower in reduced, stable pH conditions.

Like some organisms, juvenile spiny lobsters may find fluctuating low pH conditions stressful; fluctuating reduced pH conditions raised oxidative stress levels in the mussel *Mytilus edulis* (Mangan et al., 2017). In this study, negative effects tended to be greater under reduced pH with high fluctuations than with low fluctuations. Potentially, the negative effects may result from the pH dropping below a threshold value at night around 7.55-7.60 pH units, which lobsters do not appear to encounter frequently, if at all, in the kelp forest habitat where they were collected (Frieder et al., 2012). Thus, OA may breach the sensitivity thresholds of organisms in fluctuating environments more rapidly than in relatively stable habitats, necessitating consideration of dynamics when developing

predictions for when impacts on species and ecosystems will become more apparent.

Conclusions

In this study on juvenile California spiny lobsters, we found that fluctuating reduced pH conditions affect the mineral composition and mechanical properties of some of their exoskeletal defense structures, thereby adding *P. interruptus* to the list of species sensitive to OA-like conditions. This is the first study to establish spiny lobsters' exoskeleton sensitivity to reduced pH, adding to the evidence of sensory impacts to this group (Ross and Behringer, 2019; Gravinese et al., 2020; Boco et al., 2021) that also has implications for predator defenses. The effects were variable across exoskeletal structures, demonstrating localized responses within an individual that should be accounted for when assessing vulnerability across crustacean species. While the magnitudes of these effects were not appreciably large, it is noteworthy that significant changes to the exoskeleton occurred during the intermolt phase, when the cuticle is generally considered to be stable. This observation reveals that the crustacean exoskeleton can be continuously responsive to environmental pH/pCO_2 conditions, and not just during the peak post molt period. Furthermore, the correlation between mineralization and mechanical properties is not always straightforward under OA-like conditions such that changes in mineralization are not necessarily a good indicator of impacts on mechanical properties. Thus, assumptions about mechanical integrity and function cannot be made based on mineral content alone.

Worldwide, 19 *Panulirus* species (Ptacek et al., 2001) live in shallow, dynamic habitats, such as coral reefs, rocky reefs, and kelp forests. Our study on the temperate *P. interruptus* shows that the natural daily fluctuations in pH typical of these habitats does not necessarily afford spiny lobsters with a helpful respite from greater pH variations associated with climate change predictions. Rather, reduced/fluctuating pH conditions induced exoskeletal changes not observed under stable reduced pH. Dynamic pH conditions should therefore be considered when assessing the vulnerabilities of other species of spiny lobsters, as well as other crustaceans occupying these habitats. Under future ocean conditions, the California spiny lobster may engage with predators using altered exoskeletal defenses that could potentially affect the outcomes of these interactions.

Data availability statement

The datasets presented in this study can be found in online repositories. The names of the repository/repositories and accession number(s) can be found below: Data and metadata are available through PANGAEA: Lowder, Kaitlyn; deVries, Maya S; Hattingh, Ruan; Day, James M D; Andersson, Andreas J; Zerofski, Phillip; Taylor, Jennifer (2022): Exoskeletal predator defenses of juvenile California spiny lobsters (*Panulirus interruptus*) are affected by fluctuating ocean acidification. PANGAEA, https://doi.org/10.1594/PANGAEA.945362.The R code is accessible at: https://github.com/kblowder/Spiny-lobster-exoskeleton-OA.

Author contributions

KL and JT conceptualized the research and wrote the manuscript. KL carried out the experimental study, water chemistry measurements, hardness and stiffness nanoindentation measurements, SEM and EDX measurements, statistical analyses, and aided in animal collection. JT carried out flexural stiffness and ICP-MS measurements. MdV helped carry out SEM and EDX measurements, and RH aided in ICP-MS measurement and analysis. JD contributed to ICP-MS analysis. AA aided in designing water chemistry treatments and analyzing water chemistry results. PZ led animal collection and aided in experimental setup. JD, AA, and MdV edited the manuscript. All authors contributed to the article and approved the submitted version.

Funding

This work was partially supported through access and utilization of the NanoEngineering Materials Research Center (NE-MRC) and the Nano3 facility at UC San Diego. This work was supported by the National Science Foundation Graduate Research Fellowship Program, the UC San Diego Frontiers of Innovation Scholars Program, and the PADI Foundation to KL.

Acknowledgments

Many volunteers were critical for carrying out this work: Cierra Kelly, Jack Shurtz, Duc Tran, Steven Ly, Eric Young, Grace Chan, Kyle Perdue, Zoe Sebright, and Alex Hill. Travis Buck, Kevin Hovel, Brett Pickering, Lyndsay Sutterley, Matt Costa, and Georgie Zelanak either provided traps, helped set them up, or helped recover trapped lobsters. Sebastian Davis, Yaamini Venkataraman, and Summer Webb helped collect water samples from La Jolla seagrass beds. David Cervantes from the Dickson Laboratory provided the sampling protocol and analyzed water samples. Scripps Coastal & Open Ocean BiogeochemistrY lab members, including Alyssa Griffin, Sam Kekuewa, and Ariel Pezner, helped train and troubleshoot while analyzing experimental water samples. Sabine Faulhaber provided training at the NanoEngineering Materials

Research Center (NE-MRC). We also thank the editor and reviewers for their thoughtful comments. Portions of this work are contained in the dissertation of KL (Lowder, 2019).

Conflict of interest

The authors declare that the research was conducted in the absence of any commercial or financial relationships that could be construed as a potential conflict of interest.

Publisher's note

All claims expressed in this article are solely those of the authors and do not necessarily represent those of their affiliated organizations, or those of the publisher, the editors and the reviewers. Any product that may be evaluated in this article, or claim that may be made by its manufacturer, is not guaranteed or endorsed by the publisher.

Supplementary material

The Supplementary Material for this article can be found online at: https://www.frontiersin.org/articles/10.3389/fmars.2022.909017/full#supplementary-material

References

Addadi, L., Raz, S. and Weiner, S. (2003). Taking advantage of disorder: amorphous calcium carbonate and its roles in biomineralization. *Advanced Materials* 15, 959–970. doi: 10.1002/adma.200300381

Alenius, B. and Munguia, P. (2012). Effects of pH variability on the intertidal isopod, *Paradella dianae*. *Mar. Freshw. Behav. Physiol.* 45, 245–259. doi: 10.1080/10236244.2012.727235

Al-Sawalmih, A., Li, C., Siegel, S., Fabritius, H., Yi, S., Raabe, D., et al. (2008). Microtexture and chitin/calcite orientation relationship in the mineralized exoskeleton of the American lobster. *Advanced Funct. materials* 18, 3307–3314. doi: 10.1002/adfm.200800520

Amato, C. G., Waugh, D. A., Feldmann, R. M. and Schweitzer, C. E. (2008). Effect of calcification on cuticle density in decapods: a key to lifestyle. *J. Crustacean Biol.* 28, 587–595. doi: 10.1651/08-2985.1

Andersson, A. J., Kline, D. I., Edmunds, P. J., Archer, S. D., Bednaršek, N., Carpenter, R. C., et al. (2015). Understanding ocean acidification impacts on organismal to ecological scales. *Oceanography* 28, 16–27. doi: 10.5670/oceanog.2015.27

Andersson, A. and Mackenzie, F. (2012). Revisiting four scientific debates in ocean acidification research. *Biogeosciences* 9, 893–905. doi: 10.5194/bg-9-893-2012

Auzoux-Bordenave, S., Wessel, N., Badou, A., Martin, S., M'zoudi, S., Avignon, S., et al. (2020). Ocean acidification impacts growth and shell mineralization in juvenile abalone (*Haliotis tuberculata*). *Mar. Biol.* 167, 1–14. doi: 10.1007/s00227-019-3623-0

Avignon, S., Auzoux-Bordenave, S., Martin, S., Dubois, P., Badou, A., Coheleach, M., et al. (2020). An integrated investigation of the effects of ocean acidification on adult abalone (*Haliotis tuberculata*). *ICES J. Mar. Sci.* 77, 757–772. doi: 10.1093/icesjms/fsz257

Barshaw, D. E., Lavalli, K. L. and Spanier, E. (2003). Offense versus defense: responses of three morphological types of lobsters to predation. *Mar. Ecol. Prog. Ser.* 256, 171–182. doi: 10.3354/meps256171

Boßelmann, F., Romano, P., Fabritius, H., Raabek, D. and Epple, M. (2007). The composition of the exoskeleton of two crustacea: The American lobster H*omarus americanus* and the edible crab *Cancer pagurus*. *Thermochimica Acta* 463, 65–68. doi: 10.1016/j.tca.2007.07.018

Boco, S. R., Pitt, K. A. and Melvin, S. D. (2021). Ocean acidification impairs the physiology of symbiotic phyllosoma larvae of the lobster *Thenus australiensis* and their ability to detect cues from jellyfish. *Sci. Total Environ.* 793, 148679. doi: 10.1016/j.scitotenv.2021.148679

Briones-Fourzán, P., Pérez-Ortiz, M. and Lozano-Álvarez, E. (2006). Defense mechanisms and antipredator behavior in two sympatric species of spiny lobsters, *Panulirus argus* and *P. guttatus*. *Mar. Biol.* 149, 227–239. doi: 10.1007/s00227-005-0191-2

California Department of Fish and Wildlife (2004). *Annual status of the fisheries report through 2003* (California Department of Fish and Wildlife). Berkeley, CA, United States

Challener, R. C., Robbins, L. L. and McClintock, J. B. (2015). Variability of the carbonate chemistry in a shallow, seagrass-dominated ecosystem: implications for ocean acidification experiments. *Mar. Freshw. Res.* 67, 163–172. doi: 10.1071/MF14219

Chan, F., Barth, J. A., Blanchette, C. A., Byrne, R. H., Chavez, F., Cheriton, O., et al. (2017). Persistent spatial structuring of coastal ocean acidification in the California current system. *Sci. Rep.* 7, 1–7. doi: 10.1038/s41598-017-02777-y

Chan, N. C. and Connolly, S. R. (2013). Sensitivity of coral calcification to ocean acidification: a meta-analysis. *Global Change Biol.* 19, 282–290. doi: 10.1111/gcb.12011

Chen, P.-Y., Lin, A. Y.-M., McKittrick, J. and Meyers, M. A. (2008). Structure and mechanical properties of crab exoskeletons. *Acta Biomaterialia* 4, 587–596. doi: 10.1016/j.actbio.2007.12.010

Clark, H. R. and Gobler, C. J. (2016). Diurnal fluctuations in CO_2 and dissolved oxygen concentrations do not provide a refuge from hypoxia and acidification for early-life-stage bivalves. *Mar. Ecol. Prog. Ser.* 558, 1–14. doi: 10.3354/meps11852

Coffey, W. D., Nardone, J. A., Yarram, A., Long, W. C., Swiney, K. M., Foy, R. J., et al. (2017). Ocean acidification leads to altered micromechanical properties of the mineralized cuticle in juvenile red and blue king crabs. *J. Exp. Mar. Biol. Ecol.* 495, 1–12. doi: 10.1016/j.jembe.2017.05.011

Cribb, B. W., Rathmell, A., Charters, R., Rasch, R., Huang, H. and Tibbetts, I. R. (2009). Structure, composition and properties of naturally occurring non-calcified crustacean cuticle. *Arthropod Structure Dev.* 38, 173–178. doi: 10.1016/j.asd.2008.11.002

Currey, J. D., Nash, A., and Bonfield, W. (1982). Calcified cuticle in the stomatopod smashing limb. Journal of Materials Science 17, 1939–1944. doi: 10.1007/BF00540410

Currey, J. D. (1984). Effects of differences in mineralization on the mechanical properties of bone. *Philos. Trans. R. Soc. London. B Biol. Sci.* 304, 509–518. doi: 10.1098/rstb.1984.0042

Davis, K. L., Colefax, A. P., Tucker, J. P., Kelaher, B. P. and Santos, I. R. (2021). Global coral reef ecosystems exhibit declining calcification and increasing primary productivity. *Commun. Earth Environ.* 2, 1–10. doi: 10.1038/s43247-021-00168-w

Davis, K. J., Dove, P. M. and De Yoreo, J. J. (2000). The role of Mg^{2+} as an impurity in calcite growth. *Science* 290, 1134–1137. doi: 10.1126/science.290.5494.1134

deVries, M. S., Webb, S. J., Tu, J., Cory, E., Morgan, V., Sah, R. L. et al. (2016). Stress physiology and weapon integrity of intertidal mantis shrimp under future ocean conditions. *Sci. Rep.* 6, 38637. doi: 10.1038/srep38637

Dickinson, G. H., Bejerano, S., Salvador, T., Makdisi, C., Patel, S., Long, W. C., et al. (2021). Ocean acidification alters properties of the exoskeleton in adult tanner crabs, *Chionoecetes bairdi*. *J. Exp. Biol.* 224, jeb232819. doi: 10.1242/jeb.232819

Dickson, A. G. (1990). Standard potential of the reaction: AgCl (s)+ $12H_2$ (g)= Ag (s)+ HCl (aq), and the standard acidity constant of the ion HSO_2^- in synthetic sea water from 273.15 to 318.15 K. *J. Chem. Thermodynamics* 22, 113–127. doi: 10.1016/0021-9614(90)90074-Z

Dickson, A. and Millero, F. J. (1987). A comparison of the equilibrium constants for the dissociation of carbonic acid in seawater media. *Deep Sea Res. Part A. Oceanographic Res. Papers* 34, 1733–1743. doi: 10.1016/0198-0149(87)90021-5

Dickson, A. G., Sabine, C. L. and Christian, J. R. (2007). *Guide to best practices for ocean CO_2 measurements* (Sidney, BC: North Pacific Marine Science Organization).

Dillaman, R., Hequembourg, S. and Gay, M. (2005). Early pattern of calcification in the dorsal carapace of the blue crab, *Callinectes sapidus*. *J. Morphology* 263, 356–374. doi: 10.1002/jmor.10311

Duquette, A., McClintock, J. B., Amsler, C. D., Pérez-Huerta, A., Milazzo, M. and Hall-Spencer, J. M. (2017). Effects of ocean acidification on the shells of four Mediterranean gastropod species near a CO_2 seep. *Mar. pollut. Bull.* 124, 917–928. doi: 10.1016/j.marpolbul.2017.08.007

Dutil, J., Rollet, C., Bouchard, R. and Claxton, W. (2000). Shell strength and carapace size in non-adult and adult male snow crab (*Chionoecetes opilio*). *J. Crustacean Biol.* 20, 399–406. doi: 10.1163/20021975-99990051

Engle, J. M. (1979). *Ecology and growth of juvenile California spiny lobster, panulirus interruptus (Randall)* (Los Angeles, California, United States: University of Southern California).

Fabritius, H.-O., Karsten, E. S., Balasundaram, K., Hild, S., Huemer, K. and Raabe, D. (2012). Correlation of structure, composition and local mechanical properties in the dorsal carapace of the edible crab *Cancer pagurus*. *Z. für Kristallographie-Crystalline Materials* 227, 766–776. doi: 10.1524/zkri.2012.1532

Fitzer, S. C., Zhu, W., Tanner, K. E., Phoenix, V. R., Kamenos, N. A. and Cusack, M. (2015). Ocean acidification alters the material properties of *Mytilus edulis* shells. *J. R. Soc. Interface* 12, 20141227. doi: 10.1098/rsif.2014.1227

Frieder, C. A., Gonzalez, J. P., Bockmon, E. E., Navarro, M. O. and Levin, L. A. (2014). Can variable pH and low oxygen moderate ocean acidification outcomes for mussel larvae? *Global Change Biol.* 20, 754–764. doi: 10.1111/gcb.12485

Frieder, C. A., Nam, S. H., Martz, T. R. and Levin, L. A. (2012). High temporal and spatial variability of dissolved oxygen and pH in a nearshore California kelp forest. *Biogeosciences* 9, 3917–3930. doi: 10.5194/bg-9-3917-2012

Glandon, H. L., Kilbourne, K. H., Schijf, J. and Miller, T. J. (2018). Counteractive effects of increased temperature and pCO_2 on the thickness and chemistry of the carapace of juvenile blue crab, *Callinectes sapidus*, from the Patuxent River, Chesapeake Bay. *J. Exp. Mar. Biol. Ecol.* 498, 39–45. doi: 10.1016/j.jembe.2017.11.005

Gravinese, P. M., Page, H. N., Butler, C. B., Spadaro, A. J., Hewett, C., Considine, M., et al. (2020). Ocean acidification disrupts the orientation of postlarval Caribbean spiny lobsters. *Sci. Rep.* 10, 1–9. doi: 10.1038/s41598-020-75021-9

Henry, R., Kormanik, G., Smatresk, N. and Cameron, J. (1981). The role of $CaCO_2$ dissolution as a source of HCO_3^- for the buffering of hypercapnic acidosis in aquatic and terrestrial decapod crustaceans. *J. Exp. Biol.* 94, 269–274. doi: 10.1242/jeb.94.1.269

Higgins, B. A., Law, C. J. and Mehta, R. S. (2018). Eat whole and less often: ontogenetic shift reveals size specialization on kelp bass by the California moray eel, *Gymnothorax mordax*. *Oecologia*. 188(3), 875-887 doi: 10.1007/s00442-018-4260-x

Hofmann, G. E., Smith, J. S., Johnson, K. S., Uwe, S., Levin, L. A., Fiorenza, M., et al. (2011). High-frequency dynamics of ocean pH: a multi-ecosystem comparison. *PloS One* 6:e28983. doi: 10.1371/journal.pone.0028983

Huner, J. V., Colvin, L. B. and Reid, B. (1979). Whole-body calcium, magnesium and phosphorous levels of the California brown shrimp, *Penaeus californiensis* (Decapoda: Penaeidae) as functions of molt stage. *Comp. Biochem. Physiol. Part A: Physiol.* 64, 33–36. doi: 10.1016/0300-9629(79)90426-2

IPCC (2014). Climate Change 2014: Synthesis Report. Contribution of Working Groups I, II and III to the Fifth Assessment Report of the Intergovernmental Panel on Climate Change [Core Writing Team, Pachauri, R. K. and Meyer, L. A. (eds.)].

James, R. K., van Katwijk, M. M., van Tussenbroek, B. I., van der Heide, T., Dijkstra, H. A., van Westen, R. M., et al. (2019). Water motion and vegetation control the pH dynamics in seagrass-dominated bays. *Limnology Oceanography*. 65(2), 349-362. doi: 10.1002/lno.11303

Jarrold, M. D., Humphrey, C., McCormick, M. I. and Munday, P. L. (2017). Diel CO_2 cycles reduce severity of behavioural abnormalities in coral reef fish under ocean acidification. *Sci. Rep.* 7, 10153. doi: 10.1038/s41598-017-10378-y

Johnson, M. D., Rodriguez, L. M., O'Connor, S. E., Varley, N. F. and Altieri, A. H. (2019). pH variability exacerbates effects of ocean acidification on a Caribbean crustose coralline alga. *Front. Mar. Sci.* 6, 150. doi: 10.3389/fmars.2019.00150

Johnson, Z. I., Wheeler, B. J., Blinebry, S. K., Carlson, C. M., Ward, C. S. and Hunt, D. E. (2013). Dramatic variability of the carbonate system at a temperate coastal ocean site (Beaufort, North Carolina, USA) is regulated by physical and biogeochemical processes on multiple timescales. *PloS One* 8, 1-8. doi: 10.1371/journal.pone.0085117

Kanciruk, P. (1980). Ecology of juvenile and adult *Palinuridae* (spiny lobsters). *Biol. Manage. lobsters* 2, 59–96. doi: 10.1016/B978-0-08-091734-4.50009-3

Kapsenberg, L. and Hofmann, G. E. (2016). Ocean pH time-series and drivers of variability along the northern Channel Islands, California, USA. *Limnology Oceanography* 61, 953–968. doi: 10.1002/lno.10264

Kekuewa, S. A. H. (2020). Seawater CO2-chemistry variability in the near-shore environment of the Southern California Bight. MS thesis, Scripps Institution of Oceanography, University of California San Diego, La Jolla, CA, USA.

Knapp, J. L., Bridges, C. R., Krohn, J., Hoffman, L. C. and Auerswald, L. (2015). Acid–base balance and changes in haemolymph properties of the South African rock lobsters, *Jasus lalandii*, a palinurid decapod, during chronic hypercapnia. *Biochem. Biophys. Res. Commun.* 461, 475–480. doi: 10.1016/j.bbrc.2015.04.025

Kroeker, K. J., Kordas, R. L., Crim, R., Hendriks, I. E., Ramajo, L., Singh, G. S., et al. (2013). Impacts of ocean acidification on marine organisms: quantifying sensitivities and interaction with warming. *Global Change Biol.* 19, 1884–1896. doi: 10.1111/gcb.12179

Kroeker, K. J., Kordas, R. L., Crim, R. N. and Singh, G. G. (2010). Meta-analysis reveals negative yet variable effects of ocean acidification on marine organisms. *Ecol. Lett.* 13, 1419–1434. doi: 10.1111/j.1461-0248.2010.01518.x

Kunkel, J. G. (2013). Modeling the calcium and phosphate mineralization of American lobster cuticle. *Can. J. Fisheries Aquat. Sci.* 70, 1601–1611. doi: 10.1139/cjfas-2013-0034

Kunkel, J. G., Nagel, W. and Jercinovic, M. J. (2012). Mineral fine structure of the American lobster cuticle. *J. Shellfish Res.* 31, 515–526. doi: 10.2983/035.031.0211

Lindberg, R. G. (1955). *Growth, population dynamics, and field behavior in the spiny lobster, Panulirus interruptus (Randall)* (University of California Press, Berkeley, California, United States).

Loflen, C. L. and Hovel, K. A. (2010). Behavioral responses to variable predation risk in the California spiny lobster *Panulirus interruptus*. *Mar. Ecol. Prog. Ser.* 420, 135–144. doi: 10.3354/meps08850

Long, W. C., Swiney, K. M. and Foy, R. J. (2013). Effects of ocean acidification on the embryos and larvae of red king crab, *Paralithodes camtschaticus*. *Mar. pollut. Bull.* 69, 38–47. doi: 10.1016/j.marpolbul.2013.01.011

Lowder, K., Allen, M. C., Day, J. M., Deheyn, D. D., and Taylor, J. R. (2017). Assessment of ocean acidification and warming on the growth, calcification, and biophotonics of a California grass shrimp. *ICES J. Mar. Sci.* 74, 1150–1158. doi: 10.1093/icesjms/fsw246

Lowder, K. (2019). "Integrity of crustacean predator defenses under ocean acidification and warming conditions," in Dissertation (San Diego (CA: University of California San Diego).

Lowder, K., deVries, M. S., Hattingh, R., Day, J. M. D., Andersson, A. J., Zerofski, P., Taylor, J. (2022) Exoskeletal predator defenses of juvenile California spiny lobsters (*Panulirus interruptus*) are affected by fluctuating ocean acidification. PANGAEA, https://doi.org/10.1594/PANGAEA.945362

Lyle, W. G. and MacDonald, C. D. (1983). Molt stage determination in the Hawaiian spiny lobster *Panulirus marginatus*. *J. Crustacean Biol.*, 3, 208–216. doi: 10.2307/1548257

Mangan, S., Urbina, M. A., Findlay, H. S., Wilson, R. W. and Lewis, C. (2017). Fluctuating seawater pH/pCO_2 regimes are more energetically expensive than static pH/pCO_2 levels in the mussel *Mytilus edulis*. *Proc. R. Soc. B* 284, 20171642.

McDonald, M. R., McClintock, J. B., Amsler, C. D., Rittschof, D., Angus, R. A., Orihuela, B., et al. (2009). Effects of ocean acidification over the life history of the barnacle *Amphibalanus amphitrite*. *Mar. Ecol. Prog. Ser.* 385, 179–187. doi: 10.3354/meps08099

McElhany, P. and Busch, D. S. (2013). Appropriate pCO_2 treatments in ocean acidification experiments. *Mar. Biol.* 160, 1807–1812. doi: 10.1007/s00227-012-2052-0

Mehrbach, C., Culberson, C. H., Hawley, J. E. and Pytkowicz, R. M. (1973). Measurement of the apparent dissociation constants of carbonic acid in seawater at atmospheric pressure. *Limnol. Oceanogr.* 18, 897–907. doi: 10.4319/lo.1973.18.6.0897

Melnick, C., Chen, Z. and Mecholsky, J. (1996). Hardness and toughness of exoskeleton material in the stone crab, *Menippe mercenaria*. *J. Materials Res.* 11, 2903–2907. doi: 10.1557/JMR.1996.0367

Menu-Courey, K., Noisette, F., Piedalue, S., Daoud, D., Blair, T., Blier, P. U., et al. (2018). Energy metabolism and survival of the juvenile recruits of the American lobster (*Homarus americanus*) exposed to a gradient of elevated seawater pCO2. *Mar. Environ. Res.* 143, 111-123. doi: 10.1016/j.marenvres.2018.10.002

Newcomb, L. A., Milazzo, M., Hall-Spencer, J. M. and Carrington, E. (2015). Ocean acidification bends the mermaid's wineglass. *Biol. Lett.* 11, 20141075. doi: 10.1098/rsbl.2014.1075

Onitsuka, T., Takami, H., Muraoka, D., Matsumoto, Y., Nakatsubo, A., Kimura, R., et al. (2017). Effects of ocean acidification with pCO_2 diurnal fluctuations on survival and larval shell formation of ezo abalone, *Haliotis discus hannai*. *Mar. Environ. Res.* 134:28-36. doi: 10.1016/j.marenvres.2017.12.015

Ou, M., Hamilton, T. J., Eom, J., Lyall, E. M., Gallup, J., Jiang, A., et al. (2015). Responses of pink salmon to CO_2-induced aquatic acidification. *Nat. Climate Change* 5, 950–955. doi: 10.1038/nclimate2694

Page, H. N., Andersson, A. J., Jokiel, P. L., Ku'ulei, S. R., Lebrato, M., Yeakel, K., et al. (2016). Differential modification of seawater carbonate chemistry by major coral reef benthic communities. *Coral Reefs* 35, 1311–1325. doi: 10.1007/s00338-016-1490-4

Pane, E. F. and Barry, J. P. (2007). Extracellular acid-base regulation during short-term hypercapnia is effective in a shallow-water crab, but ineffective in a deep-sea crab. *Mar. Ecol. Prog. Ser.* 334, 1–9. doi: 10.3354/meps334001

Pierrot, D., Lewis, E. and Wallace, D. (2006). *MS excel program developed for CO_2 system calculations*. doi: 10.3334/CDIAC/otg.CO2SYS_XLS_CDIAC105a

Ptacek, M. B., Sarver, S. K., Childress, M. J. and Herrnkind, W. F. (2001). Molecular phylogeny of the spiny lobster genus Panulirus (Decapoda: Palinuridae). *Mar. Freshw. Res.* 52, 1037–1047. doi: 10.1071/MF01070

Raabe, D., Sachs, C. and Romano, P. (2005). The crustacean exoskeleton as an example of a structurally and mechanically graded biological nanocomposite material. *Acta Materialia* 53, 4281–4292. doi: 10.1016/j.actamat.2005.05.027

Ragagnin, M. N., McCarthy, I. D., Fernandez, W. S., Tschiptschin, A. P. and Turra, A. (2018). Vulnerability of juvenile hermit crabs to reduced seawater pH and shading. *Mar. Environ. Res*. 142:130-140 doi: 10.1016/j.marenvres.2018.10.001

R Core Team (2019). *R: A language and environment for statistical computing* (Vienna, Austria: R Foundation for Statistical Computing). Available at: https://www.R-project.org.

Rosen, M. N., Baran, K. A., Sison, J. N., Steffel, B. V., Long, W. C., Foy, R. J., et al. (2020). Mechanical resistance in decapod claw denticles: Contribution of structure and composition. *Acta Biomaterialia* 110, 196–207. doi: 10.1016/j.actbio.2020.04.037

Ross, E. and Behringer, D. (2019). Changes in temperature, pH, and salinity affect the sheltering responses of Caribbean spiny lobsters to chemosensory cues. *Sci. Rep.* 9, 4375. doi: 10.1038/s41598-019-40832-y

Sachs, C., Fabritius, H., and Raabe, D. (2006). Hardness and elastic properties of dehydrated cuticle from the lobster Homarus americanus obtained by nanoindentation. Journal of Materials Research 21, 1987–1995. doi: 10.1557/JMR.2006.0241

Schofield, R. M. S., Niedbala, J. C., Nesson, M. H., Tao, Y., Shokes, J. E., Scott, R. A., et al. (2009). Br-rich tips of calcified crab claws are less hard but more fracture resistant: a comparison of biomineralized and heavy-element biomaterials. *J. Struct. Biol.* 166, 272–287. doi: 10.1016/j.jsb.2009.01.007

Semesi, I. S., Beer, S. and Björk, M. (2009). Seagrass photosynthesis controls rates of calcification and photosynthesis of calcareous macroalgae in a tropical seagrass meadow. *Mar. Ecol. Prog. Ser.* 382, 41–47. doi: 10.3354/meps07973

Shechter, A., Berman, A., Singer, A., Freiman, A., Grinstein, M., Erez, J., et al. (2008). Reciprocal changes in calcification of the gastrolith and cuticle during the molt cycle of the red claw crayfish *Cherax quadricarinatus*. *Biol. Bull.* 214, 122–134. doi: 10.2307/25066669

Siegel, K., Kaur, M., Grigal, A. C., Metzler, R. and Dickinson, G. (2022). Meta-analysis suggests variable, but pCO_2-specific, effects of ocean acidification on crustacean biomaterials. *Ecol. Evol.* 12 (6), e8922. doi: 10.22541/au.164370924.40403866/v1

Silbiger, N. J. and Sorte, C. J. (2018). Biophysical feedbacks mediate carbonate chemistry in coastal ecosystems across spatiotemporal gradients. *Sci. Rep.* 8, 796. doi: 10.1038/s41598-017-18736-6

Small, D. P., Calosi, P., Boothroyd, D., Widdicombe, S. and Spicer, J. I. (2016). The sensitivity of the early benthic juvenile stage of the European lobster *Homarus gammarus* (L.) to elevated pCO_2 and temperature. *Mar. Biol.* 163, 1–12. doi: 10.1007/s00227-016-2834-x

Spanier, E. and Zimmer-Faust, R. K. (1988). Some physical properties of shelter that influence den preference in spiny lobsters. *J. Exp. Mar. Biol. Ecol.* 121, 137–149. doi: 10.1016/0022-0981(88)90251-1

Spicer, J. I., Raffo, A. and Widdicombe, S. (2007). Influence of CO_2- related seawater acidification on extracellular acid–base balance in the velvet swimming crab *Necora puber*. *Mar. Biol.* 151, 1117–1125. doi: 10.1007/s00227-006-0551-6

Takeshita, Y., Frieder, C., Martz, T., Ballard, J., Feely, R., Kram, S., et al. (2015). Including high-frequency variability in coastal ocean acidification projections. *Biogeosciences* 12, 5853–5870. doi: 10.5194/bg-12-5853-2015

Tarsitano, S., Lavalli, K., Horne, F. and Spanier, E. (2006). The constructional properties of the exoskeleton of homarid, palinurid, and scyllarid lobsters. *Issues Decapod Crustacean Biol.*, 557, 9–20. doi: 10.1007/1-4020-4756-8_3

Taylor, J. R., and Kier, W. M. (2006). A pneumo-hydrostatic skeleton in land crabs. *Nature* 440, 1005–1005. doi: 10.1038/4401005a

Taylor, J. R. A., Gilleard, J. M., Allen, M. C. and Deheyn, D. D. (2015). Effects of CO_2-induced pH reduction on the exoskeleton structure and biophotonic properties of the shrimp *Lysmata californica*. *Sci. Rep.* 5, 10608. doi: 10.1038/srep10608

Travis, D. F. (1954). The molting cycle of the spiny lobster, *Panulirus argus* latreille. i. molting and growth in laboratory-maintained individuals. *Biol. Bull.* 107, 433–450. doi: 10.2307/1538591

Travis, D. F. (1963). Structural features of mineralization from tissue to macromolecular levels of organization in the decapod Crustacea. *Ann. New York Acad. Sci.* 109, 177–245. doi: 10.1111/j.1749-6632.1963.tb13467.x

Truchot, J. (1979). Mechanisms of the compensation of blood respiratory acid-base disturbances in the shore crab, *Carcinus maenas* (L.). *J. Exp. Zoology* 210, 407–416. doi: 10.1002/jez.1402100305

Tukey, J. W. (1977). *Exploratory data analysis* (Reading, Mass: Addison-Wesley Publishing Company).

Uppström, L. R. (1974). The boron/chlorinity ratio of deep-sea water from the Pacific Ocean. *Deep Sea Res. Oceanographic Abstracts (Elsevier)*, 21:161–162. doi: 10.1016/0011-7471(74)90074-6

Vigh, D. A. and Dendinger, J. E. (1982). Temporal relationships of postmolt deposition of calcium, magnesium, chitin and protein in the cuticle of the Atlantic blue crab, *Callinectes sapidus* Rathbun. *Comp. Biochem. Physiol. Part A: Physiol.* 72, 365–369. doi: 10.1016/0300-9629(82)90232-8

Wahl, M., Saderne, V. and Sawall, Y. (2015). How good are we at assessing the impact of ocean acidification in coastal systems? limitations, omissions and strengths of commonly used experimental approaches with special emphasis on the neglected role of fluctuations. *Mar. Freshw. Res.* 67, 25–36. doi: 10.1071/MF14154

Wahl, M., Schneider Covachã, S., Saderne, V., Hiebenthal, C., Müller, J., Pansch, C., et al. (2018). Macroalgae may mitigate ocean acidification effects on mussel calcification by increasing pH and its fluctuations. *Limnology Oceanography* 63, 3–21. doi: 10.1002/lno.10608

Weaver, J. C., Milliron, G. W., Miserez, A., Evans-Lutterodt, K., Herrera, S., Gallana, I., et al. (2012). The stomatopod dactyl club: a formidable damage-tolerant biological hammer. *Science* 336, 1275–1280. doi: 10.1126/science.1218764

Whiteley, N. M. (2011). Physiological and ecological responses of crustaceans to ocean acidification. *Mar. Ecol. Prog. Ser.* 430, 257–271. doi: 10.3354/meps09185

Whiteley, N. M., Suckling, C. C., Ciotti, B. J., Brown, J., McCarthy, I. D., Gimenez, L., et al. (2018). Sensitivity to near-future CO_2 conditions in marine crabs depends on their compensatory capacities for salinity change. *Sci. Rep.* 8, 15639. doi: 10.1038/s41598-018-34089-0

Wickham, H. (2016a). *ggplot2: elegant graphics for data analysis*. 2nd ed. (New York: Springer International Publishing).

Wickham, H. (2016b). *Tidyr: Easily tidy data with spread () and gather () functions. version 0.6.0.*

Wickham, H. (2017). "Forcats: Tools for working with categorical variables (factors)," in *R package version 0.2. 0.* Available at: https://CRAN.R-project.org/package=forcats.

frontiers | Frontiers in Marine Science

TYPE Original Research
PUBLISHED 22 August 2022
DOI 10.3389/fmars.2022.957836

OPEN ACCESS

EDITED BY
Rebecca Metzler,
Colgate University, United States

REVIEWED BY
Yongshuang Xiao,
Institute of Oceanology, Chinese Academy of Sciences (CAS), China
Xiuzhen Sheng,
Ocean University of China, China

*CORRESPONDENCE
Hongmei Zhang
zhanghongmei@dzu.edu.cn
Zhiyi Shi
zyshi@shou.edu.cn

SPECIALTY SECTION
This article was submitted to Marine Biology, a section of the journal Frontiers in Marine Science

RECEIVED 31 May 2022
ACCEPTED 18 July 2022
PUBLISHED 22 August 2022

CITATION
Zhang H, Xu Z, Xu J, Wei Z and Shi Z (2022) The differential expression and effects of *Drosha* on metamorphosis of Japanese flounder (*paralichthys olivaceus*). *Front. Mar. Sci.* 9:957836. doi: 10.3389/fmars.2022.957836

The differential expression and effects of *Drosha* on metamorphosis of Japanese flounder (*paralichthys olivaceus*)

Hongmei Zhang[1]*, Zhaobin Xu[1], Junxiao Xu[1], Zhenlin Wei[1] and Zhiyi Shi[2]*

[1]Shandong Provincial Key Laboratory of Biophysics, Shandong Universities Key Laboratory of Functional Biological Resources Utilization and Development, College of Life Science, Dezhou University, Dezhou, China, [2]Key Laboratory of Freshwater Aquatic Genetic Resources, Shanghai Ocean University, Ministry of Agriculture, Shanghai, China

Drosha is critical for producing mature microRNAs (miRNAs) from their precursor molecules and small interfering RNAs (siRNAs). Although *Drosha* has been well characterized in most vertebrate species, identifying the Japanese flounder *Drosha* has remained elusive. In this study, we cloned the Japanese flounder *Drosha* gene, which has 4,122 nucleotides (nt), including a 5′-untranslated region (UTR) of 14 nt, a 3′-UTR of 230 nt, and a 3,879 nt open reading frame (ORF) encodes a 1,292 amino acid polypeptide. Then, we analyzed the conservation and phylogenetic evolution of *Drosha* in some species. Real-time quantitative PCR revealed that *Drosha* mRNA is highly expressed in the brain, and a lower amount of mRNA was also found in muscle than in other tissues. *Drosha* plays a vital role in controlling flounder development and metabolism, and its mRNA levels were relatively high at 36 dph (days post-hatching) in the period of metamorphosis and growth of the Japanese flounder. *Drosha* expression showed in advance with a peak at 23 dph following TH (thyroid hormone) treatment. To further investigate the role of *Drosha* in metamorphosis, we performed siRNA knockdown of *Drosha* in flounder embryonic cells (FEC) cells. The result shows that the *Drosha*-specific siRNA significantly down-regulated *Drosha* mRNA and miR-1,133,17,214,181a,181b levels, while primary miRNA (pri-miRNA) levels were not significantly different from negative control (NC). These results suggest that *Drosha* plays a vital role in Japanese flounder development and metamorphosis through processing to produce mature miRNAs, providing essential information for further studying of the part of the *Drosha* gene in the Japanese flounder development.

KEYWORDS

***Drosha*, metamorphosis, thyroid hormone (TH), siRNA, Japanese flounder (*Paralichthys olivaceus*)**

1 Introduction

Japanese flounder (*Paralichthys olivaceus*) is one of the most critical economic fish in marine aquaculture in China, Korea, and Japan (Gawantka et al., 1998). The Japanese flounder market has increased in economic value due to high consumption (Han et al., 2006). The best-studied example of vertebrate metamorphosis is the anuran amphibian—the frog. However, the Japanese flounder is a noteworthy example of a commercially valuable metamorphosis. The planktonic larvae are symmetrical before metamorphosis. After metamorphosis, one eye migrates to the opposite side of the head and produces asymmetric bottom larvae (Campinho et al., 2010). Japanese flounder takes about 40 days to complete metamorphosis (Policansky and Sieswerda, 1979). During metamorphosis, tissues are also reconfigured, and their structure and function are altered due to tissue-specific expression of genes. Retinoic acid signaling plays a critical role in the developmental regulatory system of ocular-side-specific asymmetric pigmentation in flounders (Chen et al., 2020). During metamorphosis of flounder larvae, Sox10-positive progenitor cells migrate from the base of the dorsal fin to the blind side of the skin starting from a specific stimulus and causing ectopic pigmentation (Togawa et al., 2018). Tissue-specific expression of genes is induced directly or indirectly by thyroid hormones. Treatment of Japanese flounder with exogenous thyroid hormones induces premature metamorphosis, whereas thiourea inhibits metamorphosis (Hoke et al., 2006; Mullur et al., 2014). In addition, the regulation of gene expression is tissue-specific during metamorphosis of Japanese flounder. Thyroid hormones (TH) have been shown to be a necessary and sufficient factor during metamorphic development in Japanese flounders (Miwa and Inui, 1987; Manchado et al., 2008; Power et al., 2008).

Nevertheless, TH-regulated cellular and molecular events driving eye migration during Japanese flounder asymmetric development remain elusive. The forces behind driving Japanese flounder eye migration have also been troubling biologists, and recently, it has been proposed that cell proliferation in the subocular region is the primary cause (Bao et al., 2011). However, this model cannot account for remodeling during metamorphosis of the ventral blind lateral jaw and eye still migrate when cell proliferation has been inhibited.

MicroRNA is a class of small non-coding RNA consisting of about 22 bases, which, usually, negatively regulates mRNA expression of target genes at the translation level (Hatfield et al., 2005). MicroRNA is an endogenous small molecule RNA encoded by the genome, which must be processed to become a functional microRNA. In general, the processing of RNA transcripts into mature miRNAs can be divided into four steps: primary miRNAs (pri-miRNAs), pre-miRNAs, miRNA/miRNA* duplexes, and mature miRNAs. *Drosha* enzyme is mainly responsible for cleaving pri-miRNA into pre-miRNA (about 70 nt) in the nucleus and exporting pre-miRNA from the nucleus to the cytoplasm under the action of Export5. Then, the precursor is cleaved into mature miRNA(about 22 nt) by Dicer in the cytoplasm (Denli et al., 2004; Okada et al., 2009; Ha and Kim, 2014; O'Brien et al., 2018).

Drosha belongs to the RNaseIII family, which contains a rich thymine domain, arginine domain, a CED domain, a double-stranded RNA binding domain, and two RNA catalytic domains (Lee et al., 2006; Kwon et al., 2016). Drosha and DGCR8 form a microprocessor complex, and both act synergistically for precise cleavage of the stem-loops of pri-mRNA to create pre-mRNA (Luhur et al., 2014). They play a major role in miRNA formation. If *Drosha* is knocked out, the production of pre-miRNA and mature miRNA will be affected (Jeong et al., 2016), which will eventually cause cellular dysfunction and even apoptosis. It has been shown that microRNAs play an essential role in the metamorphosis of Japanese flounders (Fu et al., 2011; Zhang et al., 2015). Here, we cloned *Drosha*, a critical gene in the miRNA synthesis pathway of Japanese flounder, and analyzed its expression levels in different tissues and metamorphosis stages by QRT-PCR and the effect of exogenous TH on the expression of the *Drosha* gene. The result provides a reference for further study on the effect of the *Drosha* gene on the metamorphosis of Japanese flounders.

2 Material and methods

2.1 Experimental fish and sample collection

Japanese flounder embryos, larvae, and adult fish were collected from Beidaihe Central Experimental Station (Chinese Academy of Fishery Sciences, China). Embryos and larvae were maintained in tanks with circulating water, and the temperature was 16°C. The samples were periodically collected (n=3 pools, 15–30 specimens/pool) at 0 h (unfertilized egg), 26 hpf (hour post-fertilization, gastrula stage), 71 hpf (heart-beating stage), 3 dph (days post-hatching), 9 dph, 14 dph, 17 dph (pre-metamorphosis, the stage before the start of eye migration), 23 dph (pro-metamorphosis, the right eye moved toward the dorsal margin but still could not be seen from the left/ocular side), 29 dph (climax metamorphosis, the right eye has become visible from the ocular side while not reached the dorsal midline), 36 dph (post-metamorphosis, the right eye has just located on the dorsal margin), and 41 dph (completed metamorphosis) (Policansky and Sieswerda, 1979). Under standard conditions in our laboratory, larvae survive an average of 41 days from hatching to completion of metamorphosis. Referring to the Policansky and Miwa's classification method for the metamorphosis development period of Japanese flounder (Policansky and Sieswerda, 1979; Miwa, 1987), according to

the changes in the appearance of the fish, the metamorphism process corresponds to the number of days after hatching as shown in the Supplementary Table 1.

Collected samples were immediately cryopreserved in liquid nitrogen at -196°C until RNA extraction.

To study the effect of TH on *Drosha* in Japanese flounder metamorphosis, we divided the 15-day-old larvae into three groups with 5,000 larvae in each. We reared them in seawater containing either 0.1 ppm concentration of TH (T3), 30 ppm of TU (Inui and Miwa, 1985), or none. We replace the 1/3 water daily to keep T3 and TU concentrations constant. Until day 41, we terminated the TH and TU treatments. Larvae (n=3 pools, 15–30 specimens/pool) were collected at 17, 23, 29, and 36 dph, frozen in liquid nitrogen, and stored at −196°C until RNA extraction.

The adult fish's heart, liver, spleen, stomach, kidney, brain, gill, muscle, gonad, and intestine (n=3) were separated, frozen in liquid nitrogen directly, and stored at -196°C until RNA extraction.

Japanese flounder embryonic cells (FEC) (the Yellow Sea Fisheries Research Institute, Chinese Academy of Fishery Sciences) were cultured in DMEM (GIBCO, CA) supplemented with 10% fetal bovine serum (GIBCO) and 1x penicillin/streptomycin (Gibco), then maintained at 24°C in an ambient air incubator (Chen et al., 2004).

2.2 RNA extraction and cDNA cloning of Drosha

Total RNA was isolated from embryos, whole larvae (including control, TH-treated or TU-treated) and adult tissues/organs (gill, heart, intestine, stomach, spleen, muscle, kidney, and liver) using TRIZOL reagent (Life Technologies, CA, USA) genomic DNA contamination was removed using RQ1 RNASE-FreeDNASE (Promega, Madison, WI, USA) according to the manufacturer's instructions. RNA integrity was detected by agarose gel electrophoresis using a NANODROP2000 spectrophotometer (ThermoScientific, Waltham, MA, USA) to quantify the RNA concentration, and the ratio of A260/A280 was between 1.8 and 2.0.

Using M-MLV Reverse Transcriptase (Promega), DNase-treated total RNAs (1.0 μg) from each sample were reverse-transcribed by Oligodt (Takara, China). We compare the published *Drosha* cDNA sequences on NCBI (http://www.ncbi.nlm.nih.gov) and then design five pairs of primers for cloning the partial fragments of *Drosha* from Japanese flounder. The components for PCR amplification were combined: 1 μl of cDNA template, 2.0 μl of 10× Ex Taq buffer, 1.6 μl of dNTP (2.5 mM of each), 2 μl of each the forward and reverse primers (10 μM), and 0.2 μl of Ex Taq® DNA polymerase (TaKaRa, Japan) and 11.2 μl dH_20 in a final volume of 20 μl. The PCR amplification condition: denaturation at 94°C for 4 min, with 35 cycles at a melting temperature of 94°C for 30 s, an annealing temperature of 50–60°C (according to the primers) for 30 s, and an extension temperature of 72°C for 60–150 s (according to the primers). The gene-specific primers for the 3' and 5' RACE were designed based on the partial fragment, and adaptor primers and the full-length cDNA of Japanese flounder *Drosha* were cloned using the 5' and 3' -Full RACE Kit (Takara, Japan). The primers used in the present study are listed in Table 1.

The amplified products were separated by 1.5% agarose gel electrophoresis. The desired band was present and ligated into PMD®19-T vector (TAKARA, Japan) after purification using a Gel Extraction Kit (Tiangen, China), and transformed into *Escherichia coli* strain DH5α competent cells. The positive clones were sequenced on an ABI PRISM 3730 Automated Sequencer (ABI, USA).

2.3 Sequence and phylogenetic evolution analysis

Other species homologues were obtained by a BLASTX search of the Japanese flounder DROSHA protein, which was our cloned. The accession numbers of which are in the Supplementary Table 2. The Drosha amino acid sequences were aligned and the phylogenetic tree was constructed using the MEGA program (version 11.013; www.megasoftware.net) with the neighbor-joining method and maximum-likelihood method with 1,000 bootstraps. Then, the phylogenetic tree was visualized by Evolview (https://www.evolgenius.info/evolview) (Subramanian et al., 2019).

2.4 Real-time quantitative PCR

Total RNA from adult tissues, embryos, and larvae was isolated using Trizol® reagent (Invitrogen, USA) and treated with DNase (5 U/μl) (TaKaRa, Japan) for 1 h. RNA integrity was assessed by 0.8% agarose gel electrophoresis, and the concentration of RNA samples was determined by spectrophotometer NANODROP2000C (Thermo). The ratio of A260/A280 is between 1.83 and 2.02. DNase (Promega, Madison, WI, USA) without RQ1RNase eliminated genomic DNA contamination. We then used PCR amplification to confirm that the genomic DNA was free of contamination.

We used CFX96 Touch™ Real-Time PCR Detection System (Bio-Rad, USA) to accomplish the Real-time quantitative PCR. The components of reactions were in a 20 μl volume containing 1 μl cDNA generated from the RNA template, 2 μl of each of the specific forward and reverse primers (*Drosha* qPCR1- F and *Drosha* qPCR1- R, 10 μM), and 10 μl of 2 × iO™ SYBR Green Supermix (Bio-Rad, USA).

10.3389/fmars.2022.957836

TABLE 1 The primer sequences for the PCR used in the present study.

Primers	Sequences (5'-3')	Annealing temperature, °C	Application
Drosha-F1	CGCCAGAAGAACACTATGC	54.0	Gene amplification
Drosha-R1	CAGGTGCGAGTGGTGAATA		Gene amplification
Drosha-F2	CATCGCCGAGATCAAGAG	53.0	Gene amplification
Drosha-R2	GCGTATTTCTGCCACTCC		Gene amplification
Drosha-3'race	GTTCGCTGGTAAACAACCGCACGCA	61.0	Gene amplification
Drosha-5'race outer primer	TTACACAGGGGACCATCATTCATCT	63.7	Gene amplification
Drosha-5'race inner primer	CTTCACCGTCTGATTCACAGTCCGA	67.3	Gene amplification
Drosha-F3	CGCTTCAACATAGATTACACCA	60.0	Real-time RT-PCR
Drosha-R3	CACCATCAGGTAAGAATCGG		Real-time RT-PCR
β-actin-F	GGAAATCGTGCGTGACATTAAG	60.0	Real-time RT-PCR
β-actin-R	CCTCTGGACAACGGAACCTCT		Real-time RT-PCR
Cdc42 F	GACAGATTACGACCACTAAG	60.0	Real-time RT-PCR
Cdc42 R	GCCGAACACTCAACATAT		Real-time RT-PCR
Pri-miR-1 F	CCGCTGTATGAGCCCTACCA	60.0	Real-time RT-PCR
Pri-miR-1 R	GGCGTAGAAAAAAATCTGATGTGT		Real-time RT-PCR
Pri-miR-17 F	GGCAGGAAAGATGGGAGTAGTT	60.0	Real-time RT-PCR
Pri-miR-17 R	CAAAGCCGTTAGGTTGGGTG		Real-time RT-PCR
Pri-miR-133a F	GAGGAAGAGACTACAGCACT	60.0	Real-time RT-PCR
Pri-miR-133a R	ACAGGACCAGAGCAAAG		Real-time RT-PCR
Pri-miR-214 F	GCCAGGGCCTAGCTGCTTATT	60.0	Real-time RT-PCR
Pri-miR-214 R	CGCTGGATGACACCAAGATGAGT		Real-time RT-PCR
Pri-miR-181a F	CGGTTCTAAAGCATCAGAGGACT	60.0	Real-time RT-PCR
Pri-miR-181a R	TCGGGCCTGGGACTGTTAA		Real-time RT-PCR
miR-1-F	ACACTCCAGCTGGGTGGAATGTAAAGAAG	60.0	Real-time RT-PCR
miR-1-R	AACTGGTGTCGTGGAG		Real-time RT-PCR
miR-133a-F	CTCTATTGGTCCCCTTCAACC	60.0	Real-time RT-PCR
miR-133a-R	GTGCAGGGTCCGAGGT		Real-time RT-PCR
miR-17- F	CCGCCCAAAGTGCTTACAGT	60.0	Real-time RT-PCR
miR-17-R	CGCAGGGTCCGAGGTATTC		Real-time RT-PCR
miR-181a-F	TGTCATTCAACGCTGTCGGT	60.0	Real-time RT-PCR
miR-181a-R	GTCACGTCCCAGGCTCCATA		Real-time RT-PCR
miR-214-F	AACAGCAGGCACAGACAGGC	60.0	Real-time RT-PCR
miR-214-R	GTCACGTCCCAGGCTCCATA		Real-time RT-PCR
5sRNA-F	CCATACCACCCTGAACAC	60.0	Real-time RT-PCR
5sRNA-R	CGGTCTCCCATCCAAGTA		Real-time RT-PCR

The condition of amplification was used as follows: initial denaturation for 1 min at 95°C, followed by 40 cycles of 95°C for 30 s, and 60°C for 10 s and a melting curve was obtained for assessing the specificity of the qPCR amplification, additional cycles were performed by reading the fluorescence value from 55 to 95°C. We used sterile deionized water instead of a cDNA template for negative controls. Each experiment was repeated in duplicate. For normalization of cDNA loading, the housekeeping gene β-actin was run in parallel with all samples. A standard curve of each pair of primers was generated to estimate amplification efficiencies based on known quantities of cDNA (4-fold serial dilutions corresponding to cDNA transcribed from 100 to 0.1 ng of total RNA). All calibration curves exhibited correlation coefficients higher than 0.99, and the corresponding real-time PCR efficiencies (E) were higher than 0.95. We used the $2^{-\Delta\Delta CT}$ method to determine the relative mRNA expression for the *Drosha* gene. The primer sequences see the Table 1.

2.5 siRNA inhibit *Drosha* expression *in vitro*

Based on the synthesized *Drosha* sequences, three interfering sequences (*Drosha*-siRNA1, *Drosha*-siRNA2, and *Drosha*-

siRNA3) targeting *Drosha* silencing and one negative control (*Drosha*-siRNA-FAM-NC) with fluorescence were designed. The negative control is a sequence that is not present in the fish. The siRNA sequences were synthesized by Shanghai Jima Pharmaceutical Technology Co.

The FEC cells in the culture flasks were digested with 0.25% trypsin 1 day before transfection, and about 0.4×10^{6} cells were inoculated into 6-well culture plates, and the cells were transfected after 24 h when they reached about 70%–80% confluence. Three *Drosha* (siRNA-1, siRNA-2, and siRNA-3) and *Drosha*-siRNA-FAM-NC (Table 2) were transfected into FEC cells with Lipofectamine 2000 (Invitrogen).

The LipoFiter TM-DNA mixture was prepared at a certain ratio and 500 ul of LipoFiter TM-DNA mixture was added to each well, followed by gentle 8-word shaking and mixing; after 6 h of incubation in the cell culture incubator, the culture medium containing LipoFiter TM-DNA was removed. The culture was continued by adding 2 ml of fresh cell culture medium per well and detected under fluoroscopy after 48 h. The expression of pri-miRNA (pri-mir-1,133,17,214,181a,181b), the corresponding miRNA and Cdc42 were assessed at the mRNA level by Realtime-PCR When Drosha was knocked down in FEC cells by siRNA against Drosha. Real-time PCR was performed according to the method in 2.4, 5sRNA was used as an internal reference. The primer sequences are shown in Tables 1, 2.

2.6 Statistical analysis

The one-way ANOVA and *post-hoc* Dunnett's T3 test was used to analyze the comparisons among different stages and adult tissues. As for the comparisons among drug treatments, we used two-way ANOVA and a Bonferroni *post-hoc* analysis. All experimental data were shown as the mean ± Standard Error (SE) (n=3). At the level of $p < 0.05$, the results of significance were accepted.

TABLE 2 siRNA target site and sequence.

Target site	Sequence (5'—3')
siRNA-1 (383)	target sequence AUUCUGAGCAGACACCUGGTT
	interfering sequence CCAGGUGUCUGCUCAGAAUTT
siRNA-2 (1346)	target sequence AUCCAGUUUGGUCUUGGGCTT
	interfering sequence GCCCAAGACCAAACUGGAUTT
siRNA-3 (2225)	target sequence AUCUGGGUUGAACUGUUCCTT
	interfering sequence GGAACAGUUCAACCCAGAUTT
FAM-NC	UUCUCCGAACGUGUCACGUTT

3 Results

3.1 Characters and analysis of Japanese flounder *Drosha*

The *Drosha* fragment was amplified with some primers (Table 1). The 5'-RACE fragment and the 3'-RACE fragment were amplified based on the *Drosha* fragment, respectively. The complete cDNA consists of 14 bp 5'-UTR, 230 bp 3'-UTR, and an open reading frame (ORF) of 3879 bp. In addition, the ORF encodes a polypeptide of 1292 amino acids.

Drosha sequences from five species were aligned. As shown in Figure 1, *Drosha* had five highly conservative amino acid sequence domains: DEXD/H-box, DUF283, PAZ_*Drosha*_like, two neighboring RNase III, and dsRBD domain. BLAST analysis showed an average homology of 78% to other species. The highest homology of 89% was found between the amino acid sequence of *Oreochromis niloticus* and that of Japanese flounder. Moreover, it showed that the lowest identity of 72% was found between the amino acid sequence of *Xenopus laevis* and that of *Paralichthys olivaceus*.

A phylogenetic tree of *Drosha*, which used DROSHA protein sequences for 26 species in animal, was constructed to ascertain the evolutionary relationship of *Drosha* in metazoan. Both neighbor-joining (NJ) and maximum likelihood (ML) methods were used for evolutionary analysis. The evolutionary relationship between the ML tree and the NJ tree is very similar (Figures 2A, B). The *Paralichthys olivaceus* was clustered with *Scophthalmus-maximus*, located in the *osteichthyes* branch. The phylogeny (based on amino acid sequence) of DROSHA was largely consistent with that of the expected species.

3.2 Tissue distribution of *Drosha* mRNA

We used real-time quantitative PCR to conduct the expression pattern of *Drosha* mRNA in different tissues of adult Japanese flounder. As shown in Figure 3, *Drosha* mRNA was detected in all investigated tissues. It was observed that the brain was the highest, the ovaries, gills, and kidneys were the lowest, and other tissues were medium. *Drosha* levels, which are about equal among heart, stomach, and liver, are significantly lower than that in muscle and intestine ($p < 0.05$).

3.3 Expression of *Drosha* mRNA during embryonic and larval development

The mRNA of *Drosha* could be detected in all developmental stages (Figure 4). As shown in Figure 4, the highest expression

10.3389/fmars.2022.957836

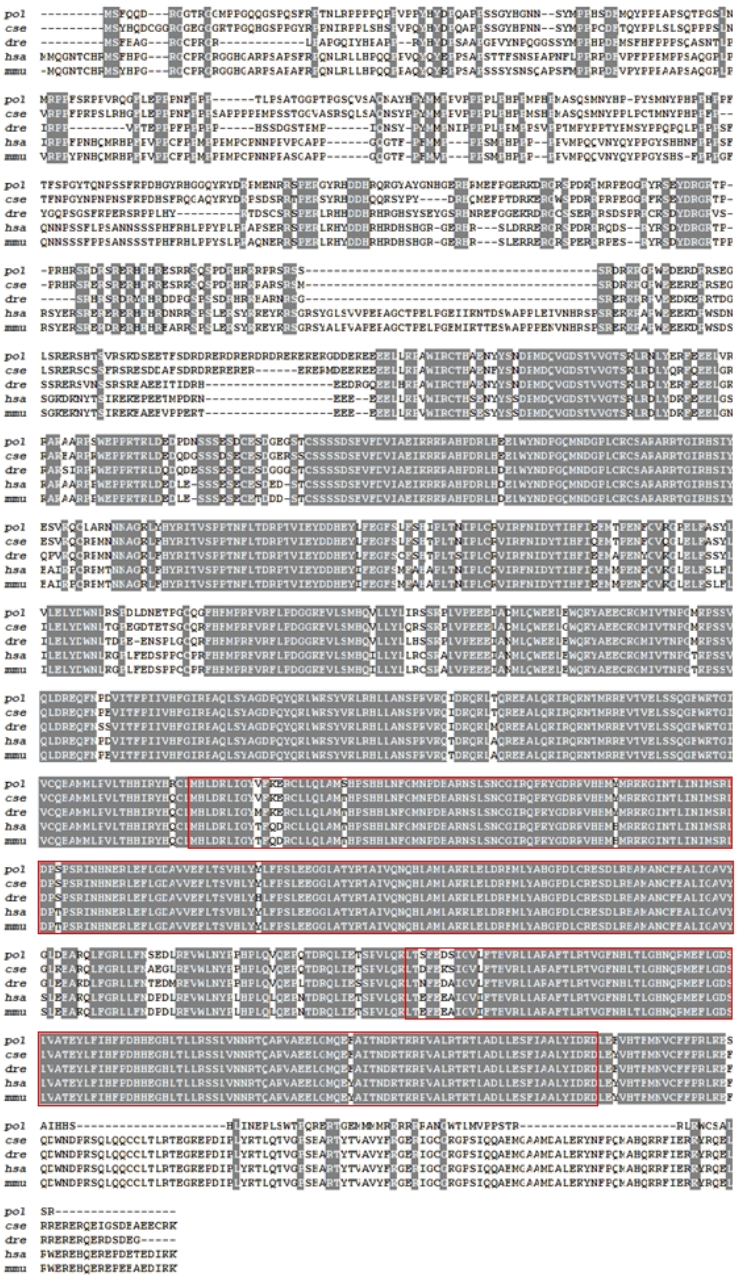

FIGURE 1
Amino acid sequence alignment of Japanese flounder *Drosha* with that of other species. Light gray blocks showed a few different residues between those sequences shown. The red box contains the active region of the RNase III superfamily. *pol*: *Paralichthys olivaceus*; *cse*: *Cynoglossus semilaevis* (XP_008306545.1); *dre*: *Danio rerio* (NP_001103942.1); *hsa*: *Homo sapiens* (NP_037367.3); *mmu*: *Mus musculus* (NP_081075.3).

level of *Drosha* was detected in 36 dph. The *Drosha* gene is hardly expressed during unfertilized eggs. Additionally, it significantly declined at 3 dph, when the yolk absorption was almost complete. However, the expression of *Drosha* kept a higher level and was no significant difference at four metamorphic stages.

3.4 Effect of TH and TU on the expression of *Drosha* mRNA during metamorphosis

We determined the expression pattern of *Drosha* in larvae sampled 17, 23, 29, and 36 days after TH and TU treatment

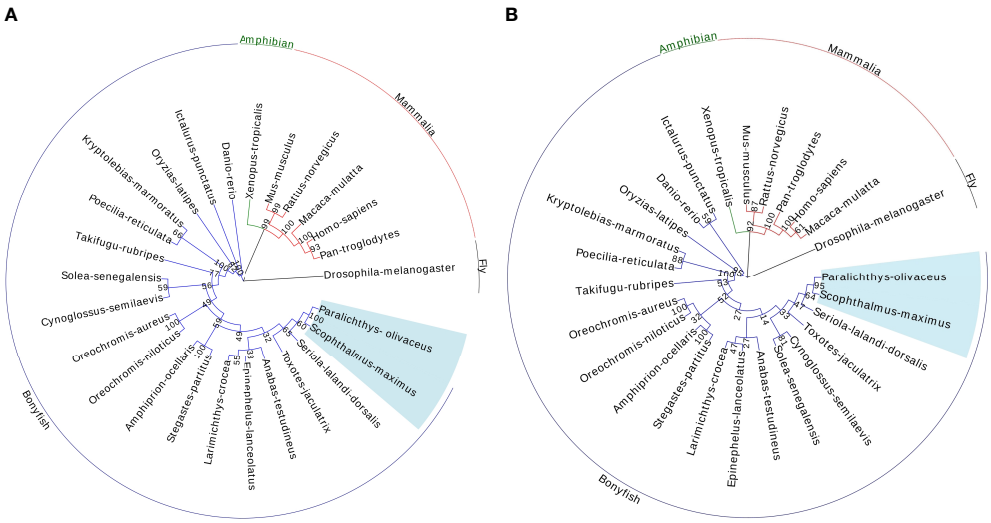

FIGURE 2
Phylogenetic tree of the selected *Drosha* sequences by the Neighbor-Joining method (1000 bootstrap) **(A)** and by the maximum-likelihood method (1000 bootstrap) **(B)**. Bootstrap values are shown at the branch points. Scale bar indicates the number of changes inferred as having occurred along each branch. The *Drosha* amino acid sequences used for analysis are extracted from the GenBank database.

(Figure 5). In 17 d, 23 d, and 29 d, the expression of *Drosha* was not significantly different between TH and TU. Significantly, the level of *Drosha* in TH-treated at 36 d declined compared to the CK (untreated group), and 29 d was higher than that in other states. The expression of *Drosha* in TU-treated larvae was kept at the same level among the other three stages except 23 d. Moreover, the level of *Drosha* in the untreated group was almost steady except 36 d. There were significant differences in *Drosha* mRNA

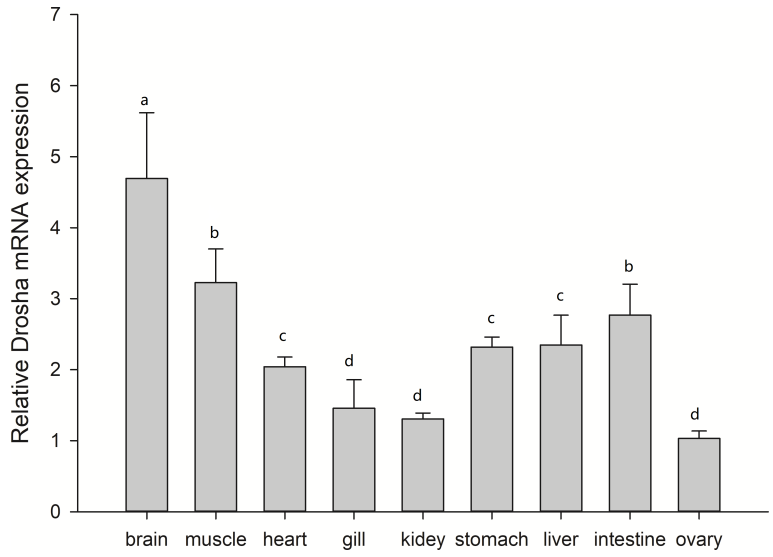

FIGURE 3
Relative expression levels of *Drosha* mRNA in adult tissues of Japanese flounder. The data are expressed as the mean ± Standard Error (SE) (n = 3) from the calibrator group (Muscle) and expression were normalized to those of β-actin. Different letters indicate significant differences between the two tissues ($P < 0.05$).

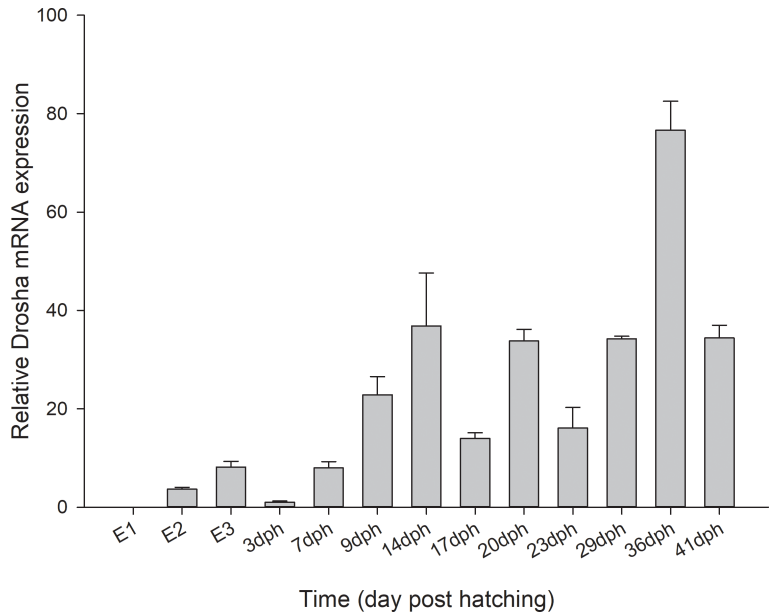

FIGURE 4
Relative levels of *Drosha* mRNA during early development of Japanese flounder. Expression values were normalized to those of β-actin, and data are expressed as the mean ± Standard Error (SE) (n = 3) from the calibrator group (E1). E1, unfertilized stage; E2, gastrula stage; E3, heart-beating stage.

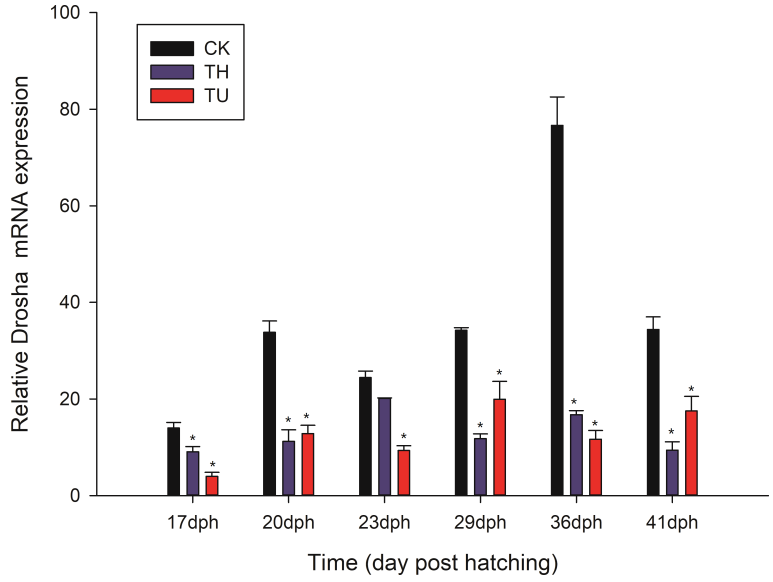

FIGURE 5
Relative *Drosha* mRNA expression levels in TH- and TU-treated larvae during Japanese flounder metamorphosis. Expression values were normalized to those of β-actin, and data are expressed as the means ± Standard Error (SE) (n = 3) from the calibrator group (36 d-TU). CK displayed the untreated group; TH and TU displayed the thyroid hormone and thiourea-treated group. *, indicates a significant difference (*, $p < 0.05$) compared to control.

in the TH (17, 20, 29, 36, 41 dph) and TU (17, 20, 23, 29, 36, 41 dph) treated groups compared to the control group ($p < 0.05$).

3.5 Drosha-siRNA transfection

3.5.1 Drosha-siRNA transfection

To further confirm the role of *Drosha* in Japanese flounder metamorphosis, we used siRNA interference. The interference efficiency of siRNA was routinely assessed by fluorescence at 24 h after transfection of FEC cells with *Drosha*-siRNA-FAM-NC. A large amount of fluorescence appeared and the transfection efficiency was 51%. Figure 6A shows the observation results under white light 24 h after transfection, and Figure 6B shows the observation results under green fluorescence light under the same field of view 24 h after transfection.

3.5.2 *Drosha* expression after *Drosha* gene silencing

We designed three siRNAs to knockdown *Drosha* and found that siRNA-2 has the highest interference efficiency among three designed siRNAs in FEC cells. Then, 2 ug/ml *Drosha*-siRNA2 was transfected into FEC cells. The FEC cells were collected after 24 h, 48 h, and 72 h incubation, and the NC (siRNA sequence is not present in the fish) was used as the control. Finally, fluorometric quantification and Western blot assay were performed. The results showed that *Drosha* mRNA and protein expression were inhibited in the 24 h, 48 h, and 72 h transfected groups compared with the NC group, and the difference between transfection 48 h and 72 h groups was not statistically significant ($P>0.05$) (Figure 7).

3.5.3 Expression of pri-miRNA and miRNA after *Drosha* gene silencing

To determine if *Drosha* knockdown was reducing mature miRNAs or pri-miRNAs, we examined the levels of mature and pri-miRNAs. *Drosha*-siRNA2 was used to transfect FEC cells for 48 h. The FEC cells were collected and Real-time PCR assay of pri-miRNA and miRNA was performed, and the results showed that pri-miRNAs (pri-miR-1, 133, 17, 214, 181a, 181b) were not affected after transfection with *Drosha*-siRNA, while that mature miRNAs were significantly reduced, as shown in Figures 8A, B. This suggests that the reduction of these miRNAs occurs at the precursor stage and *Drosha* knockdown reduced the levels of some miRNAs in FEC cells.

3.5.4 Gene expression of Cdc42 after *Drosha* gene silencing

To assess the effect of *Drosha* knockdown on cell proliferation, we examined the expression level of *Cdc42* in FEC cell. The *Cdc42* gene was associated with apoptosis and proliferation, Cdc42 protein is a cell division cyclin, which belongs to the Rho family of proteins and acts as a "molecular switch" in cell signaling. *Drosha* silencing resulted in decreased Cdc42 mRNA expression, indicating decreased cell proliferation (Figure 9). This result implicates the role of *Drosha* in the development and growth of Japanese flounder.

4 Discussion

Drosha is an important gene in the miRNA synthesis pathway. In this study, we obtained the full-length sequence of

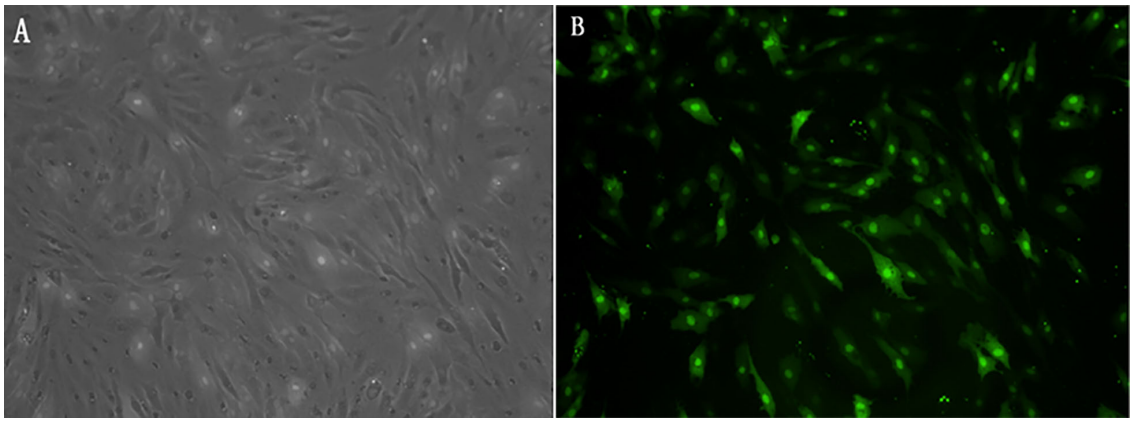

FIGURE 6
(A) *Drosha*-siRNA white-light; **(B)** *Drosha*-siRNA-FAM-NC green fluorescence *Drosha*-siRNA-FAM-NC: The siRNA sequence is not present in the fish.

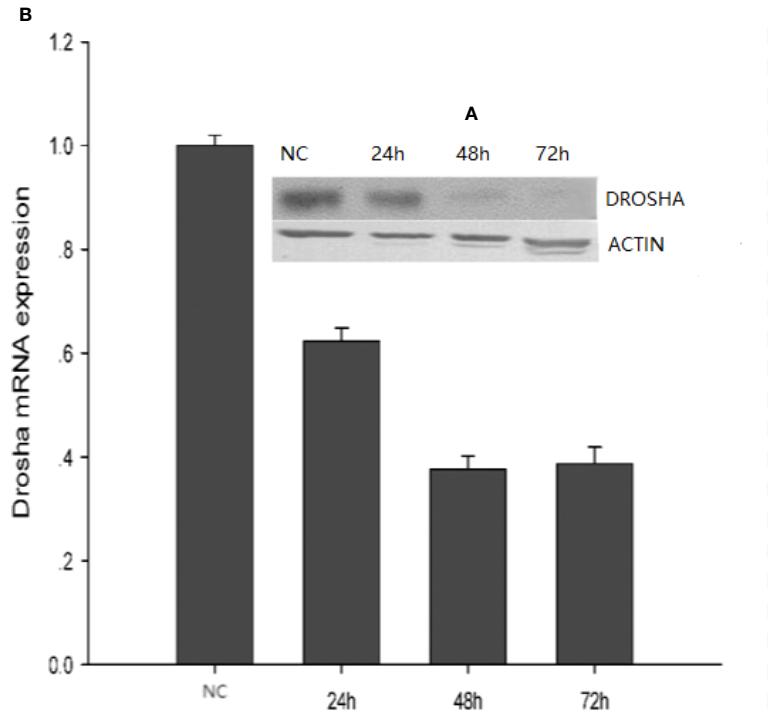

FIGURE 7
Expression of *Drosha* protein **(A)** and mRNA **(B)** at different transfection times. NC: *Drosha*-siRNA-FAM-NC. The siRNA sequence is not present in the fish.

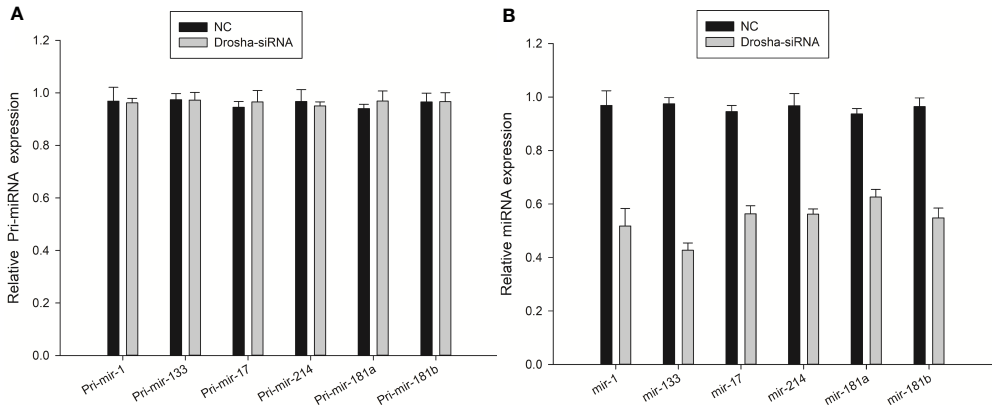

FIGURE 8
Expression of pri-miRNA **(A)** and mature miRNA **(B)** in transfected *Drosha*-siRNA. NC: *Drosha*-siRNA-FAM-NC, The siRNA sequence is not present in the fish.

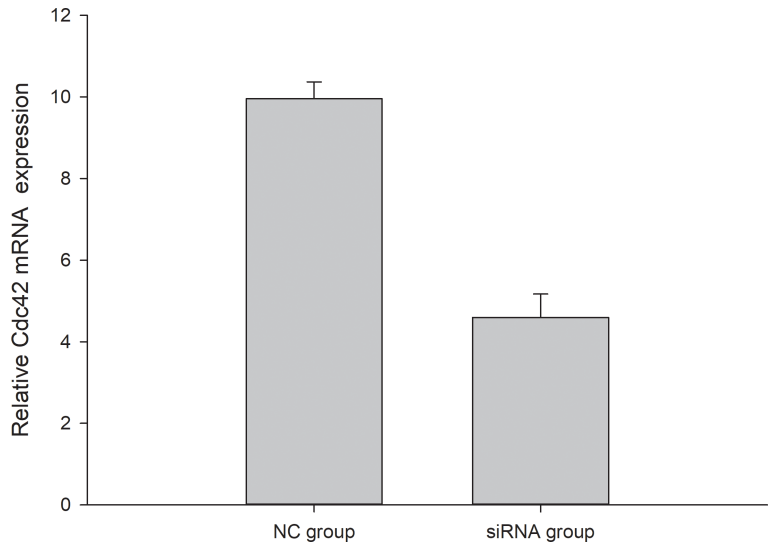

FIGURE 9
The expression of Cdc42 in NC and transfected *Drosha*-siRNA. NC: *Drosha*-siRNA-FAM-NC, The siRNA sequence is not present in the fish.

Drosha gene cDNA from Japanese flounder. Sequence analysis revealed that *Drosha* contains two adjacent RNA enzyme III structural domains (RIIIDa and RIIIDb) and one dsRBD, which belong to the RNA enzyme III family. The RIIIDa and RIIIDb structural domains can each bind a DGCR8 and perform their double-stranded RNA shearing function (Filippov et al., 2000; Wu et al., 2012).

In this study, the results of tissue differential expression analysis of the *Drosha* gene in Japanese flounder showed that it was expressed in all the tissues examined, but the expression differed significantly in different tissues, with significantly higher expression in both brain and muscle, followed by intestine. The results suggest that the *Drosha* gene may play a regulatory role in neural and muscle development. The results of differential expression analysis of *Drosha* gene in embryos and juveniles of Japanese flounder showed that it was expressed in all periods examined except the unfertilized egg (E1) period, but the expression varied greatly in different tissues and reached the highest point after the peak of metamorphosis (36 dph). However, it was found that the expression of *Drosha* was significantly decreased at 3 dph. It is speculated that a large amount of DROSHA protein is stored in the E2 phase, and the yolk is completely absorbed to provide nutrients at this time (Miwa, 1987), and there is no need to synthesize a large amount of mature miRNA. There is no relevant research so far, and the specific reasons need to be further explored. In a word, the results suggest that the *Drosha* gene may play a regulatory role in the development of metamorphosis in Japanese flounder.

Thyroid hormone induced the metamorphosis, while thiourea inhibits the metamorphosis of Japanese flounder (Inui and Miwa, 1985). The *Drosha* enzyme plays a regulatory role in the metamorphosis of flounder, so we designed TH and TU experiments, and further explore the mechanism of TH and TU regulating the metamorphosis of Japanese flounder. The results showed that the peak expression of *Drosha* gene in TH-treated group was advanced to day 23, compared with the peak expression of *Drosha* gene in control group on day 36. This result is consistent with TH promoting the metamorphosis of Japanese flounder. Thyroid hormone (TH) promotes the development of symmetrical larvae into asymmetric benthic larvae in pelagic fish. One eye wanders to the other on the other side of the head (Campinho et al., 2018). In all teleost studies to date, thyroid hormone (TH) promotes metamorphosis. TH is a necessary and a sufficient factor for this developmental change (Campinho, 2019).

As shown in the present study, there is a positive relationship between time to metamorphosis and *Drosha* expression. To further explore the role of *Drosha*, we performed siRNA knockdown experiments. *Drosha* is a miRNA processor (Kim et al., 2015). Figures 8A, B and Figure 9 showed the maturation of miRNAs and miRNA-targeted of Cdc42 were repressed when *Drosha* was knockdown. Cdc42 (cell division cycle 42) is the target gene of miR17 (Zhang et al., 2016), and regulates cell cycle. This is consistent with previous findings that knockdown of the *Drosha* gene in vascular smooth muscle cells decreases the proliferation of vascular smooth muscle cells (Fan et al., 2013). In Japanese flounder, miRNAs have been reported to regulate metamorphosis development (Li et al., 2020).

5 Conclusions

The mechanisms underlying metamorphosis development in Japanese flounder remain unclear. We cloned and characterized the *Drosha* gene in Japanese flounder for the first time and explored the role of *Drosha* in early development and metamorphosis in Japanese flounder. Our research shows that *Drosha* is highly expressed during the metamorphosis stage.

In this research, T3 has been shown to have a positive regulatory effect on *Drosha* expression in Japanese flounder during metamorphosis, which this mechanism is consistent with the T3-induced metamorphosis. The results suggest that T3-induced metamorphosis of Japanese flounder is accelerated upon regulation of miRNAs by *Drosha*. We concluded that one of the developmental mechanisms of flounder metamorphosis may be regulated by the T3-*Drosha*-miRNA signaling pathway. However, further studies are needed to confirm the findings.

Data availability statement

The original contributions presented in the study are included in the article/Supplementary Material. Further inquiries can be directed to the corresponding authors.

Ethics statement

The animal study was reviewed and approved by The Shanghai Ocean University Review Committee.

Author contributions

ZH:Conceptualization, Methodology, Software, Investigation, Formal Analysis, Writing - Original Draft. XZ: Data Curation, Writing - Original Draft. XJ: Resources, Supervision. WZ: Software, Validation. SZ: Conceptualization, Funding Acquisition, Resources, Supervision. All authors contributed to the article and approved the submitted version.

Conflict of interest

The authors declare that the research was conducted in the absence of any commercial or financial relationships that could be construed as a potential conflict of interest.

Publisher's note

All claims expressed in this article are solely those of the authors and do not necessarily represent those of their affiliated organizations, or those of the publisher, the editors and the reviewers. Any product that may be evaluated in this article, or claim that may be made by its manufacturer, is not guaranteed or endorsed by the publisher.

Supplementary material

The Supplementary Material for this article can be found online at: https://www.frontiersin.org/articles/10.3389/fmars.2022.957836/full#supplementary-material

References

Bao, B., Ke, Z., Xing, J., Peatman, E., Liu, Z., Xie, C., et al (2011). Proliferating cells in suborbital tissue drive eye migration in flatfish. *Dev. Biol.* 351 (1), 200–207. doi: 10.1016/j.ydbio.2010.12.032

Campinho, M. A. (2019). Teleost metamorphosis: The role of thyroid hormone. *Front. Endocrinol.* 10. doi: 10.3389/fendo.2019.00383

Campinho, M. A., Galay-Burgos, M., Sweeney, G. E., and Power, D. M. (2010). Coordination of deiodinase and thyroid hormone receptor expression during the larval to juvenile transition in sea bream (Sparus aurata, Linnaeus). *Gen. Comp. Endocrinol.* 165 (2), 181–194. doi: 10.1016/j.ygcen.2009.06.020

Campinho, M. A., Silva, N., Martins, G. G., Anjos, L., Florindo, C., Roman-Padilla, J., et al (2018). A thyroid hormone regulated asymmetric responsive centre is correlated with eye migration during flatfish metamorphosis. *Sci. Rep.* 8 (1), 12267. doi: 10.1038/s41598-018-29957-8

Chen, S. L., Ren, G. C., Sha, Z. X., and Shi, C. Y. (2004). Establishment of a continuous embryonic cell line from Japanese flounder paralichthys olivaceus for virus isolation. *Dis. Aquat. Organ.* 60 (3), 241–246. doi: 10.3354/dao060241

Chen, Q., Sato, K., Yokoi, H., and Suzuki, T. (2020). Developmental regulatory system of ocular-side-specific asymmetric pigmentation in flounder: Critical role of retinoic acid signaling. *J. Exp. Zool. Part B Mol. Dev. Evol.* 334 (3), 156–167. doi: 10.1002/jez.b.22934

Denli, A. M., Tops, B. B., Plasterk, R. H., Ketting, R. F., and Hannon, G. J. (2004). Processing of primary microRNAs by the microprocessor complex. *Nature* 432 (7014), 231–235. doi: 10.1038/nature03049

Fan, P., Chen, Z., Tian, P., Liu, W., Jiao, Y., Xue, Y., et al (2013). miRNA biogenesis enzyme drosha is required for vascular smooth muscle cell survival. *PloS One* 8 (4), e60888. doi: 10.1371/journal.pone.0060888

Filippov, V., Solovyev, V., Filippova, M., and Gill, S. S. (2000). A novel type of RNase III family proteins in eukaryotes. *Gene* 245 (1), 213–221. doi: 10.1016/S0378-1119(99)00571-5

Fu, Y., Shi, Z., Wu, M., Zhang, J., Jia, L., and Chen, X. (2011). Identififfication and differential expression of microRNAs during metamorphosis of the Japanese flJapanese flounder (Paralichthys olivaceus). *PloS One* 6, e22957. doi: 10.1371/journal.pone.0022957

Gawantka, V., Pollet, N., Delius, H., Vingron, M., Pfister, R., Nitsch, R., et al (1998). Gene expression screening in xenopus identifies molecular pathways, predicts gene function and provides a global view of embryonic patterning. *Mech. Dev.* 77 (2), 95–141. doi: 10.1016/S0925-4773(98)00115-4

Ha, M., and Kim, V. N. (2014). Regulation of microRNA biogenesis. *Nat. Rev. Mol. Cell Biol.* 15 (8), 509–524. doi: 10.1038/nrm3838

Han, J., Lee, Y., Yeom, K. H., Nam, J. W., Heo, I., Rhee, J. K., et al (2006). Molecular basis for the recognition of primary microRNAs by the drosha-DGCR8 complex. *Cell* 125 (5), 887–901. doi: 10.1016/j.cell.2006.03.043

Hatfield, S. D., Shcherbata, H. R., Fischer, K. A., Nakahara, K., Carthew, R. W., and Ruohola-Baker, H. (2005). Stem cell division is regulated by the microRNA pathway. *Nature* 435 (7044), 974–978. doi: 10.1038/nature03816

Hoke, K. L., Evans, B. I., and Fernald, R. D. (2006). Remodeling of the cone photoreceptor mosaic during metamorphosis of flounder (Pseudopleuronectes americanus). *Brain Behav. Evol.* 68 (4), 241–254. doi: 10.1159/000094705

Inui, Y., and Miwa, S. (1985). Thyroid hormone induces metamorphosis of flounder larvae. *Gen. Comp. Endocrinol.* 60 (3), 450–454. doi: 10.1016/0016-6480(85)90080-2

Jeong, G., Lim, Y. H., and Kim, Y. K. (2016). Precise mapping of the transcription start sites of human microRNAs using drosha knockout cells. *BMC Genomics* 17 (1), 908. doi: 10.1186/s12864-016-3252-7

Kim, Y., Kang, Y. S., Lee, N. Y., Kim, K. Y., Hwang, Y. J., Kim, H. W., et al (2015). Uvrag targeting by Mir125a and Mir351 modulates autophagy associated with Ewsr1 deficiency. *Autophagy* 11 (5), 796–811. doi: 10.1080/15548627.2015.1035503

Kwon, S. C., Nguyen, T. A., Choi, Y. G., Jo, M. H., Hohng, S., Kim, V. N., et al (2016). Structure of human drosha. *Cell* 164, 81–90. doi: 10.1016/j.cell.2015.12.019

Lee, Y., Han, J., Yeom, K. H., Jin, H., and Kim, V. N. (2006). Drosha in primary microRNA processing. *Cold Spring Harbor Symp. Quantitative Biol.* 71, 51–57. doi: 10.1101/sqb.2006.71.041

Li, X., Hu, H., Li, R., Wang, Z., Qi, J., and Wang, Z. (2020). The role of miR-92 in regulating early development and metamorphosis of Japanese flounder paralichthys olivaceus. *Genes Genet. Syst.* 95 (1), 1–10. doi: 10.1266/ggs.18-00047

Luhur, A., Chawla, G., Wu, Y. C., Li, J., and Sokol, N. S. (2014). Drosha-independent DGCR8/Pasha pathway regulates neuronal morphogenesis. *Proc. Natl. Acad. Sci. United States America* 111 (4), 1421–1426. doi: 10.1073/pnas.1318445111

Manchado, M., Infante, C., Asensio, E., Planas, J. V., and Cañavate, J. P. (2008). Thyroid hormones down-regulate thyrotropin beta subunit and thyroglobulin during metamorphosis in the flatfish Senegalese sole (Solea senegalensis kaup). *Gen. Comp. Endocrinol.* 155 (2), 447–455. doi: 10.1016/j.ygcen.2007.07.011

Miwa, S. (1987). Histological changes in the pituitary-thyroid axis during spontaneous and artificially-induced metamorphosis of larvae of the flounder paralichthys olivaceus. *Cell Tissue Res.* 249 (1), 117–123. doi: 10.1007/BF00215425

Miwa, S., and Inui, Y. (1987). Effects of various doses of thyroxine and triiodothyronine on the metamorphosis of flounder (Paralichthys olivaceus). *Gen. Comp. Endocrinol.* 67 (3), 356–363. doi: 10.1016/0016-6480(87)90190-0

Mullur, R., Liu, Y. Y., and Brent, G. A. (2014). Thyroid hormone regulation of metabolism. *Physiol. Rev.* 94 (2), 355–382. doi: 10.1152/physrev.00030.2013

O'Brien, J., Hayder, H., Zayed, Y., and Peng, C. (2018). Overview of microrna biogenesis, mechanisms of actions,and circulation. *Front. Endocrinol.* 9. doi: 10.3389/fendo.2018.00402

Okada, C., Yamashita, E., Lee, S. J., Shibata, S., Katahira, J., Nakagawa, A., et al (2009). A high-resolution structure of the pre-microRNA nuclear export machinery. *Sci. (New York N.Y.)* 326 (5957), 1275–1279. doi: 10.1126/science.1178705

Policansky, D., and Sieswerda, P. (1979). Early life history of the starry flounder, platichthys stellatus, reared through metamorphosis in the laboratory. *Trans. Am. Fish. Soc.* 108, 326–327. doi: 10.1577/1548-8659(1979)108<326:ELHOTS>2.0.CO;2

Power, D. M., Einarsdóttir, I. E., Pittman, K., Sweeney, G. E., Hildahl, J., Campinho, M. A., et al (2008). The molecular and endocrine basis of flatfish metamorphosis. *Rev. Fish. Sci.* 16:sup1, 95–111. doi: 10.1080/10641260802325377

Subramanian, B., Gao, S., Lercher, M. J., Hu, S., and Chen, W. H. (2019). Evolview v3: a webserver for visualization, annotation, and management of phylogenetic trees. *Nucleic Acids Res.* 47 (W1), W270–W275. doi: 10.1093/nar/gkz357

Togawa, M., Endo, Y., Suzuki, N., Yokoi, H., and Suzuki, T. (2018). Identification of Sox10-positive cells at the dorsal fin base of juvenile flounder that are correlated with blind-side skin ectopic pigmentation. *J. Exp. Zool. Part B Mol. Dev. Evol.* 330 (8), 427–437. doi: 10.1002/jez.b.22842

Wu, Q., Song, R., Ortogero, N., Zheng, H., Evanoff, R., Small, C. L., et al (2012). The RNase III enzyme drosha is essential for microRNA production and spermatogenesis. *J. Biol. Chem.* 287 (30), 25173–25190. doi: 10.1074/jbc.M112.362053

Zhang, H., Fu, Y., Shi, Z., Su, Y., and Zhang, J. (2016). miR-17 is involved in Japanese flounder (Paralichthys olivaceus) development by targeting the Cdc42 mRNA. *Comp. Biochem. Physiol. Part B Biochem. Mol. Biol.* 191, 163–170. doi: 10.1016/j.cbpb.2015.10.005

Zhang, H., Fu, Y., Su, Y., Shi, Z., and Zhang, J. (2015). Identification and expression of HDAC4 targeted by miR-1 and miR-133a during early development in paralichthys olivaceus. *Comp. Biochem. Physiol. Part B Biochem. Mol. Biol.* 179, 1–8. doi: 10.1016/j.cbpb.2014.08.005

frontiers | Frontiers in Marine Science

TYPE Original Research
PUBLISHED 14 September 2022
DOI 10.3389/fmars.2022.984989

OPEN ACCESS

EDITED BY
Shiguo Li,
Research Center for Eco-environmental Sciences, (CAS), China

REVIEWED BY
Chuang Liu,
Hohai University, China
Jingliang Huang,
Tsinghua University, China

*CORRESPONDENCE
Qinzeng Xu
xuqinzeng@fio.org.cn;
xqz08@163.com

SPECIALTY SECTION
This article was submitted to Marine Molecular Biology and Ecology, a section of the journal Frontiers in Marine Science

RECEIVED 03 July 2022
ACCEPTED 19 August 2022
PUBLISHED 14 September 2022

CITATION
Ge M, Mo J, Ip JC-H, Li Y, Shi W, Wang Z, Zhang X and Xu Q (2022) Adaptive biomineralization in two morphotypes of Sternaspidae (Annelida) from the Northern China Seas. *Front. Mar. Sci.* 9:984989. doi: 10.3389/fmars.2022.984989

Adaptive biomineralization in two morphotypes of Sternaspidae (Annelida) from the Northern China Seas

Meiling Ge[1,2], Jing Mo[2], Jack Chi-Ho Ip[3], Yixuan Li[2,3], Wenge Shi[2], Zongling Wang[1,2], Xuelei Zhang[2] and Qinzeng Xu[2]*

[1]College of Environmental Science and Engineering, Ocean University of China, Qingdao, China, [2]Key Laboratory of Marine Eco-Environmental Science and Technology, First Institute of Oceanography, Ministry of Natural Resources, Qingdao, China, [3]Department of Biology, Hong Kong Baptist University, Kowloon, Hong Kong SAR, China

Polychaetes are segmented annelid worms that play a key role in biomineralization in modern oceans. However, little is known about the underlying processes and evolutionary mechanisms. The ventro-caudal shield of Sternaspidae is a typical phosphate biomineral in annelids. Here, we investigated two sternaspids from the northern China Seas, *Sternaspis chinensis* and *Sternaspis liui* syn. n, which evolved diverse shield characteristics as local adaptation. Genetic distances, phylogenetic analyses of nuclear markers (*18S* and *28S* genes), and mitochondrial genomes revealed that the latter is a junior synonym of the former. The integration of elemental composition and the transcriptomic analysis provided insights into phenotypic shield differences. The electron probe microanalysis showed that shields in *S. chinensis* were more biomineralized (i.e., with higher iron, phosphorus, and calcium contents) than those in *S. liui* syn. n. Transcriptomes of the body wall around shields determined 17,751 differentially expressed genes (DEGs) in two morphotypes of the synonymous species. Function enrichment analysis of DEGs showed that *S. chinensis* has an enrichment of the putative biomineralization pathways (i.e., ion transport and calmodulin binding), while *S. liui* syn. n consumed more energy and produced more proteins (i.e., oxidative phosphorylation and ribosome). DEGs allowed to identify seven shell matrix proteins expressed differentially in the two morphotypes, especially calponin, filamin, chitinase, and protease inhibitor BPTI/kunitz, which might contribute to shield evolutionary plasticity response to their living habitats. Overall, this study 1) revealed an environmental biomineralization adaptation in two polychaete morphotypes of one species by integrating shield chemical composition of shields and transcriptome analyses and 2) provided insights into the molecular mechanisms underlying polychaete biomineralization.

KEYWORDS

biomineralization, shell matrix protein, Sternaspidae, shield composition, mitochondrial genome, transcriptome

Introduction

Biomineralization is a biological process allowing living organisms to produce minerals. In invertebrates, biomineralization has been mainly studied in mollusks, corals, brachiopods, bryozoans, and echinoderms (Takeuchi et al., 2016; Malachowicz and Wenne, 2019; Clark, 2020; Murdock, 2020). However, polychaetes are also important biomineralization organisms in marine environments whose study will help in understanding biomineralization and evolutionary adaptation in invertebrates (Vinn, 2021). The tubes of serpulids, sabellids, and cirratulids are composed of calcite, aragonite, or a mixture of both (Vinn, 2021). Serpulid tubes contain soluble and insoluble organic matrices that control biomineralization (Tanur et al., 2010). Sabellids and cirratulids are characteristic of matrix-mediated biomineralization (Vinn et al., 2008; Vinn, 2021). The formation of the chitinous tube in the deep-sea siboglinid tubeworm *Paraescarpia echinospica* is also controlled by matrix proteins (Sun et al., 2021). Other polychaetes produce biominerals as parts of their bodies (e.g., chaetae, elytra, and shields) (Heffernana1, 1990; Vinn, 2021). However, little is known about their chemical composition and formation in these cases.

The ventro-caudal shields are typically phosphate biominerals in Sternaspidae (Polychaeta: Terebellida) and some Fauveliopsidae, formed by amorphous ferric phosphate hydrogel (composed of FeO, P_2O_5, CaO, MgO, BaO, and MnO) (Lowenstam, 1972; Sendall and Salazar-Vallejo, 2013). Particularly, sternaspids were considered key animals in oceanic ferric phosphate hydrogel-sinking processes (Lowenstam, 1972) due to their worldwide distribution from shallow to deep waters (Salazar-Vallejo and Buzhinskaja, 2013).

In addition, shield morphology is a diagnostic feature for the four genera of Sternaspidae (*Sternaspis* Otto, 1821, *Caulleryaspis* Sendall & Salazar-Vallejo, 2013, *Petersenaspis* Sendall & Salazar-V allejo, 2013 and *Mauretanaspis* Fiege & Barnich, 2020) and 43 valid species (Fiege and Barnich, 2020). Recently, however, *Sternaspis sendalli* and *Sternaspis monroi* proved to be genetically identical based on the mitochondrial cytochrome oxidase I (*COI*) and *16S* ribosomal RNA (*16S*) markers despite having different shield features (Drennan et al., 2019).

Sternaspids are habitually found in China seas, especially in the Bohai and Yellow Seas (Jin-Bao et al., 2006), while Wu et al., (2015) described *Sternaspis chinensis* Wu, Salazar-Vallejo & Xu, 2015 and *Sternaspis liui* Wu, Salazar-Vallejo & Xu, 2015 from the northern China Seas. *S. chinensis* has a stiff shield with easy-to-brush sediment particles attached, while *S. liui* has a slightly sclerotized and soft shield with firmly adhered sediment. Based on *COI* and *16S* and the nuclear *18S* ribosomal RNA (*18S*) and *28S* markers, we have revealed that they are genetically identical, *S. liui* (Wu et al., 2015) syn. n being a junior synonym of *S. chinensis*. This led us to question the molecular mechanisms contributing to shield evolutionary plasticity of the two morphotypes.

Therefore, this study aims at 1) further confirming *S. chinensis* and *S. liui* syn. n as two morphotypes being the same species based on sequencing their mitochondrial genomes, 2) revealing the shield chemical composition leading to the observed stiffness, and 3) elucidating the gene regulatory mechanisms underlying biomineralization.

Materials and methods

Specimen collection, morphological identification, and molecular taxonomy

Specimens of *S. chinensis* and *S. liui* syn. n (Yellow Sea) were collected using an Agassiz trawl (Figure 1, Table S1) and those of *S. sendalli* (South Shetland Islands) and *Sternaspis buzhinskajae* (Salazar-Vallejo, 2014) (Arctic Ocean) with a box corer. These two polar species were used to analyze the genetic distance and phylogeny of the two morphotypes of synonymous species (Figure 1, Table S1). All specimens were preserved in 75% ethanol for morphological examination and DNA extraction or directly frozen at −80°C for RNA extraction on board.

Shield morphological features (Figures S1–S4) were analyzed following Wu et al. (2015) using a Nikon SMZ1270 stereomicroscope and NIS-Elements 4.50 software. Species identity was further confirmed by amplifying fragments of *COI*, *16S*, *18S*, and *28S* and comparing the obtained sequences (Tables S1, S2) with those available in GenBank. The uncorrected paired *p* distances of *COI*, *16S*, *18S*, and *28S* between and within species were calculated by the Kimura 2-parameter (K2P) model implemented in MEGA v7.0.26 (Kumar et al., 2016).

Mitochondrial genome sequencing and analysis

Total genomic DNA was extracted from body walls around shields using MicroElute Genomic DNA Kit (OMEGA, USA). Genomic DNA libraries with an insert size of approximately 350 bp were constructed with NEBNext® Ultra™ DNA Library Prep Kit (Illumina, USA) and sequenced on the Illumina Hiseq 2500 sequencer (Illumina, USA) in Qingdao Insight Exbio Technology Corporation (China) to generate 150-bp paired-end reads. Raw reads were quality controlled and filtered using FastQC v0.11.9 (Andrews, 2010) and Trimmomatic v0.39 (Bolger et al., 2014), respectively, under default parameters. Clean reads were assembled using SPAdes v3.13 (Nurk et al., 2013) under default settings. The putative mitochondrial contig was identified using BLASTn against the available annelid mitogenome in the NCBI database. The mitogenome was annotated using the MITOs webserver (Bernt et al., 2013)

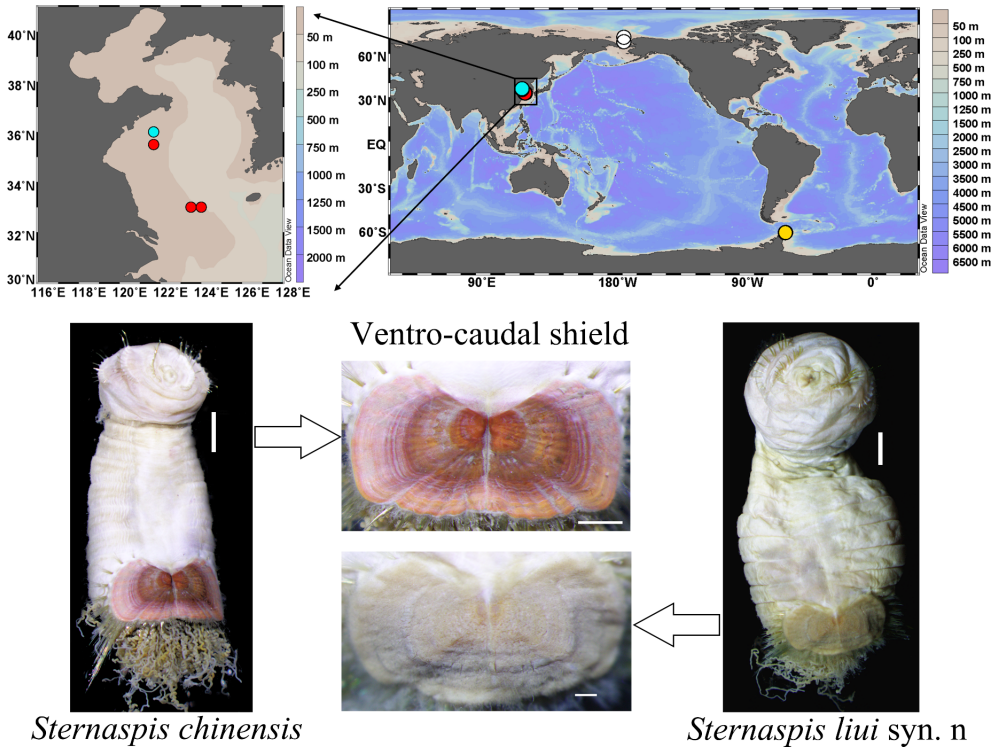

FIGURE 1
Sampling locations of sternaspid specimens used in the present study and morphological images of two sternaspids from the China Seas. Red circle, *Sternaspis chinensis*; cyan circle, *Sternaspis liui* syn. n; white circle, *Sternaspis buzhinkajae*; yellow circle, *Sternaspis sendalli*. Scale bars: *S. chinensis* body = 2 mm, shield = 1 mm; *S. liui* syn. n body = 2 mm, shield = 500 µm.

under default settings with the invertebrate mitochondrial genetic code. The gene start and stop codons were manually inspected and adjusted by MEGA v7.0.26 (Kumar et al., 2016). All assembled mitochondrial genomes were deposited in GenBank (Table S3).

Thirteen protein-coding genes (PCGs) and two rRNA genes of 27 polychaetes with complete mitogenomes, covering all families of Sedentaria, as well as those of *Chloeia pocicola* and *Cryptonome barbada* (outgroups) deposited in GenBank were used for the phylogenetic analysis (Table S3). Maximum likelihood (ML) analysis was analyzed by IQ-TREE v. 1.6.8 (Nguyen et al., 2015) with 1,000 bootstrap replicates (Supplementary Material).

Analysis of shield elemental composition

Complete ventro-caudal shields were dissected from three individuals of *S. chinensis* and three of *S. liui* syn. n. Sediment organic contaminations were removed by first cleaning the shields with a soft brush, then rinsing with distilled water, soaking in sodium hypochlorite (10 vol%) for 10 min, ultrasonic cleaning, and air-dried.

Cleaned shields were trimmed, polished to 10–30-µm thick using lapping machine and polishing machine, and sputter-coated with carbon using a JEE-420 vacuum evaporator (JEOL Ltd., Japan) for electron probe microanalysis (EPMA), which were performed with the electron probe analyzer JOEL JXA-8230 at the Marine Geology and Geophysics Lab of the First Institute of Oceanography (Ministry of Natural Resources, China). As shields are not formed by chitin (Goodrich, 1897), the carbon coating acted as the conductive media without influencing the analysis. The accelerating voltage was set to 15 kV with a beam current of 10 nA and a beam diameter of 1 µm.

Based on results of previous shield element analyses (Lowenstam, 1972) and our total element qualitative analyses, Iron (Fe), phosphorus (P), calcium (Ca), magnesium (Mg) and manganese (Mn), nitrogen (N) and sulfur (S) and silicon (Si) were selected for quantitative analyses. Eight random points per shield and three shields for each morphotype (n = 8 × 3) were chosen for element quantified analyses. Student's t-test (SPSS 26.0 software IBM SPSS Inc., USA) allowed comparing each element distribution [as mean ± standard deviation (SD)] between two morphotypes, which were plotted with Origin 9.5 (Origin Lab, USA). Backscattered electron (BSE) image intensity indicating the mean atomic number was used to locate the

compositional differences (Llovet et al., 2021). EPMA maps showing individual element distribution in shields were obtained for microscopic, local, and lateral shields by scanning with beam diameters of 0.3, 1, and 3 μm, respectively.

RNA extraction, sequencing, and bioinformatic analyses

Total RNA was extracted from the body wall around shields of five specimens of *S. chinensis* and five specimens of *S. liui* syn. n using MicroElute Total RNA Kit (OMEGA, USA) according to manufacturer's instructions. RNA quantity and quality were evaluated using a NanoDrop 2000 (Thermo Scientific, USA) and a Bioanalyzer 2100 (Agilent Technologies, USA). The cDNA libraries were prepared using the TruSeq RNA Library Prep Kit (Illumina, USA) and then sequenced on an Illumina HiSeq2000 sequencer to produce 150-bp paired-end reads at Shanghai OE Biotech Co., Ltd. (China).

Adaptors and low-quality Illumina reads were filtered using Trimmomatic v0.36 (Bolger et al., 2014) under the default parameters. To compare the two morphotypes' gene expression profiles, we assembled their RNA sequencing (RNAseq) data (Sandoval-Castillo et al., 2020). All clean reads were *de novo* assembled using Trinity v2.4.0 (Grabherr et al., 2011) under the default settings. The longest isoform from each gene was selected as "unigene," and the redundancy was eliminated using CD-HIT v4.8.1 with 95% similarity (Li et al., 2001). Unigenes were annotated using Diamond BLASTx v2.0.14 (Buchfink et al., 2015) with an E-value threshold of $1e^{-5}$ against the NCBI NR, Swiss-Port, euKaryotic Orthologous Groups (KOG), Gene Ontology (GO), eggNOG, and Kyoto Encyclopedia of Genes and Genomes (KEGG). The protein family for each unigene was determined using HMMER 3.3.2 (Mistry et al., 2013) against the Pfam database with an E-value threshold of $1e^{-5}$.

Gene expression levels were determined using Bowtie2 (Langmead and Salzberg, 2012). The results were normalized as transcripts per kilobase of exon model per million mapped reads (FPKM) (Trapnell et al., 2010). Principal component analysis (PCA; visualized using the R package PCAtools v2.5.13) allowed comparing the gene expression profiles among morphotypes and individuals. Differentially expressed genes (DEGs) between the two morphotypes were determined using DESeq (Anders and Huber, 2012). Only unigenes with $\log_2$fold change >1 and a *p*-value <0.05 were selected. GO and KEGG enrichment analyses of DEGs were conducted using Goseq R and KOBAS software packages, respectively (Kanehisa et al., 2007; Young et al., 2010). DEG heatmap and volcano plot were created using the R package pheatmap and ggplot, respectively.

Differential biomineralization mechanisms in *S. chinensis* and *S. liui* syn. n were revealed by identifying the putative biomineralization-related genes by BLASTx-identified DEGs against the Shell Matrix Protein (SMP) database (https://doi.org/10/cz2w) with a threshold of E-value $1e^{-10}$ and a >50% identity (Altschul et al., 1997). The correlation heatmap was created using the R package ComplexHeatmap v2.11.1.

Real-time PCR validation

Gene expression profiles were validated using real-time polymerase chain reaction (RT-PCR) analysis. Five representative SMP-like DEGs were selected, and the corresponding primers were designed using the online NCBI primer-BLAST tool (Table S4). The identical RNA samples were used for RT-PCR and RNAseq analyses, and cDNA was synthesized from 0.5 μg of DNase-treated RNA using TransScript First-Strand cDNA Synthesis SuperMix (TransGen Biotech, China). RT-PCR was performed on an ABI7500 instrument (Applied Biosystems, USA) with SYBR®Green (Applied Biosystems, USA) with three technical replicates per individual and three individuals for each morphotype. A three-step method was employed for RT-PCR amplification. The annealing temperature was done at 58°C. Relative expression levels were calculated using the $2^{-\triangle\triangle Ct}$ method (Livak and Schmittgen, 2001), with the mean expression levels of *18S* and *α-tubulin* being used as references. Expression profiles and Pearson correlation coefficient between RT-PCR and RNAseq were calculated and visualized using GraphPad Prism 8.

Results

Synonymy of *S. chinensis* with *S. liui* syn. n based on DNA barcoding and mitogenomes

The interspecific uncorrected *p* distance (0–0.007) of *COI*, *16S*, and the nuclear *18S* and *28S* markers between *S. chinensis* and *S. liui* syn. n was at least one order of magnitude smaller than that of between other species but was equivalent to their intraspecific genetic distance (0–0.009, Table S5), suggesting that they might be genetically identical (Drennan et al., 2019).

The mitogenome size of *S. chinensis*, *S. liui* syn. n, *S. sendalli*, and *S. buzhinskajae* ranged from 15,287 to 17,728 bp (Table S6) and contained 13 PCGs, two rRNAs, and 22 tRNAs. Their gene orders were the same, while the order of the 13 PCGs was conserved with the putative ground pattern of Pleistoannelida (Weigert et al., 2015), except for the translocation of NADH-ubiquinone oxidoreductase chain 1 (*nad1*) (Figure S5).

The four sternaspids showed a monophyletic relationship (Figure 2). *Sternaspis liui* syn. n and *S. chinensis* had a branch length close to 0 (Figure 2), mitochondrial genomes with a 99.9% sequence similarity (Table S7), and paired nucleotide distances

for the 13 PCGs and the two rRNAs ranging from 0 to 0.002 (Table S8), supporting that the former should be a junior synonym of the latter despite having two morphotypes.

Elements

Fe, P, Ca, Mg, and Mn were significantly more abundant in *S. chinensis* than in *S. liui* syn. n, while N and S were significantly less abundant (Figure 3; Figures S6, S7). The distribution of these elements was relatively uniform in *S. chinensis* and heterogeneous in *S. liui* syn. n (Figures S6, S7). N and S, which might represent proteins, were more abundant in the areas with low contents of Fe, P, Ca, Mg, and Mn in *S. liui* syn. n (Figure S6). The two shield types showed higher abundances of Fe, P, and Ca in the central shield area, with external radiation strip regions (Figure 4), which corresponded to the ribs on the shield surface (Figures S1, S2). Notably, a polygonal microstructure was found in the shields of the two shield types (Figure 5, Figure S6B), with the highest Fe, P, and Ca contents at the edge, intermediately inward, and zero-areas scattered inside (Figure 5). This structure occurred in the whole shield of *S. chinensis* but only in the central with radiation strip regions with high Fe, P, and Ca contents in *S. liui* syn. n (Figure 5, Figure S6).

Transcriptomes

The body wall around the shield of the two morphotypes produced 493.39 million clean reads (49.34 million reads per individual on average) (Table S9). *De novo* assembly resulted in 128,181 unigenes with an N50 of 1,146 bp and a GC content of 40.11%. These unigenes were successfully annotated with any of the seven protein databases (Tables S10, S11).

The first axis of the PCA accounted for 77.49% of variations and allowed to clearly distinguish the two morphotypes, while they showed a strong clustering for the individual samples (Figure 6A). The mitochondrial genes cytochrome b (*cob*) and NADH dehydrogenase subunit 2 (*nad2*) that showed a high loading in PCI (Figure 6B) were highly expressed in *S. liui* syn. n, while the genes encoding actin-related protein (*arp*) and myosin regulatory light chain (*mrlc*) with high loading in PCI exhibited a high expression in *S. chinensis* (Figure 6B).

Sternaspis chinensis and *S. liui* syn. n showed 17,751 DEGs, with 6,503 and 11,248 upregulated genes, respectively (Figures 6C, D). Upregulated genes in *S. chinensis* were mainly annotated GO terms related to biomineralization (ion transport and calmodulin binding) (Figure 7). While upregulated genes in *S. liui* syn. n were associated with protein synthesis and energy

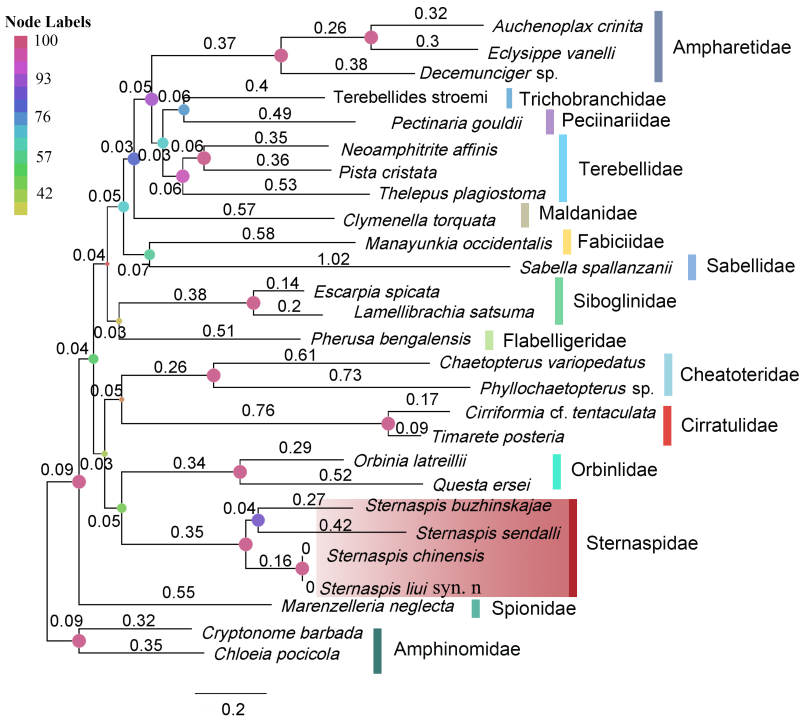

FIGURE 2
Maximum-likelihood tree based on nucleotide sequences of 13 PCGs and two rRNAs. The node labels indicated bootstrap supports. Branch lengths are indicated above the branch.

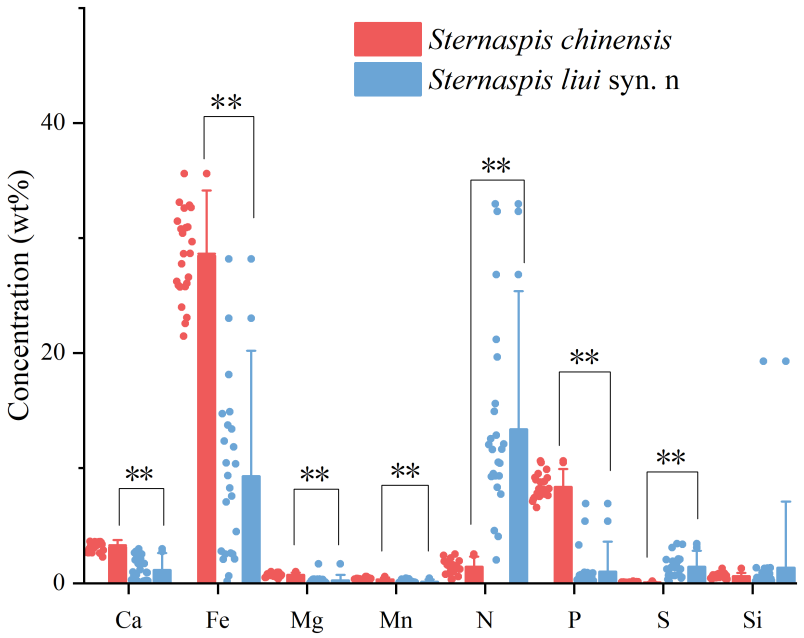

FIGURE 3
Comparison of the main element contents in the ventro-caudal shields of the two sternaspid morphotypes. Bars: mean ± SD (n = 24). Double asterisk (**) above the bars represents a significant difference between the two synonymous species ($p < 0.01$, Student's t-test).

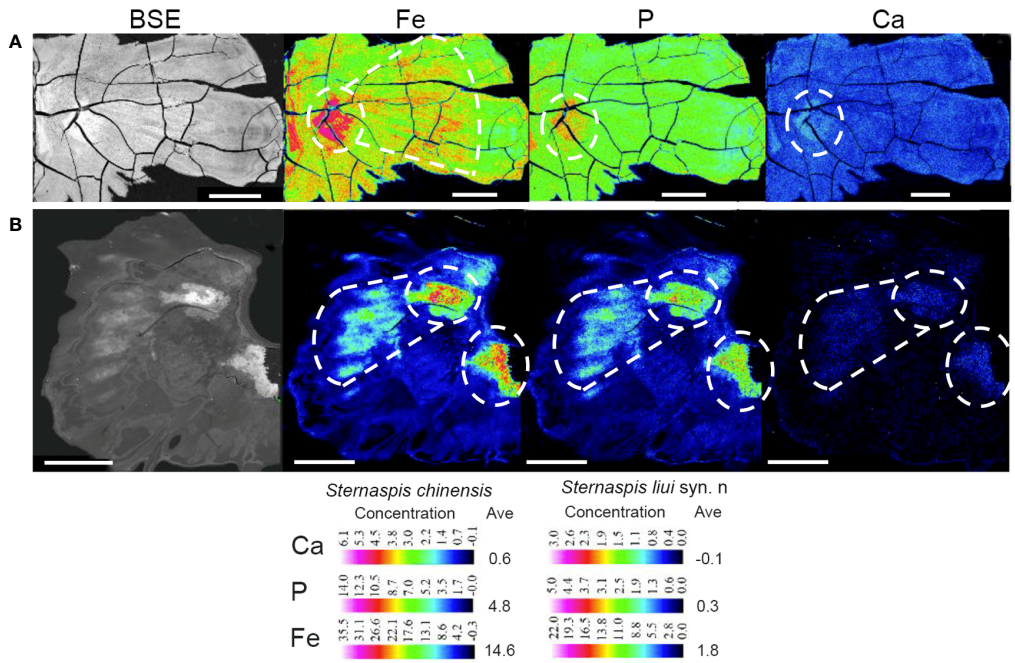

FIGURE 4
Backscattered electron (BSE) images and electron probe microanalysis (EPMA) elemental maps of Fe, P, and Ca in shield plates of **(A)** *Sternaspis chinensis* and **(B)** *Sternaspis liui* syn. n. Ave, average concentration. BSE image scale bar: 100 μm; Fe, P, and Ca EPMA map scale bar: 500 μm. White circles, high element abundance.

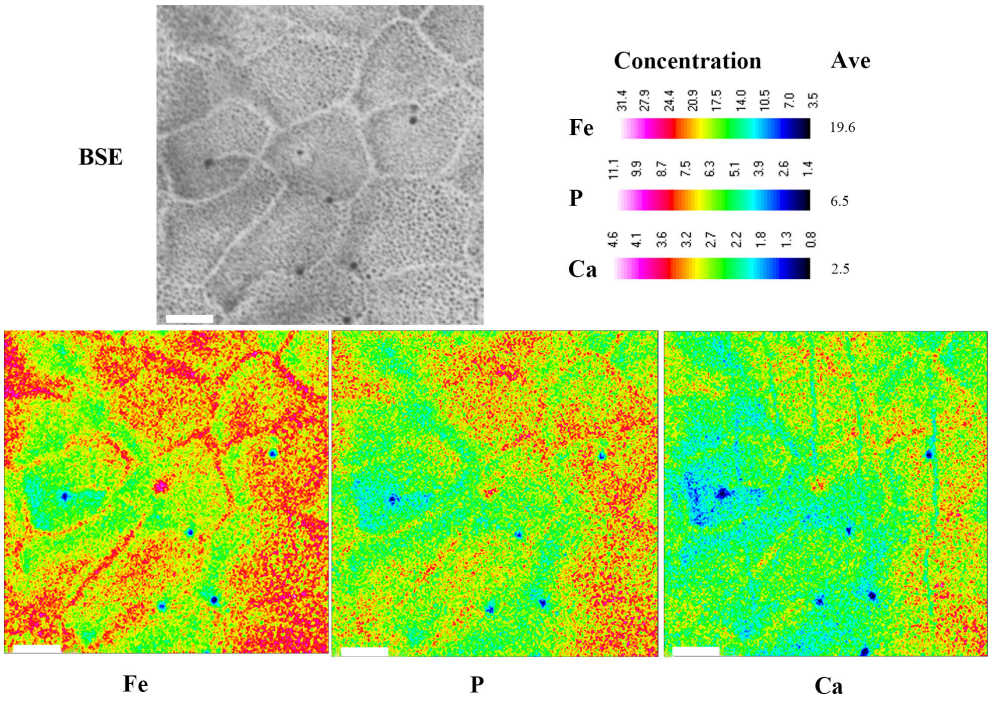

FIGURE 5
Backscattered electron (BSE) images and electron probe microanalysis (EPMA) elemental maps of Fe, P, and Ca for *Sternaspis chinensis*. Ave, average concentration. Scale bar: 10 μm.

production (respiratory chain, respiratory chain complex III, and cytosolic large/small ribosomal subunits) (Figure 7). In addition, shield formation-related pathways (calcium signaling and pantothenate and coenzyme A (CoA) biosynthesis) were enriched in *S. chinensis* and transcription and energy metabolism-related pathways (ribosome and oxidative phosphorylation) in *S. liui* syn. n (Figure S8).

Biomineralization-related differentially expressed genes and proteins

Among the two sternaspid morphotypes, a total of 24 DEGs were identified as SMP-related genes through the homolog search against an SMP database, including two BPTI/Kunitzs, nine Cyclophilin PPIases, one Filament/Filmin, eight fructose–bisphosphate aldolase (FBPA), one Glycoside hydrolase, Peroxiredoxin, and two Transgelin-Calponin (Table S12). Six of them were highly expressed in *S. chinensis*, and 18 SMP-related genes were actively transcribed in *S. liui* syn. n (Figure 8, Table S12). FBPA, Transgelin-Calponin, and BPTI/Kunitzs were highly expressed in both morphotypes (Figure 8).

Gene expression validation by RT-PCR

Five DEGs possibly related to shield formation were selected for RT-PCR analysis: two encoding SMPs (FBPA and transgelin-calponin), two of chitin synthesis-related GO terms (chitin-based embryonic cuticle biosynthetic process and chitin synthase activity), and one of heat shock protein (Table S4). Their $\log_2$fold change values in RT-PCR and RNAseq were significantly correlated (R^2 = 0.89, $p < 0.05$), and all of them were upregulated in both data in *S. chinensis* compared to *S. liui* syn. n (Figure S9), implying the high quality of our transcriptome data.

Discussion

Shield morphological variation and chemical composition

Sternaspis chinensis and *S. liui* syn. n were originally described based on morphological features (Wu et al., 2015), including the shields. In *S. liui* syn. n, they are soft, with prominent ribs and concentric lines near the margin, while in *S. chinensis*, they are stiff, with flat ribs and concentric lines (Wu

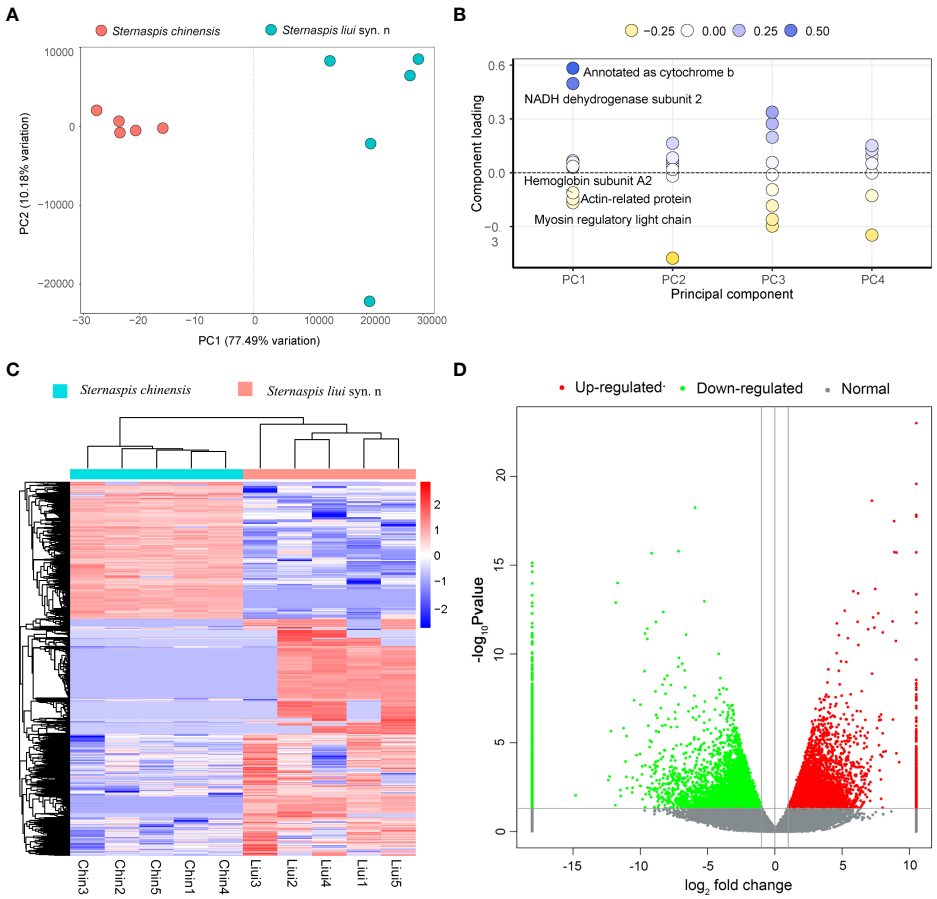

FIGURE 6
Comparative analysis of gene expression. **(A)** PCA for all genes. **(B)** Loading plot of the first five principal components. **(C)** Heatmap showing the profiles of the differentially expressed genes (DEGs) (red, upregulated; blue, downregulated). **(D)** DEG volcano plot. DEGs were filtered by *p*-value <0.05 and |$\log_2$fold change| >1.

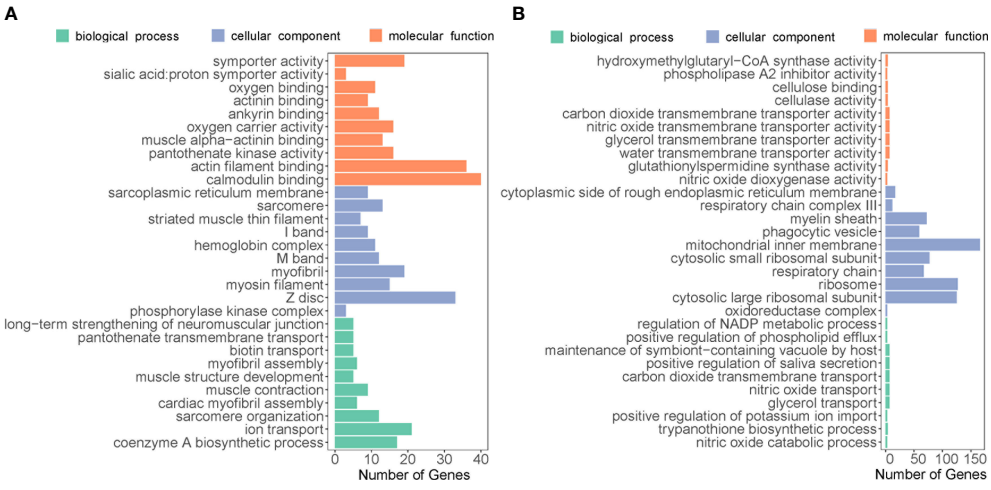

FIGURE 7
Top 30 enriched Gene Ontology categories associated with upregulated genes in **(A)** *Sternaspis chinensis* and **(B)** *Sternaspis liui* syn. n.

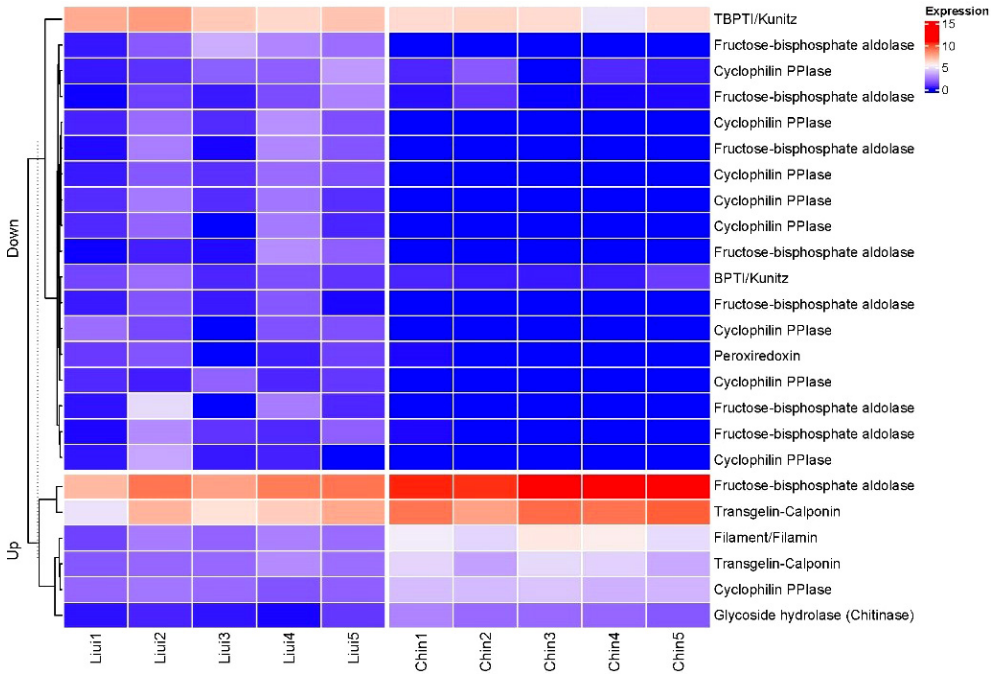

FIGURE 8
Heatmap of the hierarchical clustering showing the profiles for the SMP-related differentially expressed genes. Expression: $\log_2$(FPKM+1); Up, upregulated genes in *Sternaspis chinensis vs. Sternaspis liui* syn. n; Down, downregulated genes in *S. chinensis vs. S. liui* syn. n; Liui1–5, specimens of *S. liui* syn. n; Chin1–5, specimens of *S. chinensis*.

et al., 2015). However, we have demonstrated that these two species are genetically identical, with 0–0.007 pairwise genetic distances for *COI*, *16S*, *18S*, and *28S*. The monophyletic relationship, low branch length, and intraspecies level genetic distance based on mitogenomes clearly support that the two morphotypes correspond to synonyms instead of species. Therefore, shield examination and molecular evidence must be integrated into the taxonomic diagnosis of sternaspids, as postulated by Drennan et al. (2019). However, whether they are the two ecotypes of *S. chinensis* including the genetic variations of the two populations needs to be further analyzed using nuclear DNA single nucleotide polymorphisms (SNPs).

The shield elemental compositions of the two morphotypes revealed Fe, P, and Ca as being higher in *S. chinensis* than in *S. liui* syn. n. The hardness of the sternaspid shield seemed to be determined by the abundance of mineralized Fe (Bartolomaeus, 1992), which might imply a higher level of shield biomineralization and stiffness in *S. chinensis* than *in S. liui* syn. n. Variations in structure and composition of biominerals are also common in mollusks, usually in association with the environmental condition and fostering local adaptations (Hoffman et al., 2009; Zieritz et al., 2010). Iron sulfide contents in the sclerites of scaly-foot snails were positively correlated with its environmental concentration, likely being a detoxication mechanism (Nakamura et al., 2012), while water chemistry and food and nutrient supply highly impacted the shell production in the blue mussel *Mytilus edulis* (Michalek, 2019). Therefore, variations in shield element contents in the two morphotypes might be related to their living environments, although further detailed analysis of the elemental composition of their habitats is required to evaluate this hypothesis.

The mechanical properties of the biominerals can be affected by many factors, including chemical composition, microstructure, and organic matrix embedded in the minerals (Marcus et al., 2017; Bianco-Stein et al., 2020; Yamagata et al., 2022). Herein, Fe, P, and Ca are critical elements of shield components, distributed as polygonal microstructures in the whole shield of *S. chinensis* but only in the center with radiation strip regions in *S. liui* syn. n (Figure 5, Figure S6). The polygonal microstructure is commonly found with various functions in skeletons of marine organisms, such as strengthening hardness and lightening weight in sea urchin *Cidaris rugosa* exoskeleton and changing body color in polychaete *Aphrodita aculeata* spines (Murray, 2018). Furthermore, the polygonal microstructure proved to be excellent in economizing materials because hexagonal cells require the least total wall length when filling a flat plane (Murray, 2018). However, the interrelationship between the chemical composition, microstructure, and mechanical properties especially shield hardness needs further exploration.

Differential gene expression

The divergent shield biomineralization shown by the two morphotypes may be associated with their differential gene regulation, especially in biomineralization-related gene expression. Two mitogenes (*cob* and *nad2*) identified in PCA were highly expressed in *S. liui* syn. n, which may be a reflection of the difference in energy metabolism involved in biological processes, including biomineralization. Mitogenes are involved in complex bioenergetic pathways helping marine animals cope with disturbances by phenotype selection, habitat translocations, and responses to climate-related conditions. Some mitogenes in the mantle of *Mytilus chilensis* from two different habitats played key roles in its adaptive responses to biomineralization, feeding, and locomotion (Yévenes et al., 2022). The other two genes identified in PCA actively transcribed in *S. chinensis* were *mrlc* and *arp*, which may foster a high level of shield biomineralization. The former is a calcium-binding protein with the SMP-related EF-hand domain that is involved in shell formation (Guan et al., 2017), while the latter could control biomineralization by forming dynamic scaffolds and templates (Tyszka et al., 2019).

A large number of DEGs and GO enrichments between the two sternaspid morphotypes showed their unique physiological functions. Given that tissues around the shield may play multiple functions, these differential expressions were not just representative biomineralization-specific genes. For *S. chinensis*, the enriched ion transport (Yarra et al., 2021) and calmodulin binding (Yan et al., 2007; Fang et al., 2008; Mao et al., 2019) were suspected to be associated with hypothetical biomineralization pathways. Compared with *S. chinensis*, the transcripts of *S. liui* syn. n has more upregulated DEGs involved in energy metabolism and protein synthesis. For example, 1) "respiratory chain" and "respiratory chain complex III" are protein complexes forming electron transport systems, highly expressed in the mineralized teeth region of *Cryptochiton stelleri*, providing the energy for iron transport required for mineralization (Nemoto et al., 2019), and 2) "cytosolic large/small ribosomal subunits" are the places for intracellular protein synthesis (Brar and Weissman, 2015). Although mitochondrial and ribosomal genes are not biomineralization genes, they were among the most abundantly expressed in the mollusk mantles that is the shell formation tissue (Shi et al., 2013; Shi et al., 2019).

Proteins involved in differential biomineralization

Seven SMP-related proteins involved in molluskan biomineralization were annotated from the DEGs of the two sternaspid morphotypes (Figure 8). These proteins contained some key biomineralization domains, for example, Glyco_18, CH (Calponin homology domain), IG_FLMN (Filamin-type immunoglobulin domain), KU (BPTI/Kunitz family of serine protease inhibitors domain), and TIL (Trypsin Inhibitor like cysteine-rich domain) (Table S12) (Liao et al., 2021; Yarra et al., 2021). The genes coding FBPA and cyclophilin PPIase were differentially expressed in the two morphotypes (Figure 7). These two proteins proved to have multiple biological functions not limited to biomineralization. Thus, they could invoke different expression profiles in the two morphotypes. FBPA containing glycolytic domain plays a role in the stabilization of amorphous calcium carbonate in crustacean exoskeleton mineralization (Sato et al., 2011; Abehsera et al., 2018), participates in carbohydrate metabolism, and provides energy for the organism (Guo et al., 2010; Di et al., 2017). Cyclophilins with pro_isomerase domain was found to be integral to primary mesenchymal sea urchin cells as well as protein folding (Wilt and Killian, 2008; Manno et al., 2012; Nemoto et al., 2012).

Protease inhibitor BPTI/kunitz and peroxiredoxin were actively transcribed in this junior synonym species. Protease inhibitors with KU and TIL domains are common mollusk shell matrix proteins, having an inhibitory function on biomineralization (Y.-J. Rose-Martel et al., 2015; Luo, 2017; Takeuchi et al., 2021). Peroxiredoxin is involved in the reduction of iron oxide in the mineralized cusp of chiton teeth (Kisailus and Nemoto, 2018). Therefore, their expression in *S. liui* syn. n might contribute to the biomineralization process.

The SMP-related proteins chitinase, transgelin-calponin, and filament/filamin were highly expressed in *S. chinensis* (Figure 8). Chitinase with the conserved Glyco_18 domain is an enzyme that hydrolyzes chitin oligosaccharides (Zhang et al., 2019; Liao et al., 2021; Liu et al., 2021) and participates in the formation of the metazoan chitin scaffold (Le Pabic et al., 2017). Calponin with the CH domain is an important protein involved in calcification in mollusks and branchiopods (Y. J. Luo et al., 2015; Sun et al., 2021). Filamin proteins with CH and IG_FLMN domains in humans and pearl oysters could interact with the calcium-sensing receptor and promote the calcification Rho signaling pathway (Awata et al., 2001; Pi et al., 2002; Matsuura et al., 2018). Therefore, these upregulated genes might contribute to the high shield biomineralization level in *S. chinensis*, while the differential expression of protease inhibitors with the function of biomineralization inhibition between the two morphotypes might govern their differential levels in biomineralization.

Conclusion

This study proved that *S. liui* syn. n is, in fact, a junior synonym of *S. chinensis*. Shield biomineralization in these two morphotypes of synonymous species has been revealed by composition and structure analysis, showing the natural formation of a polygonal microstructure composed of ferric phosphate hydrogels. Our study also showed that higher abundance of Fe, P, and Ca in *S. chinensis* shield corresponds to more polygonal microstructures than that in *S. liui* syn. n. Transcriptome analyses provided insights into the respective biomineralization molecular mechanism, suggesting that *S. chinensis* exhibited higher biomineralization activities, especially high expression of some SMP-related proteins (i.e., calponin, filamin, chitinase) resulting in a high level of shield biomineralization. *Sternaspis chinensis*. syn. n exhibited a high expression of energy mechanism-related genes and encoding protease inhibitor genes, reflecting its low level of biomineralization. Overall, our findings enhance the understanding of the mechanisms underlying biomineralization in sternaspids, with chemical and molecular data generated being also useful for further studies on the evolution of the mineralization process in polychaete annelids.

Data availability statement

The datasets presented in this study can be found in online repositories. The names of the repository/repositories and accession number(s) can be found in the article/Supplementary Material.

Author contributions

QX and MG conceived and designed the original research, wrote the initial manuscript. MG and JM analyzed the data. YL and WS collected samples and help interpret the data. JI, QX, ZW and XZ revised and approved the manuscript. All authors contributed to the article and approved the submitted version.

Funding

This study was supported by the foundation of the National Natural Science Foundation of China (42176135, 4181101341).

Acknowledgments

We thank the captains, crews and operation teams of the research vessels "Xiangyanghong 01" and "Xiangyanghong 18" for collecting the samples. We thank Dr. Xuwen Wu for his guidance on morphological identification of sternaspids. We acknowledge the Lab of Marine Geology and Geophysics of First Institute of Oceanography, Ministry of Natural Resources for electron probe microanalysis. We are grateful to the previous reviewers for their constructive suggestions for this paper and corrections of language.

Conflict of interest

The authors declare that the research was conducted in the absence of any commercial or financial relationships that could be construed as a potential conflict of interest.

Publisher's note

All claims expressed in this article are solely those of the authors and do not necessarily represent those of their affiliated organizations, or those of the publisher, the editors and the reviewers. Any product that may be evaluated in this article, or claim that may be made by its manufacturer, is not guaranteed or endorsed by the publisher.

Supplementary material

The Supplementary Material for this article can be found online at: https://www.frontiersin.org/articles/10.3389/fmars.2022.984989/full#supplementary-material

References

Abehsera, S., Weil, S., Manor, R., and Sagi, A. (2018). The search for proteins involved in the formation of crustacean cuticular structures. *Hydrobiologia* 825, 29–45. doi: 10.1007/s10750-018-3684-y

Altschul, S. F., Madden, T. L., Schäffer, A. A., Zhang, J., Zhang, Z., Miller, W., et al. (1997). Gapped blast and psi-blast: A new generation of protein database search programs. *Nucleic Acids Res.* 25, 3389–3402. doi: 10.1093/nar/25.17.3389

Anders, S., and Huber, W. (2012). Differential expression of rna-seq data at the gene level–the deseq package. *Heidelberg Germany: Eur. Mol. Biol. Lab. (EMBL)* 10, f1000research.

Andrews, S. (2010). *Fastqc: A quality control tool for high throughput sequence data*. Available at: http://www.bioinformatics.babraham.ac.uk/projects/fastqc

Awata, H., Huang, C., Handlogten, M. E., and Miller, R. T. (2001). Interaction of the calcium-sensing receptor and filamin, a potential scaffolding protein. *J. Biol. Chem.* 276, 34871–34879. doi: 10.1074/jbc.M100775200

Bartolomaeus, T. J. M. M. (1992). On the ultrastructure of the cuticle, the epidermis and the gills of *sternaspis* scutata (annelida). *Microfauna Marina* 7, 237–252.

Bernt, M., Donath, A., Jühling, F., Externbrink, F., Florentz, C., Fritzsch, G., et al. (2013). Mitos: Improved *de novo* metazoan mitochondrial genome annotation. *Mol. Phylogenet. Evol.* 69, 313–319. doi: 10.1016/j.ympev.2012.08.023

Bianco-Stein, N., Polishchuk, I., Seiden, G., Villanova, J., Rack, A., Zaslansky, P., et al. (2020). Helical microstructures of the mineralized coralline red algae determine their mechanical properties. *Adv. Sci. (Weinh)* 7, 2000108. doi: 10.1002/advs.202000108

Bolger, A. M., Lohse, M., and Usadel, B. (2014). Trimmomatic: A flexible trimmer for illumina sequence data. *Bioinformatics* 30, 2114–2120. doi: 10.1093/bioinformatics/btu170

Brar, G. A., and Weissman, J. S. (2015). Ribosome profiling reveals the what, when, where and how of protein synthesis. *Nat. Rev. Mol. Cell Biol.* 16, 651–664. doi: 10.1038/nrm4069

Buchfink, B., Xie, C., and Huson, D. H. (2015). Fast and sensitive protein alignment using diamond. *Nat. Methods* 12, 59–60. doi: 10.1038/nmeth.3176

Clark, M. S. (2020). Molecular mechanisms of biomineralization in marine invertebrates. *J. Exp. Biol.* 223, jeb206961. doi: 10.1242/jeb.206961

Di, G., Kong, X., Miao, X., Zhang, Y., Huang, M., Gu, Y., et al. (2017). Proteomic analysis of trochophore and veliger larvae development in the small abalone *haliotis diversicolor*. *BMC Genomics* 18, 809. doi: 10.1186/s12864-017-4203-7

Drennan, R., Wiklund, H., Rouse, G. W., Georgieva, M. N., Wu, X., Kobayashi, G., et al. (2019). Taxonomy and phylogeny of mud owls (annelida: Sternaspidae), including a new synonymy and new records from the southern ocean, north east atlantic ocean and pacific ocean: Challenges in morphological delimitation. *Mar. Biodiversity* 49, 2659–2697. doi: 10.1007/s12526-019-00998-0

Fang, Z., Yan, Z., Li, S., Wang, Q., Cao, W., Xu, G., et al. (2008). Localization of calmodulin and calmodulin-like protein and their functions in biomineralization in *p. fucata*. *Prog. Natural Sci.* 18, 405–412. doi: 10.1016/j.pnsc.2007.11.011

Fiege, D., and Barnich, R. (2020). A new genus and species of sternaspidae (annelida: Polychaeta) from the deep eastern atlantic. *Eur. J. Taxonomy* 699, 1–13. doi: 10.5852/ejt.2020.699

Goodrich, E. (1897). Memoirs: Notes on the anatomy of sternaspis. *Q. J. Microscopical Sci.* 40, 233–245. doi: 10.1242/jcs.s2-40.158.233

Grabherr, M. G., Haas, B. J., Yassour, M., Levin, J. Z., Thompson, D. A., Amit, I., et al. (2011). Trinity: Reconstructing a full-length transcriptome without a genome from rna-seq data. *Nat. Biotechnol.* 29, 644. doi: 10.1038/nbt.1883

Guan, Y., He, M., and Wu, H. (2017). Differential mantle transcriptomics and characterization of growth-related genes in the diploid and triploid pearl oyster *pinctada fucata*. *Mar. Genomics* 33, 31–38. doi: 10.1016/j.margen.2017.01.001

Guo, D., Keightley, A., Guthrie, J., Veno, P. A., Harris, S. E., and Bonewald, L. F. (2010). Identification of osteocyte-selective proteins. *Proteomics* 10, 3688–3698. doi: 10.1002/pmic.201000306

Heffernana1, P. (1990). Ultrastructural studies of the elytra of *pholoe minuta* (annelida: Polychaeta) with special reference to functional morphology. *J. Mar. Biol. Assoc. United Kingdom* 70, 545–556. doi: 10.1017/S0025315400036572

Hoffman, J. I., Peck, L. S., Hillyard, G., Zieritz, A., and Clark, M. S. (2009). No evidence for genetic differentiation between antarctic limpet *nacella concinna* morphotypes. *Mar. Biol.* 157, 765–778. doi: 10.1007/s00227-009-1360-5

Jin-Bao, W., Xin-Zheng, L., and Hong-Fa, W. (2006). Ecological characteristics of dominant polychaete species from the jiaozhou bay. *Curr. Zool* 52, 63–70. doi: 10.3969/j.issn.1674-5507.2006.01.007

Kanehisa, M., Araki, M., Goto, S., Hattori, M., Hirakawa, M., Itoh, M., et al. (2007). Kegg for linking genomes to life and the environment. *Nucleic Acids Res.* 36, D480–D484. doi: 10.1093/nar/gkm882

Kisailus, D., and Nemoto, M. (2018). *Structural and proteomic analyses of iron oxide biomineralization in chiton teeth biological magnetic materials and applications* (Singapore: Springer), 53–73. doi: 10.1007/978-981-10-8069-2_3

Kumar, S., Stecher, G., and Tamura, K. (2016). Mega7: Molecular evolutionary genetics analysis version 7.0 for bigger datasets. *Mol. Biol. Evol.* 33, 1870–1874. doi: 10.1093/molbev/msw054. evolution.

Langmead, B., and Salzberg, S. L. (2012). Fast gapped-read alignment with bowtie 2. *Nat. Methods* 9, 357–359. doi: 10.1038/nmeth.1923

Le Pabic, C., Marie, A., Marie, B., Percot, A., Bonnaud-Ponticelli, L., Lopez, P. J., et al. (2017). First proteomic analyses of the dorsal and ventral parts of the *sepia officinalis* cuttlebone. *J. Proteomics* 150, 63–73. doi: 10.1016/j.jprot.2016.08.015

Liao, Q., Qin, Y., Zhou, Y., Shi, G., Li, X., Li, J., et al. (2021). Characterization and functional analysis of a chitinase gene: Evidence of ch-chit participates in the regulation of biomineralization in *crassostrea hongkongensis*. *Aquaculture Rep.* 21, 100852. doi: 10.1016/j.aqrep.2021.100852

Li, W., Jaroszewski, L., and Godzik, A. (2001). Clustering of highly homologous sequences to reduce the size of large protein databases. *Bioinformatics* 17, 282–283. doi: 10.1093/bioinformatics/17.3.282

Liu, C., Ji, X., Huang, J., Wang, Z., Liu, Y., and Hincke, M. T. (2021). Proteomics of shell matrix proteins from the cuttlefish bone reveals unique evolution for cephalopod biomineralization. *ACS Biomaterials Sci. Eng.* 2373–9878, 1–12. doi: 10.1021/acsbiomaterials.1c00693

Livak, K. J., and Schmittgen, T. D. (2001). Analysis of relative gene expression data using real-time quantitative pcr and the $2^{-\delta\delta ct}$ method. *Methods* 25, 402–408. doi: 10.1006/meth.2001.1262

Llovet, X., Moy, A., Pinard, P. T., and Fournelle, J. H. (2021). Reprint of: Electron probe microanalysis: A review of recent developments and applications in materials science and engineering. *Prog. Materials Sci.* 120, 100818. doi: 10.1016/j.pmatsci.2021.100818

Lowenstam, H. A. (1972). Phosphatic hard tissues of marine invertebrates: Their nature and mechanical function, and some fossil implications. *Chem. Geology* 9, 153–166. doi: 10.1016/0009-2541(72)90053-8

Luo, Y.-J. (2017). *Insights into lophotrochozoan evolution and the origin of morphological novelties from brachiopod, phoronid, and nemertean genomes*. PhD Thesis. Okinawa Institute of Science and Technology Graduate University.

Luo, Y. J., Takeuchi, T., Koyanagi, R., Yamada, L., Kanda, M., Khalturina, M., et al. (2015). The *lingula* genome provides insights into brachiopod evolution and the origin of phosphate biomineralization. *Nat. Commun.* 6, 8301. doi: 10.1038/ncomms9301

Malachowicz, M., and Wenne, R. (2019). Mantle transcriptome sequencing of mytilus spp. and identification of putative biomineralization genes. *PeerJ* 6, e6245. doi: 10.7717/peerj.6245

Manno, D., Carata, E., Tenuzzo, B. A., Panzarini, E., Buccolieri, A., Filippo, E., et al. (2012). High ordered biomineralization induced by carbon nanoparticles in the sea urchin *paracentrotus lividus*. *Nanotechnology* 23, 495104. doi: 10.1088/0957-4484/23/49/495104

Mao, J., Zhang, W., Wang, X., Song, J., Yin, D., Tian, Y., et al. (2019). Histological and expression differences among different mantle regions of the yesso scallop (*patinopecten yessoensis*) provide insights into the molecular mechanisms of biomineralization and pigmentation. *Mar. Biotechnol.* 21, 683–696. doi: 10.1007/s10126-019-09913-x

Marcus, M. A., Amini, S., Stifler, C. A., Sun, C. Y., Tamura, N., Bechtel, H. A., et al. (2017). Parrotfish teeth: Stiff biominerals whose microstructure makes them tough and abrasion-resistant to bite stony corals. *ACS Nano* 11, 11856–11865. doi: 10.1021/acsnano.7b05044

Matsuura, A., Yoshimura, K., Kintsu, H., Atsumi, T., Tsuchihashi, Y., Takeuchi, T., et al. (2018). Structural and functional analyses of calcium ion response factors in the mantle of *pinctada fucata*. *J. Struct. Biol.* 204, 240–249. doi: 10.1016/j.jsb.2018.08.014

Michalek, K. (2019). *Scottish Mussel culture in the natural environment: Observations and implications for industry*. PhD Thesis. (University of Aberdeen).

Mistry, J., Finn, R. D., Eddy, S. R., Bateman, A., and Punta, M. (2013). Challenges in homology search: Hmmer3 and convergent evolution of coiled-coil regions. *Nucleic Acids Res.* 41, 121–121. doi: 10.1093/nar/gkt263

Murdock, D. J. E. (2020). The 'biomineralization toolkit' and the origin of animal skeletons. *Biol. Rev. Cambridge Philos. Soc.* 95, 1372–1392. doi: 10.1111/brv.12614

Murray, C. (2018). Patterns in nature: Why the natural world looks the way it does. *Crystallogr. Rev.* 24, 205–206. doi: 10.1080/0889311X.2018.1447569

Nakamura, K., Watanabe, H., Miyazaki, J., Takai, K., Kawagucci, S., Noguchi, T., et al. (2012). Discovery of new hydrothermal activity and chemosynthetic fauna on the central indian ridge at 18° -20°s. *PloS One* 7, e32965. doi: 10.1371/journal.pone.0032965

Nemoto, M., Ren, D., Herrera, S., Pan, S., Tamura, T., Inagaki, K., et al. (2019). Integrated transcriptomic and proteomic analyses of a molecular mechanism of radular teeth biomineralization in *cryptochiton stelleri*. *Sci. Rep.* 9, 856. doi: 10.1038/s41598-018-37839-2

Nemoto, M., Wang, Q., Li, D., Pan, S., Matsunaga, T., and Kisailus, D. (2012). Proteomic analysis from the mineralized radular teeth of the giant pacific chiton, *cryptochiton stelleri* (mollusca). *Proteomics* 12, 2890–2894. doi: 10.1002/pmic.201100473

Nguyen, L.-T., Schmidt, H. A., Von Haeseler, A., and Minh, B. Q. (2015). Iq-tree: A fast and effective stochastic algorithm for estimating maximum-likelihood phylogenies. *Mol. Biol. Evol.* 32, 268–274. doi: 10.1093/molbev/msu300

Nurk, S., Bankevich, A., Antipov, D., Gurevich, A., Korobeynikov, A., Lapidus, A., et al. (2013). Assembling genomes and mini-metagenomes from highly chimeric reads. *Res. Comput. Mol. Biol.* 7821, 158–170. doi: 10.1007/978-3-642-37195-0_13

Pi, M., Spurney, R. F., Tu, Q., Hinson, T., and Quarles, L. D. (2002). Calcium-sensing receptor activation of rho involves filamin and rho-guanine nucleotide exchange factor. *Endocrinology* 143, 3830–3838. doi: 10.1210/en.2002-220240

Rose-Martel, M., Smiley, S., and Hincke, M. T. (2015). Novel identification of matrix proteins involved in calcitic biomineralization. *J. Proteomics* 116, 81–96. doi: 10.1016/j.jprot.2015.01.002

Salazar-Vallejo, S. I., and Buzhinskaja, G. (2013). Six new deep-water sternaspid species (annelida, sternaspidae) from the pacific ocean. *Zookeys* 384, 1–27. doi: 10.3897/zookeys.348.5449

Sandoval-Castillo, J., Gates, K., Brauer, C. J., Smith, S., Bernatchez, L., and Beheregaray, L. B. (2020). Adaptation of plasticity to projected maximum temperatures and across climatically defined bioregions. *Proc. Natl. Acad. Sci. U. S. A.* 117, 17112–17121. doi: 10.1073/pnas.1921124117

Sato, A., Nagasaka, S., Furihata, K., Nagata, S., Arai, I., Saruwatari, K., et al. (2011). Glycolytic intermediates induce amorphous calcium carbonate formation in crustaceans. *Nat. Chem.* 7, 197–199. doi: 10.1038/nchembio.532

Sendall, K., and Salazar-Vallejo, S. I. (2013). Revision of sternaspis otto 1821 (polychaeta, sternaspidae). *Zookeys* 286, 1–74. doi: 10.3897/zookeys.286.4438

Shi, Y., Xu, M., Huang, J., Zhang, H., Liu, W., Ou, Z., et al. (2019). Transcriptome analysis of mantle tissues reveals potential biomineralization-related genes in *tectus pyramis* born. *Comp. Biochem. Physiol. Part D Genomics Proteomics* 29, 131–144. doi: 10.1016/j.cbd.2018.11.010

Shi, Y., Yu, C., Gu, Z., Zhan, X., Wang, Y., and Wang, A. (2013). Characterization of the pearl oyster (*pinctada martensii*) mantle transcriptome unravels biomineralization genes. *Mar. Biotechnol. (NY)* 15, 175–187. doi: 10.1007/s10126-012-9476-x

Sun, Y., Sun, J., Yang, Y., Lan, Y., Ip, J. C., Wong, W. C., et al. (2021). Genomic signatures supporting the symbiosis and formation of chitinous tube in the deep-sea tubeworm *paraescarpia echinospica*. *Mol. Biol. Evol.* 38, 4116–4134. doi: 10.1093/molbev/msab203

Takeuchi, T., Fujie, M., Koyanagi, R., Plasseraud, L., Ziegler-Devin, I., Brosse, N., et al. (2021). The 'shellome' of the crocus clam *tridacna crocea* emphasizes essential components of mollusk shell biomineralization. *Front. Genet.* 12, 674539. doi: 10.3389/fgene.2021.674539

Takeuchi, T., Yamada, L., Shinzato, C., Sawada, H., and Satoh, N. (2016). Stepwise evolution of coral biomineralization revealed with genome-wide proteomics and transcriptomics. *PloS One* 11, e0156424. doi: 10.1371/journal.pone.0156424

Tanur, A. E., Gunari, N., Sullan, R. M. A., Kavanagh, C. J., and Walker, G. C. (2010). Insights into the composition, morphology, and formation of the calcareous shell of the serpulid *hydroides dianthus*. *J. Struct. Biol.* 169, 145–160. doi: 10.1016/j.jsb.2009.09.008

Trapnell, C., Williams, B. A., Pertea, G., Mortazavi, A., Kwan, G., Van Baren, M. J., et al. (2010). Transcript assembly and quantification by rna-seq reveals unannotated transcripts and isoform switching during cell differentiation. *Nat. Biotechnol.* 28, 511–515. doi: 10.1038/nbt.1621

Tyszka, J., Bickmeyer, U., Raitzsch, M., Bijma, J., Kaczmarek, K., Mewes, A., et al. (2019). Form and function of f-actin during biomineralization revealed from live experiments on foraminifera. *Proc. Natl. Acad. Sci. U. S. A.* 116, 4111–4116. doi: 10.1073/pnas.1810394116

Vinn, O. (2021). Biomineralization in polychaete annelids: A review. *Minerals* 11, 1151. doi: 10.3390/min11101151

Vinn, O., Ten Hove, H. A., and Mutvei, H. (2008). On the tube ultrastructure and origin of calcification in sabellids (annelida, polychaeta). *Palaeontology* 51, 295–301. doi: 10.1111/j.1475-4983.2008.00763.x

Weigert, A., Golombek, A., Gerth, M., Schwarz, F., Struck, T. H., and Bleidorn, C. (2015). Evolution of mitochondrial gene order in annelida. *Mol. Phylogenet. Evol.* 94, 353–366. doi: 10.1016/j.ympev.2015.08.008

Wilt, F. H., and Killian, C. E. (2008). What genes and genomes tell us about calcium carbonate biomineralization. *Biomineralization: From Nat. to Appl.* 4, 36–69.

Wu, X., Salazar-Vallejo, S. I., and Xu, K. (2015). Two new species of sternaspis otto 1821 (polychaeta: Sternaspidae) from china seas. *Zootaxa* 4052, 373–382. doi: 10.11646/zootaxa.4052.3.7

Yamagata, N., Randall, G., Lavoie, E., Arola, D., and Wang, J. (2022). Microstructure, mechanical properties and elemental composition of the terrestrial isopod armadillidium vulgare cuticle. *J. Mech. Behav. BioMed. Mater* 132, 105299. doi: 10.1016/j.jmbbm.2022.105299

Yan, Z., Fang, Z., Ma, Z., Deng, J., Li, S., Xie, L., et al. (2007). Biomineralization: Functions of calmodulin-like protein in the shell formation of pearl oyster. *Biochim. Biophys. Acta* 1770, 1338–1344. doi: 10.1016/j.bbagen.2007.06.018

Yarra, T., Blaxter, M., and Clark, M. S. (2021). A bivalve biomineralization toolbox. *Mol. Biol. Evol.* 38, 4043–4055. doi: 10.1093/molbev/msab153

Yévenes, M., Núñez-Acuña, G., Gallardo-Escárate, C., and Gajardo, G. (2022). Adaptive mitochondrial genome functioning in ecologically different farm-impacted natural seedbeds of the endemic blue mussel *mytilus chilensis*. *Comp. Biochem. Physiol. Part D: Genomics Proteomics* 42, 100955. doi: 10.1016/j.cbd.2021.100955

Young, M. D., Wakefield, M. J., Smyth, G. K., and Oshlack, A. (2010). Gene ontology analysis for rna-seq: Accounting for selection bias. *Genome Biol.* 11, 1–12. doi: 10.1186/gb-2010-11-2-r14

Zhang, Y., Liu, Z., Song, X., Huang, S., Wang, L., and Song, L. (2019). The inhibition of ocean acidification on the formation of oyster calcified shell by regulating the expression of cgchs1 and cgchit4. *Front. Physiol.* 10, 1034. doi: 10.3389/fphys.2019.01034

Zieritz, A., Hoffman, J. I., Amos, W., and Aldridge, D. C. (2010). Phenotypic plasticity and genetic isolation-by-distance in the freshwater mussel *unio pictorum* (mollusca: Unionoida). *Evolutionary Ecol.* 24, 923–938. doi: 10.1007/s10682-009-9350-0

Frontiers in Marine Science

Explores ocean-based solutions for emerging global challenges

The third most-cited marine and freshwater biology journal, advancing our understanding of marine systems and addressing global challenges including overfishing, pollution, and climate change.

Discover the latest Research Topics

See more →

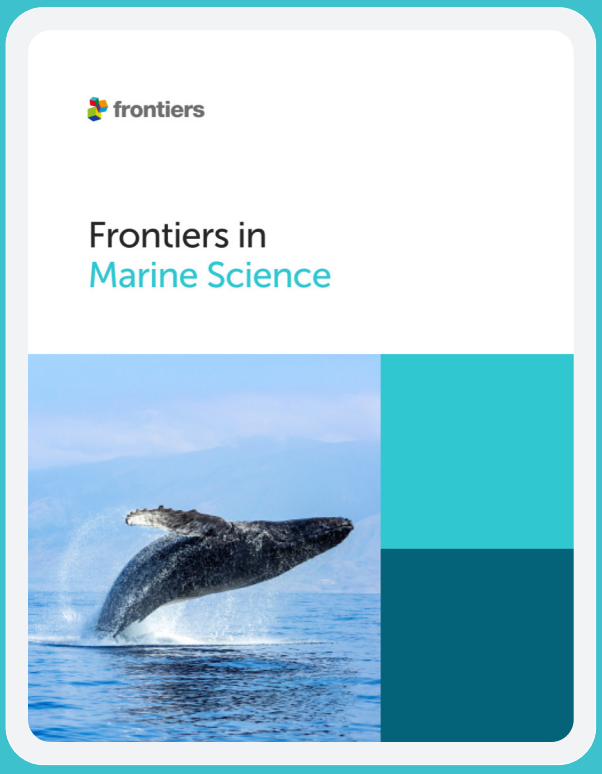

Frontiers

Avenue du Tribunal-Fédéral 34
1005 Lausanne, Switzerland
frontiersin.org

Contact us

+41 (0)21 510 17 00
frontiersin.org/about/contact